Strongly-Guided InP/$\mathrm{In}_{1-x}\mathrm{Ga}_x\mathrm{As}_y\mathrm{P}_{1-y}$ Mach-Zehnder Modulator for Optical Communications

by

IAN BRIAN BETTY

A thesis
presented to the University of Waterloo
in fulfilment of the
thesis requirement for the degree of
Doctor of Philosophy
in
Physics

Waterloo, Ontario, Canada, 2005

Library and
Archives Canada

Published Heritage
Branch

395 Wellington Street
Ottawa ON K1A 0N4
Canada

Bibliothèque et
Archives Canada

Direction du
Patrimoine de l'édition

395, rue Wellington
Ottawa ON K1A 0N4
Canada

Your file Votre référence
ISBN: 978-0-494-17436-4
Our file Notre référence
ISBN: 978-0-494-17436-4

NOTICE:
The author has granted a non-exclusive license allowing Library and Archives Canada to reproduce, publish, archive, preserve, conserve, communicate to the public by telecommunication or on the Internet, loan, distribute and sell theses worldwide, for commercial or non-commercial purposes, in microform, paper, electronic and/or any other formats.

The author retains copyright ownership and moral rights in this thesis. Neither the thesis nor substantial extracts from it may be printed or otherwise reproduced without the author's permission.

AVIS:
L'auteur a accordé une licence non exclusive permettant à la Bibliothèque et Archives Canada de reproduire, publier, archiver, sauvegarder, conserver, transmettre au public par télécommunication ou par l'Internet, prêter, distribuer et vendre des thèses partout dans le monde, à des fins commerciales ou autres, sur support microforme, papier, électronique et/ou autres formats.

L'auteur conserve la propriété du droit d'auteur et des droits moraux qui protège cette thèse. Ni la thèse ni des extraits substantiels de celle-ci ne doivent être imprimés ou autrement reproduits sans son autorisation.

In compliance with the Canadian Privacy Act some supporting forms may have been removed from this thesis.

While these forms may be included in the document page count, their removal does not represent any loss of content from the thesis.

Conformément à la loi canadienne sur la protection de la vie privée, quelques formulaires secondaires ont été enlevés de cette thèse.

Bien que ces formulaires aient inclus dans la pagination, il n'y aura aucun contenu manquant.

Canada

Abstract

The development of strongly-guided $InP/In_{1-x}Ga_xAs_yP_{1-y}$ based Mach-Zehnder optical modulators for 10Gb/s telecommunications is detailed. The modulators have insertion losses including coupling as low as 4.5dB, due to the incorporation of monolithically integrated optical mode spot-size converters (SSC's.) The modulators are optimized to produce system performance that is independent of optical coupling alignment and for wavelength operation between 1525nm and 1565nm. A negatively chirped Mach-Zehnder modulator design is demonstrated, giving optimal dispersion-limited reach for 10Gb/s ON/OFF-keying modulation. It is shown that the optical system performance for this design can be determined from purely DC based optical measurements. A Mach-Zehnder modulator design invoking nearly no transient frequency shifts under intensity modulation is also presented, for the first time, using phase-shifter implementations based on the Quantum-Confined-Stark-Effect (QCSE.)

The performance impact on the modulator from the higher-order vertical and lateral waveguide modes found in strongly-guided waveguides has been determined. The impact of these higher-order modes has been minimized using the design of the waveguide bends, MMI structures, and doping profiles. The fabrication process and optical design for the spot-size mode converters are also thoroughly explored. The SSC structures are based on butt-joined vertically tapered passive waveguide cores within laterally flared strongly-guided ridges, making them compatible with any strong-guiding waveguide structure. The flexibility of the SSC process is demonstrated by the superior performance it has also enabled in a 40Gb/s electro-absorption modulator. The presented electro-absorption modulator has 3.6dB fiber-to-fiber insertion loss, polarization dependent loss (PDL) of only 0.3dB over 15dB extinction, and low absolute chirp ($|\alpha_H| < 0.6$) over the full dynamic range.

Acknowledgments

I would like to thank my supervisor, Dr. David Yevick, for his essential guidance and support. I wish to express my sincere appreciation to Dr. Marcel Boudreau, Dr. Kelvin Prosyk, Dr. Richard Glew, Dr. Jonathan Greenspan, Dr. Frank Shepherd, Dr. Robert Griffin, Keith Anderson, Richard Clayton, and Robert Foster for sharing ideas and many fruitful discussions. I also wish to gratefully acknowledge my many other colleagues at both NORTEL Networks and Bookham. Finally, thanks goes to my wife, Christine Andress, for her continuous understanding and support during this endeavour.

Dedication

Dedicated to Penny and Brian Betty. Better late than never.

Felix qui potuit rerum cognoscere causas

Lucky is he who has been able to understand the causes of things

Virgil 70-19BC: *Georgics*

Contents

List Of Abbreviations

Acronym	Definition
3D	three dimensional
AC	alternating current
AFM	atomic force microscopy
BER	bit error rate
BPM	beam propagation method
C-Band	conventional erbium-doped fiber amplifier band
CoC	chip-on-carrier
DC	direct current
DEKTAK	trade name surface profiler
DFB	distributed feedback (laser)
DML	directly modulated laser
DP	dispersion penalty
DS-DBR	digital supermode distributed feedback reflector (laser)
DWDM	dense wavelength division multiplexing
EAM	electroabsorption modulator
EDFA	erbium-doped fiber amplifier
EF	enhancement factor
EIM	effective index method
EML	electroabsorption modulated laser
ER	extinction ratio
FDTD	finite difference time domain
FE-AES	field emission auger spectroscopy
FSRM	free space radiation method
FWHM	full width half maximum
HF	hydrofluoric acid
IBD	ion beam deposition (facet coating technique)
ICP	inductively coupled plasma (etch tool)
III-V	semiconductor based on group III and group V elements

Acronym	Definition
L-Band	long-wavelength erbium-doped fiber amplifier band
LEO	linear electro-optic effect
LIH	linear, isotropic and homogeneous
$LiNbO_3$	Lithium Niobate (modulator)
LV	light-voltage (curve)
MMI	multi-mode interference
MOCVD	metalorganic chemical vapour deposition
MORI	trade name for dielectric etch tool
MOVPE	metalorganic vapour phase epitaxy (same as MOCVD)
MPA	mode propagation method
MQW	multi-quantum well
MZ	Mach-Zehnder
n-i-n	semiconductor doping profile [n-intrinsic-n]
No	reference refractive index for BPM
NRZ	non return to zero (modulation format)
OLCR	optical low coherence reflectometry
OSNR	optical signal to noise ratio
PDL	polarization dependent loss
PECVD	dielectric deposition method
PIC	photonic integrated circuit
p-i-n	semiconductor doping profile [p-intrinsic-n]
PL	photoluminescence
PML	perfectly matched layer
PRBS	pseudo random bit sequence
Q	InGaAsP bandgap expressed by photon wavelength
QCSE	quantum confined stark effect
RC	resistance-capacitance
RF	radio frequency
RIE	reactive ion etch
SAG	selective area growth
SCCM	standard cubic centimeter per minute
SELFOC	trade name derived from self focusing (lens)

Acronym	Definition
SEM	scanning electron microscopy
SFF	transponder module standard form factor
SFP	2.5Gb/s transceiver module standard form factor
SGDBR	sampled grating distributed feedback reflector (laser)
SIMS	secondary ion mass spectroscopy
SMF	single mode fiber
SOA	semiconductor optical amplifier
SSC	spot size converter
SSRM	scanning spreading resistance microscopy
TE	transverse electric (polarization state)
TEC	thermal electric cooler
TEG	triethyl gallium (MOCVD precursor)
TEM	tunneling electron microscopy
TIR	total internal reflection
TM	transverse magnetic (polarization state)
TMI	trimethyl indium (MOCVD precursor)
UV	ultraviolet
V	Volts
WDM	wavelength division multiplexing
XFP	10Gb/s transceiver module standard form factor

Chapter 1

InP Mach-Zehnder Modulators for Optical Communications

A brief introduction to digital optical communication systems is given in Section 1.1 and an overview of the options for ON/OFF intensity modulation of data are discussed in Section 1.2. The Mach-Zehnder modulator design is introduced in Section 1.3 and the reasons for pursuing an InP-based implementation are outlined in Section 1.4. A detailed and current review[1] of the InP-based Mach-Zehnder modulators presented in the literature is provided in Section 1.5. This is followed in Section 1.6 by an outlined of the InP-based Mach-Zehnder modulator design developed in this thesis. The device operation and the system performance of the fabricated Mach-Zehnder modulators is detailed in the remainder of this Chapter.

1.1 Digital Optical Communication Systems

The transmission medium for high-speed digital optical communication systems is the single mode optical fiber (SMF), and Corning's SMF-28[2] design is the most widely deployed in the field. SMF-28 is a step-index glass fiber containing a doped 8.2μm thick core having a +0.36% refractive index increase relative to the SiO_2 cladding. The outside cladding diameter of the fiber is 125.0$\pm$0.7μm. Its attenuation is typically 0.20dB/km at 1550nm with no more than 0.02dB/km variation between 1525nm and 1575nm. The specification for the zero dispersion wavelength (λ_0) is 1302nm$\leq \lambda_0 \leq$ 1322nm, with a zero dispersion slope $S_0 \leq 0.092$ps/(nm$^2\cdot$km). The wavelength dispersion D(λ) of the fiber is given by:

$$D(\lambda) \approx \frac{S_0}{4}\left[\lambda - \frac{\lambda_0^4}{\lambda^3}\right] ps/(nm \cdot km) \tag{1.1}$$

---

[1] The review is current to September 2005.

[2] The most recent specification is SMF-28e.

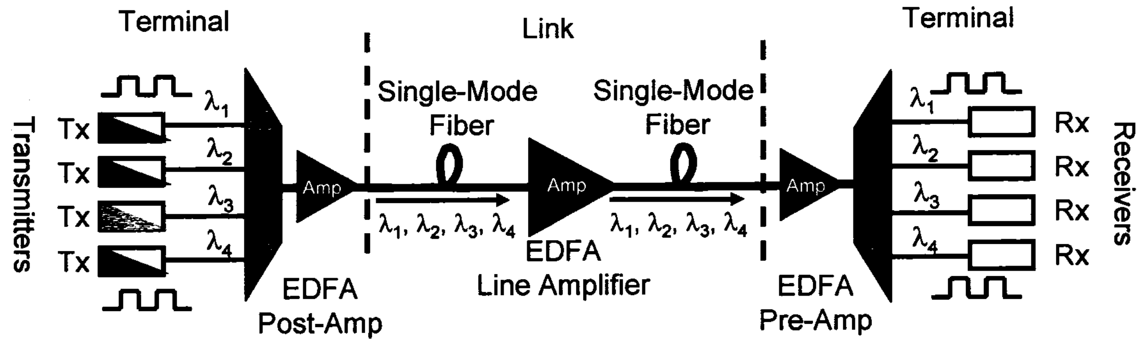

Figure 1.1: *Schematic of a Amplified Optical Fiber Communication System.*

for operating wavelengths between λ=1200nm and λ=1625nm. At 1550nm the dispersion of SMF-28 optical fiber is 16.8-18.2ps/(nm·km).

With the development of the Erbium Doped Fiber Amplifier (EDFA) in the early 1990's, the optical system fiber link length between transmission and detection became no longer loss-limited. This enabled the wavelength-division-multiplexing, shown in Figure 1.1, to be cost-effectively introduced in digital optical communication systems, providing explosive growth in the transmission capacity of optical networks. The EDFA provides optical gain simultaneously to all wavelength channels located within its gain bandwidth, compensating for the ≈0.2dB/km optical loss in SMF. The conventional EDFA gain bandwidth is often referred to as the C-Band, covering 196.3THz [1527.216nm] to 191.55THz [1565.087nm.] The centre of the C-Band is located at 1546.1515nm and it covers a total wavelength range of 37.9nm. In a dense WDM optical networks individual wavelength channels are typically separated by 50GHz-200GHz, allowing up to ≈95 wavelength channels within the EDFA C-Band. The 38nm gain bandwidth of the C-Band EDFA provides a target for desirable wavelength tunability in optical transmitter designs. Long-wavelength (L-Band) EDFA's are also commercially available to provide gain for operating wavelengths between ≈1565nm and ≈1605nm.

Long-reach digital optical communication systems now typically operate over amplified single mode fiber links, in a wavelength division multiplexed (WDM) configuration about a centre wavelength of 1.55μm. A schematic of a optical fiber communication system is given in Figure 1.1. The individual transmitters typically encode data signals onto unique wavelength channels using simple ON/OFF intensity modulation at a line rate of 2.5Gb/s or 10Gb/s. The wavelength channels are then optically multiplexed for transmission over the amplified SMF link. Following wavelength demultiplexing the intensity modulated data in each wavelength channel is detected using direct envelope photo-detection at the receiver.

The transmission of optical data over SMF became chromatic-dispersion-limited when the loss constraint was removed by the introduction of EDFA amplifiers. Optical information transmitted at high data rates has significant frequency content; in addition to the

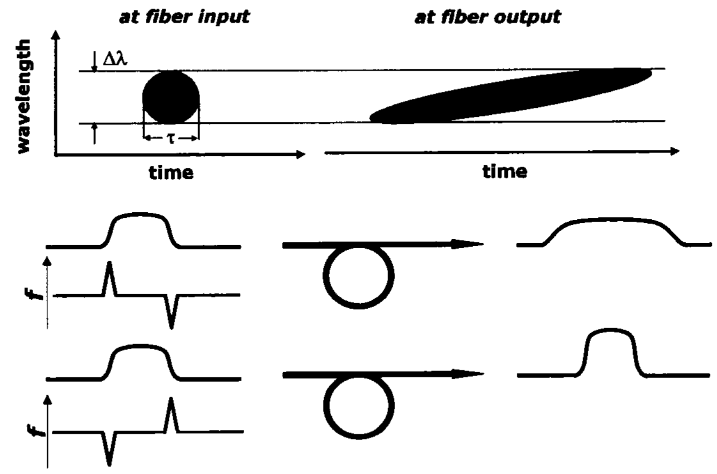

Figure 1.2: ***Impact of Rising and Falling Edge Frequency Chirp on Pulse Propagation in Optical Fiber, Figure provided by Robert Whiteman.***

information bandwidth and the linewidth of the optical source, there is often a transient change in wavelength at bit transitions (called frequency chirp.) The frequency content in a transmitted signal is transformed to a spread in the time domain by the dispersion of the SMF, defined in Equation 1.1. As illustrated in Figure 1.2, to enable pulse compression for long-reach communications over standard single-mode optical fiber, the leading edge of a pulse must possess a negative transient frequency chirp (red shift) and the falling edge must possess a positive transient frequency chirp (blue shift). The frequency chirp causing pulse compression in standard single-mode fiber is termed negative frequency chirp by convention, likewise the frequency chirp that causes pulse spreading in standard single-mode fiber is termed positive frequency chirp.

1.2 Modulators for Optical Fiber Communications

Direct Modulation

The ON/OFF intensity modulation for digital fiber communication systems can be implemented by directly modulating the semiconductor laser source. This is a simple, compact and cost-effective approach, however, in practice the transmission distances are limited by a large positive frequency chirp, especially for 10Gb/s modulation. The source of this large positive frequency chirp is the variation in carrier density, caused by the modulated injected current, modifying the refractive index of the cavity, and causing wavelength variations in the laser output. At the rising edge of a pulse, when the laser is turned on, the laser output wavelength is blue-shifted. At the falling edge of a pulse, when the laser is turned off, the output wavelength of the laser becomes red-shifted. As shown in Figure 1.2 these transient wavelength shifts at "0" to "1" and "1" to "0" bit transitions will cause the

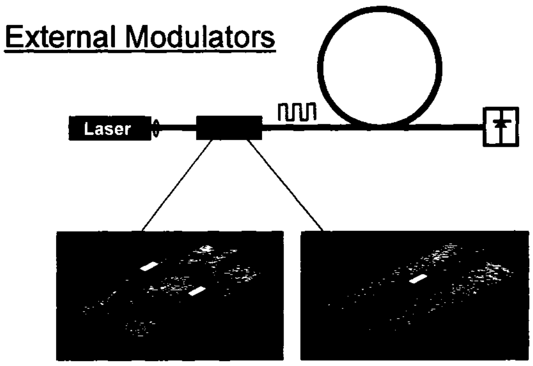

- **Refractive solutions**

Modifications to refractive index, resulting in changes in phase or direction of beam.
e.g. Linear electro-optic effect (LEO), Free carrier refraction, electro-absorption effects via the Kramers-Kronig relation.

- **Absorptive solutions**

Modify absorption coefficient, resulting in direct change in beam intensity.
e.g. Free carrier absorption, electro-absorption effects: Franz-Keldysh effect, Quantum Confined Stark Effect.

Figure 1.3: *External Modulation, Figure provided by Robert Whiteman.*

bit to spread when it is transmitted over standard single-mode optical fiber. The simplicity and low cost of direct laser modulation, however, has made it the dominant transmission source in 2.5Gb/s optical communication systems. DWDM directly modulated laser (DML) transmitter sources are commercially available for single span link lengths up to 360km [1].

External Modulation

External modulation can be used to allow for higher modulation speeds, larger ON/OFF ratios, and low/controllable frequency chirp, at the expense of implementation complexity and additional optical losses in the transmitter design. With external modulation, the narrow linewidth semiconductor laser source is run continuously, and the digital information is encoded using an external optical intensity modulator. These external optical intensity modulators can be categorized as either refractive or absorptive as shown in Figure 1.3. A tutorial on the modulation principles, material properties, optical design, and efficiency analysis for external optical intensity modulators was published by Li et al. [2] in 2003.

Only InP-based semiconductors have the appropriate operating wavelengths to enable absorptive modulators for long wavelength optical fiber communication systems[3]. Electro-absorptive modulators are typically very short (80-300μm) and are commercially available monolithically integrated with distributed feedback (DFB) laser sources [3]. These DWDM electro-absorption modulated lasers (EML) dominate deployment in 10Gb/s optical communication systems for single span link lengths up to 40km.

---

[3] Long wavelength optical fiber communication systems operate with wavelengths between 1300nm and 1610nm.

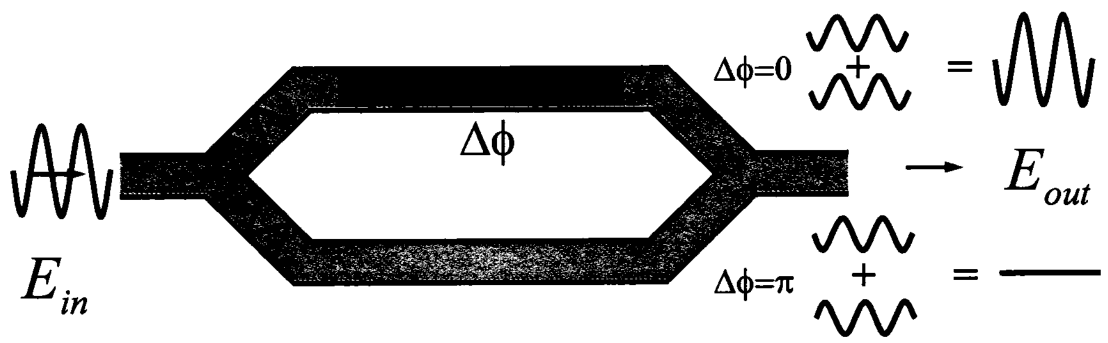

Figure 1.4: *Mach-Zehnder Modulator Operating Principle, Figure provided by Robert Whiteman.*

Refractive modulators have been implemented using Lithium Niobate ($LiNbO_3$), III-V semiconductors, and organic polymers. The first guided-wave Mach-Zehnder[4] interferometers capable of intensity modulating a laser beam were fabricated using $LiNbO_3$ in 1980 [4], and the first demonstration of Mach-Zehnder devices using semiconductors was reported by Donnelly et al. in 1984 [5]. The ability to accurately control the transient frequency chirp with a Mach-Zehnder interferometric optical modulator, along with the availability of a low-insertion loss implementation in Lithium Niobate ($LiNbO_3$), has made the Mach-Zehnder modulator dominant in long-distance optical communication systems at 10Gb/s or greater modulation.

The development of a low insertion loss InP-based Mach-Zehnder modulator for 10Gb/s long-distance optical communication systems is the focus of this thesis.

1.3 The Mach-Zehnder Optical Modulator

A Mach-Zehnder optical modulator uses an interferometric configuration of waveguides to enable the conversion of phase modulation into intensity modulation as shown in Figure 1.4. In a Mach-Zehnder modulator the continuous wave laser source signal is first split into two branches. A relative phase difference $\Delta\Phi$ is introduced between these branches, and then they are recombined at the output of the Mach-Zehnder modulator. When the differential phase shift $\Delta\Phi$ between the two arms equals $\pm\pi$, destructive interference occurs, corresponding to the off-state or "0" level for the modulator. With no differential phase shift, constructive interference occurs, corresponding to the on-state or "1" level for the modulator. In Mach-Zehnder modulators based on $LiNbO_3$, GaAs, or organic polymers, the phase difference $\Delta\Phi$ is introduced using the linear electro-optic (LEO) or Pockels effect. In InP-based semiconductor Mach-Zehnder modulators the phase difference is usually introduced using a combination of LEO and electro-absorption effects[5].

---

[4] The Mach-Zehnder interferometer was proposed independently by M. Mach and L.A. Zehnder in 1891.

[5] In multi-quantum well materials the Quantum Confined Stark Effect (QCSE) [6,7] induces strong index changes through the Kramers-Krönig relation.

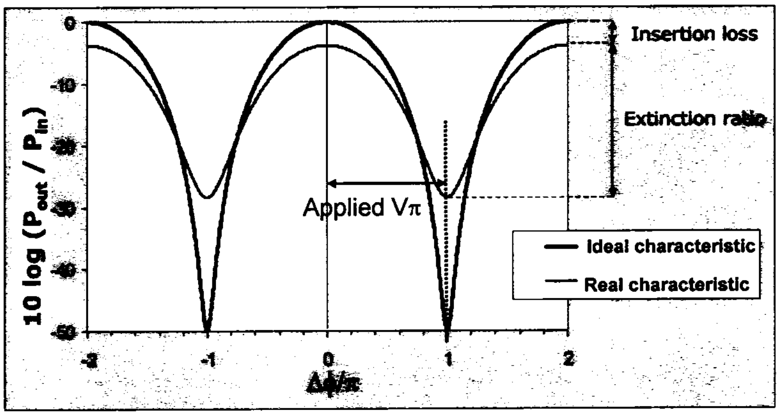

Figure 1.5: *Mach-Zehnder Modulator Transfer Function, Figure provided by Robert Whiteman.*

For equal splitting and combining ratios in the Mach-Zehnder modulator the transfer function for the transmitted power P_{out} has a cosine-squared dependence on half the phase difference between the branches,

$$P_{out} = E_{in}^2 \cos\left(\frac{\Delta\Phi}{2}\right) \tag{1.2}$$

The ideal and real characteristic transfer function of a Mach-Zehnder are shown in Figure 1.5. If the nominal phase difference between the two branches is π, such that the transfer function in normally off, the device would be called a π shifted design. Any deviation from the intended nominal phase between the branches for the Mach-Zehnder is referred to as the modulator imbalance.

There are five important characteristics for a Mach-Zehnder modulator: The ON/OFF or extinction ratio (ER), the insertion loss (IL), the required voltage for a π phase shift (V_π), the 3dB bandwidth (f_{3dB}), and the transient frequency chirp. The wavelength dependence of these modulator characteristics are also becoming more important with the recent advent of commercially available full C-Band tunable wavelength laser sources for digital communication systems. The ER, IL, and V_π are defined in Figure 1.5.

In a Mach-Zehnder modulator with lumped-element phase shift electrode designs, the electrode capacitance limits the 3dB bandwidth to,

$$f_{3dB} = \frac{1}{\pi RC} \tag{1.3}$$

where R and C are the load resistance and capacitance respectively. The Mach-Zehnder modulator developed in this thesis uses lumped-element phase shift electrode designs. To improve upon this limitation a traveling-wave RF transmission line can be arranged along side the optical waveguide to match the transmission velocity of the microwave signal to the propagation velocity of the optical mode. In this case the bandwidth for a lossless RF transmission line is given by [8],

$$f_{3dB} = \frac{1.39c_o}{\pi(n_g - n_m)L} \tag{1.4}$$

where n_m is the refractive index of the transmission line for the modulated microwave signal, n_g is the group index of the propagating optical mode in the modulator waveguide, c_o is the speed of light in a vacuum, and L is the length of the interaction.

The relative phase shift required to transition from the on-state to off-state in a Mach-Zehnder modulator must be π, however, the phase and magnitude contributions from each branch can be combined in several different ways to produce the desired sign and magnitude of net frequency chirp. For example, a push-pull electrical drive scheme on a Mach-Zehnder modulator with equal optical splitting and combining ratios, enables intensity modulation with no net frequency chirp. In a push-pull drive scheme a $\pi/2$ phase shift is added to each branch with a fixed applied voltage. In one branch the modulation voltage adds to the fixed voltage to increase the phase shift to π, while in the other arm the modulation voltage subtracts from the fixed applied voltage to decrease the phase shift to zero. The equal and opposite frequency chirp generated in the two branch signals of the modulator cancel when added at the output of the modulator during the on-state to off-state or off-state to on-state transition. The applied modulation voltage is sometimes specified as V_{p-p}.

1.4 Value of InP-Based Mach-Zehnder Modulators

A traditional transmitter optical assembly for 10Gb/s long-reach optical communications, state-of-the-art in the middle of the 1990's, is shown in Figure 1.6a. A fixed wavelength DFB laser source, a $LiNbO_3$ external Mach-Zehnder modulator, and an output optical power tap are mounted on a plastic tray that is used to route the connecting optical fibers with a controlled bend radius. Figure 1.6b shows a current state-of-the-art XFP[6] transceiver module, that provides the complete optical and electronic transmitter and receiver chains for serial 10Gb/s transmission over 40km of standard single-mode optical fiber. This XFP module is only several times larger than the gold box used for the DFB laser source in Figure 1.6a. The rise of standards-based 10Gb/s small-form-factor transponder[7] and transceiver[8] modules for digital optical communications is pushing disruptive changes in the size, power consumption and cost of opto-electronic components.

---

[6] XFP is short for 10Gb/s (X Roman numeral) Form-Factor Pluggable. It followed the SFP (Small Form-Factor Pluggable) for 2.5Gb/s modulation.

[7] 10Gb/s transponders include the complete optical and electronic transmitter and receiver chains for 10Gb/s transmission. This including the electrical multiplexing of lower bit rate input data and the electrical demultiplexing to lower bit rate output data. A transponder has pigtailed input and output optical fibers.

[8] 10Gb/s transceivers include the complete optical and electronic transmitter and receiver chains for serial 10Gb/s transmission. No electrical multiplexing or demultiplexing functions are provided. A transceiver has receptacle input and output fiber connectors.

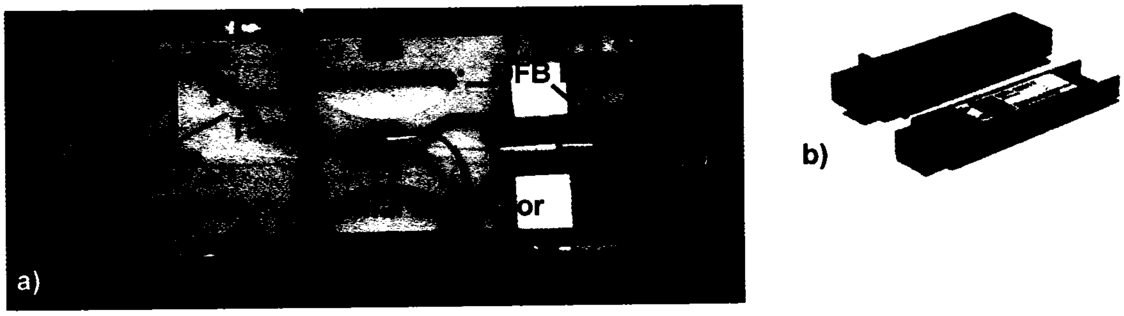

Figure 1.6: ***a) Transmitter Optical Assembly for 10Gb/s Long-Reach Optical Communications, b) XFP Transceiver Module.***

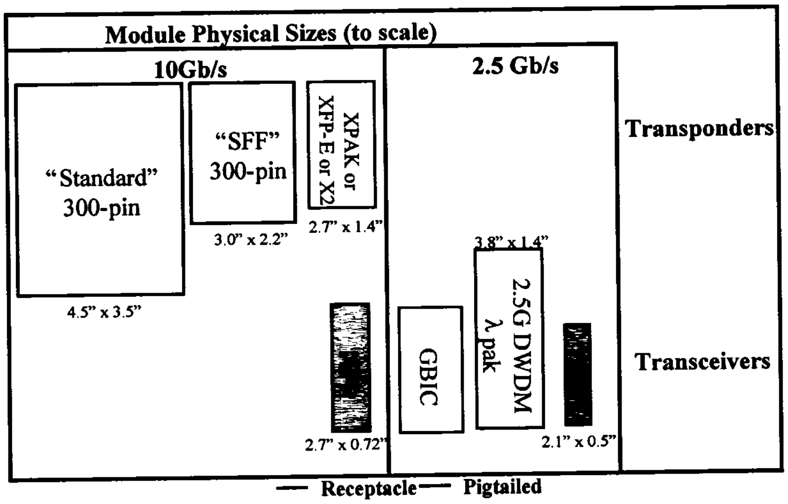

Figure 1.7: ***Size Comparison between the Standards-Based Form Factors For Transponder And Transceiver Modules.***

Figure 1.7 compares the size of the standards-based form factors for transponder and transceiver modules. The traditional $LiNbO_3$ Mach-Zehnder modulators for long-distance optical communications are not size compatible with transponders smaller than the standard 300pin design, and they are not at all size compatible with any of the transceiver form factors. As a result, InP-based Mach-Zehnder modulators, with their minimal footprint, low voltage drive requirements, and the potential for wideband tunability, are becoming increasingly attractive, since they can enable long-reach optical communications in the small-form-factor transponders and transceivers modules.

InP-based Mach-Zehnder modulators have not been as commercially successful in long-reach optical communications as $LiNbO_3$ based designs because they have traditionally suffered from substantially higher insertion losses[9]. In this thesis an InP-based Mach-

---

[9] InP-based Mach-Zehnder modulators have insertion losses typically greater than 10dB, compared with $LiNbO_3$ modulators with insertion losses typically less than 5dB.

Zehnder modulator is developed that provides insertion losses competitive with $LiNbO_3$ Mach-Zehnder modulators. Variants of this InP Mach-Zehnder modulator design have has been made commercially available co-packaged with a laser source in a footprint that enables SFF[10] transponders for 10Gb/s long-distance optical communications.

1.5 Review of InP-Based Mach-Zehnder Modulator Designs

In the Fall of 2000, at the beginning of this thesis work, the state-of-the-art in InP Mach-Zehnder modulator design was given by Rolland et al. [9]. The Mach-Zehnder design was based on strongly-guided p-i-n diode waveguides defined with a 2″ contact lithography process. The splitter and combiner functions were enabled using y-junctions [10]. The intrinsic core of the waveguide contained a multi-quantum well stack (MQW) with twenty 95Å thick Q=1.47μm[11] unstrained InGaAsP wells and twenty-one 80Å thick Q=1.1μm unstrained InGaAsP barriers [16–18]. Rolland et al. published pioneering work on the means to generate the optimal negative chirp for maximum dispersion-limited reach over standard optical fiber with these InP Mach-Zehnder modulators [11,12]. This optimal negative chirp generation required push-pull drive, on a normally-off π shifted modulator design, with non-equal optical split and combine ratios. The π phase shift between the modulator arms was incorporated using additional waveguide length in one of the s-bends following the y-junction splitter. Rolland et al. have also demonstrated monolithic integration of this Mach-Zehnder modulator with a DFB laser source [14]. As a student I measured the first of these integrated devices and studied their internal reflections as part of my Master's thesis [117]. The monolithically integrated Mach-Zehnder modulator has been published demonstrating 100km of reach at 10Gb/s with <1dB dispersion penalty [14]. As a discrete modulator at 10Gb/s, 120km of over-fiber reach has been demonstrated [13]. At 2.5Gb/s an over-fiber reach of 1102km has also been demonstrated for both the discrete and monolithic devices [15].

In 1996, Delansay and Penninckx et al. [19] at Alcatel, demonstrated a normally-on InP Mach-Zehnder modulator design that was very similar to the original design by Rolland et al. [9]. The split and combine functions were implemented using 3μm-6μm wide 1X2 MMI devices[12]. The total device insertion loss was 11dB. With this device Delansay and Penninckx et al. were the first to demonstrate system performance as a function of wavelength for an InP-based Mach-Zehnder modulator design [19]. The measured receiver sensitivity was given after 90-127km of standard single-mode fiber for 30nm of wavelength tuning with single-end drive in the normally-on Mach-Zehnder device. In a follow-up paper in 1997 Delansay and Penninckx et al. show [20] that a π phase-shifted Mach-Zehnder design enables constant receiver sensitivity after 133km of standard single-mode fiber by changing only the DC bias on the modulated phase shift electrode.

---

[10] SFF is short for Small Form Factor.

[11] The Q abbreviation is used to denote the peak photoluminescence of the material. In a MQW this peak will be an exciton resonance.

[12] The y-junction design presented by Rolland et al. [10] is actually a 4μm wide 1X2 MMI.

Following these two publications by Delansay and Penninckx et al. [19, 20] the Alcatel group moved away from transmission applications, to all-optical regeneration applications, for InP-based Mach-Zehnder modulators. Between 1998 and 2001 they published extensive analysis of various over-fiber systems using all-optical regeneration without providing any details on the optoelectronic devices required. In 2002 Shen et al. published [21] on a low insertion loss and polarization insensitive InP-based Mach-Zehnder modulator for 40Gbit/s optical regeneration. The device uses a bulk $Q=1.43\mu$m core in the <100> wafer orientation for polarization independent phase shifter operation. Separate phase and intensity modulation electrodes are present on the device. The high modulation bandwidth appears to be achieved with very short lumped-element electrodes, that produce low extinction ratios at reasonable voltages, i.e. 6dB extinction at -6V bias. The device incorporates butt-coupled passive waveguides with a $Q=1.05\mu$m core, however, this coupling structure appears to only include lateral waveguide tapers. The quoted minimum insertion loss is 9.2dB. This publication is one-year prior to the publication of the full lateral and vertical butt-jointed spot-size converter (SSC) developed in this thesis [244].

Sano et al. [22, 23] at Hitachi also published several early papers in the 1990's on InP-based Mach-Zehnder modulators. Both Alcatel and Hitachi, however, later proceeded to develop and concentrate commercially on DFB lasers integrated with electro-absorption modulators for transmitter applications.

There has been recent renewed interest in InP-based Mach-Zehnder modulator designs in the last three years with the rise of standards-based 10Gb/s small-form-factor transponders and transceivers in the marketplace. The InP-based Mach-Zehnder modulator is becoming increasingly seen as the technology of choice to enable long-haul, high performance, optical transmission, in these small footprint transponder form factors.

In 1996 NTT Optoelectronics Laboratories published a fully-polarization independent Mach-Zehnder optical switch, using a strongly-guided p-i-n diode waveguide structure, with a lattice-matched InGaAlAs/InAlAs MQW core [33]. The Mach-Zehnder interferometer used 12μm wide 2X2 MMI's for the splitter and combiner functions. The switch arms were separated by 100μm using 500μm radius circular arc bends. In 2003 Tsuzuki et al. [34] modified this original design to enable a Mach-Zehnder modulator with 40GHz traveling-wave electrodes on a semi-insulating substrate. The device has a π phase shift voltage of 2.2V using a n-i-n diode structure with 3mm long microstrip electrodes. A 50Ω impedance match and a RF-mode-to-optical-mode velocity match is achieved in the modulator arm microstrip line using an intrinsic layer thickness of 1.3μm, where only 0.3μm of the intrinsic thickness is the waveguide core [35]. The ridge width is 2μm wide and the active waveguide core contains 13 periods of 10nm thick InGaAs wells and 5nm thick InAlAs barriers ($Q=1.37\mu$m). The active MQW stack is sandwiched between 50nm $Q=1.3\mu$m separate confining heterostructure layers. 10Gb/s transmission has been shown over 100km of standard SMF [36]. The device does not have optical mode spot-size converters and no details on insertion loss have yet been provided.

The NTT group has produced the best published RF performance for a Mach-Zehnder modulator using a microstrip phase shift electrode in a modulator arm., however, several other groups have also recently published on high-speed microstrip electrode designs for a phase shifter using p-i-n diode structures [37–39].

S. Akiyama et al. [29] at Fujitsu published a InGaAsP/InP based Mach-Zehnder modulator design in 2002. In their most recent paper [25] the Mach-Zehnder interferometer uses a capacitively-loaded, traveling-wave design for the phase shift electrodes [30] to enable 10Gb/s modulation. The device is series push-pull driven with an active electrode length of 2mm. This active length is made up from twenty 100μm long p-i-n diode phase modulators in each arm. The intrinsic core is a 33 well InGaAsP/InP MQW structure, having a PL wavelength of 1.414μm and a total thickness of 0.5μm. The device length is 6.25mm. They have demonstrated 30nm of low-chirp 10Gb/s modulation with a constant 2$V_{p\text{-}p}$ modulation [25]. The DC bias voltage was varied from 3V to 9V over this wavelength range. The mean insertion loss was 10dB with 1dB variation in loss between 1530nm to 1560nm. Their previous publications have used variations on this design for 40Gb/s transmission [27–29], or have provided chirp measurements [26]. No over-fiber measurements have ever been reported.

At the 2004 European Conference on Optical Communications there was a first report by S. Nakagawa et al. [24] of FiBest Limited on a 10Gb/s InP-based directional-coupler modulator with full C-band coverage. Little detail was provided on the design. It is based on a p-i-n diode structure. The weakly-guided waveguides have 2μm ridge widths with less than 3μm between them. In similar fashion to Fujitsu, capacitively-loaded traveling-wave electrodes are used to obtain sufficient unspecified bandwidth for 10Gb/s modulation with a 5mm electrode. The structure does not appear to use any optical spot-size mode converters, although an insertion loss of 6dB is claimed. No information is given on the facet mode dimensions, and there is not sufficient design information from which to calculate it. The insertion loss of a directional coupler modulator design should be lower than a Mach-Zehnder design since there is no split and combine function required, however, the design is also limited in the range of frequency chirp that it can generate.

There has been one other reported attempt outside of Alcatel to add optical mode spot-size converters to a Mach-Zehnder modulator [31]. The integrated spot-size mode converter design, originally developed for a 40Gb/s waveguide PIN receiver [32], enables coupling to a cleaved fiber mode. Excellent misalignment tolerances have been demonstrated, but the insertion loss of the device was not given. It was only stated that the optical mode spot-size converters reduced the insertion loss of the device by 4dB. These Mach-Zehnder devices use capacitively-loaded traveling wave electrodes. 45GHz of bandwidth has been demonstrated, however, no other electro-optic properties or system performance for the device has been provided in the literature.

The University of California Santa Barbara has recently reported on attempts to integrate a Mach-Zehnder modulator with their existing widely tunable sampled-grating distributed-feedback reflector (SGDBR) laser source [52–55]. The Mach-Zehnder modulator has been integrated onto the original common waveguide layer in the laser source with the phase shifter refractive index change mechanism based primarily on band-emptying the n-doped waveguide layer. The integrated device does not contain a output optical mode spot-size converter. The publications have concentrated on the fabrication of the devices and little clear performance data has been provided.

Clearly a significant amount of research is being directed towards InP-based Mach-Zehnder modulator platforms for transmitters in high-speed optical communications. The recent innovations outlined in this Section have focused on the RF design for the phase shift electrodes. This is an area that has not been advanced in this thesis relative to the design given by Rolland et al. and it is an obvious direction for future device improvements.

There are no commercially available InP-based Mach-Zehnder modulator transmitters except for the Bookham Compact Mach-Zehnder transmitter, based on variants of the modulator developed in this thesis, and discussed in Section 1.15. All the other Mach-Zehnder modulator designs presented here will need to address optical insertion losses, either through the inclusion of optical mode spot-size converters, or the integration of the optical source, to be commercially viable.

1.6 Overview of the InP Mach-Zehnder Modulator Developed in this Thesis

Figure 1.8 illustrates the 3mm long 10Gb/s InP-based Mach-Zehnder modulator developed in this thesis. The modulator arm phase shift function is achieved using 600μm long lumped-element electrodes on 2μm wide deeply-etched ridge waveguides, through p-i-n doped epitaxial layers. The two modulator arm electrodes can be independently driven. The thin intrinsic region of the Mach-Zehnder waveguide cross-section contains the InGaAsP MQW modulator core originally designed by C. Rolland and W. Bardyszewski [16–18].

The waveguide cross-section introduced by Rolland et al. has been fundamentally redesigned to enable the monolithic integration of butt-jointed optical mode spot-size converters. The splitter and combiner functions have been optimized for fabrication tolerances and they allow targeted optical split and combine ratios independent of the input coupling alignment. The devices are now produced on 3″ wafers using highly reproducible i-line stepper-based photolithography. The complete optical design has been optimized for operation over the full C-Band wavelength range. Details on the waveguide design for the InP-based Mach-Zehnder modulator are given in Chapter 2.

The design of the optical mode spot-size converters is developed in Chapter 3 and the fabrication of the spot-size converters is detailed in Chapter 4. Careful waveguide design, the inclusion of optimized spot-size converters, and advanced processing tolerances have enabled InP-based Mach-Zehnder designs with optical insertion losses as low as 4.5dB including coupling. The mean insertion loss for the negatively chirped modulator design detailed in Section 1.12 is 6dB. These insertion losses are the lowest reported to date for an

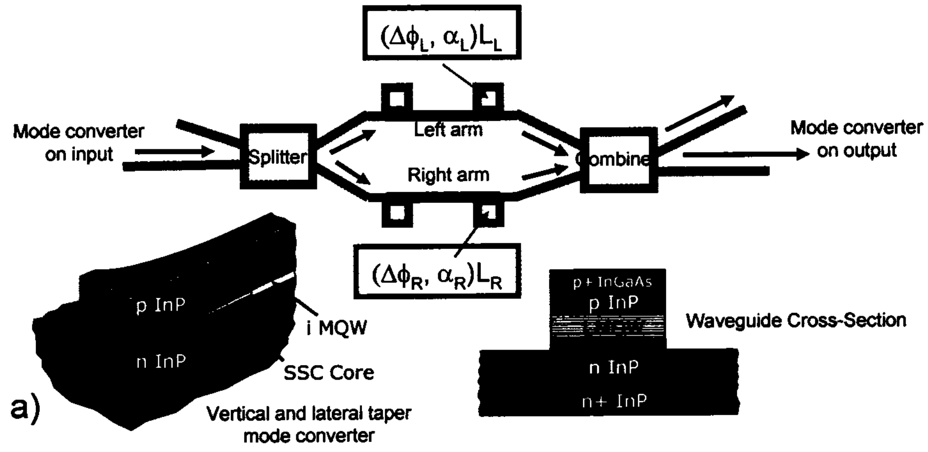

Figure 1.8: *Mach-Zehnder Device Geometry. Source: I. Betty et al., OWE5, OFC 2005.*

InP-based Mach-Zehnder modulator and were reported at the 2005 Optical Fiber Communications Conference [56]. The optical mode spot-size converter design was first published at the 2003 Optical Fiber Communications Conference [244].

In the remainder of this Chapter the device operation and system performance of the InP-based Mach-Zehnder is detailed. In Sections 1.7-1.8 the fundamental material device parameters are defined and in Sections 1.9-1.10 an InP Mach-Zehnder device model is introduced. Theoretical models for the electro-optic properties of the MQW core are adequate for a gross estimate of performance, however, they are not accurate enough for the fine optimization of yields to demanding specifications. In Section 1.11 a statistically valid empirical model for the electro-optic properties of the core is detailed as a function of wavelength. In Sections 1.12-1.14, experimentally verified, state-of-the-art modulator designs are provided, for the various modulation formats required in high-speed optical fiber communications. An overview of the best-in-class optical transmitter assembly designs incorporating the InP Mach-Zehnder modulator developed in this thesis is given in Section 1.15.

The system measurements in this Chapter are provided for completeness, but they were not carried out as part of the thesis work.

1.7 Absorption Spectra for the MQW Core Design

Figure 1.9 presents the absorption spectra for the MQW core, as a function of the applied reverse bias across the junction, with the room temperature exciton photoluminescence peak[13] ~140nm detuned from the operating wavelength. The phase shift described by the

---

[13] The Q abbreviation is used to denote the peak exciton photoluminescence of the material.

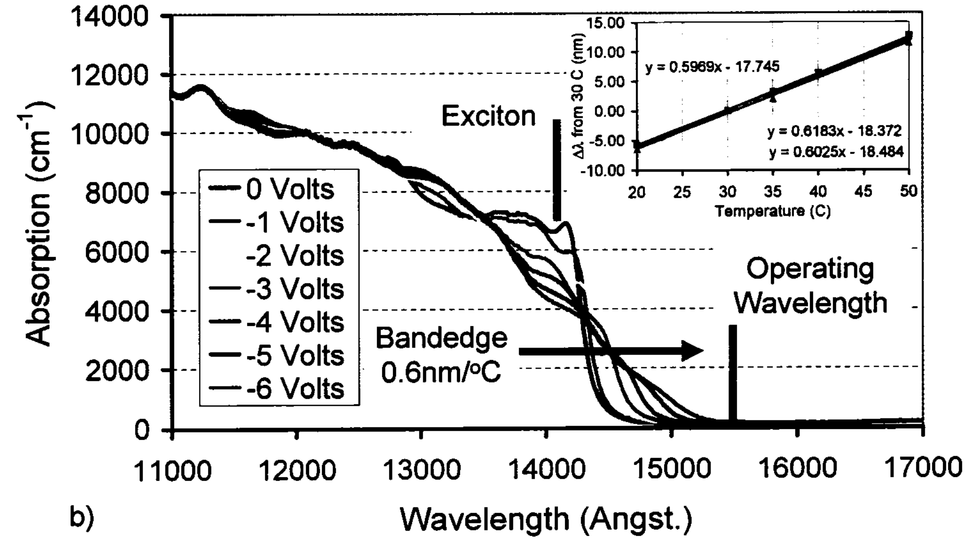

Figure 1.9: *InP Mach-Zehnder MQW Core Absorption Spectra. Source: I. Betty et al., OWE5, OFC 2005.*

Kramers-Krönig transformation of this bias induced absorption change[14] depends on the relative wavelength detuning (λ_D) between the operating wavelength and the peak of the exciton resonance at zero volt bias. The absorption bandedge is shown in the insert to undergo translation without distortion to longer wavelengths at 0.6nm/°C. A change in λ_D, can therefore, be obtained by either directly changing the operating wavelength, or by varying the operating temperature at a fixed wavelength.

1.8 Relationship Between Voltage Bias, Index Change, Frequency Shift and Phase Change

The electric field definition used to develop the Mach-Zehnder modulator model is given by,

$$E = E_o \exp(i(\omega_o t - \beta z - \delta)), \quad +z \text{ right going wave} \tag{1.5}$$

where E_o is the field amplitude constant, $\omega_o = 2\pi f$ is the angular frequency, $\beta = nk_0$ is the wavenumber in a material with refractive index n, and δ is the phase shift at time $t = 0$. Examining the time dependence of E gives,

$$\frac{dE}{dt} = i\left[\omega_o - z\frac{d\beta}{dt}\right]E \tag{1.6}$$

which allows the instantaneous frequency ω' to be defined as,

$$\omega' = \omega_o - z\frac{d\beta}{dt} = \omega_o - zk_0\frac{dn}{dt}. \tag{1.7}$$

---

[14] Manifestation of the Quantum Confined Stark Effect (QCSE) [6,7].

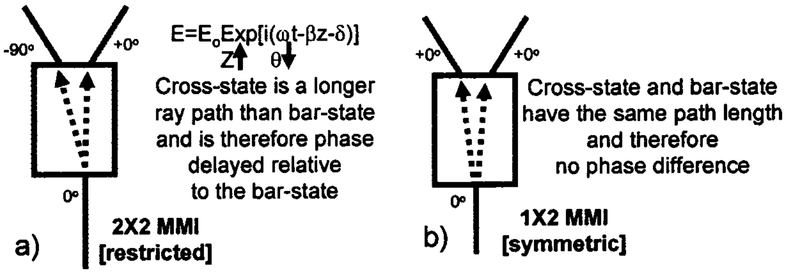

Figure 1.10: *Ray Optic Interpretation of Optical Phase Shifts in Multi-Mode Splitters and Combiners.*

Thus, if $\frac{dn}{dt} > 0$ then $\omega' < \omega_o$ and $\lambda' > \lambda_o$, causing a red-shift in the instantaneous frequency to occur. If $\frac{dn}{dt} < 0$ then $\omega' > \omega_o$ and $\lambda' < \lambda_o$, then a blue-shift in the instantaneous frequency occurs.

As the electric field strength increases in the quantum well core, the Quantum Confined Stark Effect (QCSE) [6,7] causes the real refractive index of the quantum well material to *increase*. This fact, in conjunction with Equation 1.7 and Equation 1.5, produces the following relationships between voltage bias, index change, instantaneous frequency shift and phase change:

$$\boxed{\frac{d(-V)}{dt} \Uparrow \,, \quad \frac{dn}{dt} \Uparrow \,, \quad \omega' < \omega_o \,, \quad \theta \Downarrow.} \tag{1.8}$$

The phase shifts produced by the Multimode Interference [MMI] splitter and combiner functions in the modulator are illustrated in Figure 1.10. A simple ray-optic interpretation is used for the MMI functions along with the field definition from Equation 1.5. The MMI design is treated in depth in Section 2.2.

The relationships given here are required to specify the modulator designs for frequency chirped and non-frequency chirped applications in Sections 1.12-1.14.

1.9 The InP Mach-Zehnder Device Model

The InP Mach-Zehnder modulator shown in Figure 1.8 is a 0th order interferometer with a transfer function for the output electric field $\mathrm{E}_o(V_L, V_R)$ that can be mathematically expressed, as a function of the left and right arm biases by,

$$\begin{aligned} E_o(V_L, V_R) \;&=\; \sqrt{S_{li}S_{lo}} \cdot \mathrm{e}^{-[\alpha(V_L,\lambda_D)/2 \cdot L_L]} \cdot e^{i[-\Delta\phi(V_L,\lambda_D)\cdot L_L - \delta_L]} + \\ &\quad \sqrt{(1-S_{li})(1-S_{lo})} \cdot \mathrm{e}^{-[\alpha(V_R,\lambda_D)/2 \cdot L_R]} \cdot e^{i[-\Delta\phi(V_R,\lambda_D)\cdot L_R - \delta_R]} \end{aligned} \tag{1.9}$$

assuming a unity input field amplitude E_i. The Mach-Zehnder output power transfer function can be determined from $P_o = [E_o \cdot E_o^*]$.

This DC device model is general enough to be used within any optical system simulation package to study the dynamic performance of the InP Mach-Zehnder device. There are six sets of inputs required for the model:

- The optical power split ratios—S_{li} is the input MMI power split ratio into the left modulator arm [0-1]; S_{lo} is the left modulator arm's MMI power split ratio into the output guide [0-1].
- The length of the phase shift electrodes–L_L is the length of the left arm electrode, L_R is the length of the right arm electrode.
- The zero volt phase imbalance terms—δ_L and δ_R are the phase offsets [0-2π] in the left and right arm paths respectively, introduced by the MMI splitter and combiner functions. δ_R and δ_L cannot be uniquely determined; therefore, δ_R is taken to be zero by convention. The device zero volt imbalance can be modelled by varying the δ_L parameter.
- The phase change versus voltage and λ_D—$\Delta\phi(V,\lambda_D)$ is the phase shift per micron for an applied negative voltage bias to the phase shift electrode. An example of this relationship in radians is given by $\Delta\phi(V,\lambda_D) = \frac{1}{600}\left[p_1|V| + p_2|V|^2\right]$ where p_1=0.5055 and p_2=0.0817. The empirical determination of $\Delta\phi(V,\lambda_D)$ is detailed in Section 1.11 below.
- The optical absorption versus voltage and λ_D—$\alpha(V,\lambda_D)$ is the optical power absorption coefficient in inverse microns for an applied negative voltage bias. An example of this relationship is given by $\alpha(V,\lambda_D) = \frac{1}{600}\left[a_1|V|\right]^{a_2}$ with a_1=0.2079 and a_2=4.5285. The empirical determination of $\alpha(V,\lambda_D)$ is detailed in Section 1.11 below.
- The applied voltages—V_L and V_R are reverse bias voltages applied to the left and right arm phase shift electrodes respectively. The user of the modulator has independent access to each arm so a strict relationship between the arm biases has not been fixed in the model.

The electro-optic bandwidth of the Mach-Zehnder modulator is not captured in this DC model. The nominally 600μm long electrode length for each phase shifter electrode defines this bandwidth, as discussed in Section 1.10.

1.10 RF Bandwidth of the InP Mach-Zehnder Phase Shifters

The electrodes on the arms of the Mach-Zehnder modulator are each electrical lumped-elements with highly reproducible RC limited bandwidth. These modulation electrodes are wirebonded, using an automated process, to co-planar transmission lines and 50Ω terminations on an Al_2O_3 carrier. Figure 2.5 indicates that the 600μm long modulation electrode has a measured and modelled capacitance of 0.4pF. Each input and output bonding

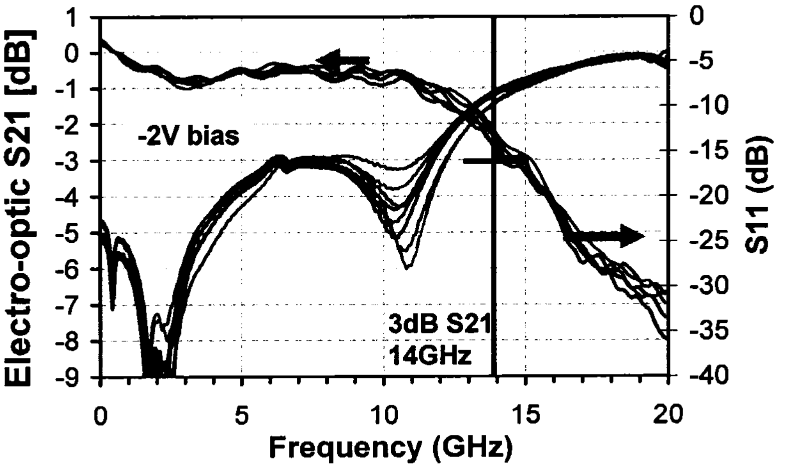

Figure 1.11: *Small Signal RF Measurements for a Sample of Negative Chirp Chip-on-Carrier Devices from a Wafer. Source: I. Betty et al., OWE5, OFC 2005.*

pad contributes an additional 45fF, for a total modulation electrode capacitance of ≈0.5pF. The RF bandwidth required for 10Gb/s operation is guaranteed by design, and it is independent of the wavelength detuning parameter λ_D. Typical small signal RF measurements are shown in Figure 1.11 for a sample set of negative chirp chip-on-carrier (CoC) devices from a wafer. The negative chirp modulators have been biased to near quadrature with a -2V DC bias. The -3dB S_{21} is 14GHz, and the S_{11} is <-15dB out to 10GHz.

1.11 Experimental Determination of the Phase and Absorption Relations versus Bandedge Offset and Voltage

The procedure described herein has been used to collect experimental data enabling empirical relationships for the change in MQW phase and absorption to be determined as a function of the bias voltage and the bandedge offset.

For each device, the light versus voltage (LV) transfer function is measured on each arm of the modulator, with the other arm biased at zero volts, as show by the solid line curves in Figure 1.12. Independently, the absorption, $\alpha(V, \lambda_D)$, is directly measured from a LV sweep of one modulator arm, with the alternate arm biased to the point of complete absorption, such that the device becomes non-interferometric. The $\alpha(V, \lambda_D)$ relationship can also be extracted from photocurrent measured simultaneously with the LV transfer functions. All these measurements are performed at multiple wavelengths to allow the device parameters, given in Section 1.9, to be extracted as a function of λ_D. The modulator imbalance V_{imb}, DC extinction ratio ER_{DC}, and voltage for π phase shift V_π, are shown in Figure 1.12. These Mach-Zehnder performance parameters were initially defined in Section 1.3.

Phase Fit	Absorption Fit
$\phi(V) = p1\|V\| + p2\|V\|^2$	$\alpha(V) = (a1\|V\|)^{a2}$
p1=-0.2856*V$_{\pi m}$ + 1.6051 p2= 0.0817	a1=-0.0699*V$_{\pi m}$+0.477 a2=2.395*V$_{\pi m}$-4.6923

Table 1.1: *Phase and Absorption Relationships:* $\alpha(V, V_{\pi m})$ *and* $\phi(V, V_{\pi m})$.

Equation 1.9 is fit to both the left and right arm measured LV curves in Figure 1.12 simultaneously, using the measured absorption relationship, $\alpha(V, \lambda_D)$, to extract the phase change versus voltage at a given wavelength, $\phi(V, \lambda_D)$, and the constant fit parameters δ_L, S_{li}, and S_{lo}. The device model LV fit is shown as dotted lines in Figure 1.12.

In Figure 1.13 the measured $\alpha(V, \lambda_D)$ relationship, and the extracted $\phi(V, \lambda_D)$ relationship, are quantified based on 1900 devices from 10 different wafers. Since the wavelength detuning parameter, λ_D, is not easily extracted for each device[15], the phase and absorption relationships have actually been quantified, in terms of the voltage required on a phase shifter electrode to obtain a π phase shift in the material. This is defined as $V_{\pi m}$[16]. Note this $V_{\pi m}$ parameter is not necessarily the same as the V$_\pi$ parameter identified in Figure 1.12.

The solid lines in Figure 1.12a show the phase change in radians, as a function of voltage, for 3 different values of $V_{\pi m}$: 3.35V, 3.85V and 4.45V. This corresponds to a range of λ_D covering 33nm. The dotted lines show the corresponding absorption curves in dB. A quadratic relationship for the phase change versus voltage provides a good fit to the experimental LV transfer curves. A two parameter power law has been used as the fit to the measured absorption data. As a result, at a given wavelength, four parameters are required to characterize the phase and absorption parameters for the MQW material. Figure 1.12b shows that these four fit parameters can themselves be linearly fit as a function of $V_{\pi m}$. The relationships summarized in Table 1.1, therefore, fully quantify the phase and absorption properties of the MQW, as a function of voltage and the wavelength detuning, expressed in terms of $V_{\pi m}$. The relationships in Table 1.1 are valid for $V_{\pi m}$ from 3.35-4.45 Volts.

There are three device requirements to take into account when determining an acceptable range for the wavelength detuning parameter λ_D:

1. The required RF modulation voltage should remain between 2-3V differential. This allows electrical drivers based on low-cost Silicon Germanium technology to be used.
2. The absorption induced in the modulation arms, by the phase shift electrodes, must remain compatible with the targeted insertion loss budget for the modulator. In the on-state of the modulator[17] only one arm will typically be significantly biased, as

---

[15] The measurement wavelength is known, but the peak exciton wavelength is available only at the wafer level.

[16] Note $V_{\pi m}$ is defined from zero volts.

[17] The on-state output will determine the insertion loss of the modulator.

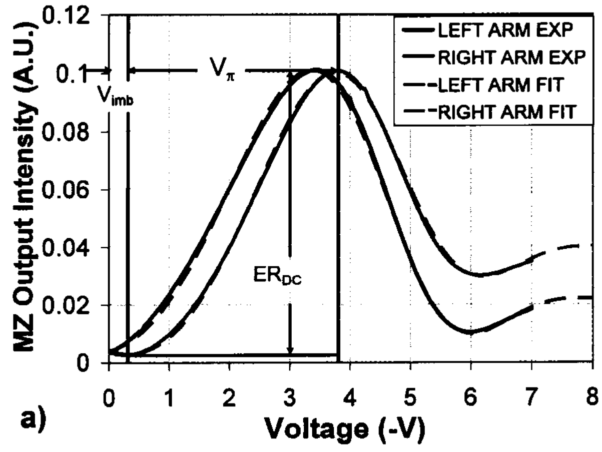

Figure 1.12: ***Measured and Fit Light versus Voltage (LV) Transfer Function [alternate arm at 0V]***
Source: I. Betty et al., OWE5, OFC 2005.

shown in Figure 1.15 and Figure 1.20. The power output of an otherwise lossless modulator is then given by $P_o \approx (\sqrt{x}+1)^2/4$, where x is the linear transmission through the arm with the high reverse voltage bias.

3. Changes in the chirp contribution from the non-linear phase change under modulation, must be compatible with the over-fiber dispersion penalty budget.

In Section 1.12 it will be shown that (3) is negligible, so λ_D can be selected based on only the switching voltage range and the insertion loss contribution. A λ_D range between 120nm and 155nm is found to be optimal for the negative chirp application described in Section 1.12.

Figure 1.14 shows the uniformity obtained for the phase and absorption properties of the MQW material across a 3" wafer. Figure 1.14a gives $V_{\pi m}$ as a function of the radial distance from the centre of the wafer. Figure 1.14b provides the phase and absorption relations as a function of voltage, at the centre of the wafer, at a 1.5cm radius, and at a 3cm radius. Due to the excellent uniformity in these parameters the chip location on the wafer does not impact yield.

1.12 Chirped InP Mach-Zehnder Design

Figure 1.15 outlines a modulator design that enables controlled frequency chirping to occur during bit transitions in the modulator output power from a "1" to "0" or "0" to "1". The modulator is nominally in the off state[18] with no bias applied to either arm. With an increasing negative bias applied to an arm, the phase shift due to optical propagation in

---

[18] minimum P_o in the output waveguide

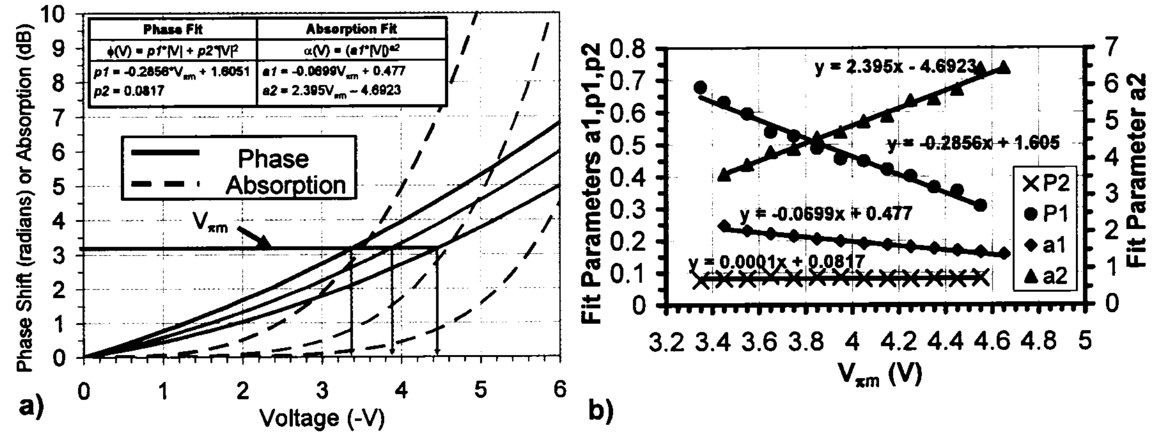

Figure 1.13: *a) Phase and Absorption Material Properties $\alpha(V, \lambda_D)$ and $\phi(V, \lambda_D)$ based on 1900 Devices from 10 Wafers with Optimal Relative Wavelength Detuning λ_D: 120nm to 155nm, b) Phase and Absorption Fit Parameters as a Function of $V_{\pi m}$.*

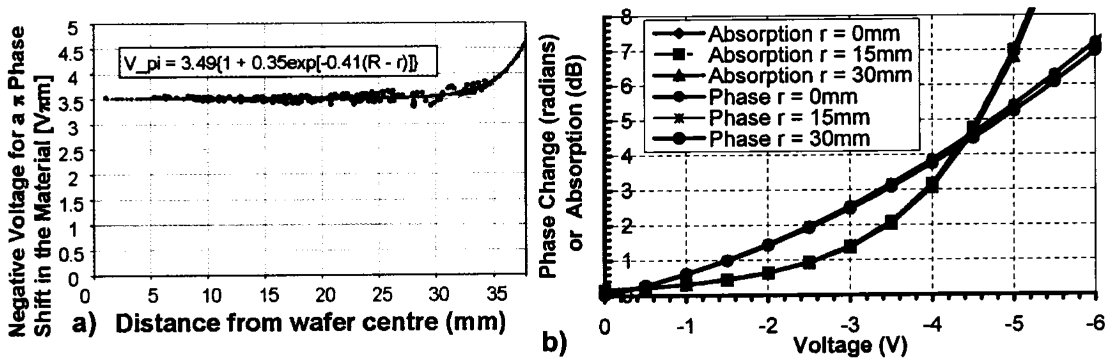

Figure 1.14: *Uniformity for the Phase and Absorption Properties of the MQW material across a 3" wafer. Source: I. Betty et al., OWE5, OFC 2005.*

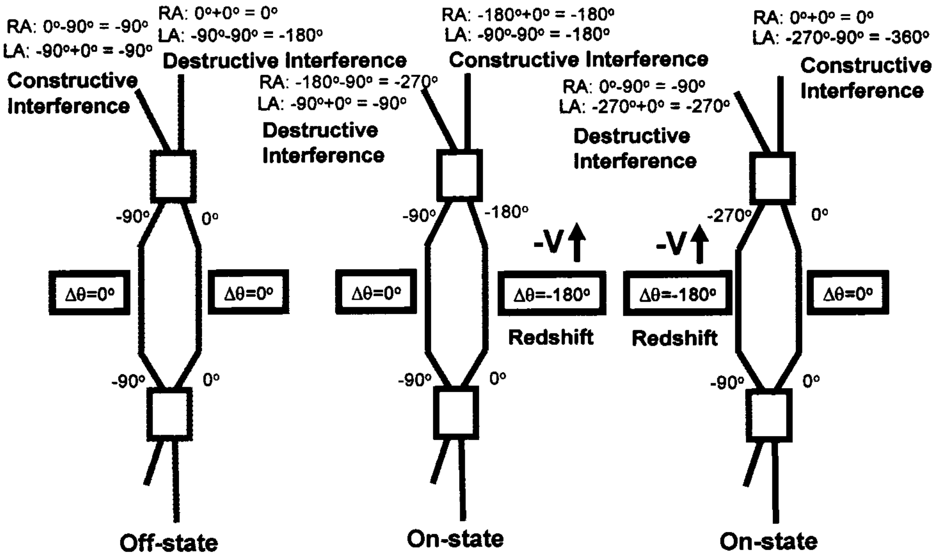

Figure 1.15: *Chirped Mach-Zehnder Operating States — Left Arm π Phase Shift ($\delta_L = \pi$).*

the arm decreases, and causes a red-shift[19] in the output phase to occur while the output intensity increases from the minimum value to the maximum. This generates negative frequency chirp which will enable pulse compression in long-reach optical communication systems as discussed in Section 1.1. The maximum output power, as shown in Figure 1.15, is obtained with a 180^0 phase shift applied to either arm.

The frequency chirp in a loss modulator can be more specifically characterized by a small signal chirp parameter α_H [40], defined as the relative variation of instantaneous phase in time, over relative variation of modulated power in time,

$$\alpha_H = \frac{2\frac{d\phi}{dt}}{\frac{dP}{dt}} \cdot P \tag{1.10}$$

In general this parameter will not be a constant through a "0" to "1" or "1" to "0" bit transition. Unlike the frequency chirp, the small signal chirp parameter is independent of bit rate. In Figure 1.16b the variation of α_H through a bit transition is shown for the optimal negative chirp modulation scheme to be presented in Figure 1.15a.

Assuming a constant small signal chirp parameter[20] allows the dispersion-limited reach for non-return to zero (NRZ) transmission over optical fiber to be determined analytically in an ideal system [41],

$$DP = 5\log_{10}\left[(1 + 8\alpha_H D(\lambda)B^2L)^2 + (8D(\lambda)B^2L)^2\right] \tag{1.11}$$

where DP is the transmission dispersion penalty, D(λ) is the wavelength dispersion of the fiber defined by Equation 1.1, B is the bit rate and L is the fiber length. The optimal α_H

---

[19] This is based on the relations in Equation 1.8.

[20] This would require the change of phase in time to have a linear relationship with the change in power.

chirp parameter, to maximize dispersion-limited reach, lies between 0 and -1 for standard SMF-28 optical fiber.

For the push-pull driven negative chirp implementation of the Mach-Zehnder detailed here, the amount of negative frequency chirp generated is tailored by varying the optical imbalance between the modulation arms, as originally proposed by Cartledge and Rolland et al. [12]. This tailored optical imbalance can be achieved in many ways, two examples are the butterfly MMI design defined in Section 2.2.7, and the tunable MMI design defined in Section 2.2.7. Recently, Bravetti et al. [42] have compared negative chirp generation in $LiNbO_3$ modulators using the traditional, commercialized, RF imbalance schemes, against negative chirp generation using optical imbalance. They show that optically unbalancing the power in the modulation arms gives superior dispersion-limited transmission performance. This is consistent with the results presented in Section 1.13.3. As shown in Figure 1.19b, the more uniform α_H chirp parameter profile with optical unbalancing provides lower group velocity variation between different points on a bit transition. Balsamo et al. [43] have also recently shown that optical unbalancing produces a chirped NRZ data stream without broadening the power spectrum relative to a zero chirp device.

With the known phase and absorption change versus voltage relationships, determined in Section 1.11, it is possible to use Equation 1.9, to map the output intensity operating space of a modulator design, as a function of the left and right arm biases. The intensity operating space for the negative chirp modulator design shown in Figure 1.15 is given in Figure 1.16a for $V_{\pi m}$=4.0V. The operating space is presented for a slight zero volt bias optical imbalance, δ_L=0.9π. This QCSE induced operating space differs from that in a linear electro-optic effect (LEO) modulator, such as those based on $LiNbO_3$. The on-state contours, in Figure 1.16a, are not parallel, they are convergent with decreasing intensity as the reverse bias increases. Recall the modulator phase shift electrodes on each arm are independently driven, hence it is possible in principle to operate the device between any set of points in this space.

Six different potential operating regimes for the modulator are identified in Figure 1.16a: A, B, and D are negative chirp; C, E, and F are positive chirp. Note also that all the operating regimes are single arm driven except for A and C, which both require dual arm differential drive[21]. The preferred operating regime for dispersion-limited transmission on standard optical fiber is the differentially driven condition A. The dispersion-limited reach application is typically specified between -500ps/nm and 1600ps/nm with less than 2dB dispersion penalty relative to back-to-back[22].

The details for drive condition A are enumerated in Figure 1.16a. Note the voltage required on one arm to switch from the off-to-on state (V_π), is different from the voltage required for a material π phase shift in the modulation arm ($V_{\pi m}$), due to the non-linearity of the $\Delta\phi(V, \lambda_D)$ relationship and the distortion introduced by $\alpha(V, \lambda_D)$ to the LV curve. The left

---

[21] Using both differential outputs from an electrical driver means that as one arm bias increases the other will decrease by the same amount. This drive condition is a 45° line within the operating space.

[22] Back-to-back is the terminology used for transmission over 0km of fiber.

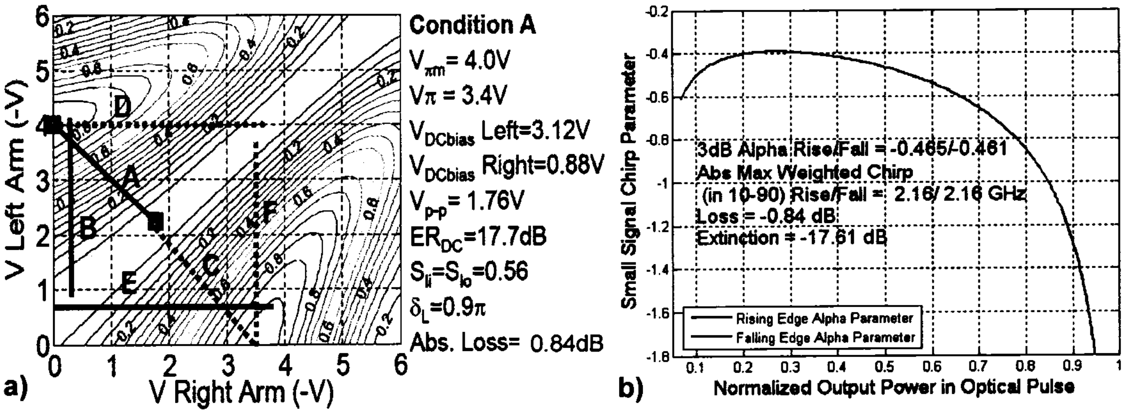

Figure 1.16: ***a) Operating Space for the Negative Chirp Modulator Design in Figure 1.15, b) Variation of the Theoretical Small Signal Chirp Parameter α_H through a Bit Transition with Drive Condition A.***

arm DC bias is -3.12V, the right arm DC bias is -0.88V, with a peak-to-peak swing voltage of 1.76V. This drive configuration exploits the non-linear phase-voltage characteristic of the device. At quadrature, the left arm is biased more deeply than the right; hence its dynamic phase shift is higher, contributing to negative chirp at the output. The negative chirp is increased, as previously stated, by unbalancing the optical split ratios to favour the more deeply biased left arm with S_{li}=S_{lo}=0.56. This unbalancing limits the DC extinction ratio to the 17.7dB indicated. In Figure 1.16b the variation of the small signal chirp parameter, α_H, through a bit transition is shown for this differential drive condition.

The device model developed here has been used to study the over-fiber performance of the optimal negative chirp drive condition[23]. It has been determined that the zero bias optical imbalance δ_L, the DC bias depth, and the relative detuning wavelength λ_D, are all minor contributors to the over-fiber system performance. The system performance is dominated by the selected value for the optical split ratios. Since these optical split ratios define the easily measured DC extinction ratio, and since the DC extinction ratio is independent of optical alignment due to the optimized waveguide geometries, it is possible to screen system performance at the chip level, enabling high transmitter module yields. This hypothesis will be proven in Section 1.13.

1.13 Experimental Performance of the Chirped InP Mach-Zehnder Design

In this section the over-fiber system performance of the negative chirp modulation scheme is studied as a function of DC extinction ratio and wavelength. The dispersion-limited reach performance is shown to be superior to -0.7α_H LiNbO3 modulators.

---

[23] The over-fiber system performance modelling was not performed by me as part of this thesis work.

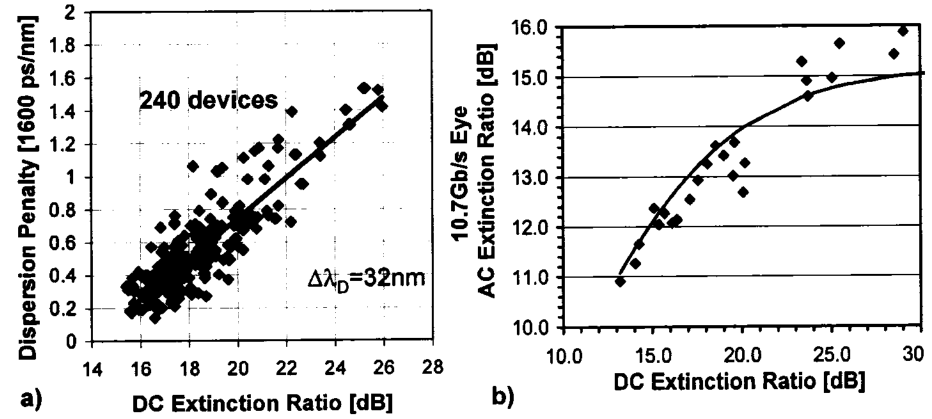

Figure 1.17: *a) Dispersion Penalty at 1600ps/nm Dispersion versus DC Extinction Ratio ER_{DC}, b) 10.7Gb/s AC Extinction Ratio versus DC Extinction Ratio. Source: I. Betty et al., OWE5, OFC 2005.*

1.13.1 Dispersion Penalty versus DC Extinction Ratio

A sample set of negative chirp devices were fabricated to study the impact of the DC extinction ratio on the over-fiber system performance of the negative chirp modulation scheme. The final population contained 240 devices, covering a range of optical split ratios and 32nm of wavelength detuning λ_D. In Figure 1.17a the obtained dispersion penalty at 1600ps/nm is given for the population versus the DC extinction ratio. A strong correlation is evident, verifying that a modulator chip screen for the DC extinction ratio can predict the over-fiber dispersion penalty. Excellent tolerance is available to the typical specification allowing 2dB maximum dispersion penalty at 1600ps/nm.

Figure 1.17b gives the relationship between the 10.7Gb/s dynamic AC extinction ratio (ER_{AC}) and the DC extinction ratio (ER_{DC}). The measurement of AC extinction ratio is a challenging measurement where no standard method exists [44,45]. These AC extinction ratio measurements have been performed with an Agilent 86105B reference receiver containing a 3/4 bit-rate 4^{th} order Bessel-Thompson filter, and using the supplied calibration factor. Figure 1.17b indicates that a 16dB DC extinction ratio is sufficient to guarantee a 11.5dB dynamic AC extinction ratio.

Based on the results in Figure 1.17 an 18dB target for the DC extinction is taken as an optimum.

1.13.2 Dynamic Performance Over Wavelength

The measured wavelength dependence of the dynamic performance for a single device is given in Figure 1.18. The blue diamonds give the 10.7Gb/s dispersion penalty at 1600ps/nm over the C-Band channels between 1529nm and 1563nm. The green squares give the corresponding DC extinction ratio. Clearly, the strong correlation between DC extinction ratio

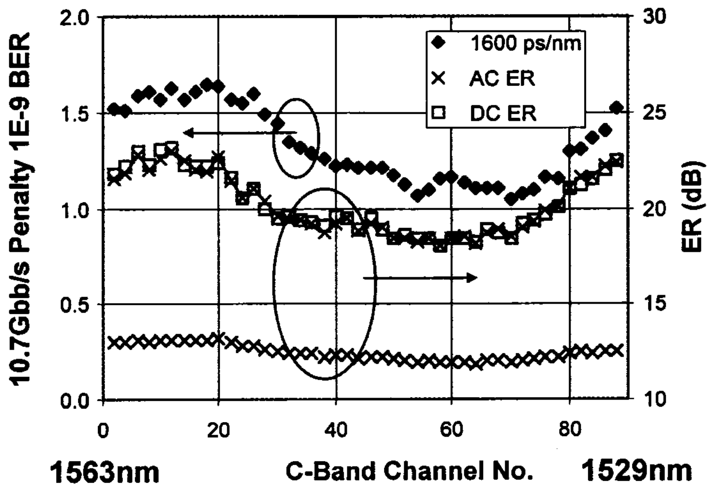

Figure 1.18: ***Dispersion Penalty at 1600ps/nm and Extinction Ratios for a Single Device Over Wavelength in C-Band.*** *Source: I. Betty et al., OWE5, OFC 2005. Data collected by Robert Griffin.*

and dispersion penalty holds over this wavelength range of 34nm. This proves the relative wavelength detuning parameter λ_D is a minor factor in the dynamic performance.

1.13.3 Chirped InP Mach-Zehnder System Performance in Comparison with a -0.7α_H LiNbO$_3$ Modulator

Figure 1.19 compares the measured dynamic system performance[24] of the negatively chirped InP Mach-Zehnder modulator design against the well studied -0.7α_H LiNbO$_3$ modulator design. In Figure 1.19a superior dispersion-limited reach is shown for the InP Mach-Zehnder devices, given by red diamonds[25] and green triangles[26], relative to the LiNbO$_3$ modulator given by the blue squares.

Figure 1.19b shows the measured small signal α_H parameter through the bit transitions in both modulator designs. This compares directly the chirp profiles generated by the optical split ratio imbalance in the InP modulator and the RF drive imbalance used in the LiNbO$_3$ modulator. The InP modulator chirp profile compares reasonably well with the theoretical profile predicted in Figure 1.15b. As discussed previously the more uniform α_H chirp profile with optical unbalancing provides lower group velocity variation between different points on a bit transition.

---

[24] 10.7Gb/s transmission with 2^{31}-1 PRBS data, 10^{-9} BER, and 35dB OSNR.
[25] ER_{AC}=12.5dB, ER_{DC}=17dB.
[26] ER_{AC}=12.2dB, ER_{DC}=17.2dB.

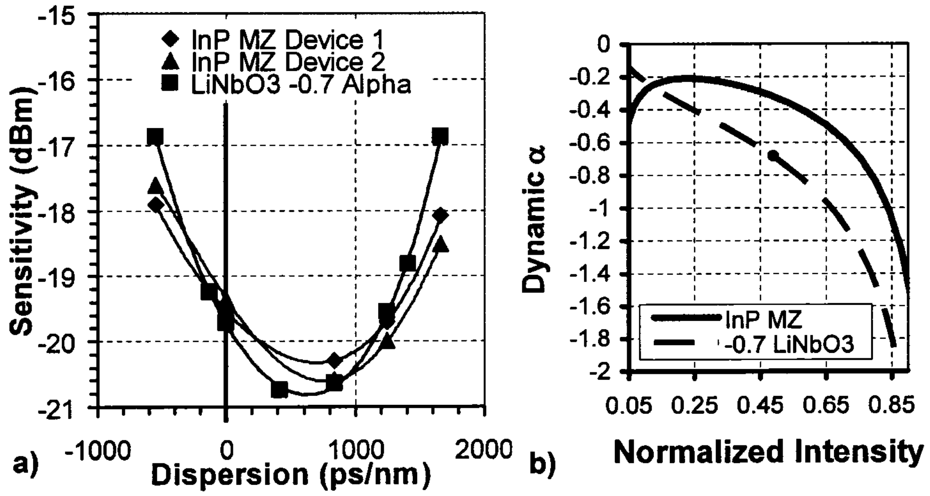

Figure 1.19: ***Chirped InP Mach-Zehnder System Performance in Comparison with a -0.7α_H LiNbO$_3$ Modulator.*** *Source: I. Betty et al., OWE5, OFC 2005. Data collected by Robert Griffin.*

1.14 Zero Chirp InP Mach-Zehnder Design

Figure 1.20 outlines a modulator design where no frequency chirp occurs during transitions in the modulator's output power. This is accomplished by having each arm counteract the frequency chirp introduced by the other under amplitude modulation. The modulator is designed nominally at quadrature ($\frac{1}{2}P_0$) with no bias applied to either arm and it must be driven differentially. The intensity operating space for the modulator design in Figure 1.20 in shown in Figure 1.21a. A pictorial representation of the frequency chirp in each arm through off-to-on and on-to-off transitions is shown in Figure 1.21b. Any deviations from zero frequency chirp are caused by mismatched electrical signals to the two independently driven phase shifters, or by non-linearities in the $\Delta\phi(V, \lambda_D)$ relationship.

In quadrature operation neither arm phase shifter receives an absolute voltage under modulation greater than $V_\pi/2$, as is clear from Figure 1.21a. This enables "effective zero chirp" propagation performance over single-mode fiber using phase shifters with non-linearity in the $\Delta\phi(V, \lambda_D)$ relationship, since only low bias operation from them is required[27]. In Figure 1.23b the theoretical variation of the small signal chirp parameter, α_H, through a bit transition is shown for the differential drive condition in Figure 1.21a. In an ideal push-pull driven zero chirp modulator, α_H would be zero through the entire bit transition.

Figure 1.22 presents the light transmission versus reverse bias voltage curves (LV) for both the left[28] and right arm phase shifters on the zero chirp modulator device, as a function of the zero bias optical imbalance. The insertion loss (IL), DC extinction ratio (ER_{DC}), off-

---

[27] With low bias on the phase shifters the phase change with voltage is nearly linear and the absorption is practically insignificant as detailed in Section 1.11.

[28] Left is defined looking into the device input, as shown in Figure 1.8.

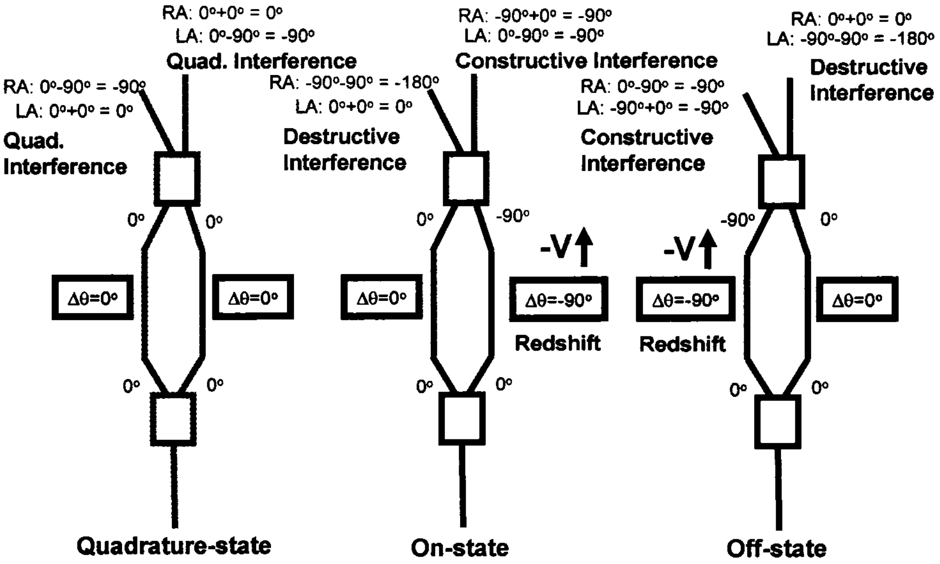

Figure 1.20: *Zero Chirp Mach-Zehnder Operating States — Left Arm $\frac{\pi}{2}$ Phase Shift ($\delta_L = \frac{\pi}{2}$).*

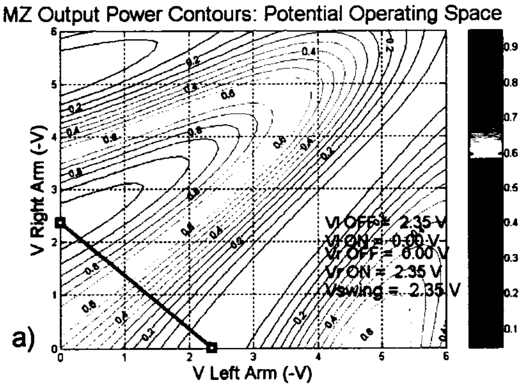

b)

Output Intensity	Left Arm	Right Arm	Left-Arm Chirp	Right-Arm Chirp
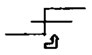	$0 \rightarrow V_{\pi/4}$	$V_{\pi/2} \rightarrow V_{\pi/4}$	$\omega' \downarrow$ Red Shift	$\omega' \uparrow\uparrow$ Blue Shift
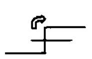	$V_{\pi/4} \rightarrow V_{\pi/2}$	$V_{\pi/4} \rightarrow 0$	$\omega' \downarrow\downarrow$ Red Shift	$\omega' \uparrow$ Blue Shift
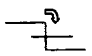	$V_{\pi/2} \rightarrow V_{\pi/4}$	$0 \rightarrow V_{\pi/4}$	$\omega' \uparrow\uparrow$ Blue Shift	$\omega' \downarrow$ Red Shift
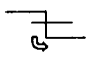	$V_{\pi/4} \rightarrow 0$	$V_{\pi/4} \rightarrow V_{\pi/2}$	$\omega' \uparrow$ Blue Shift	$\omega' \downarrow\downarrow$ Red Shift

Figure 1.21: *Zero Chirp Mach-Zehnder Drive Conditions: a) Power Contour of Potential Operating Space for $V_{\pi m}$=-4.0V and λ_D=140nm. The Differential Drive Condition is Highlighted with a Red Line. b) Pictorial Representation of the Frequency Chirp in Each Arm Through Off-to-On and On-to-Off Transitions.*

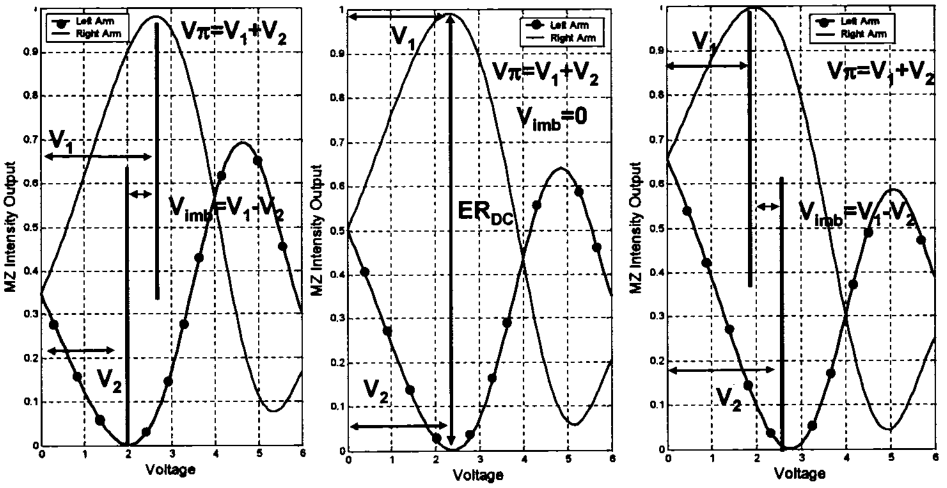

Note: Insertion loss (IL) is defined at the maximum on the right arm. It does depend slightly on V_{imb}

Figure 1.22: ***Light versus Voltage Transfer Curves for the Zero Chirp InP Mach-Zehnder Modulator as a Function of the Zero Bias Optical Imbalance.***

to-on state voltage (V_π), and imbalance voltage (V_{imb}) are defined. These Mach-Zehnder modulator performance parameters were initially introduced in Section 1.3. There is no intentional deviation from the optical split ratios S_{li}=S_{li}=0.5; DC extinction ratios in excess of 30dB are typical. Since there is also no significant on-state absorption loss, a feasible insertion loss target is <5dB including coupling.

Figure 1.23 provides the measured dynamic system performance[29] of the effectively zero chirp InP Mach-Zehnder modulator design. There is only a small deviation from the true zero chirp modulation condition, where the penalty versus dispersion would be perfectly symmetric on either side of 0ps/nm dispersion. In Figure 1.23b the theoretical variation of the small signal chirp parameter, α_H, through a bit transition, is shown for the device in Figure 1.21a. Only a small amount of small signal chirp is predicted. Both Figure 1.23a and Figure 1.23b indicate a slight tendency towards negative chirp operation.

It has been shown here that an effectively zero chirp modulator design can be achieved with a QCSE based InP Mach-Zehnder modulator. Several advanced modulation formats incorporating additional information in the phase of the transmitted signal, have also recently been demonstrated with these devices [46,58].

---

[29] 10.7Gb/s transmission with 2^{31}-1 PRBS data, 10^{-10} BER, and 35dB OSNR. The device was driven with a Vitesse VSC7984YF electrical driver.

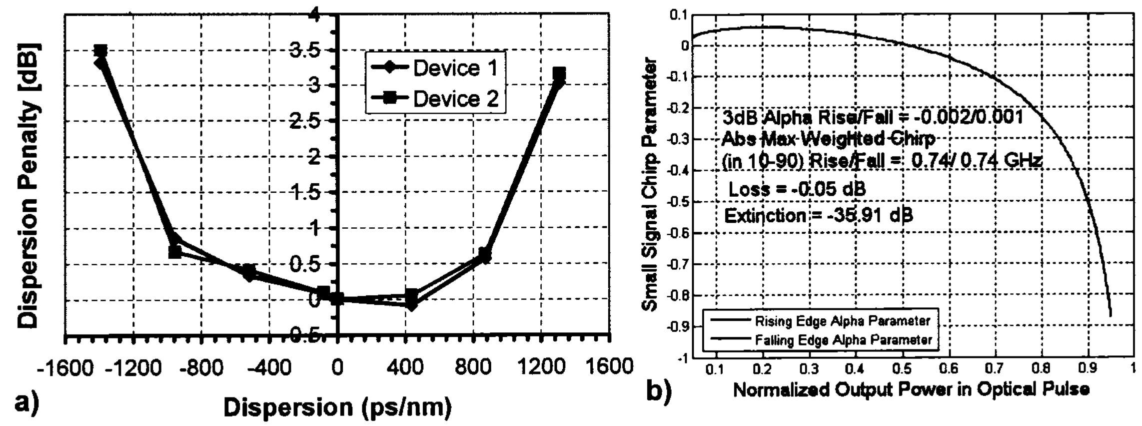

Figure 1.23: *a) Zero Chirp InP Mach-Zehnder Over-Fiber Dispersion Penalty versus Dispersion, b) Variation of the Theoretical Small Signal Chirp Parameter α_H through a Bit Transition for the Zero Chirp Drive Condition in Figure 1.21a. System Performance Data collected by Philip Mitchell.*

1.15 Transmitter Design Options Incorporating an InP-Based Mach-Zehnder Modulator

The small modulator chip size enables co-packaging with a DFB laser source. Bookham, through its acquisition of Nortel Networks Optical Components business, has been producing such co-packaged sources for 10Gb/s transmission since 1995 [50]. These early co-packaged transmitters used the original InP Mach-Zehnder modulator design by Rolland et al. [9,11]. The latest version of co-packaged transmitter [49], shown in Figure 1.24, uses variants of the Mach-Zehnder modulators developed in this thesis. The package has been optimized for transponder and dense card applications.

In the co-packaged transmitter shown in Figure 1.24, as in all high performance DFB based transmission sources, an optical isolator is needed to protect the laser from external feedback. Placing that isolator between the laser and modulator acts as a safeguard against reflections from the Mach-Zehnder output facet which, being modulated, are particularly problematic. Lenses are therefore required, first to collimate the laser output and subsequently to launch it into the input optical mode spot-size converter on the Mach-Zehnder modulator chip. These two lenses have high numerical aperture and must be mounted in a stable configuration. A relatively weak lens, in this case mounted on the optical isolator, is aligned last to steer the beam slightly and optimize the coupling into the modulator. All of the optics mount on a single ceramic platform which in turn mounts on a thermo-electric cooler (TEC). Since the Mach-Zehnder modulator chip is small and dissipates little power, mounting it on the same TEC as the laser source is quite practical. Wavelength monitoring optics are fixed on the laser subcarrier, and the RF termination components needed by the differential 10.7Gb/s data signals are incorporated into the Mach-Zehnder carrier. All of the electrical connections, including the controlled impedance differential data, are arranged along a single side of the 8.1mm high industry standard footprint package.

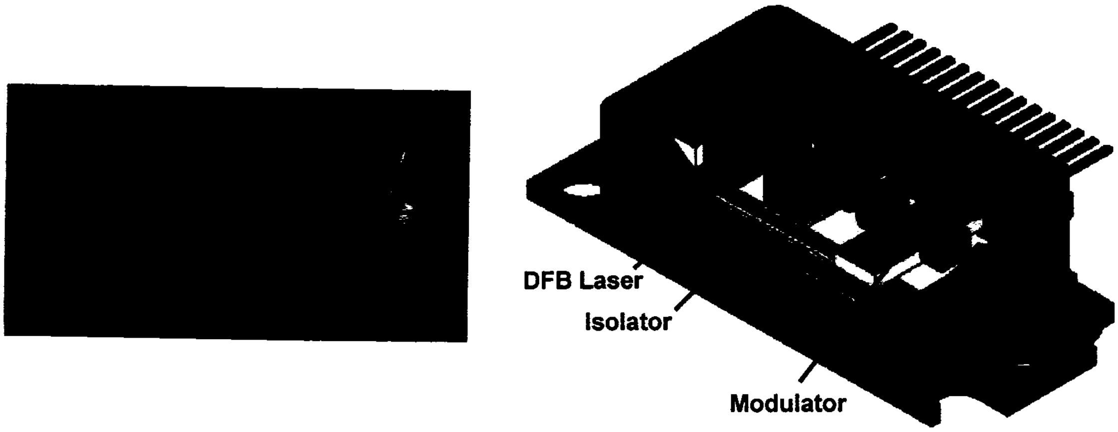

Figure 1.24: ***Lens Coupled DFB Laser and InP Mach-Zehnder in a Small Package.*** *Source: K. Anderson and I. Betty, Laser Focus World 39 (3): 101-104 March 2003.*

Recently a co-packaged transmitter solution for full C-Band operation has been reported, using variants of the Mach-Zehnder modulator developed in this thesis, with a widely tunable digital-supermode distributed-feedback reflector (DS-DBR) semiconductor laser source. [57]

The design of the InP Mach-Zehnder modulator described in this thesis achieves an optical insertion loss <6dB, enabling widely tunable packaged modules with >3dBm mean modulated output power over C-Band. Fixed wavelength packaged devices with distributed-feedback lasers have been made with >9dBm mean modulated output power.

We have presented many practical issues to consider when reviewing monolithic versus hybrid packaging options [48, 49, 51]. Rolland et al. [47] successfully monolithically integrated an InP Mach-Zehnder with a DFB laser, but it was never commercialized. Future monolithic source integration, however, will use the recently matured semiconductor-based tunable laser solutions. The monolithic integration will be driven by a combination of volume demand and package size reduction[30]. University of California Santa Barbara has recently reported on attempts to integrate a Mach-Zehnder modulator with an existing widely tunable sampled-grating distributed-feedback reflector (SGDBR) laser source [52–55]. The Mach-Zehnder modulator has been integrated onto the original common waveguide layer in the laser source with the phase shifter refractive index change mechanism based primarily on band-emptying the n-doped waveguide layer.

---

[30] There has been recent industry consolidation around small-form-factor pluggable transponders (XFP and SFP) that are expected to evolve into line-side solutions.

Chapter 2

Waveguide Design for a Strongly-Guided InP-Based Mach-Zehnder Modulator

In this Chapter the waveguide design for a strongly-guided InP-based Mach-Zehnder modulator is developed. It begins with the development of the waveguide cross-section design. This is followed by a detailed study of optimal multi-mode interference designs for mode filter, splitter and combiner functions. The practical constraints imposed by implementation in the InP material system will be emphasized. Waveguides bends are studied in the context of a strongly-guided waveguide, with designs provided for the required s-bends in the Mach-Zehnder modulator. Finally, the optimal waveguide layouts for the Mach-Zehnder modulator are given and supported by experimental measurements. Two appendixes discuss the InP material system and refractive index, along with the determination of the refractive index of a multi-quantum well structure.

2.1 Waveguide Cross-Section Design

This Section begins with a review of the basic optical waveguide design options, the limitations of weakly-guided waveguide structures for passive optical and modulation functions, and the benefits of strongly-guided waveguides for these same functions. An aside is given on a weakly-guided waveguide structure developed to enable an optical cross-connect.

An introduction to the strongly-guided waveguide designs developed in this thesis is given, and the scattering and doping losses in these designs are detailed. An experimental measurement of the total loss in the modulator waveguide is provided. The electrical properties of the modulator waveguide are discussed and a helium implantation process for electrical isolation is demonstrated.

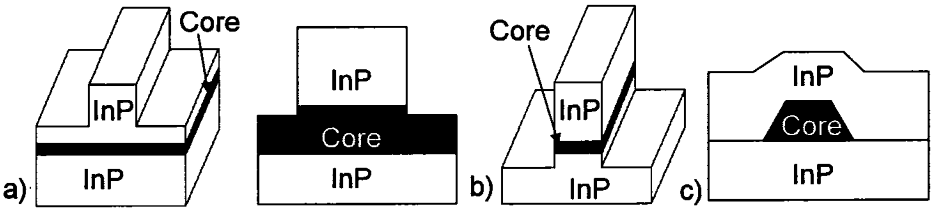

Figure 2.1: *Basic Optical Waveguide Configurations.*

The waveguide lateral modes are studied both theoretically and experimentally as a function of ridge width, etch process, core thickness, and core composition. Finally, the higher order vertical modes are studied and a method for controlling them is proposed based on the use of n-dopant controlled refractive index profiles.

2.1.1 Basic Optical Waveguide Design Options

Near single-mode waveguides in the $In_{1-x}Ga_xAs_yP_{1-y}$/InP material system can be broadly classified into three distinct groups as shown in Figure 2.1. The first group contains waveguides where a shallow rib is etched through the overcladding, or possibly into the core layers, to give weak lateral confinement to the fundamental optical mode. The second group of waveguides utilizes a deep-etch through the overcladding, core, and some fraction of the undercladding layers to give strong lateral confinement to the fundamental optical mode. The third group is buried core waveguides with equal optical confinement in both the vertical and lateral directions. There are multiple ways to define buried core waveguides, however, they all require multiple MetalOrganic-Chemical-Vapour-Deposition (MOCVD) growth steps.

2.1.2 Limitations of Weakly-Guided Waveguides for Passive Optical and Modulation Functions

The waveguide configurations in Figures 2.1a and 2.1c are predominantly used in semiconductor laser and optical amplifier device designs. These waveguide configurations suffer from a number of drawbacks when used for modulation or passive optical functions:

1. In weakly-guided waveguides the etch depth is a critical design parameter that has tolerance requirements outside the bounds of conventional reactive ion (RIE) [61] or inductive coupled plasma (ICP) [212] dry etch technologies. To define these waveguides it is necessary to follow a shallow dry etch with a finishing crystallographic wet chemical etch. This finishing wet etch terminates at a depth defined by a grown-in etch stop layer. The etch stop layer allows the ridge height, relative to the core layers, to be accurately defined in the MOCVD wafer growth. The necessity of the

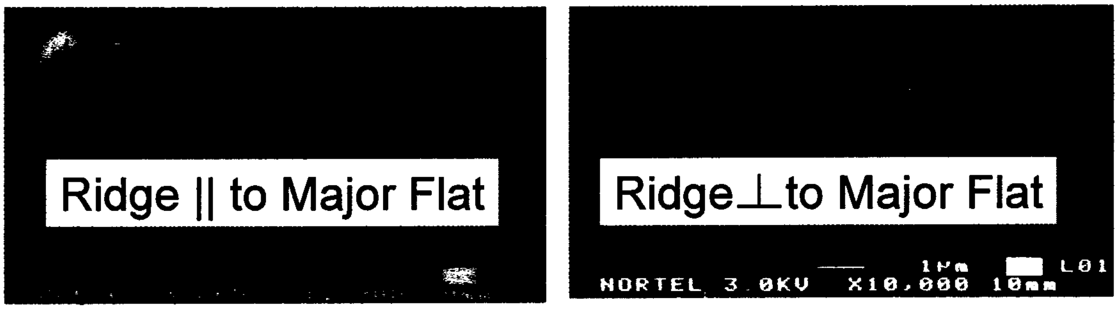

Figure 2.2: ***Impact of Ridge Wafer Orientation on*** $HCl{:}H_3PO_4$ ***Wet Chemical Etch used to Accurately Terminate the Ridge Etch.***

crystallographic wet etch, however, makes the ridge sidewall profile dependent on the ridge orientation relative to the crystal planes of the substrate. This greatly complicates the use of these waveguide configurations in applications where more than one ridge orientation is required. An example is shown in Figure 2.2.

2. With weak lateral mode confinement, light that is launched or scattered from optical circuit interfaces into higher-order lateral modes[1] may leak horizontally and cause inter-waveguide crosstalk. Background substrate scattered light may also impact the ultimate extinction ratio achievable for a modulation function in a waveguide with weak lateral mode confinement.

3. Accurate multimode interference couplers and combiners are difficult to design and fabricate in weakly-guided waveguides for the reasons discussed in Section 2.2. Any such MMI device will be physically large since its access waveguides must be sufficiently separated to limit any inter-waveguide coupling between them.

4. Weak lateral mode confinement requires any waveguide bends to have a large radius of curvature to limit radiation losses from the waveguide as detailed in Section 2.3.

5. The mode shape of a weakly-guided waveguide is elliptical and not ideal for low-loss imaging onto a circular fiber mode.

6. Buried core waveguides can have the same waveguide geometry dependence on ridge orientation discussed in point (1), since a wet chemical clean is required to condition the surface of the etched core prior to the blanket overgrowth. For the additional fabrication complexity introduced, buried core waveguides offer no compelling advantage over strongly-guided waveguides when implementing passive optical or modulation functions.

---

[1] The full mode continuum including radiation modes must be considered

2.1.3 Aside: Using a Weakly-Guided Waveguide Structure to Enable an Optical Cross-Connect Switch

An optical switching structure has been developed to exploit the difficulty experienced when trying to bend a waveguide with weak lateral confinement. The structure enables a total internal reflection (TIR) switch design having excellent crosstalk performance [70].

Cross-connect architectures of semiconductor optical switches will be useful in future packet and/or wavelength switching network applications, where electromechanical switching speeds are not sufficient. Recently, the semiconductor optical amplifier (SOA) gate has been the favoured semiconductor switch due to its excellent inter-channel crosstalk and low insertion loss. It, however, generally lacks true system transparency with limitations on the number of WDM channels, the bit rate, polarization, and the allowed power range for the input signal. The SOA gate also requires integration with a second switch having low bar-state loss to be useful in scalable architectures [71,72].

The total-internal-reflection (TIR) switch is an alternative design with none of the limitations of a SOA gate. The TIR switch still features fully digital operation, compact size and wavelength independence, though it has traditionally required difficult fabrication techniques and suffered from poor crosstalk performance. The proposed weakly-guided InGaAsP/InP TIR switch, designed for use within a novel cross-connect architecture, will allow for compact, scalable, transparent, and low-crosstalk, NxN optical cross-connect switches.

TIR Switch Geometry and Cross-Connect Architecture

The TIR switch has an asymmetric waveguide y-junction at an intersection angle of 3^o and an optical/electrical interaction length of 450μm, as shown in Figure 2.3b. The architectural building block that connects each orthogonal input-to-output waveguide consists of two TIR switches and a 45^o optical turning mirror within an area of only 1mm^2 [73] as shown in Figure 2.4f. The digital response of each TIR switch allows a single electrical chip connection in each building block, thus only N^2 connections and only N simultaneous signals are required for the NxN cross-connect operation. The orthogonal waveguide architecture minimizes the interchannel crosstalk by cascading the TIR switch performance between any input-to-output waveguide combination, and by limiting the output coupling of input stray light.

TIR Switch Design

The switch uses single-mode, 5μm wide ridge waveguides with weak [$\Delta n=2\text{x}10^{-3}$] lateral confinement and a vertical $Q=1.3\mu$m InGaAsP/InP p-i-n heterostructure as shown in

Figure 2.3a. Switching is achieved under forward bias using the large, free-carrier-density-induced refractive index change [90].

A guide layer cross-section from a TE semi-vectorial, three-dimensional, finite-difference beam propagation method [84] (BPM) simulation of the TIR switch at 1550nm is shown in Figure 2.3c. The bar-state losses and crosstalk are minimized using the waveguide geometry such that a TE bar-state loss of -0.36dB and a bar-state crosstalk of -24.9dB are theoretically expected. Figure 2.3d shows the waveguide TE_0 cross-section power contours at the switch element output in both the bar and cross-state. Switching losses of 1.3dB are theoretically expected due to unavoidable free-carrier absorption. The traditional TIR switch limitations of high switching current and poor crosstalk performance have been overcome using single-mode operation and low contrast waveguides.

Instead of trying to eliminate lateral carrier diffusion using current blocking [74], implant isolation [71,75], or semi-insulating regrowth [72], the carrier gradient has been anticipated and the electrode shaped to minimize the switching losses. This device was designed prior to the development of the implantation process discussed in Section 2.1.8.

Experimental Results for the TIR Switch

Figure 2.4a shows the lateral near field profile of an individual AR-coated TIR switch obtained at 1550nm by scanning a 5μm slit across the magnified image of the switch output. Optical coupling to the switch is via cylindrically-lensed single-mode fiber with a coupling loss of approximately 2.6dB. Switch performance is shown at 0mA and 40mA injection. An excess cross-state loss (A-C) of 1.6dB is obtained with a cross-state extinction (C-D) of 13.5dB. The bar-state crosstalk (A-D) is -15.2dB with a bar-state extinction (A-B) of 13.7dB. Note, the bar-state crosstalk and cross-state extinction values are pessimistic since the input and output waveguides are not orthogonal and no modal filtering is performed with the integrated power scan measurement. In reverse operation with light input from the cross-state of the switch, the on-off ratio at the single input is 19.6dB. Taken as a whole, this data clearly demonstrates excellent single-mode operation for the TIR switch.

Figure 2.4b shows the normalized TE fiber-to-fiber switch transfer curves. Digital switching performance after 40mA is observed. A bar-state extinction of 13.7dB and a cross-state extinction of 20.7dB are obtained. In the proposed cross-connect architecture the interchannel crosstalk is dominated by twice the cross-state extinction of the individual switch [i.e. 35-40dB interchannel crosstalk is feasible]. This demonstrates that low crosstalk performance is achieved in the TIR switches.

Using the Fabry-Perot cutback method [175–178], the bar-state loss was measured to be less than the experimental error of 0.5dB for both TE and TM polarization. This low bar-state loss should allow a 16x16 cross-connect to be built with the highest on-chip loss $<$ 12dB.

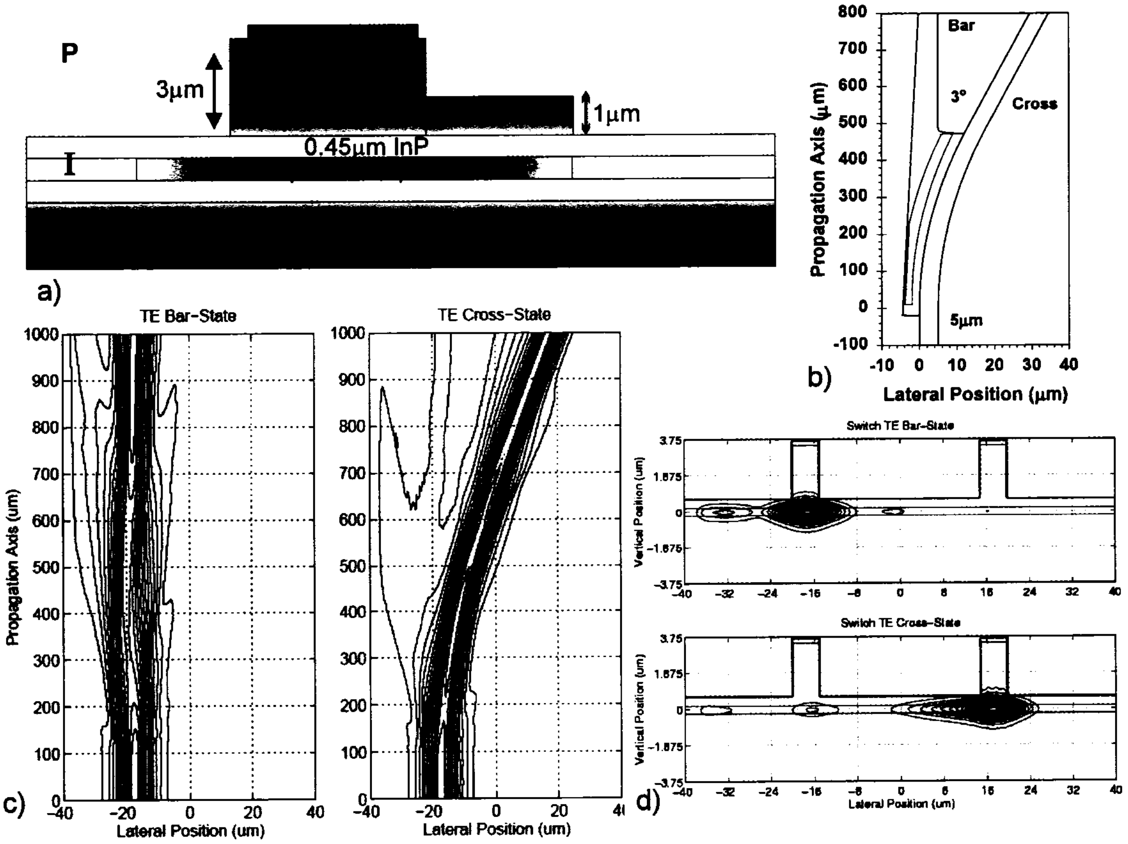

Figure 2.3: ***Waveguide Design for a Total Internal Reflection (TIR) Switching Element: a) Switch Waveguide Cross-Sectional Geometry, b) Switch Waveguide Longitudinal Geometry, c) 3D-BPM X–Z TE_0 Propagation Power Contours through the Centre of the Waveguide Core, d) 3D-BPM TE_0 Cross-Section Power Contours at the Switch Element Output in both the Bar and Cross-State.*** *Source: Ian Betty et al., Integrated Photonics Research, 1999.*

The wavelength performance of the switch was measured using fiber-to-fiber transmission loss measurements from 1528nm to 1561nm normalized against identical straight waveguide measurements. The bar-state loss uniformity was better than 0.2dB, as shown in Figure 2.4c. The cross-state uniformity was better than 0.1dB, as shown in Figure 2.4d, and the bar-state crosstalk uniformity was better than 0.5dB. This stable wavelength performance confirms true TIR operation for the switch.

Figure 2.4e confirms that cross-state switching times < 50ns can be easily obtained.

This robust TIR switch design enables a compact, scalable cross-connect architecture that should allow for 35-40dB interchannel crosstalk without the use of SOA gates in packet switching applications. All the ideal switch criteria have been satisfied with the exception of insertion loss. It is proposed that gain be handled in a system friendly manner external to the space switch.

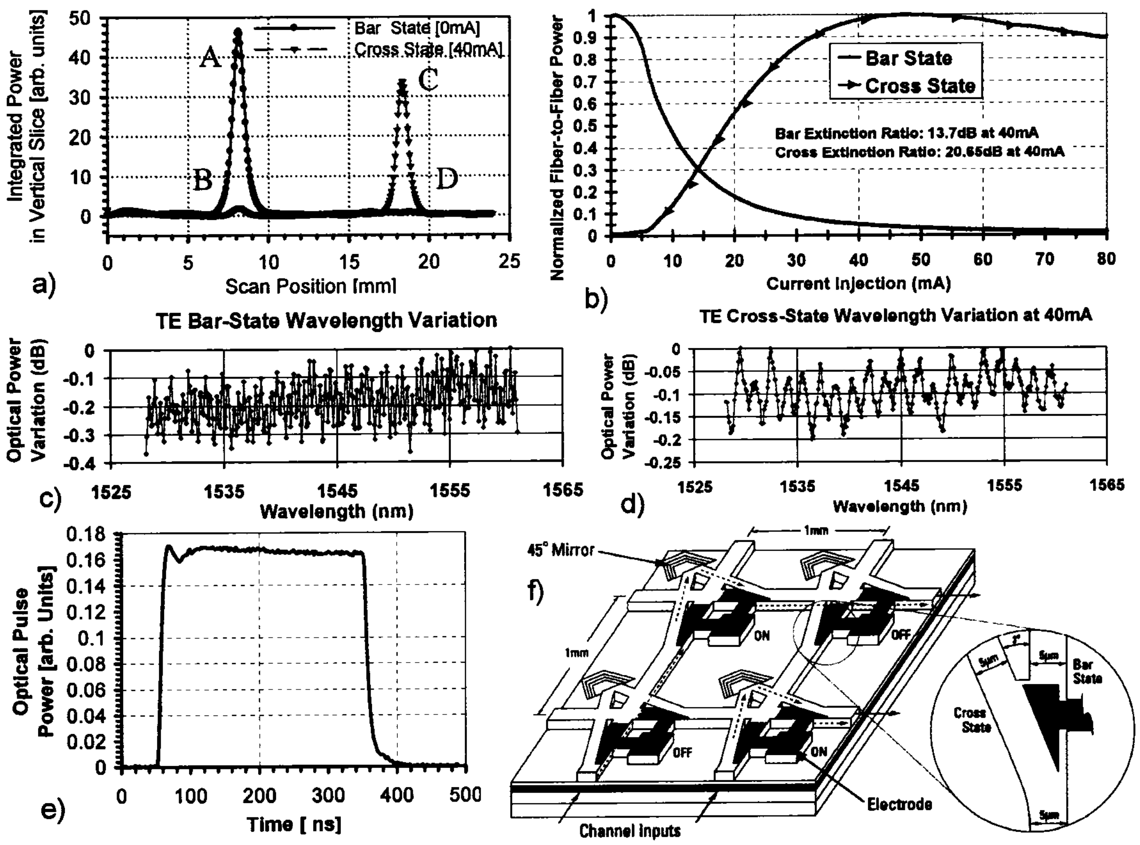

Figure 2.4: *Experimental Demonstration of a TIR Switching Element: a) Integrated Lateral Near Field Profile, b) Normalized TE Fiber-to-Fiber Switch Transfer Curves, c) Bar-State Loss Uniformity versus Wavelength, d) Cross-State Loss Uniformity versus Wavelength at Fixed Current Injection, e) Cross-State Switching Time, f) Illustration of Cross-Connect Switch Architecture. Source: Ian Betty et al., Integrated Photonics Research, 1999.*

2.1.4 Benefits of Strongly-Guided Waveguides for Passive Optical and Modulation Functions

Many of the disadvantages of shallow-etched waveguides can be overcome by using deep-etching to strongly confine the lateral semiconductor waveguide modes with air:

1. Strong-guiding greatly reduces the radiation loss from the waveguide in low radius of curvature bends since the radiation caustic remains far from the waveguide as discussed in Section 2.3.
2. Any light launched or scattered into the higher-order modes of the deeply-etched waveguide will leak vertically into the substrate rather than horizontally; thus, inter-waveguide crosstalk and background scatter into the output optics are reduced.
3. Strong lateral confinement provides more ideal self imaging in splitter and combiner multimode interference functions.
4. The number of modes supported and the properties of the fundamental modes in deeply-etched waveguides is not significantly dependent on the etch depth, thus enabling the use of the conventional dry etching techniques.
5. Deep-etched waveguides allow the spot-size of the lateral mode field to be changed over short distances using waveguide tapers as detailed in Section 3.6.
6. Strongly-guided p-i-n diode optical waveguides under reverse bias, where the intrinsic region is coincident with the guide layer, enable overlaps between the generated electric field and the optical mode that approach 80%. The confinement of the electric field lines by the air cladding also enables lower waveguide capacitance per unit length than in weakly-guided structures, where p and n doped regions surround the core over the full area of the device. The capacitance per unit length is shown in Figure 2.5 as a function of intrinsic core thickness for a strongly-guided ridge width of 2.0μm in the Mach-Zehnder waveguide. The calculations are based on a finite element solution to Laplace's equation for LIH[2] dielectrics and perfect conductors. A similar result would be obtained for any InP/InGaAsP strongly-guided waveguide design.

2.1.5 Introduction to the Strongly-Guided Waveguide Designs Developed in this Thesis

Deep-etched waveguides can be subdivided into two groups based on the ridge width and the corresponding technology required for the waveguide definition. The first type typically have a ridge width ~0.5μm[3] wide. The resist mask required to etch these narrow

---

[2] linear, isotropic and homogeneous

[3] This width is approximately the same as the wavelength in the material.

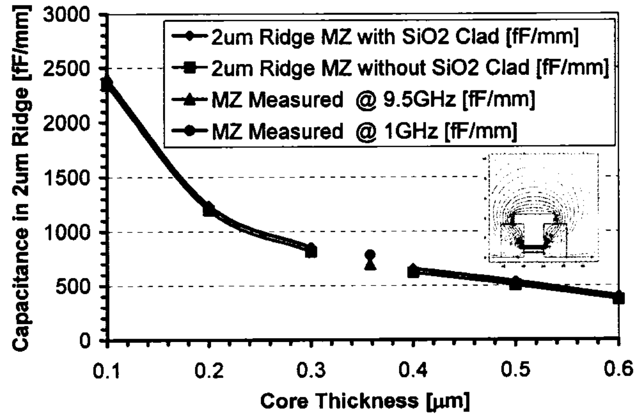

Figure 2.5: ***Capacitance per Unit Length as a Function of Intrinsic Core Thickness in a Strongly-Guided InP-Based Waveguide with a 2.0μm Ridge Width.***

waveguides must be defined using E-beam lithography to minimize the sidewall roughness, since at these ridge widths, scattering losses from the air-to-semiconductor interface are very significant [62]. The large lateral index step also leads to significant birefringence, however, these narrow waveguides are ideal for applications where low radius bends are required. A bend radius of less than 5μm has been reported in a notch filter [63]. Though these very narrow waveguide structures enable very low radius bends and guarantee single-mode operation, they have not been considered due to the cost of E-beam lithography and the still poor state-of-the-art waveguide losses.

The second category of deep-etched waveguide has a ridge width typically near 2.0μm. In these waveguides it is possible to obtain low propagation loss using conventional i-line photolithography as discussed in Sections 2.1.6 and 2.1.10. Figure 2.6 presents the two waveguide structures of this type studied extensively in this Chapter. The first is the p-i-n diode Mach-Zehnder modulator structure and the second is a structure used to study passive waveguide functions. The material composition of the modulator structure MQW wells and barriers is discussed in Section 3.9.1. In InP materials silicon (Si) is used as the n-dopant and zinc (Zn) is used as the p-dopant.

Only the TE performance is significant for the modulator waveguide structure since the modulator is integrated (monolithic or hybrid) with a semiconductor laser source having a TE polarized output. Suppressing the birefringence in the passive waveguide structure may be desired for certain applications such as arrayed waveguide demultiplexers [149]. The birefringence of the passive waveguide structure can be minimized by optimizing the core dimensions and composition as discussed in Section 2.1.11. Further design improvements to the birefringence of the passive waveguide structure shown in Figure 2.6b have been reported [60].

In optical modulator applications it is not possible to obtain single lateral mode operation using a deep-etched waveguide with a ridge width near 2.0μm. This is due to the require-

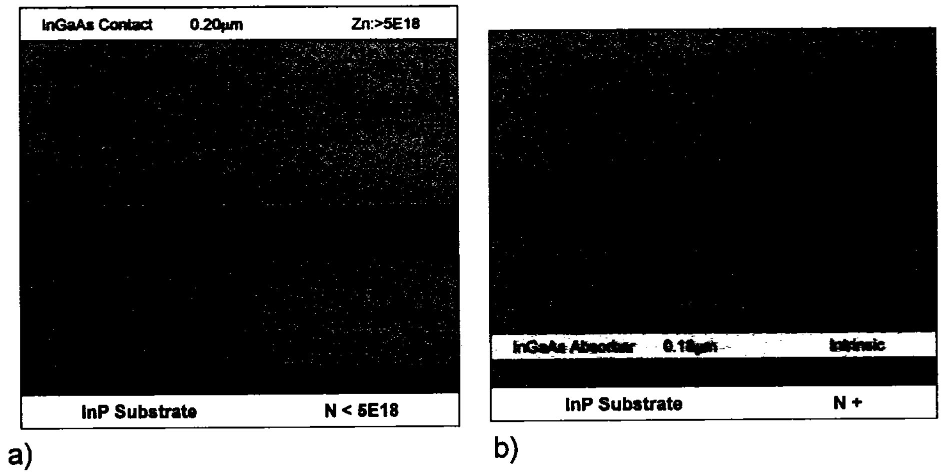

Figure 2.6: ***Optimized Strongly-Guided Waveguide Designs: a) Modulator Structure, b) Passive Waveguide Structure.***

ments imposed on the waveguide core design to enable efficient phase tuning sections in the modulator. In strongly-guided waveguides the leakage rates of the higher-order lateral modes into the substrate are also quite low even when they are not guided. The problems introduced by these higher-order lateral modes and the means of suppressing them are a large focus of this Chapter.

Figure 2.7 presents the TE modes in the modulator and passive waveguide structures for a ridge width of 2.0μm at a wavelength of 1.546μm[4]. The coordinate system used here and in all subsequent simulations in this thesis has the x-axis in the plane of the epitaxial growth, the y-axis perpendicular to the epitaxial growth, and the z-axis the direction of propagation. The refractive indices used for the materials are defined in Appendix 1 and 2. The modulator modes were calculated with a 128X256 point non-uniform grid finite-difference mode solver using Perfectly Matched Layer (PML) boundary conditions [85] in a 6μmX8μm space. The passive structure modes used the same solver technique on a 256X256 non-uniform grid in a 10μmX10μm space. The modulator structure etch depth is 4.0μm and the passive waveguide structure etch depth is 3.1μm. It is apparent the TE_1 mode is guided at the nominal ridge width of 2.0μm in the modulator structure. The model extracted TE_0 waveguide properties for the modulator structure as a function of wavelength are given in Table 2.1. The Rib mode in the passive waveguide structure is attenuated by beating with the InGaAs absorber mode as discussed in Section 2.1.12. In Table 2.2 the TE_0 and TM_0 waveguide properties for the passive waveguide structure are provided at both wavelength ends of the EDFA C-Band.

The physical modulator and passive waveguide structures can be represented in two dimensions[5] for modelling purposes using the Effective Index Method [EIM] [103]. Fig-

---

[4] The centre of the EDFA C-Band is located at 1546.1515nm.

[5] The waveguides are single-mode in the transverse y direction; therefore, the transverse y modal field

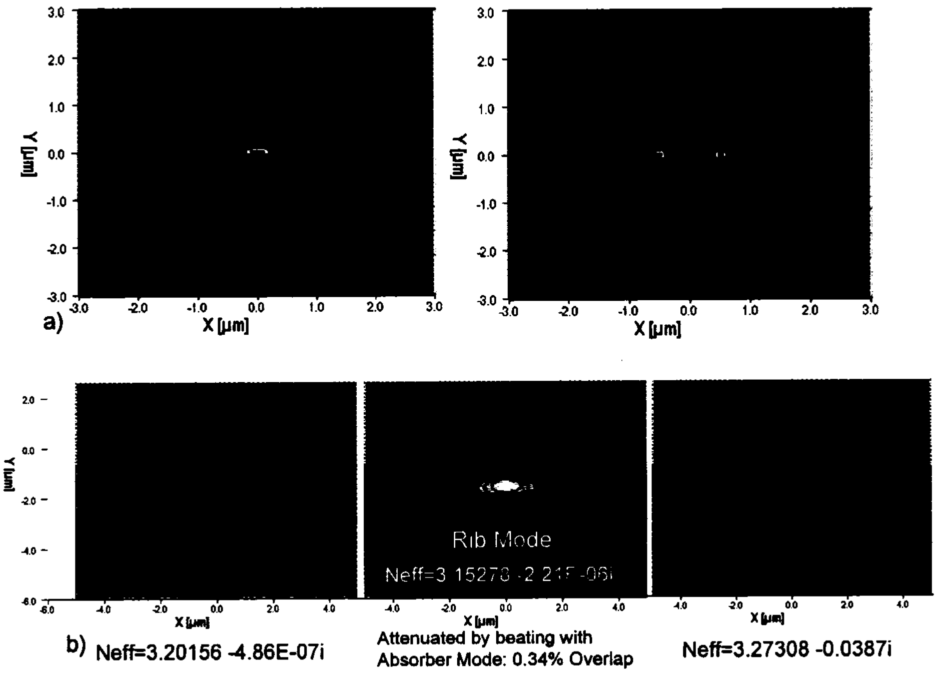

Figure 2.7: ***Guided Modes in the Optimized Strongly-Guided Waveguide Designs: a) Modulator Structure, b) Passive Waveguide Structure***

Parameter	1525nm TE_0	1546nm TE_0	1565nm TE_0
Overlap Substrate Doping	1.25E-6	1.76E-6	1.87E-6
Overlap 5E18cm^{-3} Si N Doping	2.48E-5	3.35E-5	4.38E-5
Overlap 5E17cm^{-3} Si N Doping	0.197036	0.201912	0.206367
Overlap 2.5E17cm^{-3} Zn P Doping	0.153678	0.159052	0.164029
Mode Field Fit σ_x	0.726	0.727	0.727
Mode Field Fit σ_y	0.483	0.496	0.508
N_{eff}	3.234188	3.228363	3.223181
Core Confinement	0.599987	0.589781	0.580415
Overlap InP p-Spacer	0.047937	0.047817	0.047678
Overlap InGaAs Cap	3.3E-7	5.18E-7	7.73E-7

Table 2.1: ***TE_0 Waveguide Properties for the Modulator Structure as a Function of Wavelength in C-Band.***

Parameter	1525nm TE_0	1565nm TE_0	1525nm TM_0	1565nm TM_0
Mode Field σ_x	0.723	0.731	0.770	0.772
Mode Field σ_y	0.601	0.637	0.649	0.687
N_{eff}	3.20639	3.19730	3.20486	3.19619
Core Confinement	0.559973	0.539443	0.532369	0.511716

Table 2.2: *TE_0 Waveguide Properties for the Passive Waveguide Structure at both Wavelength Ends of C-Band.*

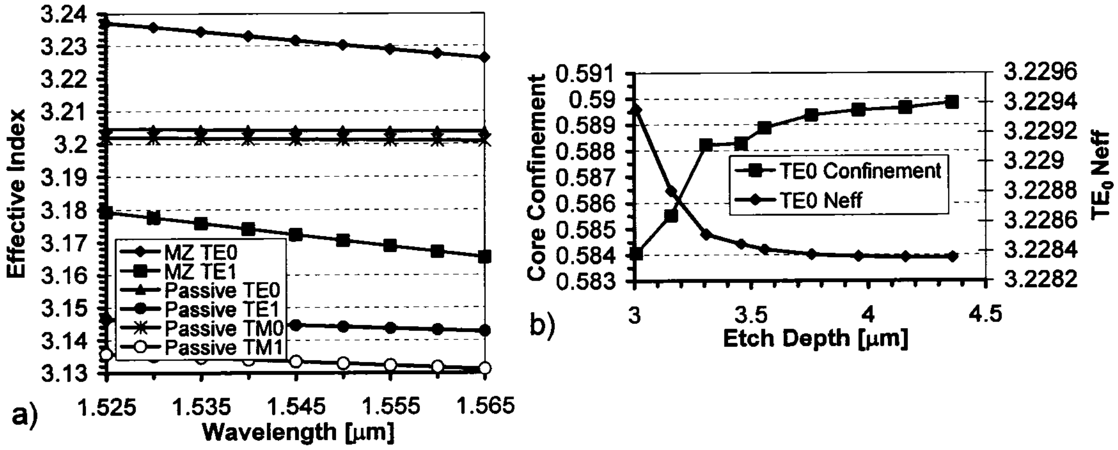

Figure 2.8: *a) Effective Indices Obtained Using the Effective Index Method for both the Modulator and Passive Waveguide Structures as a Function of Wavelength, b) Effective Index and Core Confinement for the TE_0 Mode in the Modulator Structure as a Function of Ridge Etch Depth at 1546nm.*

ure 2.8a presents the effective indices of the TE_0-TE_1 modes obtained using EIM for the modulator structure and both the TE_0-TE_1 and TM_0-TM_1 modes for the passive waveguide structure as a function of wavelength. The reduced wavelength sensitivity in the passive waveguide structure is due to the larger offset between the operating wavelength and the absorption bandedge of the core material. Figure 2.8b shows[6] that in the modulator structure the n_{eff} and core confinement for the TE_0 mode, at the centre 1546nm wavelength, are independent of ridge etch depth past the core as been as previously stated in Section 2.1.4.

---

profile will not vary along the z direction of propagation. This allows the waveguide problem to be analyzed in two dimensions (lateral and longitudinal) without loss of generality.

[6] These calculations use the simulation conditions of Figure 2.7.

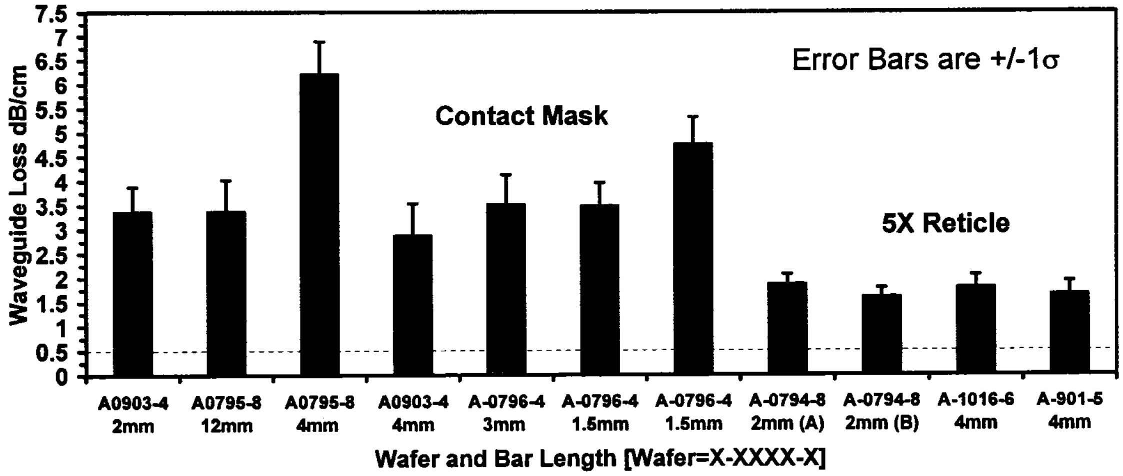

Figure 2.9: *Impact of Lithography on Scattering Losses in a 2.0μm Wide Strongly-Guided Straight Waveguide: Comparison of 0.1μm Resolution Contact g-line Lithography and 0.1μm 5X Stepper based i-line Lithography.*

2.1.6 Scattering Losses in the Strongly-Guided Waveguide Designs

Optical losses in strongly-guided waveguide structures are very dependent on the fabrication technology used due to the high optical field densities that occur at grown and etched interfaces. Figure 2.9 shows the waveguide loss dependence on the photolithography technology, as measured in a 2.0μm wide straight waveguide with the passive waveguide structure shown in Figure 2.7b. The III-V semiconductor etch used for all these samples is a CO_2:CH_4:H_2 reactive ion etch (RIE) [64], where the only difference in the samples is the quality of the resist mask used to define the waveguides. Clearly, the 0.1μm minimum feature size in the contact lithography process corresponds to an increased vertical sidewall roughness, relative to the stepper lithography process. The stepper lithography defined waveguides have measured losses that compare with the best in literature values [67]. These optical loss measurements were obtained using the cut-back Fabry-Perot method [175–178]. The Fabry-Perot spectrum through the waveguide under test was collected in real time by using a 1kHz sawtooth current ramp on a DFB laser as the swept frequency optical source. This novel approach to the measurement allowed instant feedback on the impact of misalignment in the coupling optics. This is necessary when attempting to couple to strongly-guided devices having fundamental modes with small near field dimensions.

Many different technologies exist for etching III-V semiconductors. Those used to produce the waveguide structures in this thesis include CO_2:CH_4:H_2 reactive ion etching (RIE) [64], HBr inductive coupled plasma (ICP) etching [212] and Cl_2 ICP etching [210,211]. As shown in Figure 2.10 and 2.11 both HBr ICP etching and CO_2:CH_4:H_2 RIE etching produce the required vertical and smooth ridge sidewalls for strongly-guided waveguide devices. An example of a Cl_2 ICP etched ridge waveguide is shown in Figure 2.12. This etch has only been

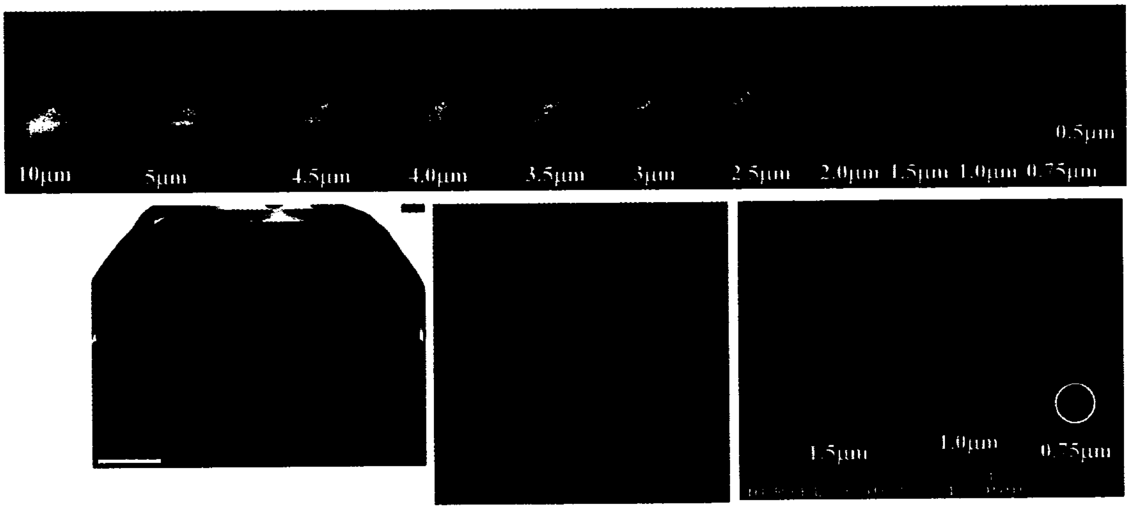

Figure 2.10: *HBr ICP III-V Semiconductor Etch.*

used in this thesis to defined the modulator-to-spot-size-converter butt-joint, as detailed in Section 4.3.1. The ridge width uniformity on a 3″ wafer is typically better than ±0.1μm using the HBr ICP etch technology with i-line stepper based photolithography [210].

Sidewall scattering is the primary loss mechanism in the passive waveguide structure. This is not the case in the modulator structure where the electro-optic design requirements introduce additional loss mechanisms. A 20 period MQW waveguide core is required in the modulator, and this structure invokes both bandedge absorption and scattering losses from the quantum well/barrier interfaces shown in Figure 2.13. The surface scattering due to roughness in the epitaxial interfaces is determined by the quality of the MOCVD growth. It is difficult to separate the epitaxial interface scattering and the bandedge absorption contributions to the waveguide optical loss without specifically studying an undoped waveguide with a MQW core far from bandedge. No opportunity was available for this study.

2.1.7 Doping Losses in the Strongly-Guided Waveguide Designs

An optimal design for the phase shifter in the modulation arms of the Mach-Zehnder modulator requires a high optical mode overlap to be obtained with a large electric field. This requires the modulator waveguide to have an electrical p-i-n diode structure as shown in Figure 2.6a, with the intrinsic region coinciding with the MQW core[7]. The required presence of the p-doping[8] and n-doping[9] introduce additional losses. The principle carrier-

---

[7] Recently an n-i-n design has been proposed and fabricated by NTT [34].

[8] Zn doping in the MOCVD grown structure

[9] Si doping in the MOCVD grown structure

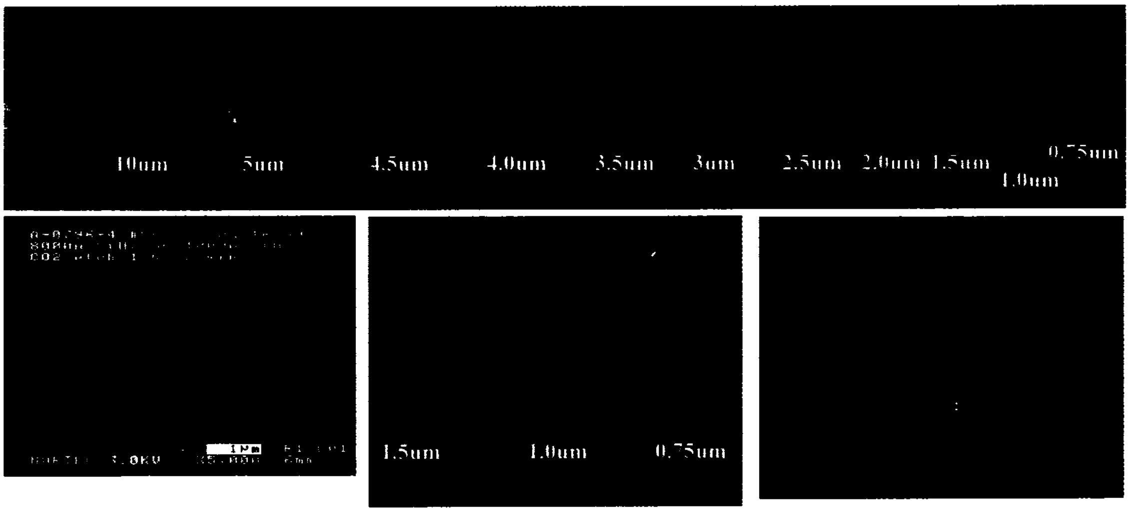

Figure 2.11: *CO_2:CH_4:H_2 RIE III-V Semiconductor Etch.*

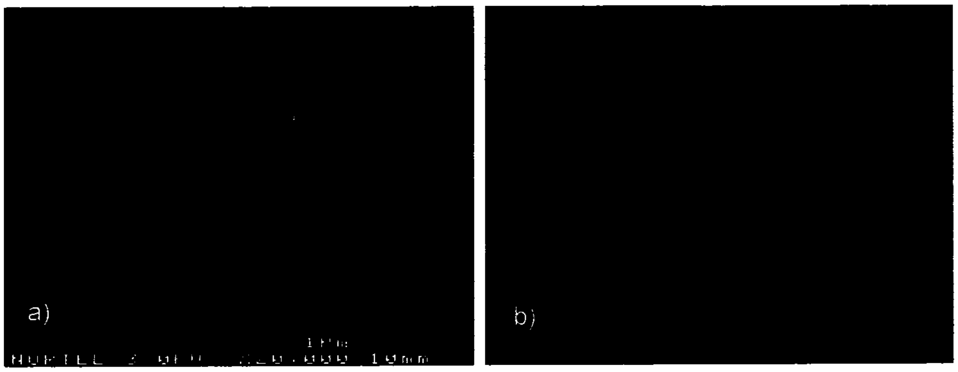

Figure 2.12: *Cl_2 ICP III-V Semiconductor Etch Source: N. Kim, F.R. Shepherd, T. Jones, C. Fragos, T.G. Lee, "ICP Etching of InP at High Rates using Chlorine Chemistry," Tenth Canadian Semiconductor Technology Conference, Ottawa, 2001.*

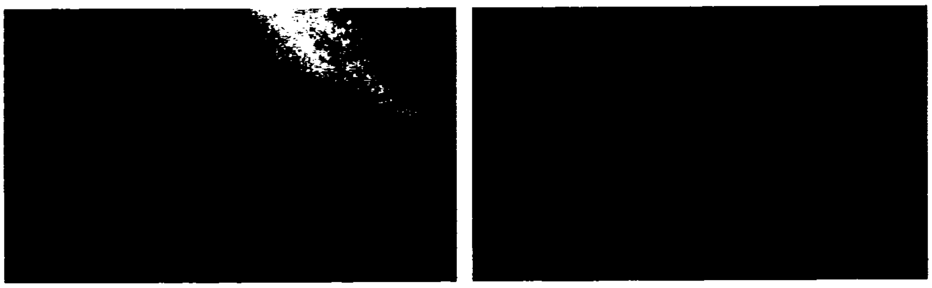

Figure 2.13: *TEM of Individual Quantum Wells in the Modulator Structure.*

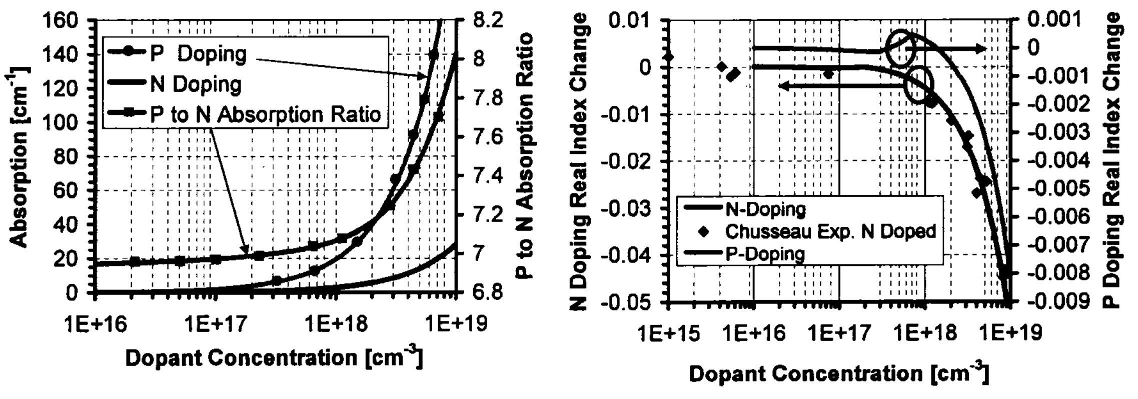

Figure 2.14: *Impact of N and P Doping on the Refractive Index of InP.*

induced effects have been calculated for a variety of materials by Bennett et al. [90] and experimentally determined for InP [91–93].

Figure 2.14 provides calculations based on the work of Bennett et al. [90] for the change in real refractive index and the optical loss in InP as a function of the doping concentration for both p and n doping species at 1550nm. Also included in Figure 2.14 are the experimentally determined values, given by Chusseau et al. [92], for the real refractive index change due to n-doping in InP. The free carrier plasma in the semiconductor reduces the real refractive index. The influence of the plasma is particularly strong for electrons since their effective mass is generally small in III-V compounds. In the waveguide designs here and in Chapter 3, use is made of both these absorption and real refractive index changes in InP materials. It is clear from Figure 2.14 that p-doping induces a factor of 7-8 greater contribution to optical loss and a negligible real refractive index change relative to n-doping. The loss given for p-doped InP in Figure 2.14a has been confirmed by experimental measurements [93]. Device loss calculations based on Figure 2.14a will over-estimate the optical losses in practice, since some hydrogen passivation of the grown-in p-doping is inevitable in the fabrication process [65].

The contribution of doping to the loss of the TE_0 mode in the modulator structure can be quantified using the calculations in Figure 2.14 and the results from Table 2.1. There is 0.35dB/mm loss due to mode overlap with the 2.5E17cm^{-3} p-doping, 0.13dB/mm loss due to mode overlap with the 5E17cm^{-3} n-doping, and 2.4E-4dB/mm loss due to mode overlap with the 5E18cm^{-3} N-doping in the antiguiding layer. The total contribution to loss from the doping profile is 0.48dB/mm.

Three design factors influence the thickness of the Zn-doped InP layers in Figure 2.6: the design of the spot-size converter outlined in Chapter 3; the minimization of the overlap between the fundamental TE_0 mode and the highly lossy InGaAs contact layer; and finally, the minimization of the stress-induced refractive index change in the intrinsic region caused by the presence of the metalization on the ridge [66]. All three design factors improve as the Zn-doped layer thickness increases, however, the fabrication complexity also increases. Dimensional control of the waveguide width at the quantum wells[10] becomes more difficult with increasing etch depth, and the complexity of the process for planarizing the wafer surface with spin-on resists also increases. A planarization process is required to enable air-bridged metal fabrication spanning the etched trenches around the waveguides.

2.1.8 Waveguide Electrical Properties

The modulator waveguide is an electric p-i-n diode structure where the MQW core coincides with the intrinsic region. The diffused ohmic n-contact is common throughout the device and is formed by sputtering a Ni/Ge/Au metal stack onto the wafer backside. Individual ohmic p-contacts are formed on the device by patterning a topside Ti/Pt/Au metal stack [69]. The titanium in the p-contact metal stack is deposited on a heavily p-doped InGaAs epitaxial layer to enable a low contact resistance.[11] The gold top layer in the stack enables low resistance along the length of the electrical contact and the platinum layer sandwiched in the middle acts as a diffusion barrier to prevent the highly soluble gold from entering the semiconductor.

A reversed biased electrical diode is generated in an optical waveguide by grounding the backside of the wafer and reverse biasing its topside p contact. A reverse biased diode does not place stringent requirements on the p and n contact resistivities since only photo-generated carriers flow under bias modulation. These photo-generated carriers contribute negligible voltage drop at the p and n contacts for easily achievable contact resistivities.

Ideally, all of the applied voltage would appear across the intrinsic region, creating a large uniform electric field in the MQW core, and thus maximizing the effect of the field dependent phase shift mechanisms. In practice the uniformity of the electric field is limited by the intrinsic region background dopant control with MOCVD growth.

In the underclad layers below the core the n-type doping is introduced by flowing SiH_4 through the MOCVD chamber during the growth. Silicon is a stable impurity and little diffusion occurs during the MOCVD growth. A sharp n-i interface can be achieved between the underclad InP layer and the MQW core.

In MOCVD growth of the overclad Zn-doped layers[12] the Zn incorporates on both substitutional and interstitial sites. It is known that diffusion of the Zn occurs during growth and that this diffusion is dominated by a small fraction of highly mobile Zn interstitial donors. J.E. Haysom et al. [81] have demonstrated a concentration dependence for this diffusion rate in InP and a +1 charge for the mobile Zn interstitial when using Diethyl zinc as the p-dopant source. They propose that it is the fast diffusion of these interstitials through the Zn-doped layers that cause a p-i interface to move, and that once at the p-i interface, these interstitial will quickly come to a stop as they convert to substitutional Zn. Based on this,

---

[10] The quantum wells are located near the bottom of the etch.

[11] There is a low Schottky barrier height at the interface.

[12] Diethyl zinc is used as the p-dopant source in MOCVD growth.

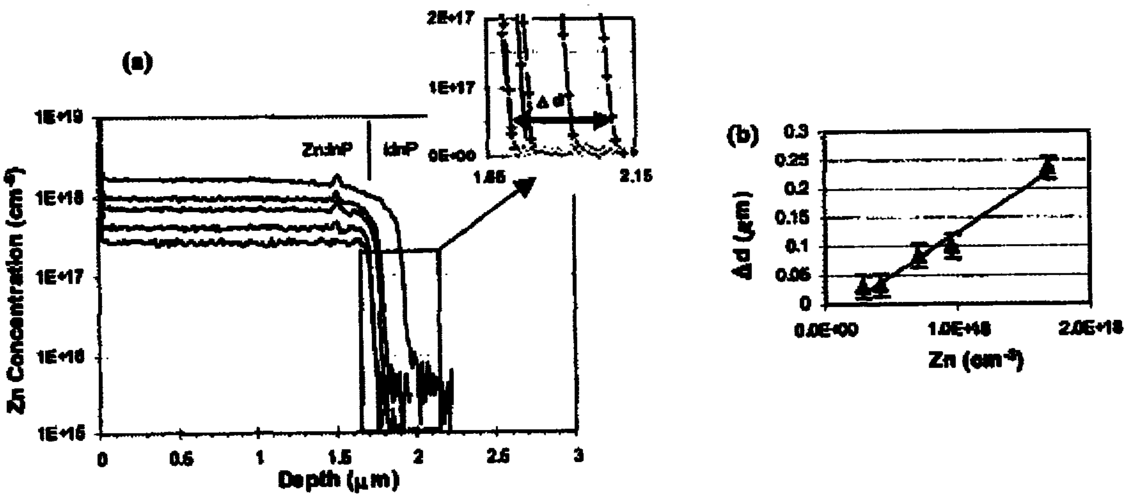

Figure 2.15: *The Use of an Undoped Spacer to Prevent a Zn Diffusion Tail: a) Secondary Ion Mass Spectroscopy (SIMS) Profiles for Five Different all-InP Wafers with Different Zn Doping Concentrations in the Top 1.7µm; the Insert Shows a Zoom-In on the p-i Interface on a Linear:Linear Scale, b) Plot of Δd versus Zn Concentration using Data Extracted from (a), Including a Linear Fit to the Data.* Source: *J.E. Haysom, R. Glew, C. Blaauw, R. Driad, D. MacQuistan, C.A. Hampel, J.E. Greenspan, and T.Bryskiewicz, Proc. 14th IPRM, 2002.*

they demonstrate that an undoped spacer layer of InP between the Zn-doped layers and the desired intrinsic region will act to prevent a Zn diffusion tail in the desired intrinsic region, as shown in Figure 2.15. J.E. Haysom et al. also demonstrated experimentally that an InGaAs cap can incorporate Zn substitutionally at much greater concentrations than can InP. They show that the addition of a 1.4E19cm^{-3} Zn-doped InGaAs cap has no effect on the position of the p-i interface. The use of an undoped spacer layer, between the MQW intrinsic core, and the Zn-doped overclad InP layer, has been applied to the modulator structure in Figure 2.6.

It is also desirable that the depletion width, x_d, of the p-i-n diode structure vary as little as possible with applied bias. In a homogenous p-i-n diode junction this depletion width is given by,

$$x_d = \sqrt{d^2 + \frac{2\epsilon_s}{q}\frac{(N_a + N_d)}{N_a N_d}(\phi_i - V_a)} \tag{2.1}$$

where d is the nominal intrinsic width, q is the charge of an electron, ϵ_s is the permittivity of the material, ϕ_i is the built in potential, V_a is the applied voltage, N_a is the p-side acceptor density, and N_d is the n-side donor density. The depletion width under applied reverse bias is a function of the p and n side doping concentrations. Little change in the depletion width occurs for large values of N_a and N_d. The change with bias introduces voltage dependent capacitance, since $C_j = \epsilon_s/x_d$, and reduces the voltage efficiency of the phase change mechanisms.[13] As detailed in Section 2.1.7, the presence of the doping in the

---

[13] The depleted width will grow in excess of the MQW region and the field outside the MQW does not

p and n InP layers contributes to the optical loss of the waveguide. The doping concentration values of $5E17\text{cm}^{-3}$ for the n-side and $2.5E17\text{cm}^{-3}$ for the p-side were selected as a reasonable compromise between optical loss, change in depletion width and capacitance under bias, and the achievable intrinsic core background doping.

Helium Implantation for Electrical Isolation

Moderate isolation between the multiple electrodes on the Mach-Zehnder modulator can be obtained by a simple wet etch removal of the InGaAs epitaxial contact layer between the electrodes. A straight-forward approach to further improve the electrical isolation is to etch away the Zn-doped overclad InP layers. This approach, however, increases the surface topology of the device and requires precision III-V etch depth control to balance the improved electrical isolation against the optical loss and backreflection at the waveguide transition. Alternatively, we have explored the use of deep helium implants [82, 83].

A helium implant creates point defects, which act to trap carriers and cause non-radiative recombination, thus removing carriers from participating in conduction with minimal impact to the optical waveguide properties. J.E. Haysom et al. developed multiple-energy implant recipes to enable uniform damage profiles across the p-doped overclad layer of the waveguide structure. An example is shown in Figure 2.16a. Three different dose regimes and three different maximum depth ranges were explored in order to optimize the electrical and optical behaviour of the device [82]. Five orders of magnitude increase in the resistance between on-chip electrodes was demonstrated simultaneously with a 1dB/cm reduction in the waveguide optical loss[14], as shown in Figure 2.17. St. J. Dixon-Warren has also demonstrated good agreement between experimentally measured implant depths using SSRM[15] and J.E. Haysom's theoretically predicted depths [83]. A example of a SSRM measurement on a waveguide ridge is given in Figure 2.16b. The implant isolation has been shown to remain stable under various extensive thermal, electrical, and optical stress conditions.

2.1.9 Experimental Measurement of the Total Loss in the Modulator Waveguide Design

Figure 2.18 presents the measured insertion loss for a straight $2.0\mu\text{m}$ wide modulator waveguide having the spot-size converter structure detailed in Chapters 3 and 4 on both the input and output of the device. The device was fabricated using an i-line stepper lithography process with both facets of the device anti-reflection coated as detailed in Section 4.6. The waveguide is biased at -0.8V to create the minimum electric field required across the intrinsic MQW core to sweep out the photo-generated carriers. The coupling optics to the waveguide are the $10\mu\text{m}$ radius lensed tapered fibers discussed in Section 3.2.3. The main

---

contribute significantly to the phase change.

[14] This is likely due to removal of free carriers in the vicinity of the optical mode.

[15] Scanning Spreading Resistance Microscopy

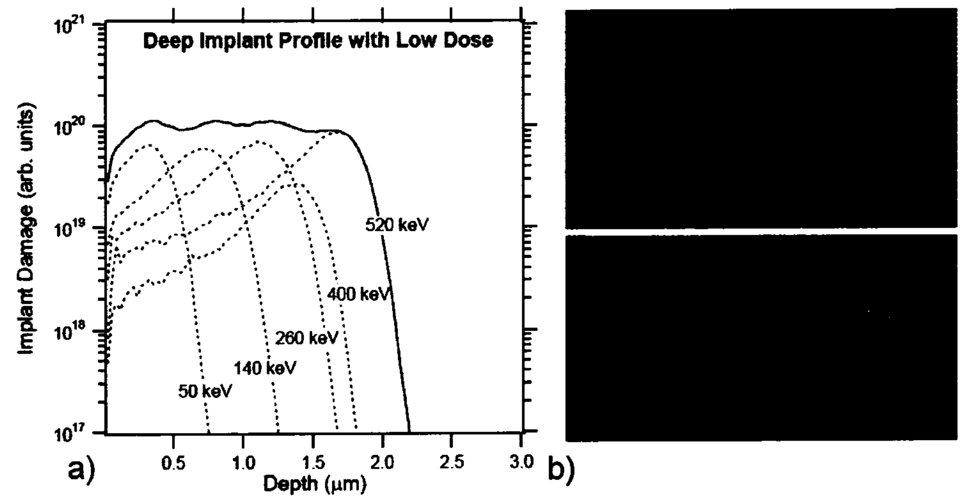

Figure 2.16: ***a)Simulation of Multiple-Energy Implant Recipes to Enable Uniform Damage Profiles Across the P-Doped Overcladding Layer of the Modulator Structure b) SSRM Measurement of an Implanted and Reference Waveguide Cross-Section*** *Source: St. J. Dixon-Warren, J. E. Haysom, I. Betty, J. Lu, and K. Hewitt, "Implant isolation in an indium phosphide optoelectronic device: A scanning spreading resistance microscopy study", J. Vac. Sci. Technol. A, Vol. 22, No. 3, pp.925-929, May/Jun 2004.*

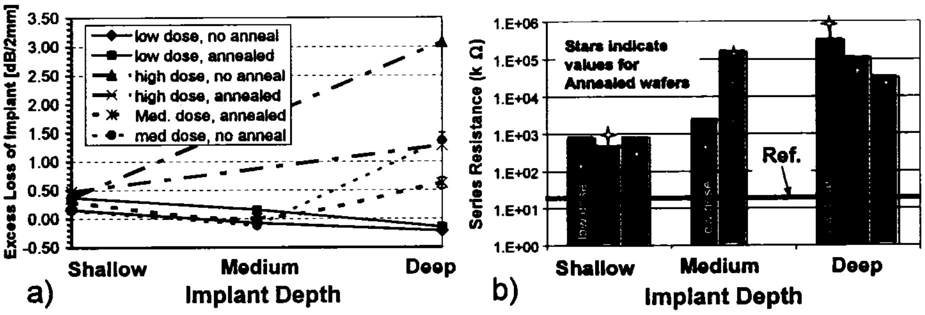

Figure 2.17: ***Impact of Implant of Waveguide Properties: a) Lateral Isolation, b) Waveguide Loss.*** *Source: J.E. Haysom, I. Betty, K. Wong, M. Poirier, R.S. Moore, A. Ait-Ouali, J. Lu , "Implant Isolation Applied to an InP Mach-Zehnder Modulator," Eleventh Canadian Semiconductor Technology Conference Ottawa, Canada - 18-22 August 2003.*

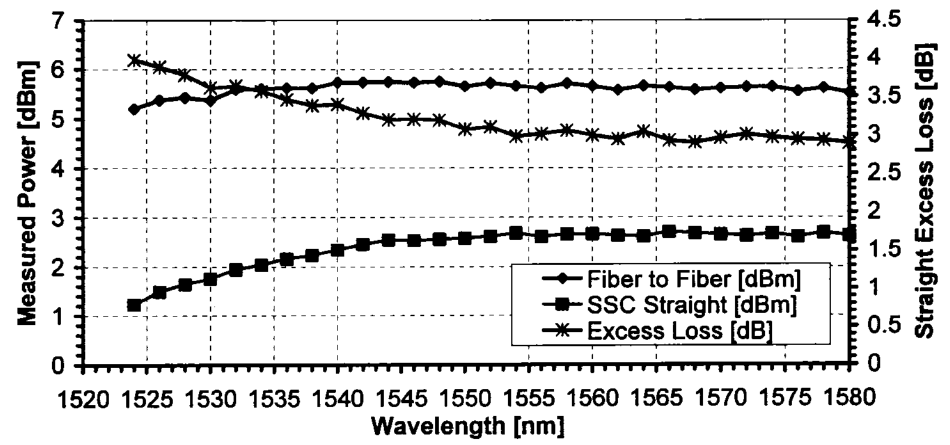

Figure 2.18: *Measured Insertion Loss for a 2150μm long 2.0μm Wide Straight Waveguide in the Modulator Structure with Input and Output Spot-Size Converters.*

source of the waveguide variability in loss is the bandedge absorption, however, the bandedge contribution to the loss is low at the nominal operating wavelength of 1550nm.[16] The excess loss of the device relative to a fiber-to-fiber measurement is only 3dB at the nominal 1550nm operating wavelength. The fiber-to-fiber insertion loss relative to a patch cord was 1.01dB at 1550nm. This is the lowest insertion loss reported for a strongly-guided InP-based phase modulator.

The expected doping loss in the 2150μm long modulator section of the measured device is 1.03dB. This is based on the calculations in Section 2.1.7. The expected ridge waveguide scattering loss in the modulator section is 0.39dB. This is based on 1.8dB/cm scattering loss in the 2.0μm wide ridge waveguide, as indicated by Figure 2.9. This leaves a total of 0.79dB of loss for each spot-size converter without the coupling optics, or 1.29dB loss for each spot-size converter including the coupling optics[17]. It has been assumed that the modulator core bandedge absorption loss and quantum well interface scattering loss is negligible at 1550nm. The inferred experimental value for the spot-size converter insertion loss is well matched to the expected value summarized in Section 3.8. This categorization of the losses may over represent the doping loss if some hydrogen passivation of the Zn in the overclad layers is occurring. If this is the case then the differential loss is more likely to be tied up in the epitaxial interface scattering from the quantum wells than additional loss in the spot-size converter.

---

[16] The nominal operating waveguide is offset 140nm red from the peak exciton absorption as introduced in Section 3.9.1.

[17] An extra 0.5dB has been included. This assumes the 1.01dB insertion loss for the two tapered fibers, relative to a patch-cord, is shared equally between both fibers.

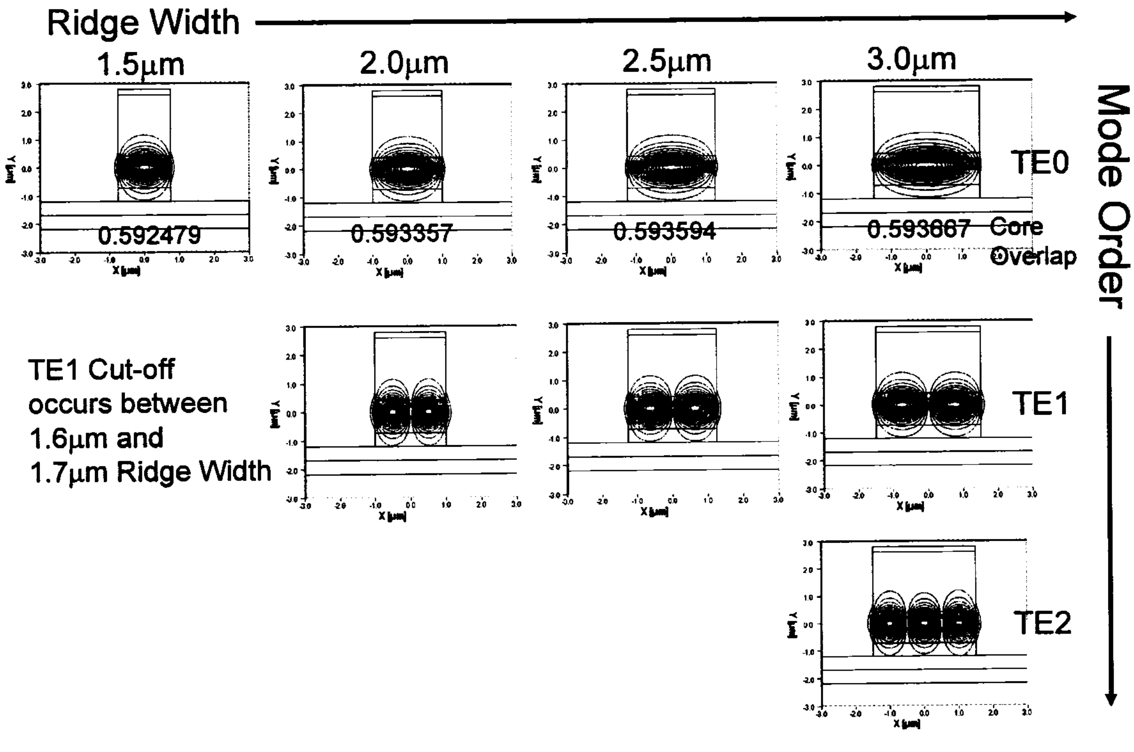

Figure 2.19: *Modulator Structure Modes as a Function of Ridge Width.*

2.1.10 Waveguide Higher Order Lateral Modes: Waveguide Properties as a Function of Ridge Width and Etch Process

Figure 2.19 shows the TE waveguide modes at 1546nm as a function of the ridge width for the modulator structure. The calculations were performed using a 128X256 point non-uniform grid finite-difference mode solver with PML boundary conditions in a 6μmX8μm space. The strongly-guided ridge etch depth is 4.0μm. Figure 2.20 gives the equivalent TE modes for the passive waveguide structure using a 256X256 point non-uniform grid in a 10μmX10μm space. From this set of calculations single-mode operation in the modulator structure requires a ridge width <1.7μm, and in the passive waveguide structure a ridge width <2.1μm is required. Note to first order there is no change in the core overlap for varying ridge width.

Figure 2.21a presents the waveguide loss in the passive waveguide structure as a function of ridge width. The waveguides were fabricated using a CO_2:CH_4:H_2 RIE semiconductor etch with i-line stepper-based lithography. The loss measurements were performed using the Fabry-Perot cut-back method mentioned previously and scanning electron microscopy (SEM) cross-sections of the waveguides were obtained to confirm the ridge widths. The waveguide loss increase for wide waveguides in Figure 2.21a can be attributed to difficulty with the experimental measurement when the TE_2 mode is available and excited by the

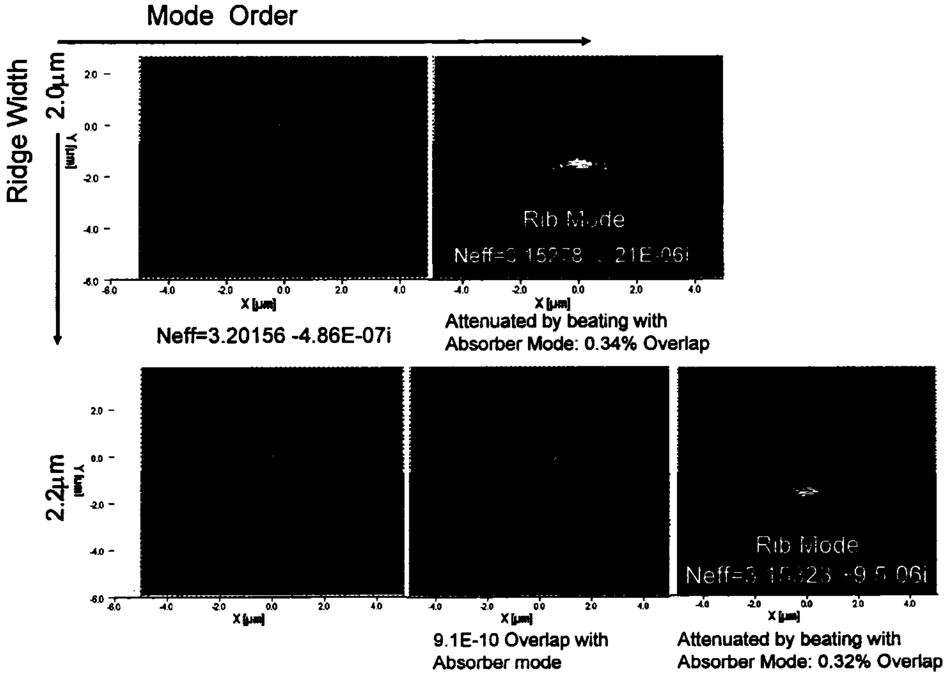

Figure 2.20: *Passive Waveguide Structure Modes as a Function of Ridge Width.*

input coupling[18]. The measured waveguide losses compare favorably with the best-in-class measurements obtained by Zhu et al. [67] and provided in Figure 2.21b.

The measurements in Figure 2.21b show also that a weakly-guided waveguide enables lower losses at narrow ridge widths. The reduced loss in weakly-guided waveguides and the loss reduction with increasing ridge width in strongly-guided waveguides can both be explained by a reduction in the mode field overlap with the fabrication-induced roughness at the semiconductor-to-air interfaces.

The waveguide loss measurements in Figure 2.21a and the mode calculation in Figure 2.19 indicate that a ridge width of 2.0μm in the modulator structure would provide reasonable sidewall scattering losses without the risk of the waveguide supporting the TE_2 mode.

Figure 2.22a shows the EIM calculated indices for the modes in the modulator structure as a function of ridge width and Figure 2.22b shows the same for the passive waveguide structure. Several individual data points obtained from full two dimensional mode calculations using a non-uniform grid finite-difference solver have been included in Figure 2.22a to verify the validity of the EIM model. There are several important observations that can be made from Figure 2.22:

- Curves are shown at 1525nm, 1546nm and 1565nm for the TE_0 and TE_1 modes in

---

[18] The TE_2 mode increases the power level in the nulls and thus reduces the peak to valley ratio which makes the losses appear greater.

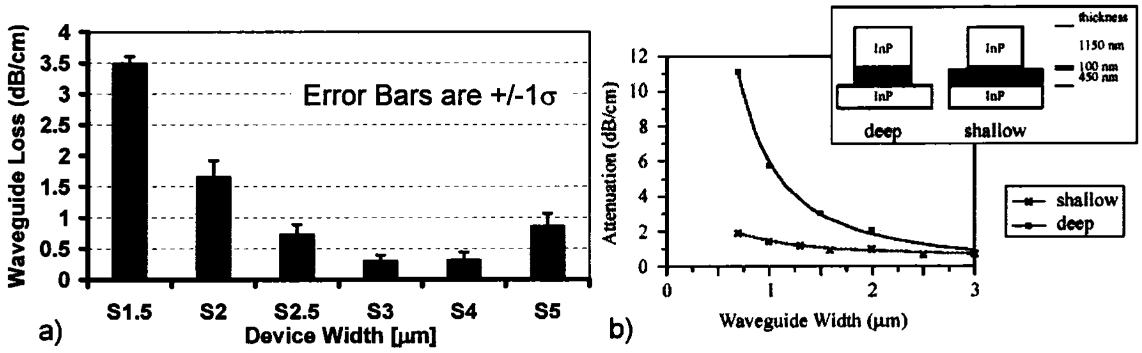

Figure 2.21: *a) Impact of Ridge Width on the Passive Structure Waveguide Loss using CO_2:CH_4:H_2 RIE III-V Semiconductor Etch and 5X i-line Stepper Lithography b) Literature Reference for Measured Attenuation as Function of the Waveguide Width in both Shallow and Deep-Etched Waveguides (TE polarization), Source: Y.C. Zhu, F.H. Groen, D.H.P. Maat, Y.S. Oei, J. Romijn, I. Moerman, "A compact PHASAR with low central channel loss", Proc. ECIO '99, pp. 219-222, 1999.*

Figure 2.22a and they indicate that wavelength variations are a small but potentially significant perturbation on the given trends.

- The effective index of each mode reduces as the ridge width decreases. When the waveguide width is less than 1.7μm in the modulator structure and 2.1μm in the passive waveguide structure the higher-order modes become cut-off and leak into the substrate since their effective indices are less than the refractive index of the N^+ doped InP substrate marked by a black horizontal line for a wavelength of 1546nm. These cut-off calculations are consistent with the two dimensional mode calculations shown in Figures 2.19 and 2.20.

- Note how steep the slope of the TE_1 mode is around the practical minimum ridge widths between 1.5μm-2.0μm. Two dimensional finite-difference measurements actually indicate that the TE_1 mode is cut-off at 1565nm with a 2.0μm ridge width in the modulator structure.

- It is desirable to have small variation in the TE_0 mode index as a function of width for a waveguide used in an interferometer to minimize the impact of localized lithographical errors on the interferometer phase imbalance.

Figure 2.23 shows the beat length[19] between the TE_0 and TE_1 modes as a function of the ridge width as calculated with the EIM. Since the beat length is dependent on the differential effective indices it is nearly identical for both the modulator and passive waveguide structures. The insert shows the beat length observed in a cross-sectional X–Z slice through the core in a TE semi-vectorial, three-dimensional, finite-difference beam propagation method [84] (BPM) simulation, confirming the EIM calculated values.

---

[19] Beat length is determined from $\Delta\beta L = 2\pi$. It is given by $\lambda_0/(n_0 - n_1)$.

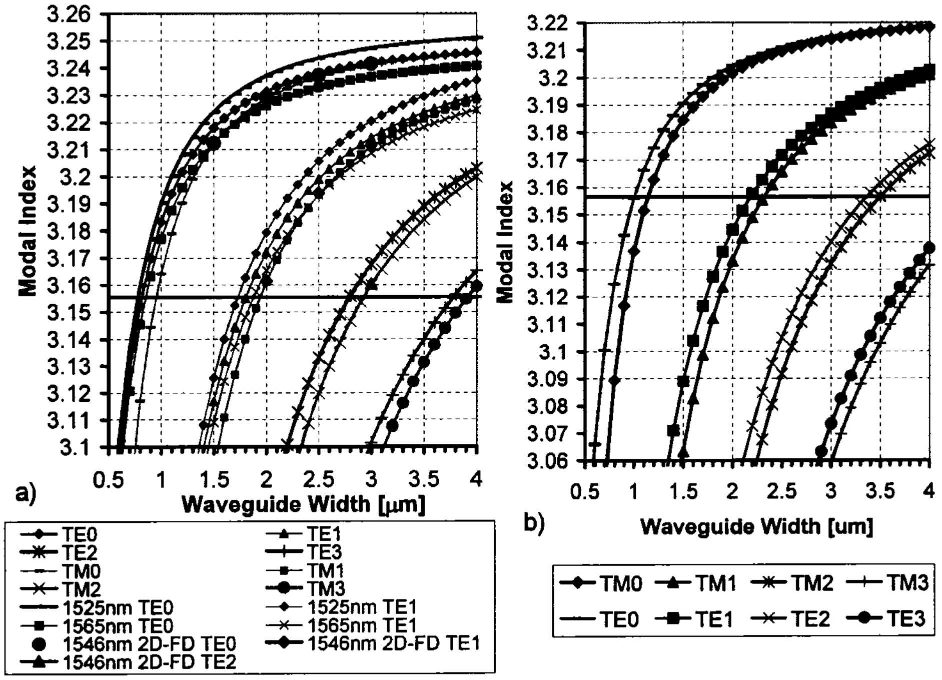

Figure 2.22: *a) Effective Indices versus Ridge Width in the Modulator Structure, b) Effective Indices versus Ridge Width in the Passive Waveguide Structure.*

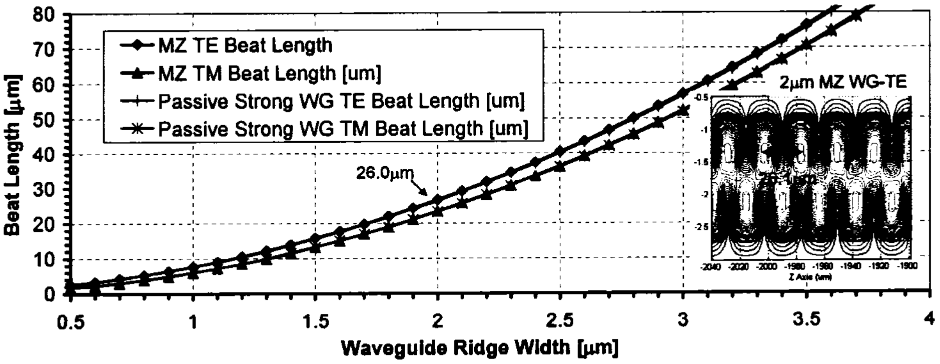

Figure 2.23: *First and Zeroth Order Mode Beat Lengths versus Ridge Width in both the Modulator and Passive Waveguide Structures.*

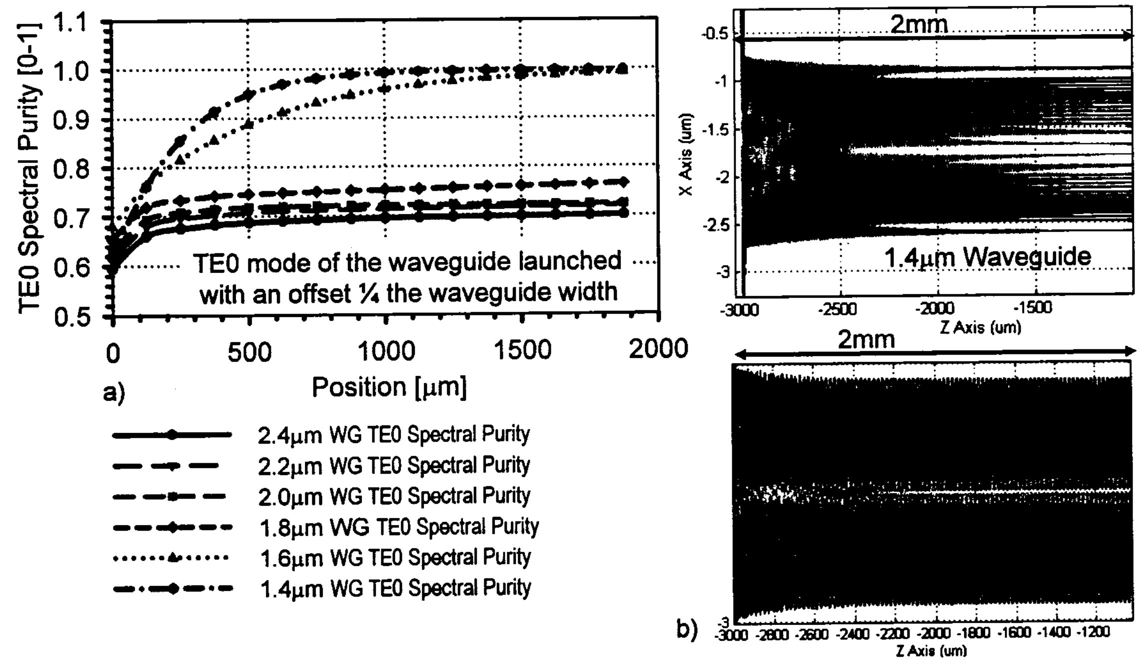

Figure 2.24: *3D Semi-Vectorial BPM Simulation of* TE_1 *Cut-Off in the Modulator Structure.*

Figure 2.24 shows the impact of mode cut-off on higher-order mode propagation in the strongly-guided modulator structure. Results are shown for a three-dimensional BPM simulation[20] of a straight waveguide as a function of ridge width in the modulator structure. The waveguide is excited by the TE_0 mode launched into the waveguide at a $x = \frac{W}{4}$ offset from the centre axis. The plotted parameter is the TE_0 spectral purity of the waveguide field, defined as the ratio of the TE_0 modal power to the total power in the waveguide[21]. It is clear that single-mode operation requires a ridge width less than 1.8μm, consistent with the mode calculations presented in Figure 2.19; however, the unguided higher-order modes have low attenuation coefficients. Even for a nominally single-mode waveguide with a ridge width of 1.4μm, a length >500μm is required to reach a TE_0 spectral purity of 0.95.

Based on Figures 2.21a, and 2.22a it may be feasible in the future to consider a ridge width of 1.5μm for the phase shifter waveguides in the modulation arms of the Mach-Zehnder. A 20% reduction in the capacitance per unit length could be achieved at a cost of 0.18dB/mm and a potentially worse distribution for the modulator arm zero volt phase imbalance[22]. From Figure 2.24 a 1.5μm wide waveguide would also attenuate any TE_1 mode excited by waveguide bends or by operating the MMI splitter outside its wavelength band of operation as discussed in Section 2.4. It would be necessary to up-taper the 1.5μm wide

---

[20] In all the BPM simulations z is the propagation direction, x is the horizontal axis parallel to the substrate, and y is the vertical axis parallel to the ridge sidewall. The centre of the waveguide MQW core is $(x, y) = (0, 0)$

[21] x=-W/2 to x=W/2, y=-∞ to y=∞

[22] This is due to a slightly increased slope in N_{eff} versus ridge width.

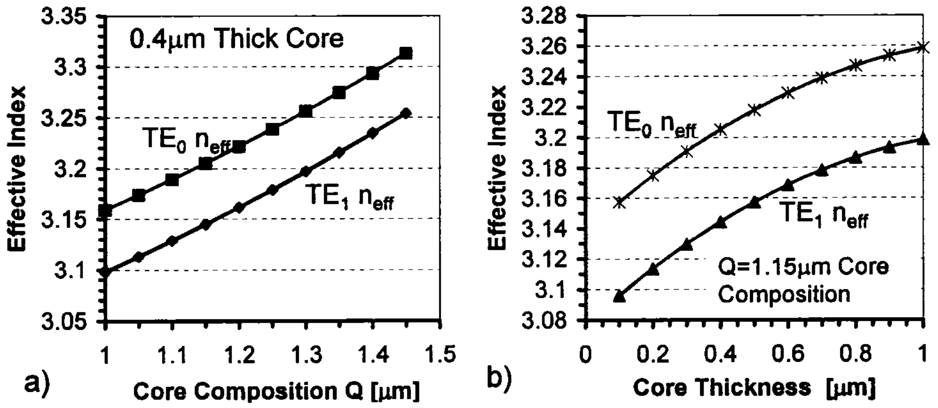

Figure 2.25: *TE_1 Effective Index as a function of Core Composition (a) and Thickness (b) for a Ridge Width of 2.0μm at the Centre Wavelength of 1546nm.*

modulation arm waveguides, as discussed in Section 3.6, prior to the MMI structures since the MMI tolerance to ridge width is a strong function of the access waveguide width.[23]

2.1.11 Waveguide Higher Order Lateral Modes: Waveguide Properties as a Function of Core Thickness and Composition

After ridge width, the most significant parameters governing the loss of higher-order lateral core modes are the core thickness and composition. Both of these parameters in the modulator structure are defined by the phase shifter requirements; however, they are free variables for optimization in the passive waveguide structure.

Higher order mode losses can be increased by using a thin core with a low composition wavelength. Reducing the core composition wavelength and/or the core thickness will increase the vertical evanescent field overlap with the substrate and, therefore, increase the loss of the higher-order lateral modes. An extreme instance of this phenomenon is provided by the spot-size converter design, where the TE_1 lateral mode is cut-off for a ridge width between 2.5μm and 3.0μm as shown in Figure 3.13. In Figure 2.25 a more general example gives the TE_1 mode effective index for a strongly-guided waveguide as a function of both the core thickness and the core composition[24]. The guiding cut-off index is the 3.15679 index of the N^+ doped substrate.

In the modulator structure higher-order lateral modes cannot be avoided without resorting to narrow ridge widths as discussed in Section 2.1.10. A thick core is required to maximize the mode confinement to the MQW region as shown in Figure 2.26, and an effectively high composition index[25] is required to make use of the Quantum Confined Stark Effect.

---

[23] See Section 2.2.2.

[24] The ridge width is 2.0μm and the wavelength for the calculations is 1546nm.

[25] See Appendix 2.6 for a discussion on the effective index of the MQW core. The simplest approximation is

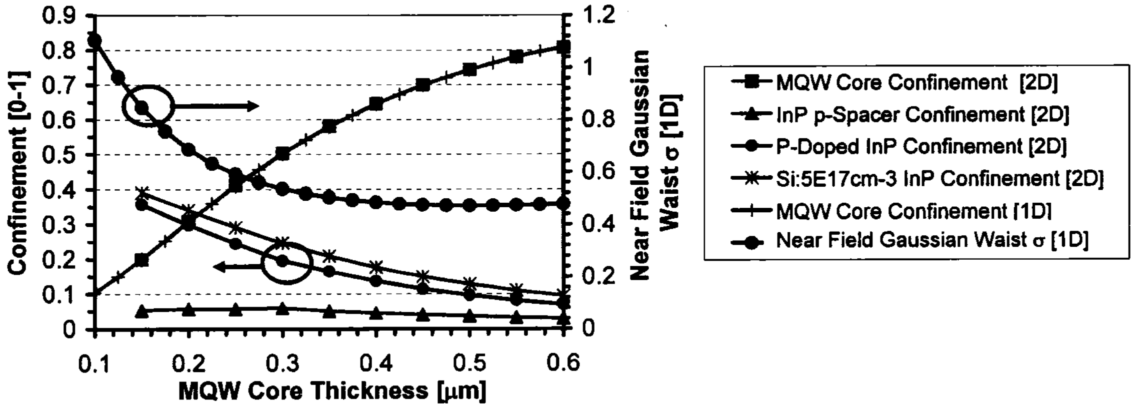

Figure 2.26: *TE_0 Epitaxial Layer Confinement and Mode Waist as a function of Core Thickness in the Modulator Structure for a Ridge Width of 2.0µm at the Centre Wavelength of 1546nm. Confinement is Calculated Using a 2D Non-Uniform Grid Finite-Difference Mode Solver; Mode Waist is Given by a Gaussian Fit to the 1D Vertical Cross-Section TE_0 Mode.*

The thickness of the core is limited only by the desire to avoid a higher-order vertical mode within the core–0.65μm is the theoretical upper thickness limit for the modulator core composition at 1546nm.

A low composition wavelength for the core has also been shown [68] to be desirable in minimizing the waveguide birefringence and the tolerance of the birefringence to ridge width. The waveguide birefringence is defined as,

$$BR = n_{group}(TE) - n_{group}(TM) = BR_0 + BR_1 \tag{2.2}$$

$$BR_0 = n_{eff}(TE) - n_{eff}(TM) \tag{2.3}$$

$$BR_1 = \lambda_0 \left[\left| \frac{dn_{eff}}{d\lambda} \right|_{\lambda_0}^{TE} - \left| \frac{dn_{eff}}{d\lambda} \right|_{\lambda_0}^{TM} \right] \tag{2.4}$$

A trade-off between the waveguide birefringence and the minimum achievable bend radius is required, however, since the ridge width for the minimum birefringence increases as the composition wavelength decreases. For example, a 0.5μm thick core with a composition wavelength of 1.0μm has the minimum birefringence at a ridge width of 3.75μm. As discussed in Section 2.3.2, the required lateral offset at a circular bend to straight waveguide interface increases as ω_0^4, where ω_o is the full $1/e$ width of the Gaussian approximation to the fundamental mode field, and ω_o is directly proportional to the ridge width as shown in Figure 2.33. Thus, a low birefringent, wide ridge waveguide, requires large bend radii to avoid lithographically challenging waveguide offsets at bend-to-straight waveguide interfaces.

The design of the passive waveguide structure in Figure 2.6 is a compromise attempting to

---

the weighted average of the well and barrier permittivities, where the well permittivity assumes the composition of the peak exciton absorption to account for the quantum size effects.

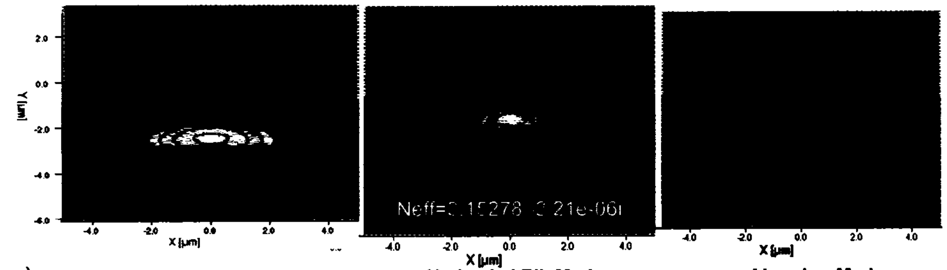

a) **Underclad Rib Mode No InGaAs Layer** **Underclad Rib Mode with InGaAs Layer** **Absorber Mode**

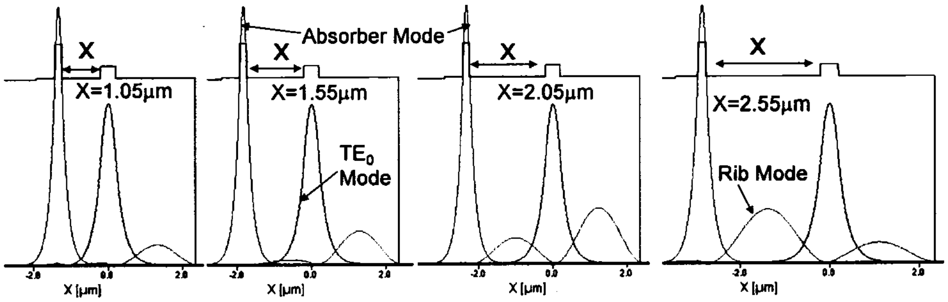

b) **3.23E-3 Rib Mode overlap with Absorber mode** **3.63E-4 Rib Mode overlap with Absorber mode** **8.53E-4 Rib Mode overlap with Absorber mode** **1.83E-3 Rib Mode overlap with Absorber mode**

Figure 2.27: ***Composite Waveguide Cavity Modes in the Passive Waveguide Structure: a) 2D FD Mode Calculations with and without InGaAs Absorbing Layer, b) 1D Vertical Modes as a Function of Underclad InP Thickness Denoted by X.***

achieve reasonable birefringence in a low-loss 2.0μm wide single-mode waveguide capable of low-loss bend radii <200μm without offsets.

2.1.12 Waveguide Higher Order Vertical Modes

The passive waveguide structure makes use of an InGaAs layer above the substrate to absorb the higher-order "composite waveguide cavity" modes identified by C. Rolland et al. [78,79]. These higher-order modes are guided laterally by the ridge etch and vertically by the positive index step between the N^+ substrate and the n-doped underclad InP layers. The higher order vertical mode, with no underclad InGaAs layer, is given in the first modal contour plot on the left in Figure 2.27a. The second and third modal contour plots in Figure 2.27a give the higher order vertical modes in the presence of an underclad InGaAs layer. The underclad rib mode is absorbed, when the InGaAs layer is present, by the overlap of this mode with the absorber mode in the InGaAs layer. Figure 2.27b quantifies in one dimension, the overlap between the underclad rib mode and the absorber mode, as a function of the separation between the absorber layer and the modulator core. Experimentally, Rolland et al. [78] demonstrated significant improvement in the extinction ratio of a strongly-guided electro-absorption modulator by the addition of the underclad InGaAs layer.

Unfortunately, the use of an InGaAs underclad absorbing layer is not compatible with the monolithic integration of the spot-size converter detailed in Chapters 3 and 4. In the spot-size converter regions of the monolithic device the fundamental mode vertically expands symmetrically about the waveguide core, such that its overlap with the absorbing InGaAs layer becomes significant.

G.M. Berry et al. [80] have shown that higher order vertical modes in a strongly-guided ridge waveguide, can be leaked into a GaAs substrate, by controlling the thickness of the AlGaAs layer directly above the substrate[26]. Higher-order vertical mode control in the InP material system can be achieved with a modification of the approach taken by Berry. The n-dopant induced refractive index change in InP can be used to create an antiguiding layer in the underclad that can leak the "composite waveguide cavity" modes into the N^+ substrate. It is well known that at high carrier concentrations the refractive index of a semiconductor is reduced. The principle carrier-induced effects have been calculated for a variety of materials by Bennett et al. [90] and experimentally determined for InP [91,92] as discussed in Section 2.1.7. If the InP antiguiding layer has an n-type doping of 5E18cm^{-3} a real refractive index reduction of -0.028 can be achieved for a free-carrier absorption loss of 14cm^{-1} in the layer.

It is necessary for the InP antiguiding layer to have the lowest optical refractive index in the vertical waveguide structure if it is to force higher-order vertical modes into the substrate. This requires the substrate N-type carrier concentration to be less than the 5E18cm^{-3} doping in the antiguiding layer. To achieve this, the InP substrates are selected from within a boule[27] based on carrier concentration calculations as derived by Pfann [76].

Figure 2.28a gives the two-dimensional higher-order vertical modes for the modulator structure as a function of n-doping concentration in the InP antiguiding layer. The substrate n-doping concentration for these calculations is 3.2E18cm^{-3}. It is clear that increasing the n doping concentration in the antiguiding layer, to a value greater than the substrate, forces the higher order vertical mode into the substrate. If the etch depth is increased to 4.0μm, as seen in Figure 2.28b, the result is similar. Calculations in Section 2.1.7 have shown that the 5E18cm^{-3} doping in the antiguiding layer has no impact on the loss of the TE$_0$ mode. Figure 3.30 gives 0.02dB as the contribution of the 5E18cm^{-3} layer to the loss in the spot-size converter.

---

[26] In these strongly-guided GaAs waveguides the substrate refractive index is the highest in the structure.

[27] The sulphur doping in the boule defines the carrier concentration in the material. The concentration of sulphur in a wafer varies with its position in the boule. The lower the wafer number (closer to the seed end of the boule) the lower the concentration of sulphur. This is due to the segregation of sulphur at the solid-liquid interface of the growing crystal - the solidifying crystal expels sulphur into the liquid melt, which becomes progressively richer in sulphur as the boule grows. As growth progresses the melt becomes enriched with sulphur and its solidification temperature drops. The crystal puller is continuously lowering the temperature of the melt so that the solid-liquid interface advances. As the solidification temperature declines the solubility of sulphur in solid InP also increases, so with each increment in boule length the concentration of sulphur increases. For a well-mixed melt the incorporation of sulphur follows a known relationship [76]. The dependence of carrier concentration on boule position is of the form $n = n_o(1-x)^{(k-1)}$, where n_o is the seed carrier concentration, x is the distance along the boule from the seed, and k is the segregation coefficient (~ 0.5 for S in InP).

a) 3.6µm Etch Depth with N=3.2E18cm^{-3} for the Substrate Doping

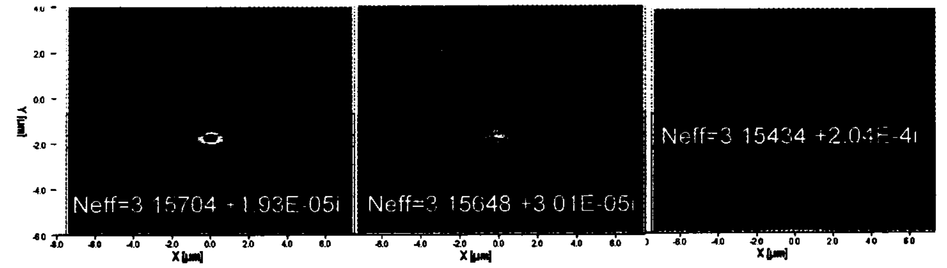

b) 4µm Etch Depth with N=3,2E18cm^{-3} for the Substrate Doping

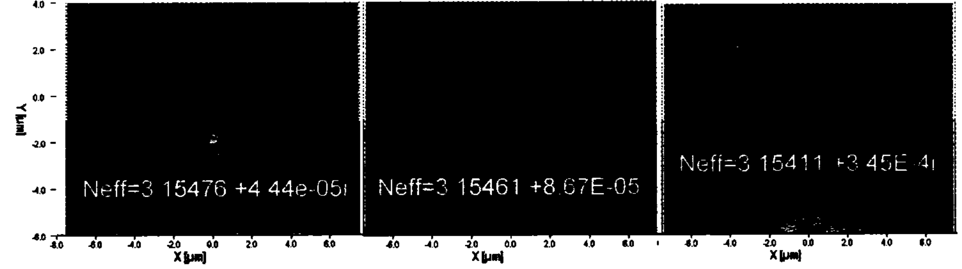

Figure 2.28: ***Composite Waveguide Cavity Mode in the Modulator Structure as a Function of the Antiguiding Layer Doping and Etch Depth for a Substrate Doping of N=3.2E18cm^{-3} at λ=1.546nm. The Simulation Space is 15μm X 10μm on a 256 X 256 non-uniform grid.***

Others have proposed using the refractive index step in n-doped InP for waveguide design. For example, Glew et al. [77] have recently demonstrated experimentally that the $\Delta n = 0.058$ index step between InP n-doping of 5E17cm^{-3} and 1E19cm^{-3} is large enough to be used for grating formation in DFB laser applications.

A second alternative for removing the higher-order "composite waveguide cavity" mode is to increase the etch depth until the rib waveguide mode is cut-off vertically in the cladding region on either side of the ridge, as shown in Figure 2.29. The cut-off depth for the waveguide at 1546nm is 4.3μm. For these calculations the substrate n-doping is 5E18cm^{-3} and the antiguiding layer n-doping is 5E17cm^{-3}. The 1546nm simulation uses 256X256 non-uniform grid points in a 15μmX10μm space. Unfortunately, the increased etch depth approach does not suppress the composite waveguide cavity mode in the regions of a monolithic device containing the spot-size converter, as shown in Figure 3.16.

2.2 Multimode Interference Couplers

The design and performance of multimode interference (MMI) devices has been well studied in the literature in recent years [122]. Here the analytic theory of the mode propagation analysis (MPA) technique for describing MMI operation will be reviewed. The details of

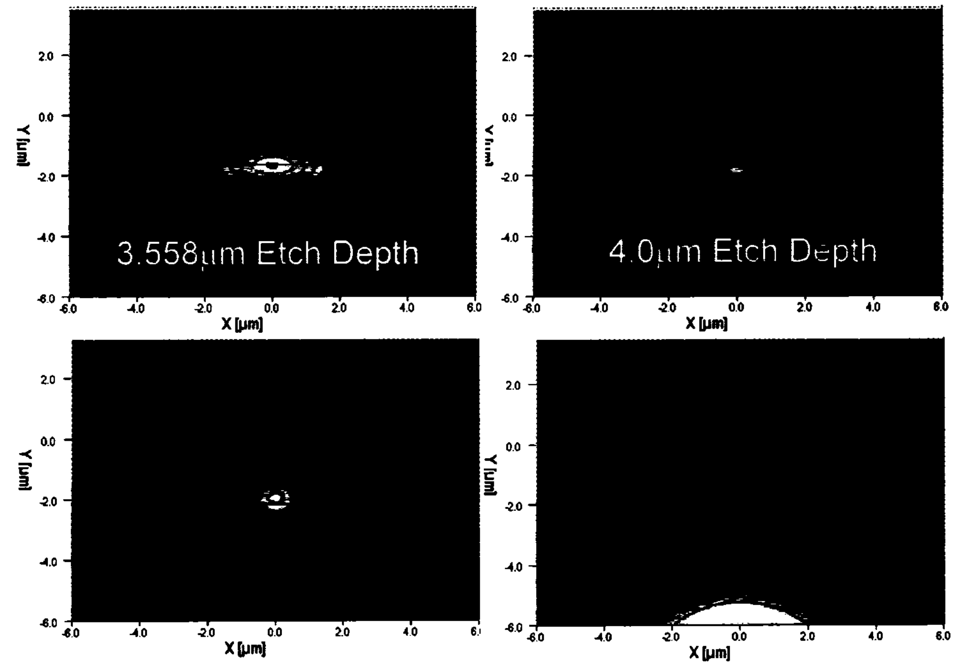

Figure 2.29: *Cut-Off of the Composite Waveguide Cavity Mode in the Modulator Structure Using Etch Depth for a Substrate Doping of N=5E18cm^{-3} and an Antiguiding Layer Doping of N=5E17cm^{-3} at λ=1.546nm. The Simulation Space is 15μmX10μm on a 256X256 non-uniform grid.*

1X2, 2X2 and 1X1 MMI designs for use in the strongly-guided Mach-Zehnder interferometer are provided. The practical constraints on the MMI designs imposed by implementation within the InP material system will be emphasized. The literature advances in MMI design that are of significance for Mach-Zehnder modulator design will also be reviewed.

2.2.1 Basic Introduction

MMI devices are based on the principle of self imaging [119] [104], which has its origins in the Talbot effect, discovered in 1836 [121]. In multimode waveguides, self imaging is the mechanism by which an input field profile is reproduced, in single and multiple images, at periodic intervals along the propagation direction of the guide.

MMI self imaging can be analytically described by analyzing propagation of the waveguide normal modes in two dimensions [104] [122]. The physical modulator structure, defined in Section 2.1, can be represented in two dimensions[28] using the Effective Index Method [EIM] [103]. Here, the two dimensional analytic MPA theory is derived since it is of practical value and provides physical insight into the MMI operation.

---

[28] The modulator waveguide structure is single-mode in the transverse y direction; therefore, the transverse y modal field profile will not vary along the z direction of propagation. This allows the waveguide problem to be analyzed in two dimensions (lateral and longitudinal) without loss of generality.

Propagation Constants

Figure 2.30a shows a two dimensional symmetric step index slab waveguide with a refractive index profile that is invariant in the propagation direction z. The waveguide in Figure 2.30a supports m guided modes in the x direction, for a free space wavelength λ_0, with mode numbers $\nu = 0, 1, ...(m-1)$. The slab waveguide core width is W_m and it has a refractive index n_g. The core is centred about $x = 0$ and is clad on either side by material of infinite extent with refractive index n_c. Figure 2.30b gives the TE$_0$, TE$_1$ and TE$_{11}$ mode field distributions from the EIM approximation to the modulator waveguide structure with $W_m = 12\mu m$ and $\lambda_0 = 1.557\mu m$. In general for mode ν, the transverse wavenumber $k_{x\nu}$ and the propagation constant β_ν are related to the waveguide core index n_g by the dispersion relationship,

$$k_{x\nu}^2 + \beta_\nu^2 = k_0^2 n_g^2 \tag{2.5}$$

with $k_0 = 2\pi/\lambda_0$. The transverse wavenumber $k_{x\nu}$ can be solved from,

$$tan(k_{x\nu} W_m) = \frac{2R\gamma k_{x\nu}}{k_{x\nu}^2 - (R\gamma)^2} \tag{2.6}$$

where $\gamma = (k_g^2 - k_c^2 - k_{x\nu}^2)^{\frac{1}{2}}$, $k_g = 2\pi n_g/\lambda_0$, $k_c = 2\pi n_c/\lambda_0$, and $R = 1$ for TE modes and $R = (n_g/n_c)^2$ for TM modes. Alternatively, the transverse wavenumber $k_{x\nu}$ in Equation 2.6 can be approximated far from cutoff [122] by,

$$k_{x\nu} = \frac{\nu + 1}{W_{e\nu}}\pi \tag{2.7}$$

where $W_{e\nu}$ is the modal effective width of the waveguide. This modal effective waveguide width includes the polarization dependent lateral penetration depth due to the Goos-Hähnchen shifts at the waveguide boundaries[29]. In strongly-guided waveguides the modal effective width $W_{e\nu}$ can be approximated by the effective width $W_{e0} = W_e$ corresponding to the fundamental mode [123]. Thus,

$$W_{e\nu} \simeq W_e = W_m + \left[\frac{\lambda_0}{\pi}\right] \left[\frac{n_c}{n_g}\right]^{2\sigma} (n_g^2 - n_c^2)^{-\frac{1}{2}} \tag{2.8}$$

where $\sigma = 0$ for TE and $\sigma = 1$ for TM. For the SiO$_2$ clad strongly-guided modulator structure the TE penetration depth is a small but not inconsequential 0.17μm at $\lambda_0 = 1.557\mu m$.

The modal propagation constants β_ν can be obtained from equations (2.5) and (2.7) using a binomial expansion[30] with $k_{x\nu}^2 \ll k_0^2 n_g^2$,

$$\beta_\nu \simeq k_0 n_g - \frac{(\nu + 1)^2 \pi \lambda_0}{4 n_g W_e^2} \tag{2.9}$$

---

[29] This is taken as the depth at which the evanescent field in the cladding layer is equal to $1/e$ of its maximum.

[30] $(1+x)^{\frac{1}{2}} = 1 + \frac{1}{2}x + O(x^2)$

The propagation constants β_ν show a nearly quadratic dependence with respect to the mode number ν. An important design parameter that is used extensively is the beat length of the two lowest order modes,

$$\boxed{L_\pi = \frac{\pi}{\beta_0-\beta_1} \simeq \frac{4n_g W_e^2}{3\lambda_0}} \tag{2.10}$$

This allows the spacing of the propagation constants to be written as,

$$\boxed{(\beta_0 - \beta_\nu) \simeq \frac{\nu(\nu+2)\pi}{3L_\pi}} \tag{2.11}$$

Equation 2.11 is the ideal mode spectrum for self imaging. Since Equation 2.11 is only an approximation, the guided modes actually accumulate small deviations from the calculated phases at the imaging distance which tends to blur and degrade the reconstructed image field.

Note that the dependence of L_π on W_e^2 in Equation 2.10 can result in different optimal imaging lengths for each of the two polarization states. Only TE performance is considered since the Mach-Zehnder modulator is intended for use in a transmitter with a continuous wave TE laser source. Polarization independent MMI operation can be achieved by designing at the intermediate MMI lengths and accepting a small increase in loss.

The mode ν phase error at L_π, $\Delta\phi_\nu$, due to the deviation of $\beta_0 - \beta_\nu$ from the ideal behaviour expressed in Equation 2.11, has been quantified [124]. The error is given approximately by,

$$\Delta\phi_\nu \approx \frac{\pi(\nu+1)^4\lambda_0^2}{6n_g^2W_m^2}\left[\frac{1}{8} - \frac{\lambda_0 n_g^2}{6\pi W_e(n_g^2-n_c^2)^{\frac{3}{2}}}\right] \tag{2.12}$$

The first error term captures the error introduced by the binomial expansion in Equation 2.9. This first error term is present even for strongly-guided waveguides and its significance scales as ν^4. Thus, if a large number of modes are excited, the phase errors associated with the higher-order modes will tend to degrade the image quality. The second term captures the modal dependence of the Goos-Hähnchen shift which was neglected in obtaining Equation 2.8. This second error term is negligible for strongly-guided high-index-contrast waveguides but it does degrade the image quality for low-index-contrast waveguides[31] [125].

The two error terms in Equation 2.12 have opposite signs, allowing an engineered choice for the index-contrast [124, 125] to improve the performance of 1XN MMI splitters with high N. For a MMI width of 10.3μm in the modulator structure Equation 2.12 predicts a very acceptable 2° phase error at L_π for the highest order guided mode at a wavelength of 1546nm. Even for a 17.8μm MMI width, Equation 2.12 predicts a borderline acceptable 4.8° phase error at L_π for the highest order guided mode at a wavelength of 1546nm.

---

[31] The higher-order modes will penetrate deeper into the n_c cladding layer than the lower order modes.

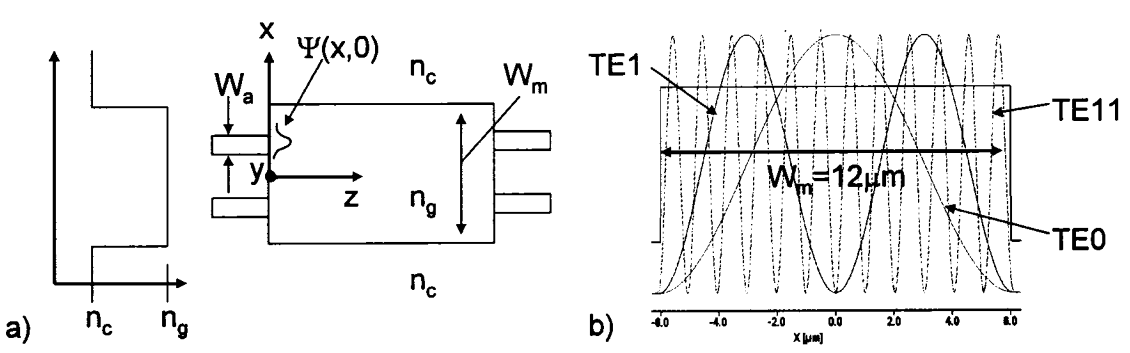

Figure 2.30: *a) Two Dimensional Representation of a Step Index Multimode Waveguide, b) TE_0, TE_1 and TE_{11} Mode Field Distributions from the EIM Approximation to the Modulator Waveguide Structure with a 12µm Waveguide Width at 1557nm.*

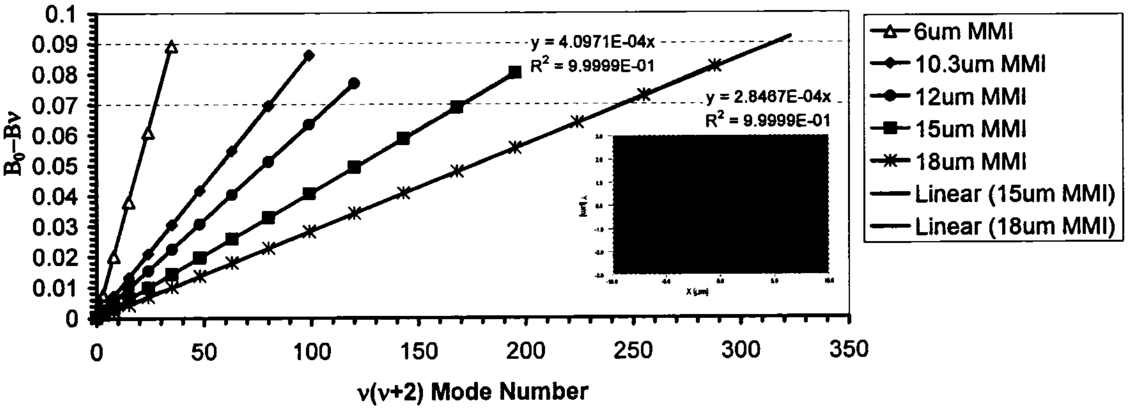

Figure 2.31: *TE Mode Spectrum Analysis for the Strongly-Guided Modulator Structure as a Function of Waveguide Width at 1546nm. Calculations obtained with a 400X128 Point 2D Non-Uniform Grid Finite Difference Mode Solver in a 20µmX10µm Space.*

Figure 2.31 plots the mode spectrum for the strongly-guided modulator structure, obtained using a two dimensional mode solver, as a function of the waveguide width. It is clear the ideal linear relationship between $\beta_0 - \beta_m$ and $\nu(\nu+2)$ is sufficiently maintained for all plotted MMI widths in the strongly-guided modulator structure.

Normal Mode Propagation Analysis

The arbitrary input field $\Psi(x,0)$ in Figure 2.30a can be decomposed into the set of m guided modes,

$$\Psi(x,0) = \sum_{\nu=0}^{m-1} c_\nu \Psi_\nu(x) \tag{2.13}$$

with c_ν the mode expansion coefficients, and $\Psi_\nu(x)$ the orthonormal mode field distributions. Neglecting the set of radiation modes is valid for this decomposition assuming the input field $\Psi(x,0)$ is totally contained within W_e and assuming the multimode waveguide has sufficient imaging resolution to fully capture the input field [120]. The mode expansion coefficients c_ν express rigourously the decomposition of the input field onto the guided modes of the multimode section but do not take into account the reflected electric field. As the refractive index difference between the single-mode waveguide and the multi-mode section is low, this last phenomenon can generally be neglected.

After propagating a distance L in the multimode waveguide, the field can be expressed as,

$$\Psi(x,L) = \sum_{\nu=0}^{m-1} c_\nu \Psi_\nu(x) e^{-j\beta_\nu L} \tag{2.14}$$

where an implicit $e^{j\omega t}$ time dependence is assumed. Taking the phase of the fundamental mode, $e^{-j\beta_0 L}$ out of the sum as a common factor and dropping it, allows the field profile to be expressed as,

$$\Psi(x,L) = \sum_{\nu=0}^{m-1} c_\nu \Psi_\nu(x) e^{\left[j\frac{\nu(\nu+2)\pi}{3L_\pi}L\right]} \tag{2.15}$$

after substitution of Equation 2.11 for $\beta_0 - \beta_\nu$ in the phase term. The field profile $\Psi(x,L)$ is determined by the mode expansion coefficients c_ν[32] and the properties of the mode phase factor,

$$exp\left[j\frac{\nu(\nu+2)\pi}{3L_\pi}L\right] \tag{2.16}$$

Under certain circumstances the profile $\Psi(x,L)$ will be a self image of the input field $\Psi(x,0)$. For example, after a propagation length of $6L_\pi$ the dephasing of each mode is an exact multiple of 2π making the image field intensity equal to the injected field intensity.

Three different operating regimes for MMI devices can be defined based on the subset of modes excited in the multimode waveguide:

- The *General Interference* regime places no restrictions on the c_ν mode expansion coefficients, allowing the access waveguides to be located at any x position on the multimode waveguide except $x = 0$ and $x = \pm W_e/6$. By inspection of Equation 2.15, it can be seen that $\Psi(x,L)$ will be an image of $\Psi(x,0)$ if Equation 2.16 equals 1 or $(-1)^\nu$. By noting that $\nu(\nu+2)$ is even for ν even and odd for ν odd, it is evident that direct and mirrored single images of the input field $\Psi(x,0)$ will be formed at distances z that are, respectively, even and odd multiples of the length $3L_\pi$ [122]. In general, multiple images are formed at the intermediate lengths between 0 and $3L_\pi$. Analytical expressions for the position and phase of these multiple images have been identified using Fourier analysis assuming sine-like mode field amplitudes and the

---

[32] The location and width of the MMI access waveguides will, therefore, be significant.

properties of generalized Gaussian sums [126]. N identical images of the input field, each with power P_{in}/N, can be found at the intermediate lengths,

$$\boxed{z = \tfrac{\rho}{N} 3L_\pi} \tag{2.17}$$

Here $\rho \geq 0$ and $N \geq 1$ are integers with no common divisor.

- The *Restricted Paired* regime has $c_\nu = 0$ for $\nu = 2, 5, 8, 11 \cdots$ to reduce the length periodicity of the mode phase factor in Equation 2.16 by a factor of three[33] relative to the general interference regime. Single images (direct and inverted) of the input field $\Psi(x, 0)$ can now be obtained at,

$$L = \rho(L_\pi) \quad with \quad \rho = 0, 1, 2, 3, \cdots \tag{2.18}$$

This selective excitation is possible by launching an even symmetric field $\Psi(x, 0)$ at $x = \pm W_e/6$ since at these positions the modes $\nu = 2, 5, 8, \cdots$ present odd symmetry against the even excitation and cause the overlap to vanish as shown in Figure 2.32. The number of MMI access waveguides is obviously limited to two. N identical images of the input field $\Psi(x, 0)$ can be found at the intermediate lengths,

$$\boxed{z = \tfrac{\rho}{N} L_\pi} \tag{2.19}$$

where $\rho \geq 0$ and $N \geq 1$ are again two integers with no common divisor.

- The *Restricted Symmetric* regime excites only the even symmetric modes ($c_\nu = 0$ for $\nu = 1, 3, 5, 7 \cdots$) to reduce the length periodicity of the mode phase factor in Equation 2.16 by a factor of four[34] relative to the general interference regime. single images of the input field $\Psi(x, 0)$ can now be obtained at,

$$L = \rho\left(\frac{3L_\pi}{4}\right) \quad with \quad \rho = 0, 1, 2, 3, \cdots \tag{2.20}$$

To achieve this excitation, the even symmetric field $\Psi(x, 0)$ is launched at the $x = 0$ midpoint in the multimode waveguide. The odd modes of the multimode waveguide are not excited by this launch due to a zero overlap caused by their zero crossing and odd symmetry at $x = 0$, as shown in Figure 2.32. This operating regime is obviously applicable only to 1XN MMI splitters. N identical images of the input field $\Psi(x, 0)$ can be found at the intermediate lengths,

$$\boxed{L = \tfrac{\rho}{N}\left(\tfrac{3L_\pi}{4}\right)} \tag{2.21}$$

where $\rho \geq 0$ and $N \geq 1$ are once again two integers with no common divisor.

---

[33] This is evident by noting that $mod_3[\nu(\nu + 2)] = 0$ for $\nu \neq 2, 5, 8 \cdots$

[34] This is evident by noting that $mod_4[\nu(\nu + 2)] = 0$ for ν even.

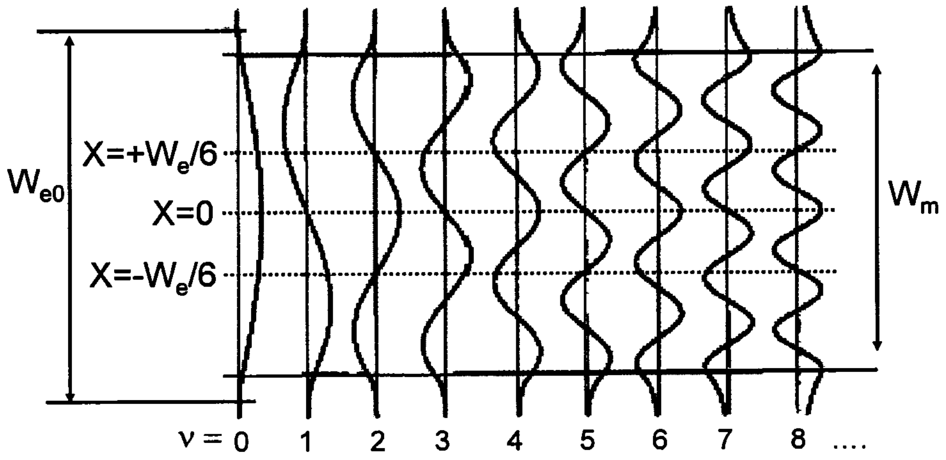

Figure 2.32: ***Restricted Paired Excitation*** *Adapted from L.C. Soldano and E.C.M Pennings, Journal of Lightwave Technology, Vol. 13, No. 4, pp. 615-627, 1995.*

2.2.2 MMI Tolerance Analysis

The fundamental mode field amplitude for the MMI access waveguides can be approximated by a Gaussian beam with waist ω_0[35]. An intuitive analysis of MMI tolerances [127] considers each MMI output image, located at the self imaging distance z=L, to be a focused Gaussian beam image of the input. The output coupling loss produced by a small δL shift in the z position of the output waveguide can be calculated by overlapping the defocused Gaussian beam with the Gaussian approximation to the output access waveguide fundamental mode. The length shift which produces a 0.5dB output overlap loss penalty is approximately equal to the Rayleigh range. The Rayleigh range is defined in the region of a Gaussian beam focus, to be the axial distance from the point of minimum beam waist ω_0 to the point where the beam diameter has increased to $\sqrt{\omega_0}$. Therefore,

$$\delta L \simeq \frac{\pi n_g \omega_0^2}{4\lambda_0} \tag{2.22}$$

Note that Equation 2.22 does not depend on the dimensions of the multimode waveguide. It is an absolute length tolerance that will depend only on the beam waist of the access waveguide mode for a given wavelength and material system. It is clear from Equation 2.22, that *the access waveguide width W_a, should be as large as possible to maximize the length tolerance of the MMI design.*

In a multimode waveguide the c_ν weighted sum of the modal phase errors $\Delta\phi_\nu$ is also minimized by using the largest access waveguide width [128]. This is due to a decrease in the c_ν mode excitation coefficients for the higher-order modes – mainly low order modes are excited with wide access waveguides. As shown in Equation 2.12, it is the phase errors associated with the higher-order modes that have the largest negative impact on the image

---

[35] This is defined as the full $1/e$ amplitude width of the Gaussian approximation to the input field $\Psi(x, 0)$.

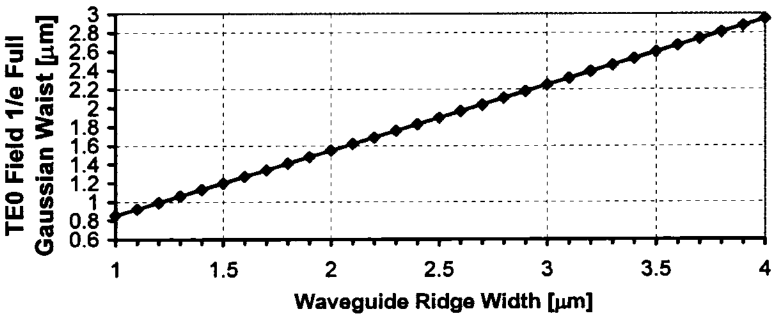

Figure 2.33: *Access Waveguide Gaussian Waist σ versus Waveguide Width.*

quality. Imperfections in the MMI image, caused by side-wall corrugation induced coupling between the MMI modes, can be assumed to be negligible for the ridge etch quality shown in Figure 2.10-2.11. [145]

Figure 2.33 presents the fitted access waveguide Gaussian beam waist ω_0, as a function of the access waveguide width for the EIM approximation to the modulator structure, at $\lambda_0 = 1.546\mu m$. Figure 2.34 shows a TE semi-vectorial three-dimensional BPM simulation, of a restricted paired interference multimode waveguide, with varying access waveguide widths W_a. The graphed property is the overlap between the field at position z along the multimode waveguide and the access waveguide fundamental mode. From Figure 2.34, it is clear there is an improvement in length tolerance with increasing access waveguide width. Figure 2.35 shows the calculated δL from Equation 2.22 and Figure 2.33 compared against the calculated value from the mode overlaps in Figure 2.34. The agreement is excellent.

The tolerance corresponding to the other design and fabrication parameters can be related to δL using Equation 2.10 and the definition of Equation 2.17 as follows:

$$\frac{\delta L}{L} = 2\frac{\delta W_e}{W_e} \simeq \frac{|\ \delta\lambda_0\ |}{\lambda_0} \simeq \frac{\delta n_g}{n_g} \tag{2.23}$$

Here it is apparent that L must be as short as possible to relax the tolerances of the other variables. The MMI designs of most interest, therefore, have $\rho = 1$ in Equations 2.17 - 2.21. As the analysis of specific MMI designs continues in Sections 2.2.3-2.2.5 it will be seen that a tight tolerance on the multimode waveguide width is one of the most challenging fabrication issues.

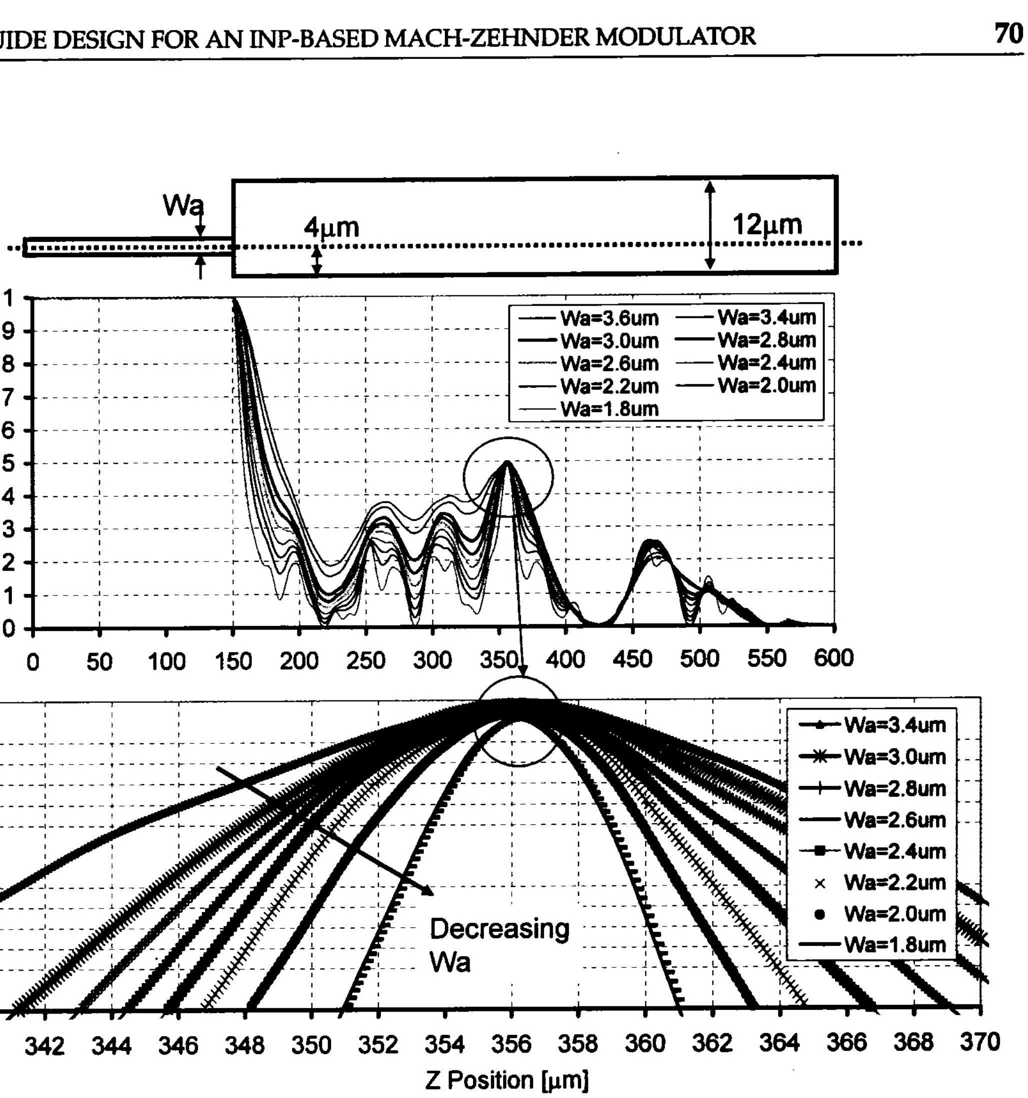

Figure 2.34: *3D TE Semi-Vectorial BPM Simulation of a Restricted Paired Interference Multimode Waveguide as a Function of Access Waveguide Width W_a.*

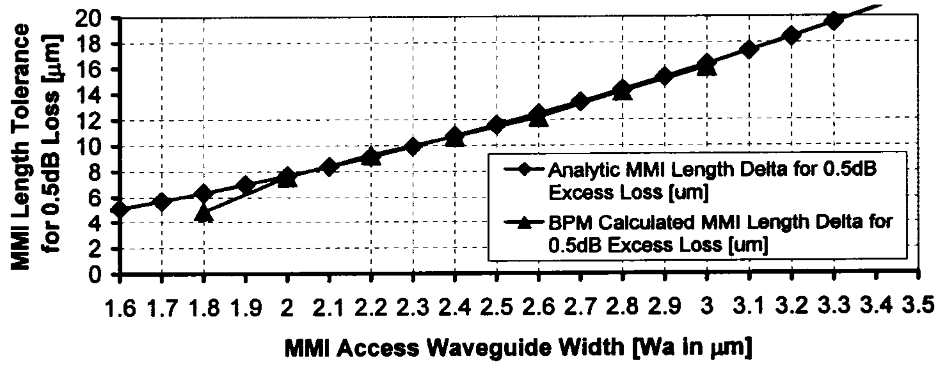

Figure 2.35: *Comparison of Length Tolerance Calculations.*

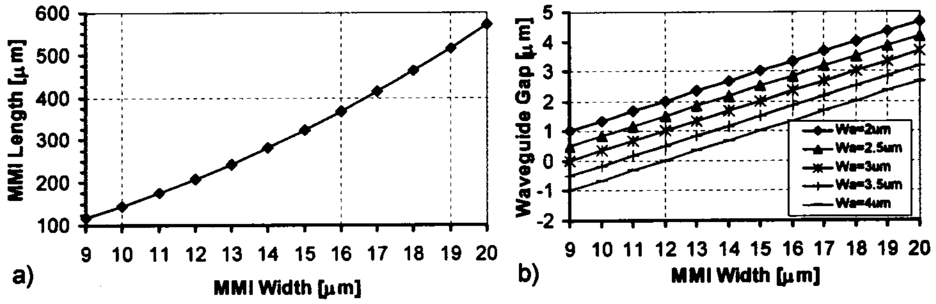

Figure 2.36: *Restricted Paired Interference 2X2 MMI: a) MMI Length versus MMI Width, b) MMI Width versus Gap between Access Waveguides for Various Access Waveguide Widths.*

2.2.3 2X2 Restricted Paired Interference

Tolerance Analysis and Design Selection

Figure 2.36a provides the MMI length versus physical width relationship for a restricted paired interference 2X2 MMI, in the modulator waveguide structure, at 1546nm, using Equation 2.19 with Equations 2.10 and 2.8. The MMI length scales as the square of the effective width as previously discussed. Figure 2.36b gives the separation between the two access waveguides as a function of both the MMI width and the access waveguide width.

In Figure 2.37 the 0.5dB excess loss tolerances for the restricted paired interference 2X2 MMI are presented, as a function of the MMI physical width and the access waveguide width, using Equations 2.22 and 2.23, with inputs from Figure 2.33. The design space has been limited to MMI's with a physical width greater than 9.0μm since this corresponds to a 1.0μm separation between 2.0μm wide access waveguides. The wavelength and width tolerances decrease with increasing MMI width, and they improve with increasing width for the access waveguides. A ridge width tolerance of 0.1μm is a challenging but feasible target for i-line stepper photolithography on a 3" wafer. The required wavelength tolerance for the MMI is defined by the EDFA amplifier wavelength window to be at least 38nm.

From Figure 2.37, it is clear that the MMI tolerances can be improved if the width of the access waveguides increases. Since strongly-guided waveguides are used for these access waveguides it is not generally necessary to consider the possibility of coupling between them; however, there is a technological limitation in accurately defining ridge waveguides with sub-micron spacing, as shown in Figure 2.10 and Figure 2.11. A reduced etch depth between the access waveguides will occur at narrow waveguide spacings, possibly allowing the two waveguide modes to couple. Any coupling between these access waveguide modes is reduced in the modulator arms since the optical phase of the left and right arm differ by 90 degrees. Three-dimensional BPM simulations have shown that as long as the etch penetrates 0.1μm into the MQW core of the waveguide there is very little impairment in performance.

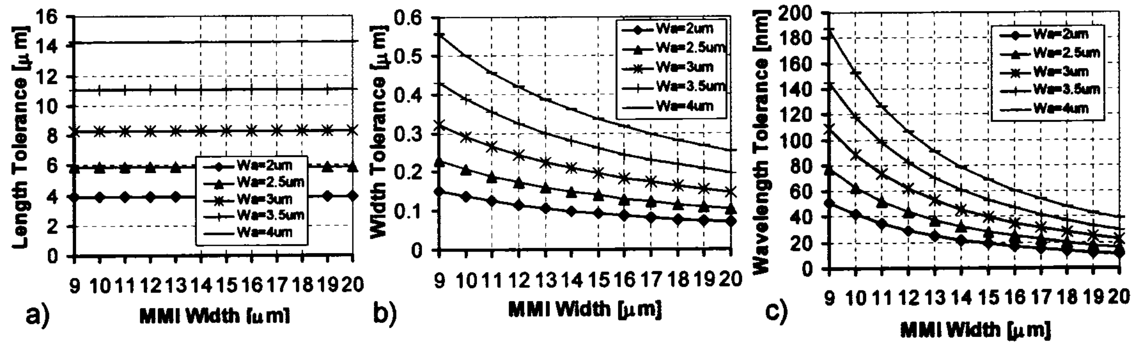

Figure 2.37: ***0.5dB Excess Loss Tolerances for the Restricted Paired Interference 2X2 MMI as a Function of MMI Width and Access Waveguide Width: a) MMI Length Tolerances, b) MMI Width Tolerances, c) MMI Wavelength Tolerances.***

Recently the imbalance and excess loss in 3dB 2X2 MMI couplers have been explored theoretically by Hill et al. [129] using Fourier analysis techniques that assume sine-like mode field amplitudes. Imbalance is defined as the ratio of power in the cross-state output waveguide, relative to the power in the bar-state output waveguide. They conclude that for small access waveguide widths W_a, where the mode expansion coefficients c_ν decrease slowly with mode number ν, a large imbalance can be expected. They also show, however, that the imbalance does not decrease monotonically with increasing W_a, and that there exists a number of local minima and maxima in the imbalance as a function of W_a. This imbalance is primarily determined by the difference in the c_ν weighted sums of the even and odd $\Psi_\nu(x)$ mode phase errors $\Delta\phi_\nu$. Using the theoretical formulations derived by Hill et al., Figure 2.38a presents, for width tolerances of 0.1μm, 0.15μm and 0.2μm, the maximum imbalance as a function of the normalized access waveguide width W_a/W_e, for both 10.5μm and 12μm effective width MMI's in the modulator structure, having 10 and 12 modes respectively.

Figure 2.38b shows the maximum excess loss as a function of the normalized access waveguide width W_a/W_e, for the same design criteria as Figure 2.38a. Figure 2.38b confirms that the power transferred to the MMI should be concentrated in the lower order modes to decrease the excess loss, i.e. the c_ν must decrease rapidly with increasing ν. This is achieved by increasing the access waveguide width W_a and the corresponding normalized access waveguide width W_a/W_e.

There are several observations to be made from the calculations in Figure 2.38. In Figure 2.38b, for a given maximum excess loss, at the same normalized width[36], the 12.0μm wide MMI has a slightly better width tolerance than the 10.5μm wide MMI. There are also no local minima for the maximum excess loss as a function of the normalized access waveguide width; the wider the access waveguides the better the excess loss at a given width tolerance. Figure 2.38a shows that there are two local minimum for the maximum

---

[36] Note that this requires a wider access waveguide width in the 12.0μm wide MMI than in the 10.5μm wide MMI.

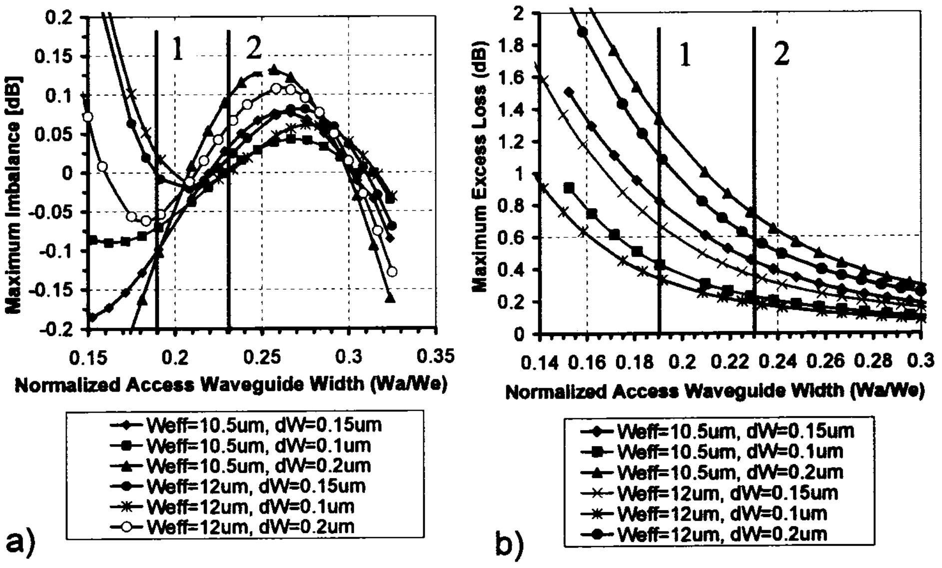

Figure 2.38: ***a) Maximum Imbalance as a Function of the Normalized Access Waveguide Width W_a/W_e, b) Maximum Excess Loss as a Function of the Normalized Access Waveguide Width W_a/W_e.***

imbalance as a function of the normalized access waveguide width. The first zero for imbalance occurs for W_a/W_e=0.21, and the second zero occurs for W_a/W_e=0.3. For a 2X2 restricted paired MMI the separation between the waveguides is $W_e/3$, therefore, the imbalance minimum near W_a/W_e=0.3 is not a practically accessible region of design space due too the technological limitations in accurately defining the ridge waveguides with sub-micron spacing.

Two design options for the normalized access waveguide width, labeled as 1 and 2, have been highlighted in Figure 2.38. Option 1 is for 2.0μm wide access waveguides into a 10.5μm wide MMI, or 2.4μm wide access waveguides into a 12.0μm wide MMI. Option 2 is for 2.4μm wide access waveguides into a 10.5μm wide MMI, or 2.8μm wide access waveguides into a 12.0μm wide MMI. For the two widths in each of these design options the separation between the access waveguides differs by only 0.1μm; however, the 10.5μm wide MMI is 46.5μm shorter than the 12.0μm. If a width tolerance of 0.1μm is assumed, the maximum excess loss and imbalance for the 12.0μm and 10.5μm wide MMI designs, are comparable at the two design options for normalized access waveguide width. A 10.5μm wide MMI is, therefore, the preferred MMI design width since it is the shortest with all else being nearly equal. Between the two normalized access waveguide width design options, option 2 clearly has a lower maximum excess loss for a given width tolerance. The maximum imbalance performance between the two design options are also comparable with only a change in sign. *The preferred design for a 2X2 paired restricted interference MMI design has a 10.5μm wide effective width and 2.4μm wide access waveguides.*

Hill et al. have also theoretically shown that the maximum imbalance is typically much greater in the 2X2 general interference coupler than in the 2X2 paired interference coupler due to a $3\sqrt{3}$ increase in the modal phase errors at the output waveguides [129]. Even for the most promising 2X2 general interference coupler design, where the access waveguides are aligned to the outside edge of the MMI, they demonstrate inferior performance relative to the 2X2 paired interference coupler. These theoretical calculations confirm our experimental investigation into general interference couplers. General interference couplers *have not* been considered for the splitter or combiner in the design of the Mach-Zehnder modulator.

TE Semi-Vectorial Three-Dimensional BPM Models for the 10.5μm Wide 2X2 MMI Design

A TE semi-vectorial, three-dimensional, finite-difference beam propagation method [84], using PML [85] boundary conditions, has been used to study the 10.5μm wide restricted 2X2 MMI designs discussed in Section 2.2.3. The cross-sectional (x,y) simulation space uses a uniform grid of 401X251 points, running from $x = -12.5\mu$m to $x = 12.5\mu$m, and $y = -5\mu$m to $y = 3\mu$m, with (0,0) the centre of the MMI waveguide core. The refractive index of a grid point (x,y) is given the area weighted average value of the materials contained between $(x\text{-}dx/2, x\text{+}dx/2)$ and $(y\text{-}dy/2, y\text{+}dy/2)$. The propagation step size is dz=0.1μm. All simulations launch the TE$_0$ mode into the -x MMI access waveguide, with the material refractive indices and the corresponding TE$_0$ launch modes, recalculated at every simulation wavelength. No doping or bandedge losses are included in the calculated refractive indices. The modulator MQW core is taken to have a peak photoluminescence wavelength at Q=1411nm in these simulations.

Figure 2.39 presents three-dimensional TE BPM simulation results, as a function of the reference refractive index N_0, for a 10.3μm[37] wide MMI that is 151.5μm long. The access waveguides are 2.0μm wide and they are placed symmetrically about the centre line of the MMI, with their centres separated by 3.5μm. Figure 2.39a provides the extracted total TE$_0$ insertion loss[38] as a function of both the wavelength and the reference refractive index. The variation of total TE$_0$ insertion loss as a function of wavelength is expected due to the finite wavelength tolerance of the MMI design, as discussed in Section 2.2.3. Changing the reference refractive index moves the optimal operation wavelength for the MMI design. The optimal operating wavelength is a very sensitive way to quantify the optimal MMI imaging length in the simulation. This N_0 dependence for the MMI effective length is a consequence of the paraxial BPM approximation that has been studied by Yevick et al. [86]. They propose that N_0 should be selected to be in the vicinity of the guided fundamental mode refractive index. Two dimensional mode calculations[39] for the MMI give 10 available modes from TE$_0$=3.250993 to TE$_9$=3.16506. For the MMI BPM simulations given in this thesis N_0 will be taken as 3.18. Although this does not agree with the approach in [86], it is based on a calibration of the BPM model against the experimental insertion loss for the concatenated 1X1 MMI structure given in Figure 2.58. In Figure 2.39b the X–Z power

---

[37] A physical width of 10.3μm corresponds to an effective width of 10.5μm.

[38] The total TE$_0$ insertion loss is calculated from the sum of the TE$_0$ power in each output access waveguide.

[39] Mode calculations are performed with a uniform-grid finite-difference solver.

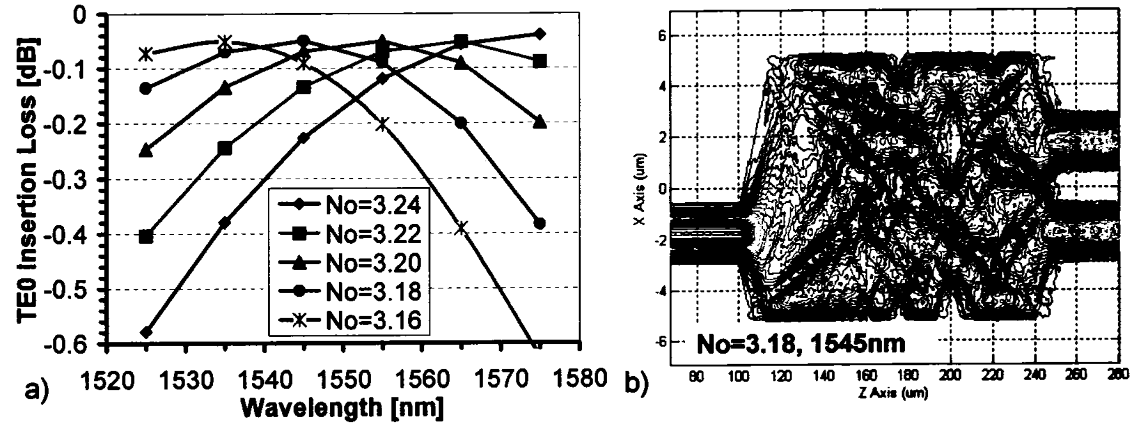

Figure 2.39: *3D TE Semi-Vectorial BPM Simulations for a Paired Interference, 10.3μm X 151.5μm 2X2 MMI Design, with 2.0μm Wide Access Waveguides, as a Function of* N_0 *and Wavelength: a) Total* TE_0 *Insertion Loss versus No and Wavelength, b) TE X–Z Power Contour Map through the Waveguide Core at 1545nm with No=3.18.*

contour map through the waveguide core (y=0) is given for N_0=3.18 at 1545nm.

Figure 2.40 presents three-dimensional TE BPM simulations for the preferred, paired interference, 2X2 MMI. The preferred geometry is 10.3μm[40] wide by 151.5μm long, where the width of the input MMI access waveguides linearly up-taper, from 2.0μm to 2.4μm, over a length of 25μm prior to the MMI. An equivalent down-taper is present on the output access waveguides. These access waveguide tapers are adiabatic transitions based on the calculations detailed in Section 3.6.4. The access waveguides are placed symmetrically about the centre line of the MMI with their centres separated by 3.5μm. The preferred 2X2 MMI geometry also employs angled end-walls, with a z:x aspect ratio of 0.8:2.75, to reduce optical backreflections from the structure, as discussed in Section 2.2.6. This preferred 2X2 MMI geometry is shown in Figure 2.40a. Figure 2.40b provides the extracted total TE_0 insertion loss for the preferred 2X2 MMI design as a function of wavelength. The wavelength tolerance improvement relative to an identical design without the linear access waveguide tapers can be seen. In Figure 2.40c the X–Z power contour map through the waveguide core (y=0) is given at 1545nm. In Figure 2.39d the X–Z power contour map through the waveguide core (y=0) is given at 1575nm. It is obvious that the MMI imaging length is short of the output access waveguides at 1575nm.

Figure 2.41a provides the total TE_0 insertion loss for the preferred 2X2 MMI design, shown in Figure 2.40a, as a function of the MMI length at 1545nm. In Figure 2.41b the X–Z power contour map through the waveguide core (y=0) is given for a 146μm long MMI. Here the output access waveguides are short of the imaging length. Note that there can be significant excitation of the TE_1 mode in the output access waveguides when the MMI imaging length is not aligned with the position of the output access waveguides in z.

---

[40] A physical width 10.3μm corresponds to an effective width of 10.5μm.

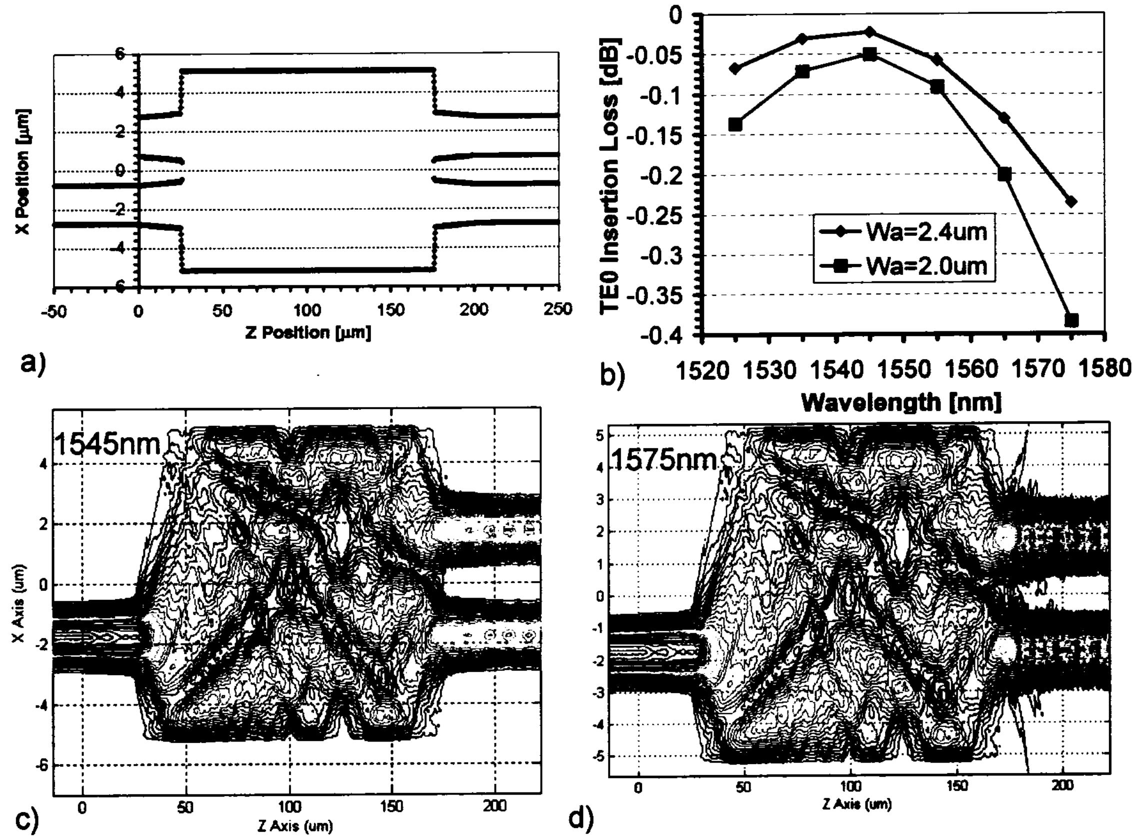

Figure 2.40: *3D TE Semi-Vectorial BPM Simulations for the Preferred Paired Interference 2X2 MMI Design as a Function of Wavelength: a) Waveguide Ridge Geometry for the Preferred 2X2 MMI Design, b) Total* TE_0 *Insertion Loss versus Wavelength with and without the Ridge Width Tapered Access Waveguides, c) TE X–Z Power Contour Map through the Waveguide Core of the Preferred 2X2 MMI Design at 1545nm, d) TE X–Z Power Contour Map through the Waveguide Core of the Preferred 2X2 MMI Design at 1575nm.*

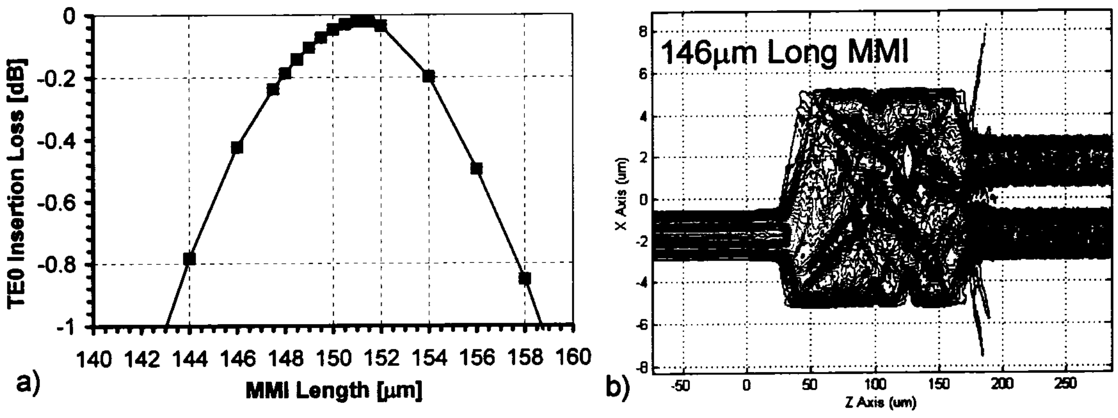

Figure 2.41: ***3D TE Semi-Vectorial BPM Simulations for the Preferred Paired Interference 2X2 MMI Design as a Function of MMI Length at 1545nm: a) Total TE_0 Insertion Loss versus MMI Length, b) TE X–Z Power Contour Map through the Waveguide Core for a 146μm Long MMI.***

Figure 2.42a quantifies the impact of misaligning the launched access waveguide mode on the optical split ratio[41] of the preferred 2X2 MMI, and on the TE_0 spectral purity[42] in the output access waveguides at 1545nm. It is clear that symmetry between the output access waveguides is maintained. In Figure 2.42b the X–Z power contour map through the waveguide core (y=0) is given for a -0.4μm misalignment of the launched TE_0 mode. Figure 2.42b shows that the modal content in the output access waveguides mirrors that of the input access waveguide. The expected 0 degree phase shift between the input access waveguide field and the bar-state output access waveguide field is evident, as is the 90 degree phase shift between the input access waveguide field and the cross-state output access waveguide field.

Here a preferred restricted paired interference 2X2 MMI design has been defined having acceptable theoretical performance within the fabrication constraints of InP semiconductor etching capability.

2.2.4 1X2 Restricted Symmetric Interference

Figure 2.43a provides the MMI length versus physical width relationship for a restricted symmetric interference 1X2 MMI, in the modulator waveguide structure, at 1546nm, using Equation 2.21 with Equations 2.10 and 2.8. Note the decreased length for a given width relative to the restricted paired 2X2 MMI design. Figure 2.43b gives the separation between the two output access waveguides as a function of both the MMI width and the access waveguide width. The gap between the access waveguides exceeds 1.5μm for physical

---

[41] The optical split ratio is defined as the ratio between the power in the $+x$ access waveguide and the power in the $-x$ access waveguide (the ratio of the cross-state power to bar-state power.)

[42] TE_0 spectral purity is defined as the ratio of the TE_0 modal power to the total power in the waveguide.

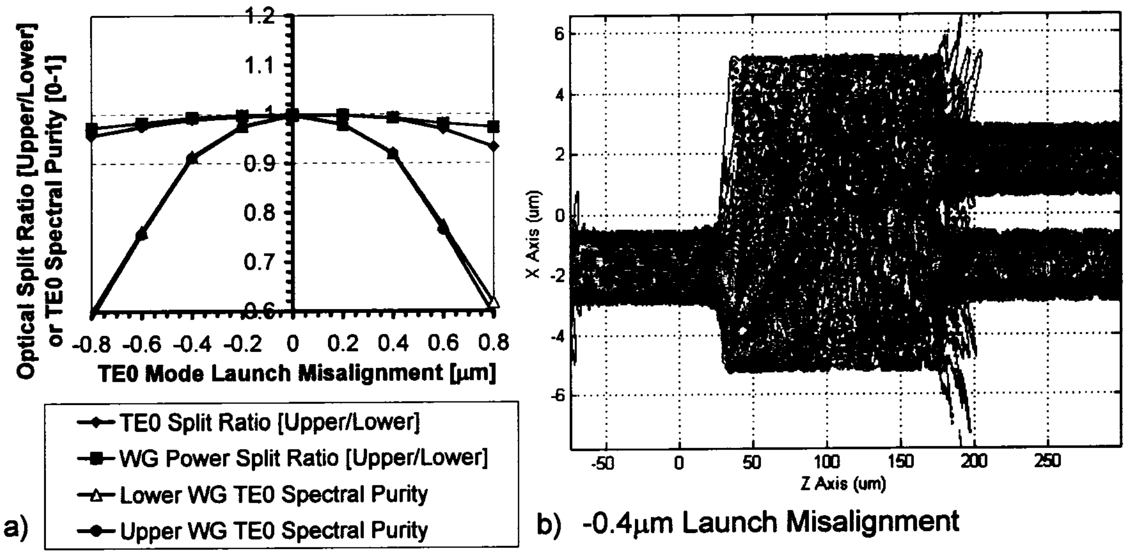

a)

b) -0.4μm Launch Misalignment

Figure 2.42: *3D TE Semi-Vectorial BPM Simulations for the Preferred Paired Interference 2X2 MMI Design as a Function of the Access Waveguide TE_0 Launch Mode Misalignment: a) Output Optical Split Ratio and TE_0 Spectral Purity versus the Launch Mode Misalignment, b) TE X–Z Power Contour Map through the Waveguide Core with a -0.4μm Misalignment of the Access Waveguide TE_0 Launch Mode.*

MMI widths greater than 7μm[43].

In Figure 2.44 the 0.5dB excess loss tolerances for the restricted symmetric interference 1X2 MMI are presented, as a function of the MMI physical width and the access waveguide width, using Equations 2.22 and 2.23, with inputs from Figure 2.33. The design space has been limited to MMI's with a physical width greater than 6.0μm since this corresponds to a 1.0μm separation between 2.0μm wide access waveguides. As with the restricted paired 2X2 MMI, the wavelength and width tolerances decrease in Figure 2.44 with increasing MMI width, and they improve with increasing width for the access waveguides. Both the

---

[43] This is true for 2.0μm wide access waveguides.

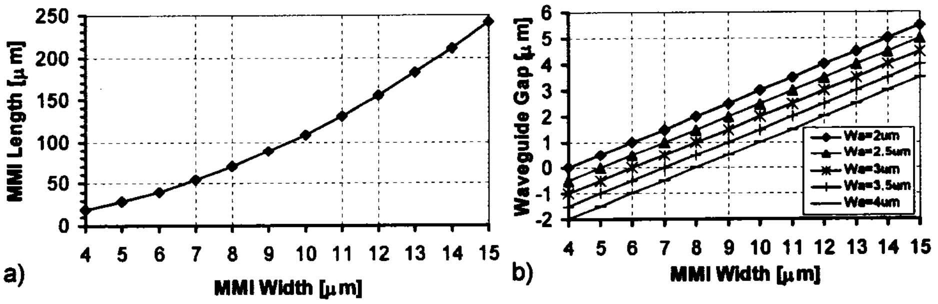

a)

b)

Figure 2.43: *Restricted Symmetric Interference 1X2 MMI: a) MMI Length versus MMI Width, b) MMI Width versus Gap between Access Waveguides for Various Access Waveguide Widths.*

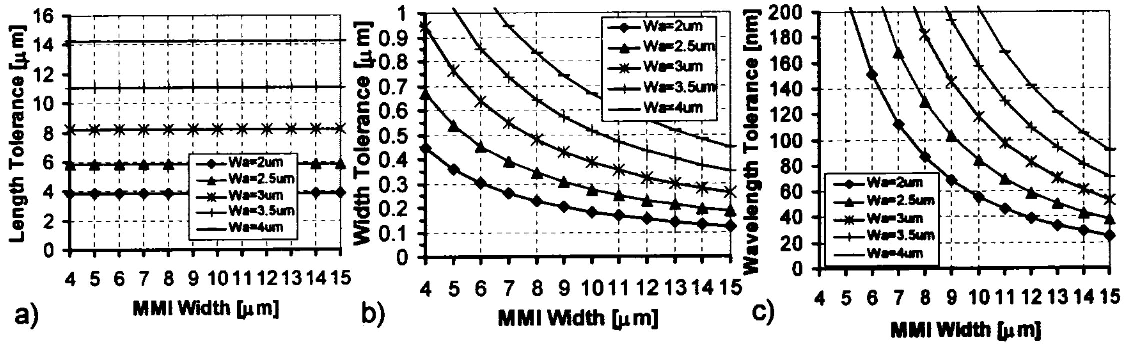

Figure 2.44: ***0.5dB Excess Loss Tolerances for the Restricted Symmetric Interference 1X2 MMI as a Function of MMI Width and Access Waveguide Width: a) MMI Length Tolerances, b) MMI Width Tolerances, c) MMI Wavelength Tolerances.***

MMI width tolerance and the MMI operating wavelength tolerance are acceptable using 2.0μm wide access waveguides with a 7μm wide MMI, where the gap between the output access waveguides is 1.5μm.

With only one access waveguide on the input of a 1X2 MMI there is significant area of end-wall exposed to the MMI. When the modulator is in the transmission minimum off-state, any optical signal backwards propagated through the modulator will be imaged onto this end-wall at the entrance to the 1X2 MMI. It is, therefore, necessary to angle the exposed end-walls to reduce the magnitude of backreflections. Experimental measurements of the MMI backreflectivities are given in Section 2.2.6. BPM simulations indicate that angling the MMI input end-wall and using a narrow MMI width both negatively impact the change in optical split ratio under launch mode misalignment. For these reasons the preferred 1X2 MMI geometry is 8.8μm[44] wide by 83.5μm long and it employs shallow angled end-walls, with a z:x aspect ratio of 1:3.4 at the MMI input, and a z:x aspect ratio of 1:2.75 at the MMI output. The input and output access waveguides are 2.0μm wide. The output access waveguides are placed symmetrically about the centre line of the MMI with their centres separated by 4.5μm.

Figure 2.45 presents three-dimensional TE BPM simulation results for the preferred symmetric interference 1X2 MMI splitter design at 1545nm. The BPM setup conditions and the simulation space used for all the 1X2 MMI calculations are identical to those used for the paired interference 2X2 MMI in Section 2.2.3. The preferred 1X2 MMI geometry is shown in Figure 2.45a. Figure 2.45b provides the extracted total TE$_0$ insertion loss for the preferred 1X2 MMI design as a function of the MMI length. In Figure 2.45c the X–Z power contour map through the waveguide core (y=0) is given at 1545nm.

Figure 2.46a provides the extracted total TE$_0$ and waveguide insertion loss for the preferred 1X2 MMI as a function of wavelength. Figure 2.46a also indicates the wavelength tolerance improvement that can be achieved using an identical MMI design with the same 2.0μm to

---

[44] A physical width of 8.8μm corresponds to an effective width of 9.0μm.

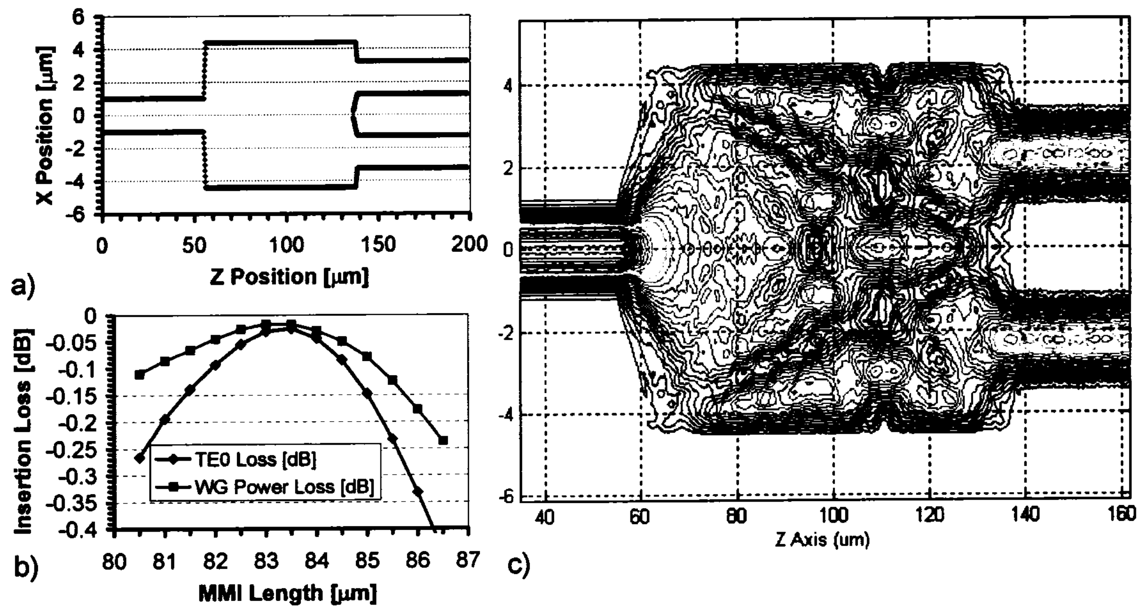

Figure 2.45: ***3D TE Semi-Vectorial BPM Simulations for the Preferred Restricted Symmetric Interference 1X2 MMI Design at 1545nm: a) Waveguide Ridge Geometry, b) Total TE$_0$ and Waveguide Power Insertion Loss as a Function of the MMI Length, c) TE X–Z Power Contour Map through the Waveguide Core.***

2.4μm ridge width tapered access waveguides used on the preferred 2X2 MMI design. This wavelength tolerance improvement is not required if the MMI is only required to operate over the C-Band from 1527nm to 1565nm. Figure 2.46b interprets the data in Figure 2.46a in terms of the TE$_0$ spectral purity in the output access waveguides. The preferred 1X2 MMI geometry is shown in Figure 2.46c and the 1X2 MMI geometry including the ridge width tapered access waveguides is shown in Figure 2.46d.

Figure 2.47a quantifies the impact of misaligning the launched TE$_0$ access waveguide mode on the optical split ratio of the preferred 1X2 MMI, and on the TE$_0$ spectral purity in the output access waveguides, at 1545nm. The two output waveguides have identical spectral purity, and the split ratio is acceptably maintained, under the misalignment of the launched mode. In Figure 2.47b the X–Z power contour map through the waveguide core (y=0) is given for a -0.4μm misalignment of the launched TE$_0$ access waveguide mode.

Figure 2.48 presents identical simulations to those shown in Figure 2.47, however, the 1X2 MMI access waveguides now include 2.4μm wide ridge width up-tapers as shown in Figure 2.46d. Here the two output waveguides no longer have identical spectral purity under launch mode misalignment and the variation in the TE$_0$ optical split ratio under misalignment has increased. Since the up-tapered access waveguides are not required for MMI width or wavelength tolerances they have not been included in the preferred design.

Here a preferred restricted symmetric interference 1X2 MMI design has been defined having acceptable theoretical performance within the fabrication constraints of InP semicon-

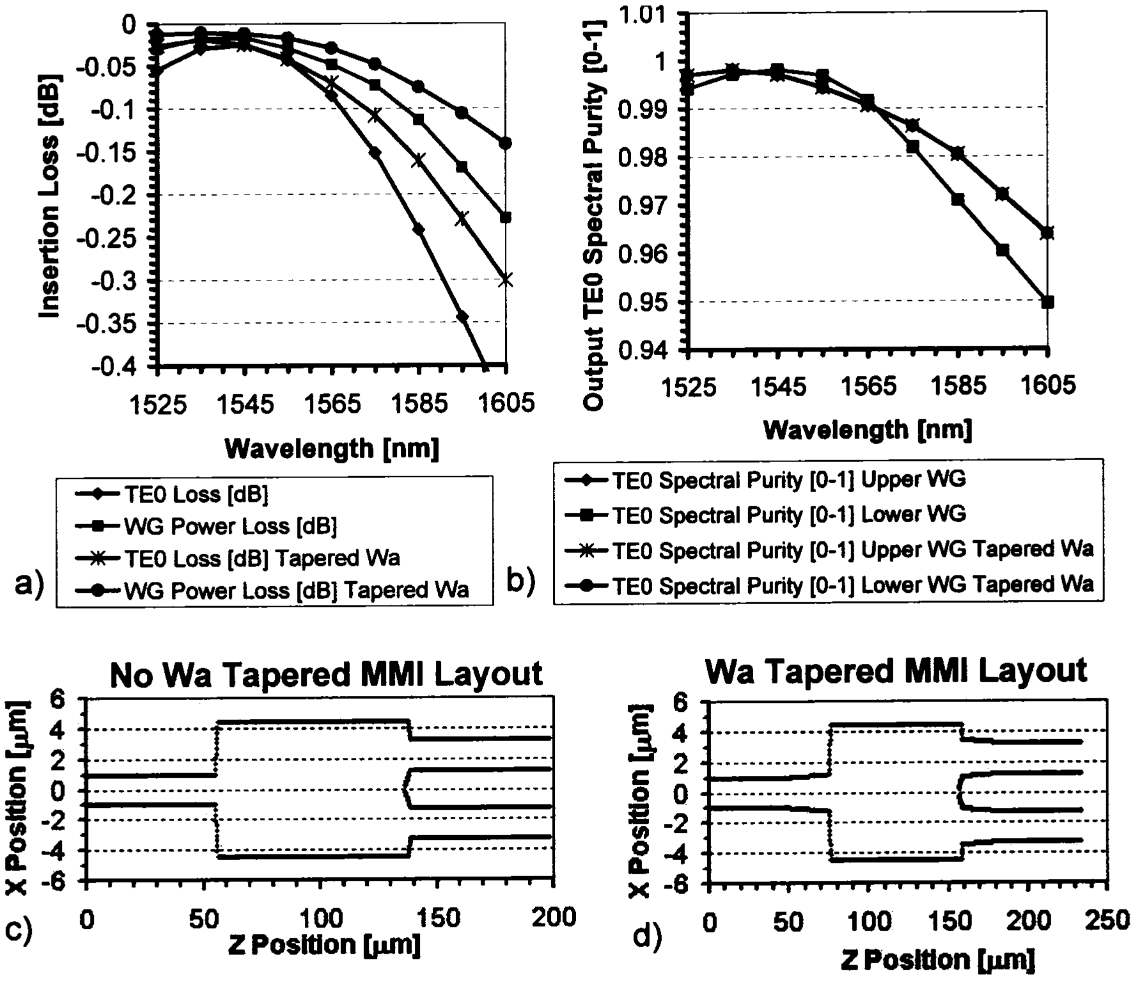

Figure 2.46: *3D TE Semi-Vectorial BPM Simulations for the Preferred Restricted Symmetric Interference 1X2 MMI Design over Wavelength: b) Total* TE_0 *and Waveguide Power Insertion Loss as a Function of Wavelength, with and without Ridge Width Tapered Access Waveguides, b) Output* TE_0 *Spectral Purity as a Function of Wavelength, with and without Ridge Width Tapered Access Waveguides, c) Waveguide Ridge Geometry without Width Tapered Access Waveguides, d) Waveguide Ridge Geometry with Width Tapered Access Waveguides.*

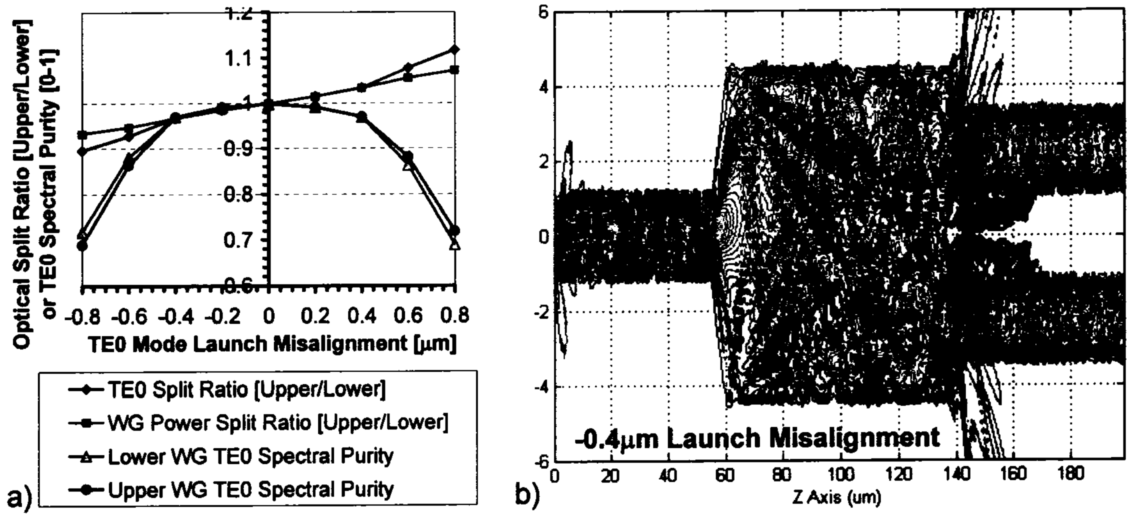

Figure 2.47: *3D TE Semi-Vectorial BPM Simulations for the Preferred Symmetric Interference 1X2 MMI Design as a Function of the Access Waveguide TE_0 Launch Mode Misalignment: a) Output Optical Split Ratio and TE_0 Spectral Purity versus the Launch Mode Misalignment, b) TE X–Z Power Contour Map through the Waveguide Core with a -0.4µm Misalignment of the Access Waveguide TE_0 Launch Mode.*

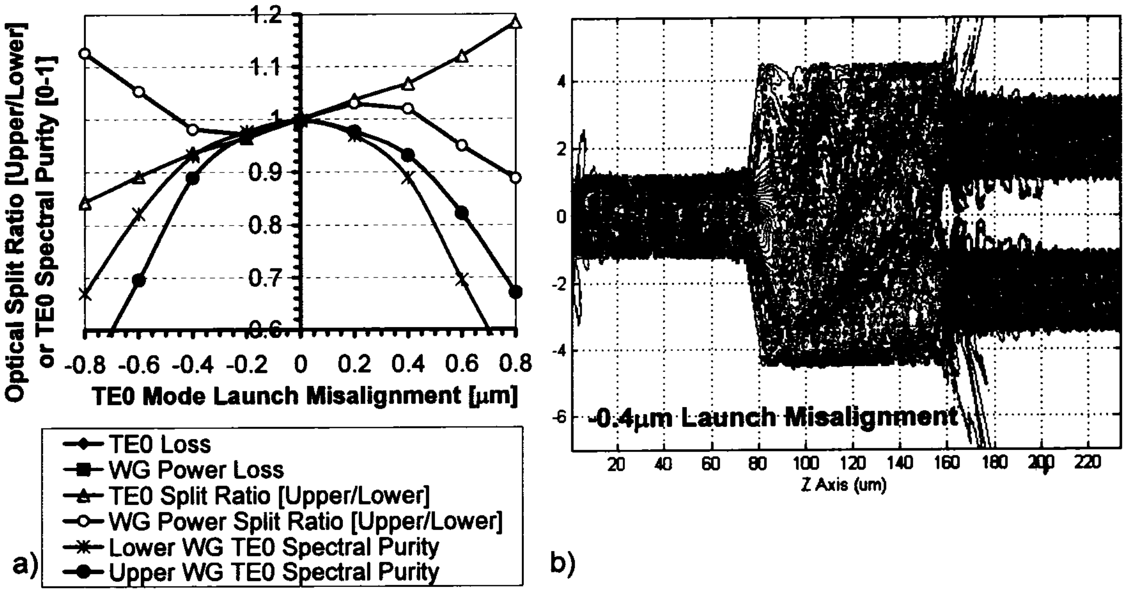

Figure 2.48: *3D TE Semi-Vectorial BPM Simulations for the Preferred Symmetric Interference 1X2 MMI Design including Up-Tapered Access Waveguides as a Function of the Access Waveguide TE_0 Launch Mode Misalignment: a) Output Optical Split Ratio and TE_0 Spectral Purity versus the Launch Mode Misalignment, b) TE X–Z Power Contour Map through the Waveguide Core with a -0.4µm Misalignment of the Access Waveguide TE_0 Launch Mode.*

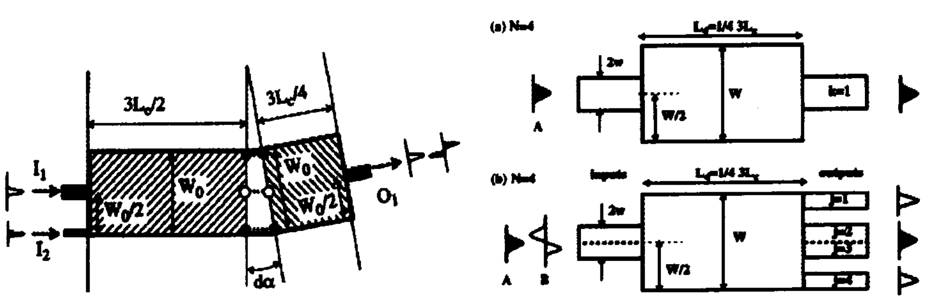

Fig. 9. Design of a mode converter-combiner based on MMI couplers. The fundamental mode of the input I_1 is imaged in the fundamental mode of the output O_1. The fundamental mode of the input I_2 goes to the first order mode at the output O_1. The angle variation $d\alpha$ produces a phase shift of $\pi/2$ between the two outer images after the first section.

a)

Fig. 1. Mapping characteristics of two MMI's of the same length for (a) a symmetric zero-order mode (filled shapes) and (b) a zero-order mode and an antisymmetric first-order mode (open shapes). (a) Using an input guide at the center of the MMI, we map the symmetric mode for lengths $L = 3/NL_c$, with $N = 4K$ and $K = 1$, onto one central output guide. (b) Using the central input guide for an antisymmetric mode, we map the antisymmetric mode onto the two outer output guides.

b)

Figure 2.49: ***a) 100% Efficient MMI Mode Converter-Combiner Design,*** *Source: Besse et al. Journal of Lightwave Technology, Vol. 14, No. 10, pp.2286-2293, Oct. 1996.,* ***b) MMI Spatial Filter,*** *Source: J. Leuthold et al., Optics Letters, Vol. 21, No. 11, pp. 836-838, June 1st 1996.*

ductor etching capability.

2.2.5 Mode Filter Design

Section 2.1.10 showed that the deep-etched modulator structure guides a lateral higher-order TE_1 mode. Obviously, it would be advantageous for this TE_1 mode to be stripped from the waveguide since, as shown in Section 2.4, it can negatively impact the modulator performance as a function of wavelength.

Figure 2.49a shows a 100% efficient MMI mode converter-combiner design introduced by Besse et al. [107]. For applications where the higher-order mode is not required, a shorter and simpler MMI filter was introduced by Leuthold et al. [112]. The principle of Leuthold's spatial MMI mode filter, shown in Figure 2.49b, relies on the different mapping characteristic of symmetric and antisymmetric modes in 1XN MMI splitters. Recently, Kohtoku et al. have used optical low coherence reflectometry [233] (OLCR) to experimentally measure 40dB of first order mode rejection through two passes in a deep-etched 5.9μm wide 1X1 MMI mode filter [111].

Here the properties of a 1X1 MMI, used as an inline TE_1 mode filter, placed between the modulator input and the 1X2 or 2X2 MMI splitter function, are explored. Since the preferred 2X2 MMI design uses 2.4μm wide access waveguides, it is desirable for the output access waveguide from the mode filter to also be 2.4μm wide. This will remove the need for waveguide ridge width tapers to interconnect the two functions.

Figure 2.50 provides the MMI length versus physical width relationship for a restricted symmetric interference 1X1 MMI, in the modulator waveguide structure, at 1546nm, using

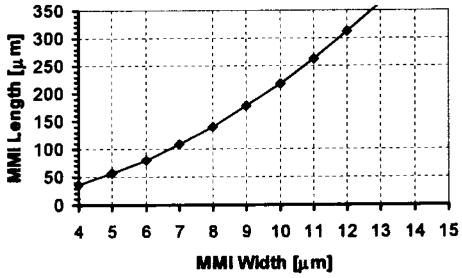

Figure 2.50: ***Restricted Symmetric Interference 1X1 MMI Mode Filter Length versus Width.***

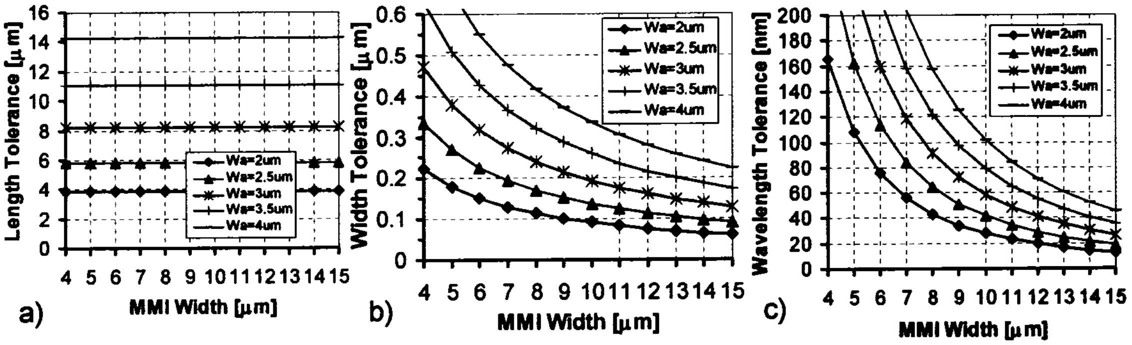

Figure 2.51: ***0.5dB Excess Loss Tolerances for the Restricted Symmetric Interference 1X1 MMI Mode Filter as a Function of MMI Width and Access Waveguide Width: a) MMI Length Tolerances, b) MMI Width Tolerances, c) MMI Wavelength Tolerances.***

Equation 2.21 with Equations 2.10 and 2.8. Note the factor of two increase in length for a given width relative to the restricted symmetric 1X2 MMI design.

In Figure 2.51 the 0.5dB excess loss tolerances for the restricted symmetric interference 1X1 MMI are presented, as a function of the MMI physical width and the access waveguide width, using Equations 2.22 and 2.23, with inputs from Figure 2.33. Both the MMI width tolerance and the MMI operating wavelength tolerance are acceptable using 2.4μm wide access waveguides with a 6.0μm wide MMI. For a mode filter, the MMI width and wavelength tolerances need to be large, since a TE_0 input field, poorly imaged through a 1X1 MMI, will excite the TE_1 mode that the MMI is intended to filter in the output waveguide.

Figure 2.52a presents three-dimensional TE BPM simulation results for the TE_0 spectral purity at the output waveguide, for a set of symmetric interference 1X1 MMI mode filter designs at 1545nm, as a function of the access waveguide TE_0 launch mode misalignment. The BPM setup conditions and the simulation space used for all the 1X1 MMI calculations are identical to those used for the paired interference 2X2 MMI in Section 2.2.3. Curve A in Figure 2.52a provides the TE_0 spectral purity in the input access waveguide, at launch, for all the filter design variants. Filter design B is 9μm wide and 235.5μm long, with no end-wall or access waveguide ridge width tapers. The 1X1 MMI mode filter for all remaining

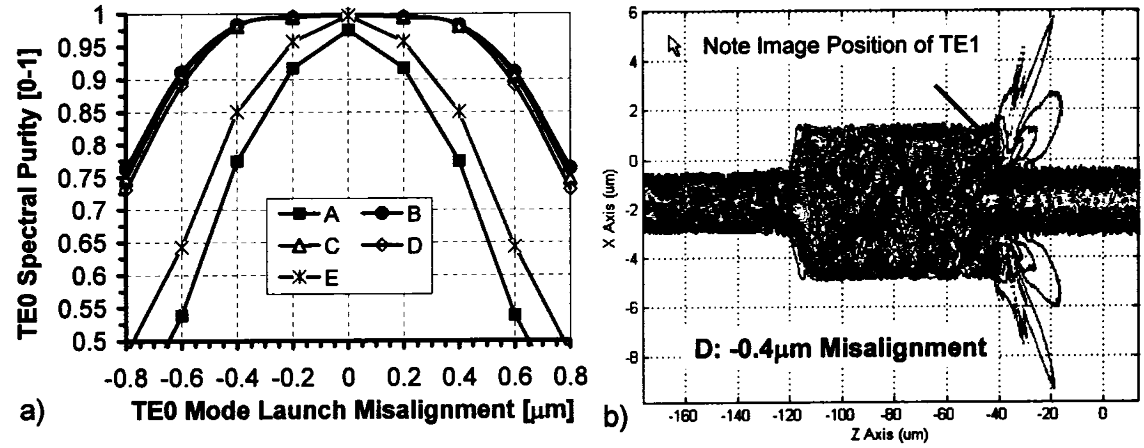

Figure 2.52: *3D TE Semi-Vectorial BPM Simulations for a Set of Symmetric Interference 1X1 MMI Designs as a Function of the Access Waveguide TE_0 Launch Mode Misalignment: a) TE_0 Spectral Purity in the Output Waveguide versus the Launch Mode Misalignment for all 1X1 MMI Designs, b) TE X–Z Power Contour Map through the Waveguide Core in Design D with a -0.4μm Misalignment of the Access Waveguide TE_0 Launch Mode.*

[C-E] designs in Figure 2.52a is 6μm wide and 78.5μm long. Filter design C has no end-wall or access waveguide ridge width tapers. Filter design D has the same 25μm long, 2.0μm to 2.4μm wide, input access waveguide taper as used in the preferred 2X2 MMI design. The output access waveguide in filter design D is 2.4μm wide, and both the input and output end-walls are angled into the MMI with a z:x aspect ratio of 1:3.6. Figure 2.52a shows that filter designs B-D are all excellent at filtering the TE_1 mode from the 1X1 MMI output waveguide. Filter design E is identical to filter design D, except the input and output end-walls are angled into the MMI with a z:x aspect ratio of 3.3:1. The TE_1 filtering performance of this design is very poor. The 1X1 MMI filter performance is therefore strongly dependent on the geometry of the end-wall tapers included to reduce the optical backreflection from the filtered TE_1 mode. If the taper length is long enough to start to look adiabatic, then the TE_1 mode can be recollected into the output waveguide. Design D will be the preferred 1X1 MMI mode filter design. In Figure 2.52b the X–Z power contour map through the waveguide core (y=0) of the preferred design D, is given for a -0.4μm misalignment of the launched TE_0 access waveguide mode. The filtering of the TE_1 mode is evident.

Figure 2.53a provides the extracted total TE_0 and waveguide insertion loss, for the preferred 1X1 MMI filter, as a function of wavelength. Figure 2.53a also indicates the wavelength tolerance, for filter design C in Figure 2.52a, labeled with the suffix "No Tapers." The preferred 1X1 MMI geometry is shown in Figure 2.53b. In Figure 2.53c, the X–Z power contour map through the waveguide core (y=0) is given, for the preferred 1X1 MMI filter design at 1545nm. It is also given at 1585nm in Figure 2.53d. Figure 2.54 gives a similar set of simulations as a function of the 1X1 MMI length. Together Figure 2.53 and Figure 2.54 indicate the preferred mode filter design has good wavelength and fabrication tolerances.

Figure 2.55 and Figure 2.56 quantify, with three-dimensional TE BPM simulations, the ben-

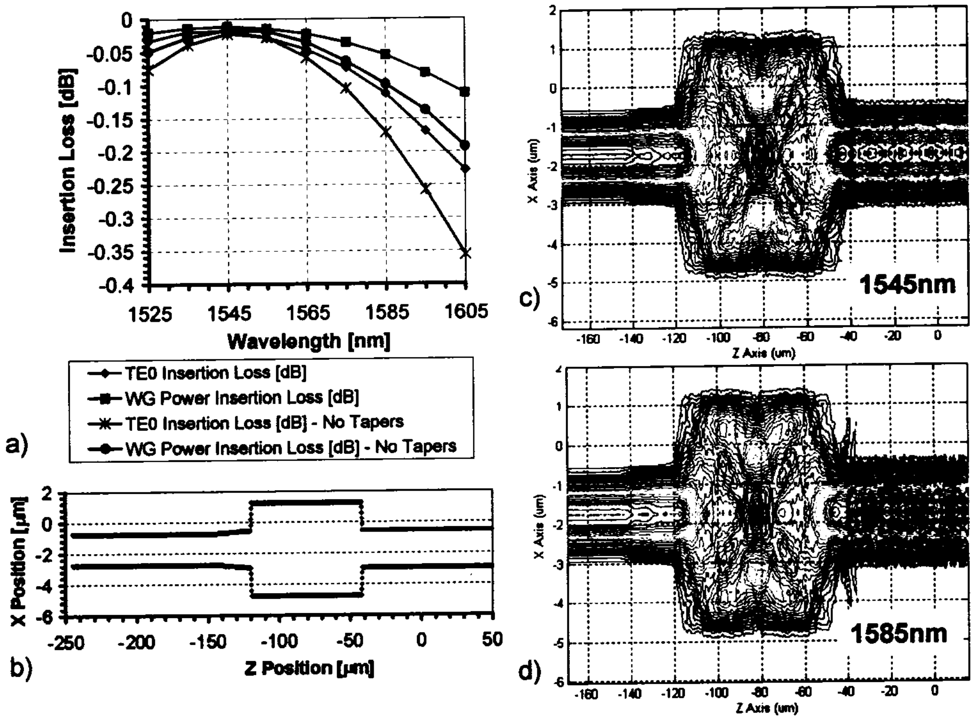

Figure 2.53: *3D TE Semi-Vectorial BPM Simulations for the Preferred Symmetric Interference 1X1 MMI Design as a Function of Wavelength: a) Total* TE_0 *and Waveguide Power Insertion Loss versus Wavelength, b) Waveguide Ridge Geometry for the Preferred 1X1 MMI Design, c) TE X–Z Power Contour Map through the Waveguide Core of the Preferred 1X1 MMI Design at 1545nm, d) TE X–Z Power Contour Map through the Waveguide Core of the Preferred 1X1 MMI Design at 1585nm.*

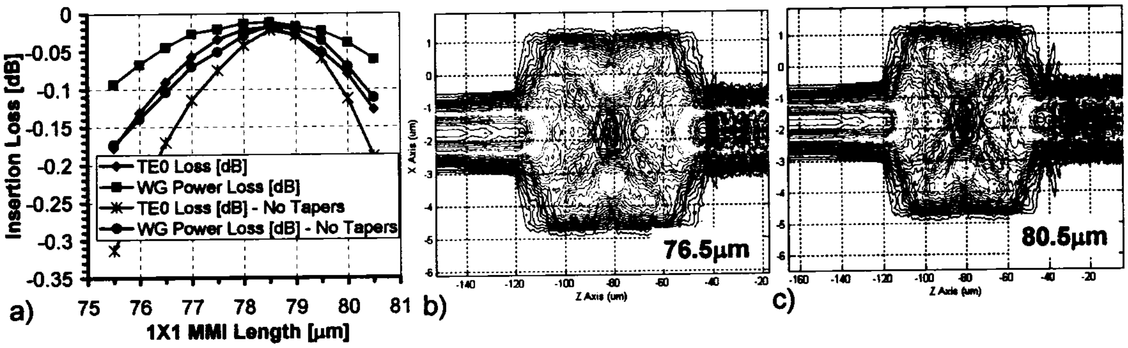

Figure 2.54: *3D TE Semi-Vectorial BPM Simulations for the Preferred Symmetric Interference 1X1 MMI Design as a Function of MMI Length at 1545nm: a) Total* TE_0 *and Waveguide Power Insertion Loss as a Function of Length, b) TE X–Z Power Contour Map through the Waveguide Core for the Preferred 1X1 MMI Design 76.5μm Long 1X1 MMI Design, b) TE X–Z Power Contour Map through the Waveguide Core for a 80.5μm Long 1X1 MMI Design.*

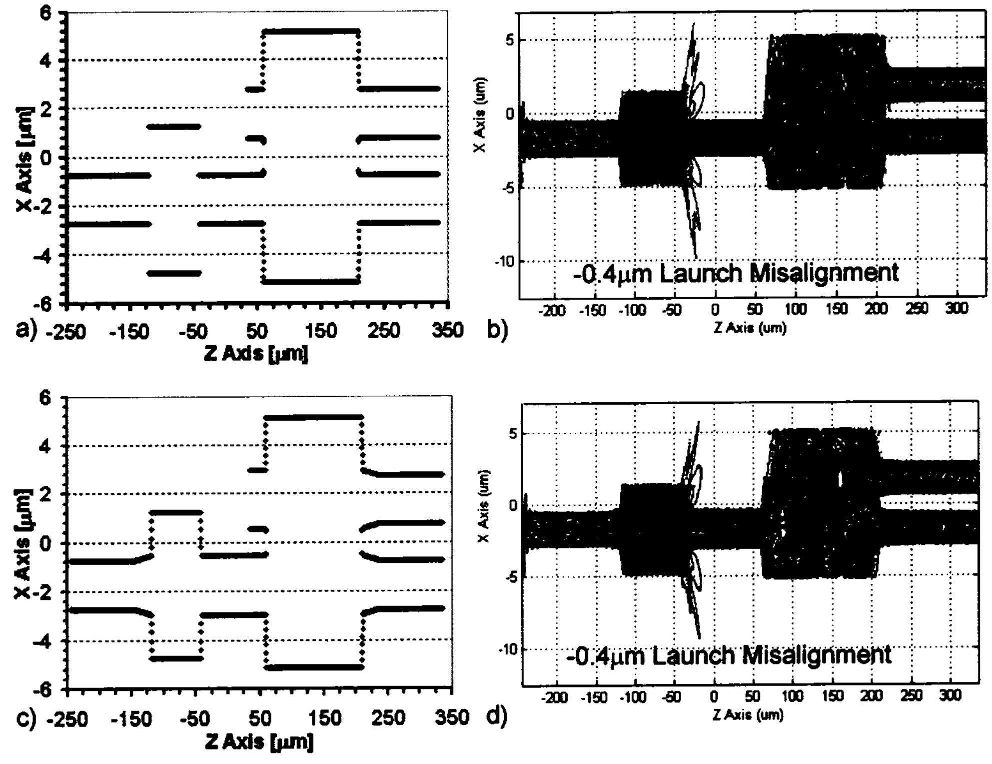

Figure 2.55: *Impact of a 1X1 MMI Mode Filter on the Performance of a 2X2 MMI Splitter under Launch Mode Misalignment at 1545nm-I: a) Waveguide Ridge Simulation Geometry using the Preferred 2X2 MMI Design with 2.0µm Wide Access Waveguides and a 6µm Wide by 78.5µm Long 1X1 MMI Mode Filter having 2.0µm Access Waveguides and No End-Wall Tapers, b) TE X–Z Power Contour Map through the Waveguide Core for the Waveguide Geometry in (a) with a -0.4µm Misalignment of the Access Waveguide* TE_0 *Launch Mode, c) Waveguide Ridge Simulation Geometry using Both the Preferred 2X2 MMI Design and the Preferred 1X1 MMI Design, d) TE X–Z Power Contour Map through the Waveguide Core for the Waveguide Geometry in (c) with a -0.4µm Misalignment of the Access Waveguide* TE_0 *Launch Mode.*

efit of a 1X1 MMI mode filter in the optical path prior to a 2X2 MMI splitter. In Figure 2.55 two waveguide simulation geometries are defined. The corresponding TE X–Z power contour maps, through the waveguide cores, at 1545nm, and for a -0.4µm misalignment of the launched TE_0 access waveguide mode, are provided. The waveguide geometry in Figure 2.55c uses the preferred 1X1 MMI mode filter in-line with the preferred 2X2 MMI mode splitter. The filter and splitter are separated by 50µm of 2.4µm wide interconnect waveguide. The waveguide geometry in Figure 2.55a is similar, except all access waveguides are 2.0µm wide, and the 1X1 MMI filter has no end-wall tapers. Figure 2.56a provides the optical split ratio and output TE_0 spectral purity, from the waveguide geometry given in Figure 2.55a, as a function of the launch mode misalignment. Figure 2.56b provides the same for the preferred waveguide geometries given in Figure 2.55c.

Comparing Figure 2.55 and Figure 2.56 against Figure 2.42 shows significant improvement in the TE_0 spectral purity in the output waveguides, under launch mode misalign-

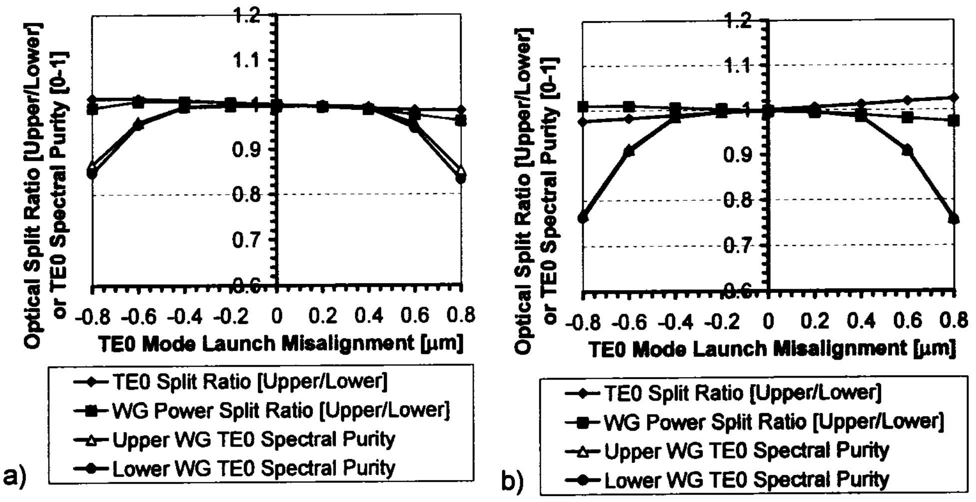

Figure 2.56: ***Impact of a 1X1 MMI Mode Filter on the Performance of a 2X2 MMI Splitter under Launch Mode Misalignment at 1545nm-II: a) Optical Split Ratio and Output TE_0 Spectral Purity from the Waveguide Geometry Given in Figure 2.55a as a Function of Launch Mode Misalignment, b) Optical Split Ratio and Output TE_0 Spectral Purity from the Waveguide Geometry Given in Figure 2.55c as a Function of Launch Mode Misalignment.***

ment, when a 1X1 MMI mode filter is present in the optical path. Comparing Figure 2.56a with Figure 2.56b indicates that the preferred 1X1 MMI and 2X2 MMI designs, having tapered access waveguides to improve the wavelength tolerances and tapered MMI end-walls to reduce optical backreflections, do not sacrifice the spectral purity in the output waveguides.

Figure 2.57 demonstrates that the poor and asymmetric TE_0 spectral purity under launch mode misalignment, in the output waveguides of the 1X2 MMI shown in Figure 2.48, can be dramatically improved by adding the preferred 1X1 MMI mode filter design into the optical path, prior to the 1X2 MMI splitter.

The 1X1 MMI mode filter has been shown to be a tolerant MMI design that is effective at improving the TE_0 spectral purity in the output waveguides of various MMI splitter designs. The preferred 2X2 MMI design and the preferred 1X2 MMI design are, however, by themselves, good at maintaining the critical[45] TE_0 optical split ratio under launch mode misalignment. The value of the in-line 1X1 MMI mode filter is therefore limited. As a non-essential additional component in the optical path of the modulator, the 1X1 MMI must provide the modal filter function with negligible excess insertion loss. As an aside, the 1X1 MMI mode filter would have extra utility in filtering the composite waveguide cavity modes discussed in Section 2.1.12. Experimental measurements on several 1X1 MMI mode filter designs are detailed in the following Section.

---

[45] A fixed optical split ratio is critical for a splitter because it impacts the chirp of the modulator.

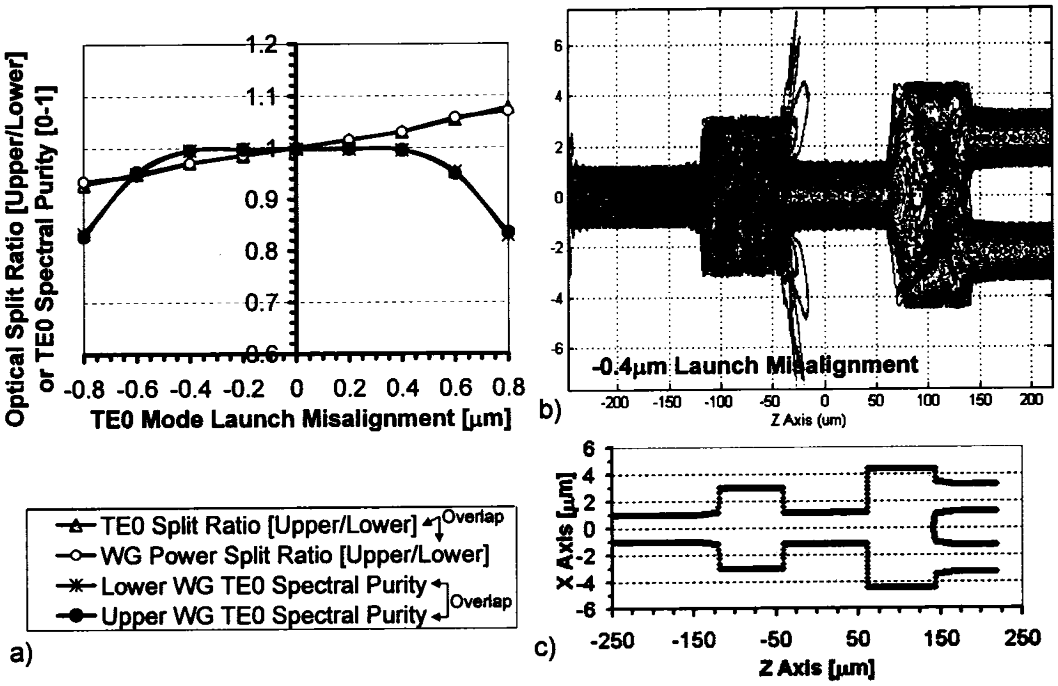

Figure 2.57: *3D TE Semi-Vectorial BPM Simulations with the Preferred 1X1 MMI Mode Filter Design Included in the Optical Path Prior to the 1X2 MMI Splitter Given in Figure 2.48: a) Optical Split Ratio and TE$_0$ Spectral Purity in the Output Access Waveguides under Launch Mode Misalignment, b) TE X–Z Power Contour Map through the Waveguide Core with a -0.4µm Misalignment of the Access Waveguide TE$_0$ Launch Mode, c) Waveguide Ridge Geometry.*

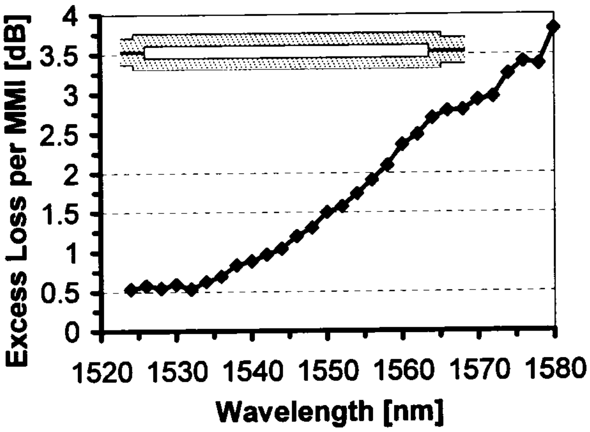

Figure 2.58: *Experimental Measurement of the Insertion Loss per MMI versus Wavelength, obtained from a Straight Waveguide Reference and a Set of Five Cascaded 10.5μm Wide by 239μm Long 1X1 MMI Devices with 2.0μm Wide Access Waveguides.*

Experimental Measurements on 1X1 MMI Mode Filters

Since it has only one input and one output, and can be easily cascaded, the 1X1 MMI is a useful test structure to verify experimentally the required lithographical dimensions of MMI structures. Figure 2.58 presents an experimental measurement of the insertion loss per MMI versus wavelength, obtained from a straight waveguide reference and a set of five cascaded 10.5μm wide by 239μm long 1x1 MMI devices with 2.0μm wide access waveguides. The insertion loss minimum in this graph corresponds to the optimal wavelength for the MMI. Since it is difficult to measure a 10.5μm ridge width with the required 0.1μm accuracy, this measurement can be used to experimentally optimize the ridge definition process, and verify any process bias between a waveguide width defined on the lithography reticles and the final fabricated waveguides. Once the optimal experimental dimensions are known, an experimental L_π value can be extracted from Equation 2.10. This experimental L_π value can then be used in Equations 2.17- 2.21 to determine process optimized dimensions for any MMI design. This procedure can also be performed using cascaded restricted paired 2X2 MMI devices designed for 100% transmission in their cross-state output waveguide. From Figure 2.58 it is clear that the insertion loss of an optimal 1X1 MMI design is not negligible.

Figure 2.59 provides an optical low coherence reflectometry [233] (OLCR) backreflectivity measurement from 10 cascaded 6μm wide by 80μm long 1X1 MMI devices with and without end-wall tapers that are 6μm long in z. The access waveguides are 2.0μm wide. These 1X1 MMI dimensions are optimal for 1530nm operation. This data was collected using a commercial implementation[46] of an optical low coherence reflectometer. This technique is ideal for exploring backreflectivity within optical components since it spatially resolves[47]

---

[46] GNNettest Win-R Reflectometer

[47] The spatial resolution is 50μm in fiber

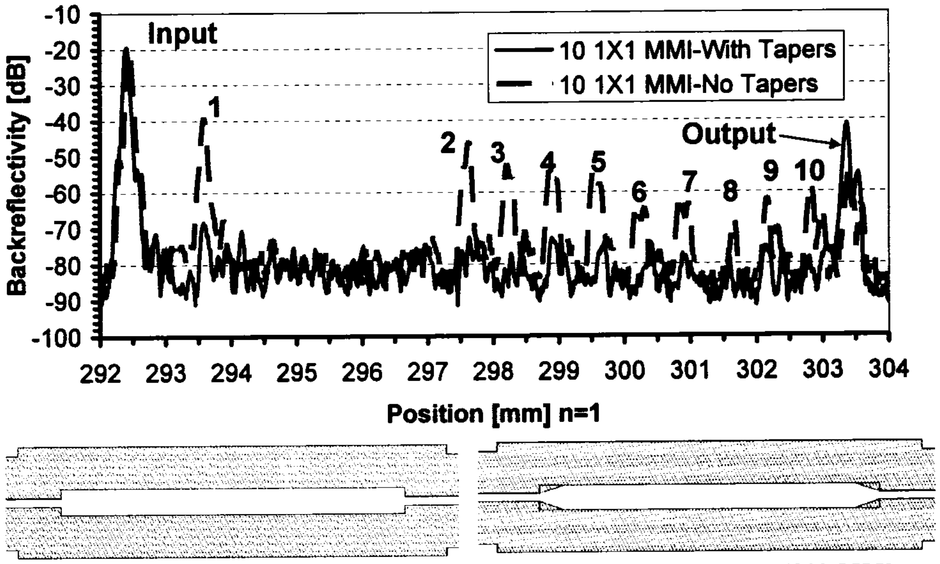

No Taper 6μmX80μm 1X1 MMI **Tapered 6μmX80μm 1X1 MMI**

Figure 2.59: *OLCR Backreflectivity from 10 Cascaded 6μm Wide by 80μm Long 1X1 MMI Devices having 2.0μm Wide Access Waveguides with and without End-Wall Tapers that are 6μm Long in Z.*

backreflections with a return-loss noise-floor better than -90dB. The centre wavelength of the low-coherent source in the reflectometry measurement is 1550nm. The impact of the MMI end-wall tapers on reducing the optical backreflections is clearly evident.

Figure 2.60 presents OLCR backreflection measurements from a negatively chirped modulator chip design with optical mode spot-size converters and a 1X1 MMI mode filter in the optical path prior to the 2X2 MMI splitter. The 1X1 MMI is 6μm wide by 80μm long, with 2.0μm wide access waveguides, and has end-wall tapers that are 6μm long in z. In Figure 2.60a the reflection originating from the end-wall of the 1X1 MMI has been circled. This reflection increases by almost 20dB for a misalignment of the input coupling fiber that generate a 1dB change in the modulator output optical power, however, the reflection remains below an absolute value of -55dB. Figure 2.60b shows the difference between the aligned and misaligned backreflection spectra. It shows that following the 1X1 MMI the differences in the spectra practically disappear. The OLCR backreflection measurement is very sensitive. The backreflection spectra from a strongly-guided straight ridge waveguide has a highly reproducible complex structure. The differences in the two spectra prior to the 1X1 MMI can be attributed to different modal content in the ridge waveguide, i.e. both TE_0 and TE_1 modes in the coupling misaligned spectra versus TE_0 only in the aligned spectra. With this interpretation of the backreflection difference spectra, it is clear that the 1X1 MMI is acting to strip the TE_1 mode. The results in Figure 2.60b indicate the 1X1 MMI with long end-wall tapers is better at filtering the TE_1 mode than would be expected from the BPM simulations in Figure 2.52-Curve E. This negatively chirped modulator chip design, incorporating the 1X1 MMI mode filter, had nearly 0.5dB of additional insertion loss

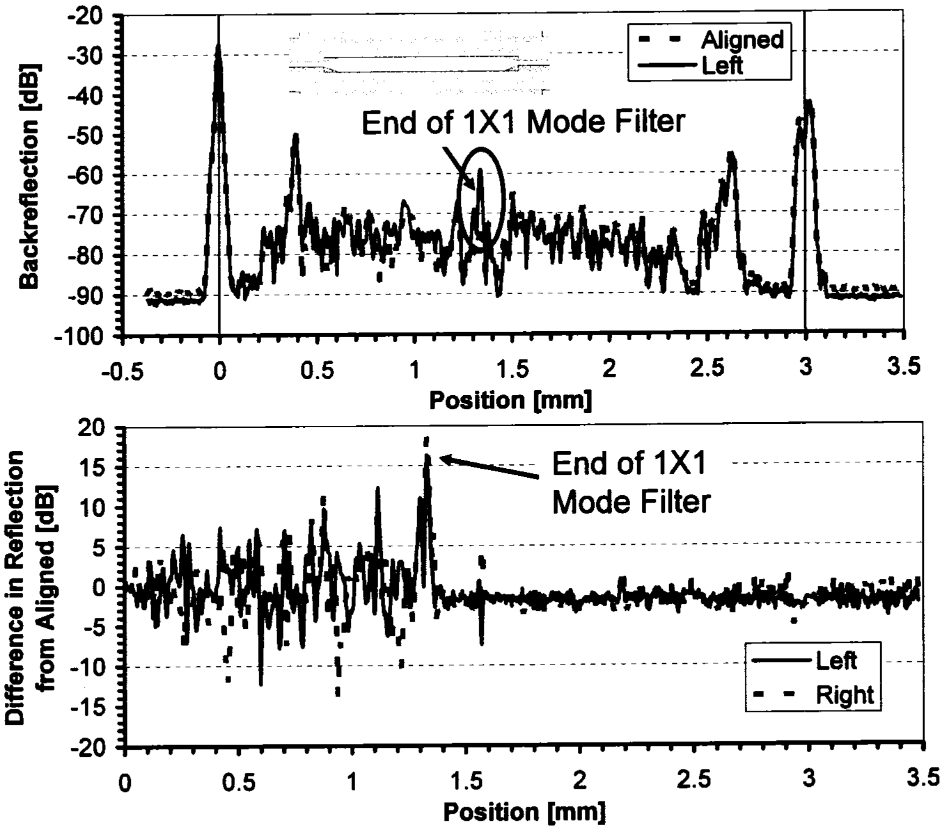

Figure 2.60: ***Impact of a 1X1 MMI in the Optical Path on the Measured OLCR Backreflectivity under Input Coupling Misalignment for the Negative Chirp Modulator Device [Off-State.] The 1X1 MMI is 6μm Wide by 80μm Long with 2.0μm Wide Access Waveguides and has End-Wall Tapers that are 6μm Long in Z.***

relative to the design without the filter.

It has been shown that the 1X1 MMI mode filter will strip the TE_1 mode and that the backreflectivity from its tapered end-walls is <-55dB, even with the maximum feasible input mode coupling misalignment. Unfortunately the additional insertion loss with the inclusion of the mode filter was not negligible, therefore it has not been included in the final modulator designs.

2.2.6 1X2 and 2X2 MMI Backreflections

Pennings et al. reported on the reflection properties of multimode interference devices in 1994 [118]. They were the first to propose the use of angled or rough ends to minimize the effectiveness of reflections from the end-walls of the MMI section. Shibata et al. [114] reported in 1996 quantitative reflection characteristics of deeply-etched 2X2 MMI couplers using optical low coherence reflectometry (OLCR). The origin of the MMI reflection was

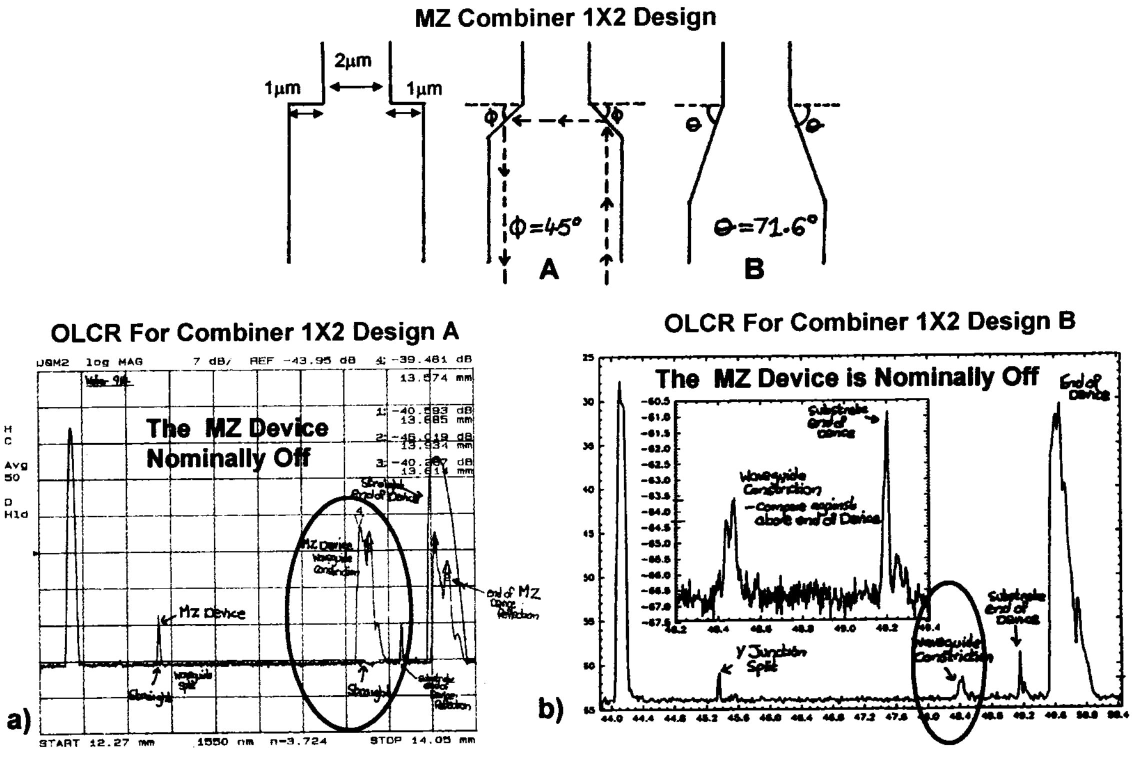

Figure 2.61: *a) Backreflectivity from a 1X2 MMI as a Combiner at the Transmission Minimum with 45° Degree End-Wall Angles, b) Backreflectivity from a 1X2 MMI as a Combiner at the Transmission Minimum with 72° Degree End-Wall Angles. Source: Ian Betty, M.Sc, Queen's University, 1998.*

identified with the output waveguide interface and the reflectivity was shown to be < −30dB. Erasme et al. found that for sidewalls 4° off vertical, the reflection back into the input guide from an end-face of a deeply-etched 1X2 MMI splitter or a 2X2 MMI coupler with no output waveguides, was generally below -20dB [113]. Erasme et al. also found that the reflections fall below -40dB in practical cases where the exit waveguides exist.

The deeply-etched 1X2 MMI, when used as a combiner in an interferometer, can produce substantial backreflections at the transmission minimum [117, 122]. To address this Gottesman et al. proposed the incorporation of additional lossy waveguides at the output of the structure [115, 116]. Using OLCR they measured backreflection reductions of up to 30dB with the inclusion of these additional waveguides. I have also demonstrated previously [117], that simply tapering[48] the end-face sidewalls of the 1X2 MMI will provide equivalent backreflectivity reductions (up to 30dB) at the transmission minimum, as shown in Figure 2.61. In the Mach-Zehnder modulator designs for negative and zero chirp applications, shown in Figures 1.15 and 1.20, a 2X2 3dB MMI coupler was deliberately chosen as the combiner element to avoid the potential reflection from a 1X2 MMI combiner at the modulator transmission minimum.

---

[48] The simple tapering used a z:x aspect ratio of 3:1.

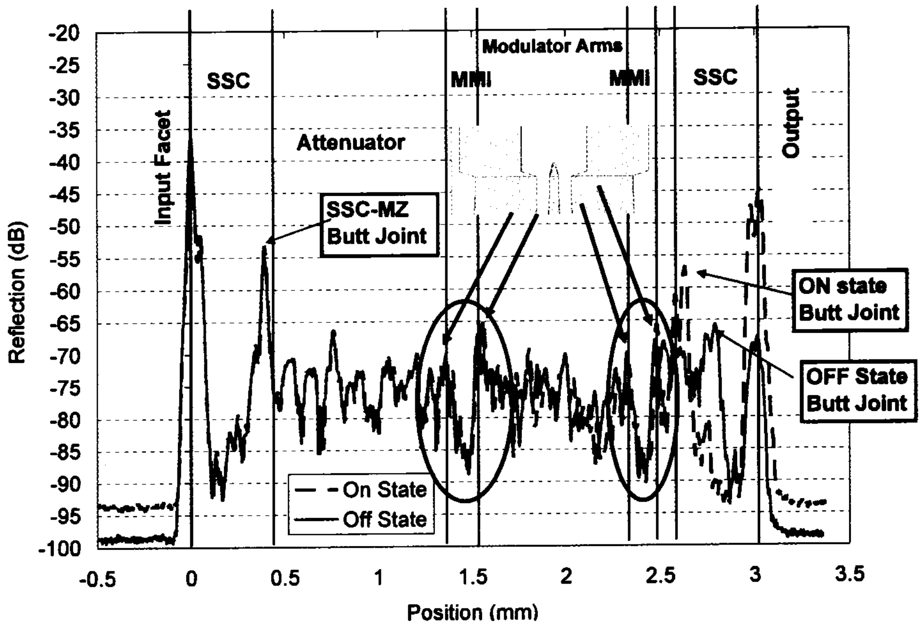

Figure 2.62: ***OLCR Backreflection Measurement of the 2X2 MMI End Wall Reflectivity for both Bar and Cross State Transmission in a Negatively Chirped Modulator Chip Design.***

Figure 2.62 presents OLCR backreflection measurements from a negatively chirped modulator chip design. Angled end-walls with a z:x aspect ratio of 0.8:2.5 are incorporated at both ends of the 2X2 MMI splitter and combiner functions, as shown in the insert on Figure 2.62. Note the magnitude of the backreflections from the input and output end-walls of the 2X2 MMI splitter and combiner are below -65dB in both the on-state and off-state of the modulator. The ridge sidewall backscatter is also reduced in the 10.3μm wide MMI functions relative to the 2.0μm wide modulator arm waveguides. The spot-size converter structures on either end of the chip also show decreasing ridge sidewall backscatter as the ridge width tapers up to 4.5μm at the device facets, from the 2.0μm width at the butt-joint to the modulator waveguide.

Backreflections from Light Launched into the Output of the Mach-Zehnder Modulator

The modulator design for zero chirp applications, shown in Figure 1.14, incorporates an angled end-wall at the 1X2 MMI splitter entrance. This angled end-wall has a z:x aspect ratio of 1:3.4, as shown in Figure 2.63a. When the modulator is in the transmission minimum off-state, any optical signal backwards propagated through the modulator will be imaged onto the end-wall of the entrance to the 1X2 MMI splitter. Figure 2.63b shows that the measured integrated backreflectivity from the modulator chip under these conditions remains below the required -27dB.[49]

---

[49] Telcordia SONET GR-253-CORE Standard.

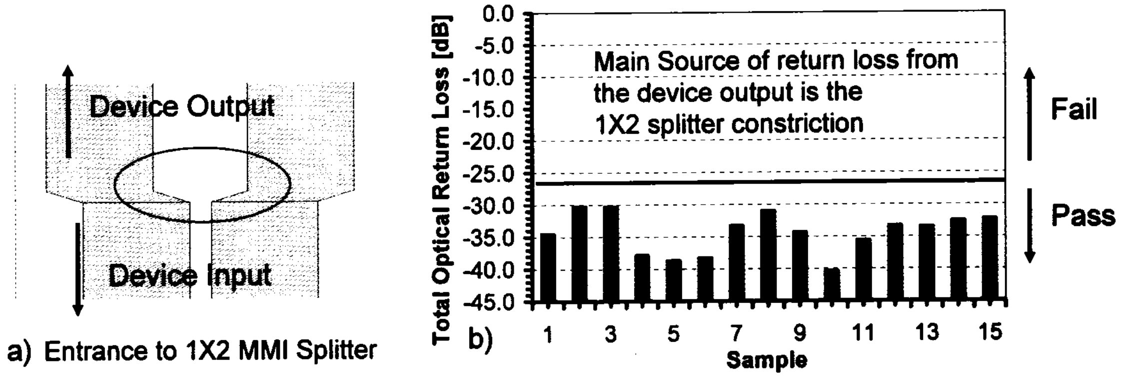

a) Entrance to 1X2 MMI Splitter

b)

Figure 2.63: ***a) Top View of the Input Access Waveguide to the Symmetric 1X2 MMI Splitter in the Modulator Design for Zero Chirp Applications, b) Integrated Optical Return Loss from the Zero Chirp Modulator Chip Design at the Transmission Minimum.***

The modulator design for chirped applications, shown in Figure 1.12, has an unused waveguide on the 2X2 MMI input splitter. When the modulator is in the transmission minimum off-state, any optical signal backwards propagated through the modulator will be imaged into this unused input waveguide. To prevent backreflections from the waveguide it has been terminated abruptly into the semiconductor mesa, in an extreme limit of a strong-to-weak guiding waveguide transition. Figure 2.64a demonstrates that no backreflection occurs from a strong-to-weak guiding waveguide transition, since sufficient forward propagating radiation modes are available to collect the strongly-guided waveguide mode. The electrical connection of the input waveguide to the semiconductor mesa is tolerable, due to the isolation provided by the helium implant discussed in Section 2.1.8 and the wet etch removal of the InGaAs contact layer. Note that Figure 2.64b indicates that a backreflection would be expected from a weak-to-strong guiding waveguide transition.

2.2.7 MMI Advances of Significance for Strongly-Guided Optical Modulators

Three significant advances in MMI design are reviewed in this Section. They are the butterfly MMI design, techniques for MMI length reduction, and MMI designs for tunable optical split ratios.

Butterfly MMI Design

Besse et al. [106] introduced a class of MMI couplers that rely on a shaped interference section to achieve freely selectable splitting ratios. They replaced the standard rectangular geometry of the interference section with two linear transformed sections of equal length. The first section is linearly down-tapered, the second linearly up-tapered, in what they define as a butterfly geometrical configuration. Ulrich [105] has previously shown that the

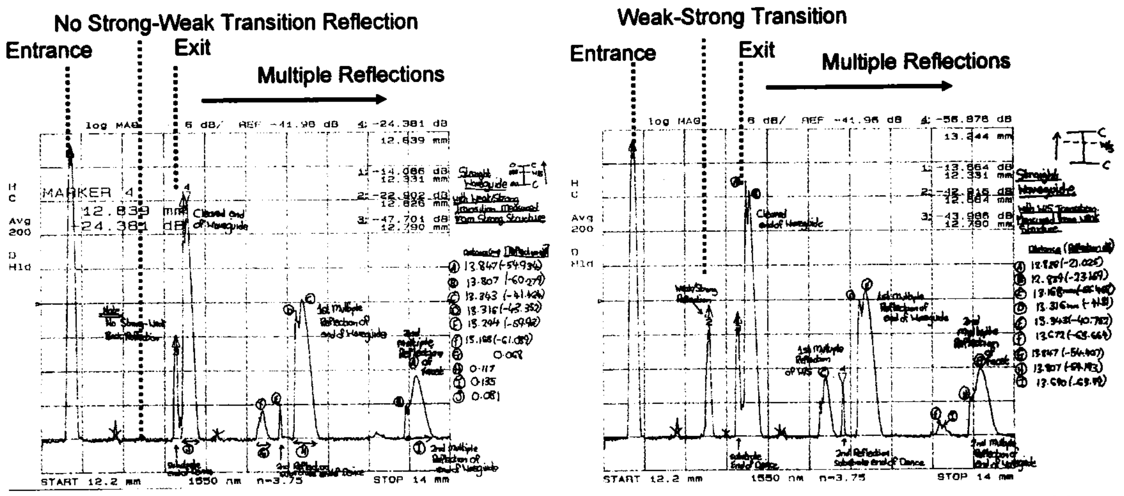

a) Strong-to-Weak Waveguide Transition b) Weak-to-Strong Waveguide Transition

Figure 2.64: ***a) OLCR Measurement of an Uncoated Straight Waveguide Containing an Abrupt Strong-to-Weak Guiding Waveguide Transition, b) OLCR Measurement of the same Waveguide in Reverse to Observe the Reflection from an Abrupt Weak-to-Strong Guiding Waveguide Transition.*** *Source: Ian Betty, M.Sc, Queen's University, 1998.*

self-imaging properties are preserved over a linear width transformation. The expression of MMI length L in terms of L_π remains unchanged in the butterfly MMI; however, L_π must now be expressed as,

$$L_\pi \cong \frac{4n_g W_{e0} W_{e1}}{3\lambda_0} \tag{2.24}$$

with W_{e0} and W_{e1} the effective widths of the MMI interference section at its input and its centre respectively.

The input and output of both MMI sections are now located on concentric circles as shown in Figure 2.65. The images after the first section are located on the curve O_0, however, the inputs to the second section are not co-incident, but located on the curve I_1. At the end of the first MMI section therefore, the optical wavefront must be propagated without lateral guiding from O_0 to I_1. The phase shift from this propagation is a continuous variable across the wavefront that depends on the position from the centre of the MMI.

Using the theory of multi-leg Mach-Zehnder interferometers Besse et al. have shown [106, 107] that the MMI splitting ratio can be evaluated from the geometrical path difference between O_0 and I_1 as a function of the normalized width variation $d\Omega = -\left(\frac{dW}{W_{e0}}\right) - \frac{1}{2}$. The cross-state output power for the butterfly MMI configuration is given by,

$$P_c \cong \cos^2\left(\frac{\pi d\Omega}{2}\right) \tag{2.25}$$

with the bar-state output power given by $P_b = 1 - P_c$.

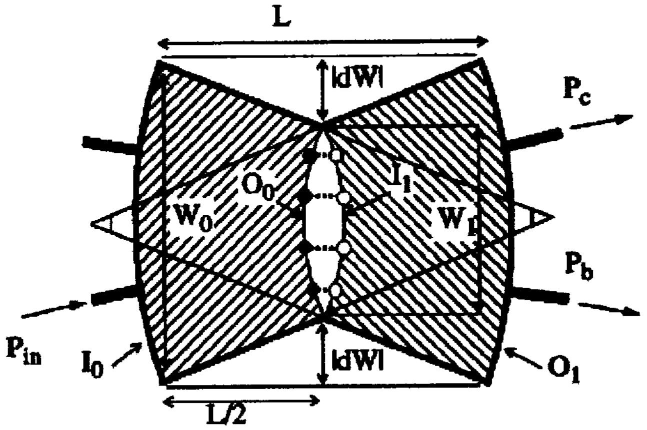

Figure 2.65: ***The Butterfly MMI*** Source: P.A. Besse et al., Journal of Lightwave Technology, Vol. 14, No. 10, pp.2286-2293, Oct. 1996.

In Figure 2.66 the optical split ratio[50] versus the butterfly waist constriction (W_0-W_1) is presented for a W_o=10.3μm 2X2 Butterfly MMI. In Figure 2.66a comparison is made between the analytic calculation given by Equation 2.25, three-dimensional TE semi-vectorial BPM simulations, and three experimental measurements with waist constrictions of 0.8μm, 0.6μm and 0.4μm. Good agreement is obtained. Figure 2.66b shows a X–Z BPM power contour map through the waveguide core for W_o=10.3μm, W_1=9.8μm, MMI Length=144.5μm, No=3.18, and λ=1545nm.

Butterfly MMI splitters and combiners are a convenient means of introducing the optical power imbalance in the modulator arms required to enable the chirped modulator designs introduced in Section 1.12.

MMI Length Reduction

Levy et al. have shown that the length of the interference section in a MMI can be reduced without impacting the output split ratio, if the MMI width is tapered along its length by a function having $dW/dz \approx 0$ at $L/2$ [109,110]. This functional form for the MMI width minimizes the phase change of the images at the centre of the MMI and, therefore, preserves the imaging properties along with the output split ratio. As in the case for the butterfly MMI, the decrease in average width leads to a reduction in the imaging length.

Levy et al. found a parabolic width taper yielded the largest length reduction [110]. The width taper is given by,

$$W(z) = W_{e1} + \frac{(W_{e0} - W_{e1})(L/2 - z)^2}{(L/2)^2} \tag{2.26}$$

---

[50] The optical split ratio defined as the cross-state TE_0 output power divided by the bar-state TE_0 output power.

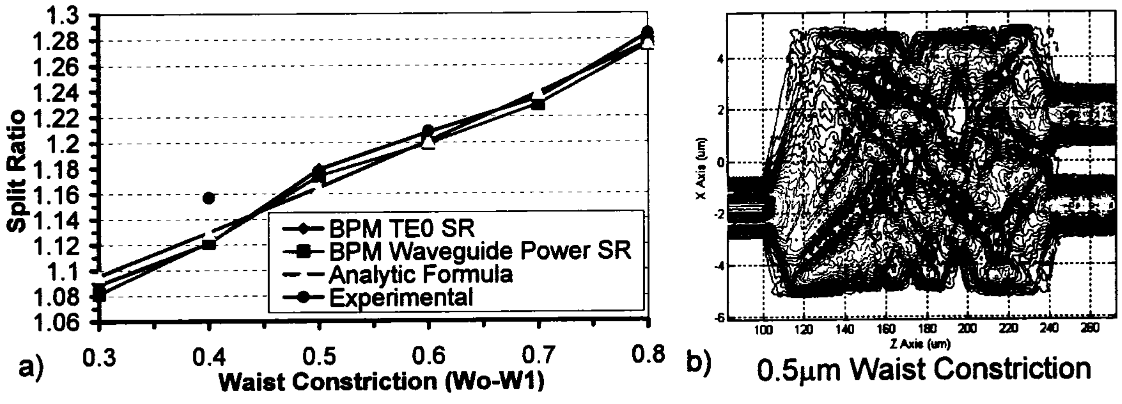

Figure 2.66: ***Optical Split Ratio versus the Waist Constriction in a W_o=10.3μm 2X2 Butterfly MMI: a) Comparison of Analytic Formula, 3D TE Semi-Vectorial BPM, and Experimental Data at 1548nm, b) X–Z 3D TE Semi-Vectorial BPM Power Contour Map through the Waveguide Core for W_o=10.3μm, W_1=9.8μm, MMI Length=144.5μm, No=3.18, and λ=1545nm.***

where z is the propagation direction, and W_{e0} and W_{e1} are the effective widths of the MMI interference section at its input and its centre respectively. L_π for this device is reduced by $1/\chi$ [110] where,

$$\chi = \frac{1}{2(1-d\Omega)^2(1+\gamma^2)} + \frac{\tan^{-1}(\gamma)}{2\gamma(1-d\Omega)^2} \tag{2.27}$$

for $\gamma^2 = W_{e0}/W_{e1} - 1$ and $d\Omega = 1 - W_{e1}/W_{e0}$. The access waveguides are tilted from the propagation axis by,

$$\theta = \tan^{-1}(4y \cdot d\Omega/L). \tag{2.28}$$

The local MMI width taper angle must remain shallow for the coupling between the modes to be negligible. Levy et al. have shown that above $d\Omega = 0.4$, where a factor of 2 reduction in the device length is achieved, the split ratio and excess loss start to become significantly impacted [109]. Themistos et al. [130] have demonstrated, using finite-element beam propagation simulations, that an untapered MMI structure exhibits better wavelength dependence, image quality, and fabrication tolerances.

The length of the <160μm long MMI structures in the current modulator design are not a limitation. This length reduction technique, therefore, adds little value to 1X2 and 2X2 MMI designs in strongly-guided waveguides.

Tunable MMI Design

Leuthold and Joyner have proposed a method to actively tune the power splitting ratio in a MMI [108]. This capability could be used to optimize the frequency chirp of a Mach-Zehnder modulator transmitter for a given fiber link [12, 42], or to compensate for manufacturing distributions in MMI split ratio imbalance. The approach used by Leuthold and

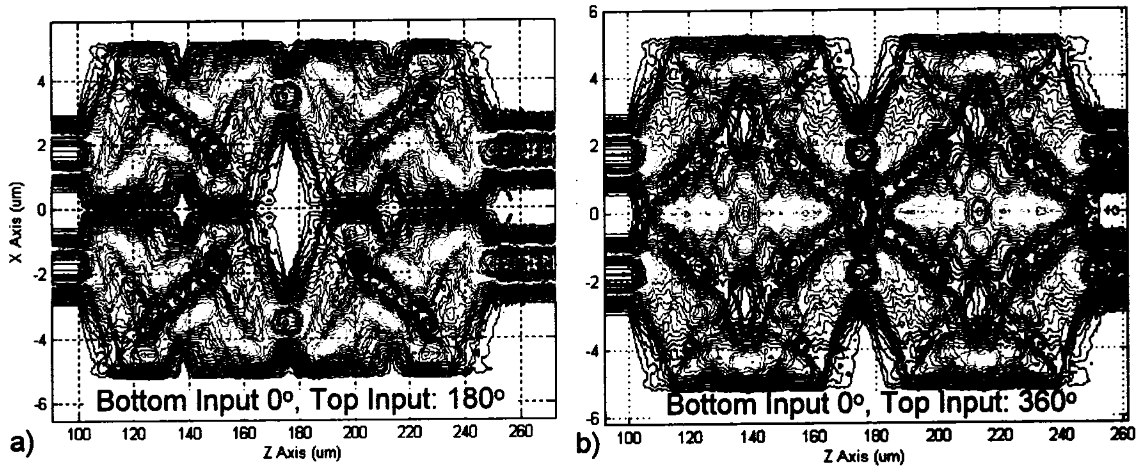

Figure 2.67: ***Dominant Self-Images in a 10.3μm Wide by 151μm Long 2X2 MMI with 2μm Wide Access Waveguides at 1545nm: a) Lower Waveguide Input with 0° Phase and Upper Waveguide Input with 180° Phase, b) Lower Waveguide Input with 0° Phase and Upper Waveguide Input with 360° Phase.***

Joyner requires the modification of the material index properties around spots in the MMI where the most dominant self-images appear.

For the 2X2 restricted interference MMI in the modulator design, the most dominant and simple self-imaging pattern occurs halfway along the propagation direction in the MMI as shown in Figure 2.67. To increase the cross-state output power P_c, the phase of images 2 and 3 must increase with respect to images 1 and 4, as is evident from Equation 2.25. For the butterfly MMI configuration defined in Section 2.2.7, the necessary phase changes are achieved by down and up taper transformations of the cross-sectional MMI width. Leuthold and Joyner have proposed actively achieving or supplementing these image phase changes by using localized refractive index changes in the region of the images at the centre of the MMI.

The MMI material refractive index can be reduced locally using the carrier-related plasma effects discussed in Section 2.1.7. The localization is achieved using patterned p-contact metalization on the top surface of the MMI with forward bias carrier injection into the core of the waveguide p-i-n diode junction. Leuthold and Joyner propose the use of a butterfly MMI to introduce a small split ratio asymmetry, which by edge biasing, can then be easily tuned towards the ideal 50:50 splitting ratio.

A refractive index change should ideally be confined with sub-micron precision to effectively isolate the phase change to a single image. Leuthold and Joyner experimentally found that the edge biased MMI had considerably better, although less efficient, tuning characteristics than the centre-biased MMI for their buried heterostructure waveguide. They attributed this to the leakage currents, which in the edge biased case flow through the InP cladding and reduce the tuning efficiency. In the centre-biased case the leakage currents flow to the MMI edges, such that with high carrier injection, the effective localized refractive index changes are reduced, leading to an observed saturation in the MMI optical split ratio change. This carrier spreading in the p-InP overclad layers can be minimized using the helium implantation process developed in Section 2.1.8.

Figure 2.68 provides BPM simulations for a tunable 10.3μmX151.5μm 2X2 MMI with edge biasing at 1545nm. Edge biasing was selected because it is an easier design to fabricate. The index change produced by carrier injection has been localized beneath the electrical contacts for these simulations. In Figure 2.68a the impact of contact width on the optical split ratio is presented for a 25μm long contact, assuming a -0.006 real refractive index change and no optical absorption in the core under the contact. The peak split ratio change occurs for a contact width around 2.5μm. In Figure 2.68b the contact width is now fixed at 2.6μm and the contact length is varied. The split ratio and TE_0 insertion loss are evaluated assuming a -0.005 real refractive index change and 20cm^{-1} of optical absorption in the core under the contact. The calculated split ratio is sub-linear with contact length. A contact length of 45μm has been selected as a good compromise between maximum split ratio and minimum TE_0 insertion loss. Figure 2.68c fixes the contact length at the optimal value of 45μm, and now varies both contact width in fine steps, and the real refractive index change in the core under the contact. The most efficient width for the contact is determined to be 2.3μm based on the maximum optical split ratio for a -0.01 change in the refractive index. In Figure 2.68d, a X–Z power contour map in the tunable MMI is shown with the optimal 2.3μm wide by 45μm long contacts superimposed.

In Figure 2.69, the experimentally measured split ratio and insertion loss are given for the tunable MMI in Figure 2.68d. This device uses the helium implantation process developed in Section 2.1.8 to localize the forward bias carrier injection. A split ratio >2.5 can be obtained, indicating a refractive index of >-0.006, with a forward bias current injection of <10mA[51]. Leuthold and Joyner have demonstrated a split ratio of 1.5 for 40mA of current injection [108] with unspecified optical losses. The results in Figure 2.69 are the best reported to date for a tunable MMI. The tunable MMI can be used for the split and combine function in Figure 1.15 to implement a controllable negative chirp modulator. The tunable MMI can also simplify a nested modulator design we have proposed to enable fully configurable chirp [59].

2.3 Waveguide Bends in the Strongly-Guided Waveguide Designs

In this Section bends in optical waveguides are studied in the context of a strongly-guided waveguide design. Bending losses, transition losses, curve options for s-bends, general approaches to optical path design, and the matched bend design concept are reviewed. Measured losses through strongly-guided waveguide bends are provided and options for waveguide bends in the Mach-Zehnder modulator are studied using BPM models.

---

[51] The applied voltage is <1.7V.

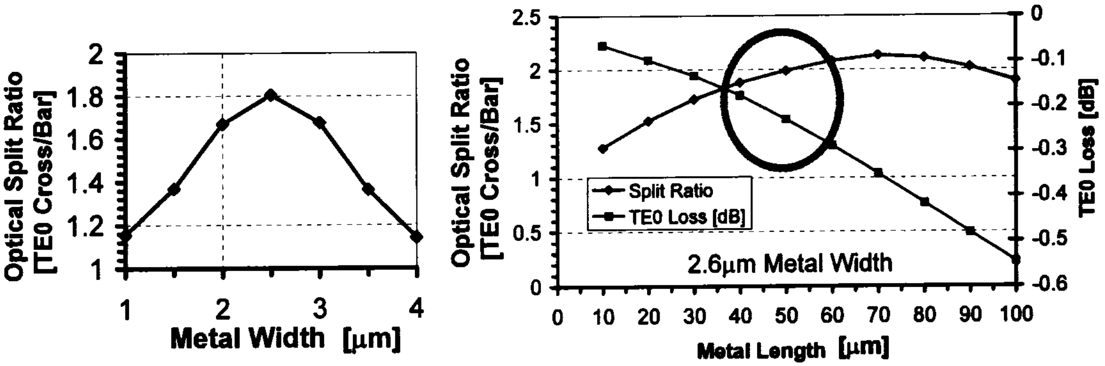

a) -0.006 Index Change, No Absorption
25um Long electrode

b) -0.005 real index change, 20cm^{-1} absorption

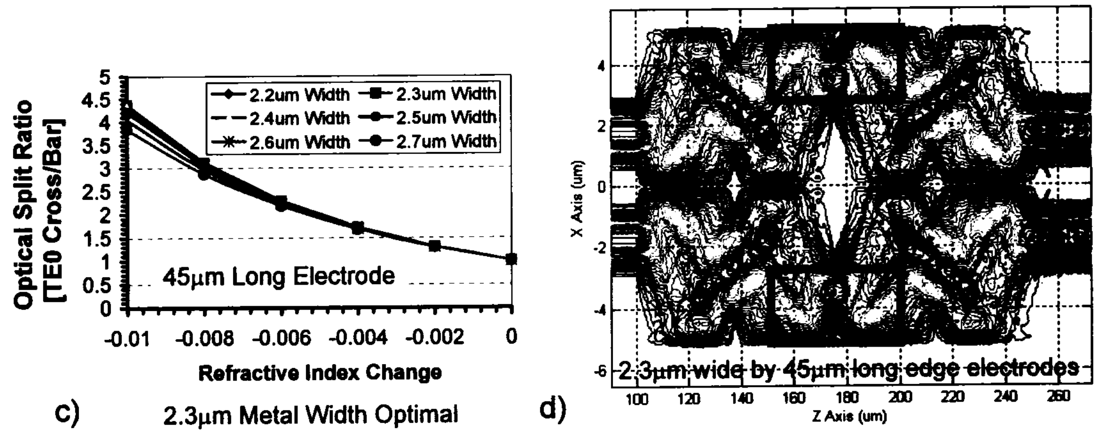

c) 2.3μm Metal Width Optimal

d)

Figure 2.68: *3D TE Semi-Vectorial BPM Simulations [1545nm, No=3.18] for a Tunable 10.3μmX151.5μm 2X2 MMI with Edge Biasing. The Index Change Produced by Carrier Injection has been Localized Beneath the Electrical Contacts. a) Impact of Contact Width on Optical Split Ratio for 25μm Long Contacts, b) Impact of Contact Length on Optical Split Ratio and Insertion Loss for 2.6μm Wide Contacts, c) Fine Optimization of Contact Width for the Optimal 45μm Long Contacts, d) X–Z Power Contour Map of the Tunable MMI Superimposed with the Optimal 2.3μm Wide by 45μm Long Contacts.*

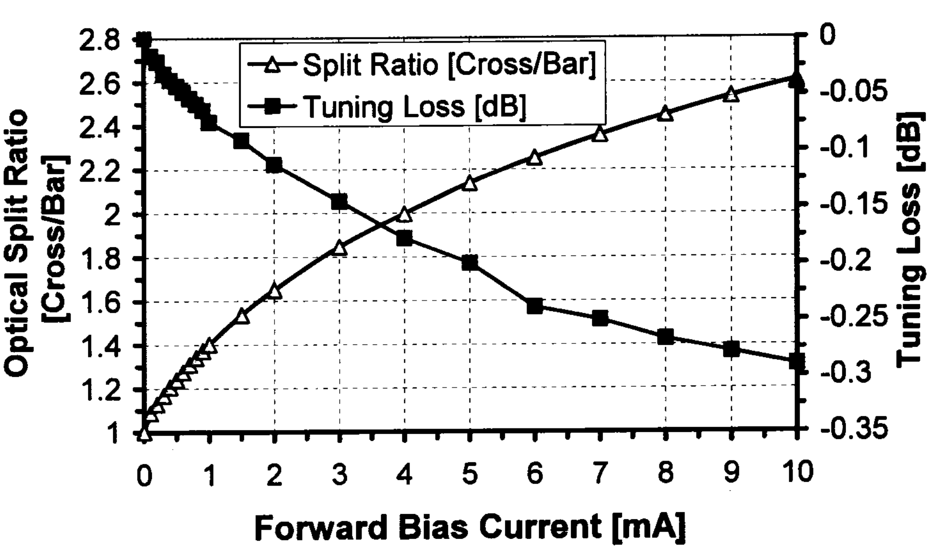

Figure 2.69: ***Measurement of the Optical Split Ratio and Insertion Loss for a Tunable 2X2 Butterfly MMI under Forward Bias with Implantation to Localize Carrier Concentrations.***

2.3.1 Bending Loss

The first theoretical paper on bends in optical dielectric guides was published in 1969 by Marcatili [147]. A simple framework for understanding bending loss was later introduced in 1975 by Heiblum and Harris [140] using conformal transformations to derive an equivalent index profile for the waveguide bend. The first order approximation to the exact equivalent index distribution obtained with their conformal transformation showed that if $n(x)$ defines the refractive index of the waveguide, then a bent waveguide with radius R behaves like a straight waveguide with a refractive index profile,

$$n_{eq}^2(x) = n^2(x)\left(1 + \frac{2x}{R}\right), \; x \ll R. \tag{2.29}$$

One consequence of this simple description of the waveguide refractive index profile is that every mode traveling around the bend must radiate energy. If the wavefront is to remain plane it must travel faster as it moves away from the centre of curvature, and at some point it must exceed the speed of light. The locus of this point is known as the radiation caustic. Beyond the radiation caustic the phase front must become curved and the field radiates away in the lateral direction. The radiation caustic moves closer to the waveguide as the radius of curvature diminishes and stronger loss is, therefore, to be expected. Bending loss is, therefore, the continuous radiation of mode power tangentially out of a curved waveguide as light travels around the bend. The radiation caustic is located far from the edge of the waveguide mode in a strongly-guided structure, therefore, pure bending losses are not a very significant issue in strongly-guided waveguides.

Obtaining a quantitative estimate for the bending loss is not a simple task. The two most commonly used expressions for the attenuation coefficient α were derived by Marcatili [147] and Marcuse [145]. These expressions are in quantitative agreement. For a single-mode step-index slab waveguide Marcatili gives α as,

$$\alpha(R) = C_1 \exp^{-C_2 R} \tag{2.30}$$

where the parameters C_1 and C_2 are independent of the bend radius R, but are functions of the guiding characteristics of the straight waveguide. The weakly-guiding simplification given for α by Marcuse [146] is,

$$\alpha = \frac{1}{kn_{eff}\rho^2} \frac{U^2 W^2}{(1+2W)V^2} \exp(2W) \exp\left(-\frac{4W^3 \Delta R}{3V^2 \rho}\right) \tag{2.31}$$

where the various symbols have the following expressions:

$$\begin{aligned}
\Delta &= \frac{n_{core}^2 - n_{clad}^2}{2n_{core}^2} && (2.32)\\
V &= k_0 \rho \, n_{core} \sqrt{2\Delta} && (2.33)\\
U &= k_0 \rho \sqrt{n_{core}^2 - n_{eff}^2} && (2.34)\\
W &= k_0 \rho \sqrt{n_{eff}^2 - n_{clad}^2} && (2.35)\\
& && (2.36)
\end{aligned}$$

and where k_0 is the free space wavenumber with ρ the waveguide core half-width. The obvious consequence of these results is that the loss decreases for decreasing curvature $(1/R)$ and the loss also decreases as the waveguide half-width increases.

Marcuse's expression for α would suggest increasing the waveguide width as the bend radius decreases. When the curvature is large however, it is not generally desirable to let the width 2ρ be large, for the effective width of the fundamental mode then becomes correspondingly large, and the bend supports many unwanted modes. Very long transitions are then required in order to excite efficiently only the fundamental mode. For this reason, bends with large width waveguides are seldom used, even though they are known to have lower loss [167].

Given the index distribution in a bend, the mode profile will shift to the outer edge of the waveguide as the bending radius is decreased. If a sufficiently small bending radius is chosen, the field strength at the inner edge vanishes and the mode will be fully guided by the outer edge, and the location of the inner edge becomes irrelevant. Such a mode is called a Whispering Gallery Mode after Lord Rayleigh who explained this phenomenon in relation to the propagation of sound waves along a curved gallery.

2.3.2 Transition Loss

When two waveguides of different radii of curvature and/or structure are connected to each other, the propagating mode supported by one waveguide transforms to every possible mode of the other waveguide at the junction. The radiation loss due to the lowest order mode field mismatch[52] at the discontinuity is looked on as the transition loss. The transmission coefficient of the power through the junction can be easily obtained from the overlap of the field profiles for the lowest order modes of the two connected waveguides.

This transition loss may be reduced by changing the curvature in a gradual manner or, as proposed by Neumann [143], laterally offsetting[53] the waveguide sections so as to reduce the overlap mode mismatch across the junction. Neumann used an approximation derived by Gambling [144] for the displacement d between the beam axis and the waveguide axis:

$$d = \frac{\pi^2 n_{\text{eff}}^2 \omega_0^4}{\lambda_0^2 R} \tag{2.37}$$

where n_{eff}, ω_0, λ_0 and R are the effective index of the fundamental waveguide mode, the mode waist, the vacuum wavelength and the bend radius of curvature respectively. Equation 2.37 reveals that the transition loss decreases monotonically with increasing bend radius and decreases dramatically with decreasing mode waist.[54] As shown in Figure 2.21, strongly-guided waveguides are practically limited to widths greater than 1.5μm to prevent significant sidewall scattering losses. The offset of the field maxima causing a change in the field tail overlap with the sidewall imperfections should be taken into account when determining the "effective ridge width" for sidewall scattering losses. Kitoh [142] confirmed Equation 2.37 for Silica-based waveguides and showed the loss characteristic of a S-shaped waveguide was insensitive to the wavelength when the optimal offset was used.

Because the amplitude distribution at a bent waveguide section is slightly asymmetric, a perfect match between the fields of the modes on two waveguide sections with different curvature cannot be achieved by simply offsetting the sections. Since the field deformation caused by the bend has a less significant impact on transition loss than the field offset, transition loss can be substantially reduced by the lateral offset method. Pennings [162] showed that an even better match is possible if not only the position of the straight waveguide, but also its width, is optimized.

It has been shown by numerical computation that the optimized offset for eliminating the first-order mode excitation is different from that for minimizing transition losses [166]. Hirono [136] obtained an equation for the offset to minimize the first order mode excitation using a perturbation method to first order in $\left(\frac{1}{R}\right)$, assuming that R is much greater than both the waveguide width, and the widths of the fundamental and first-order modes in both waveguides. Hirono also assumed that the refractive index profile of the waveguide is a symmetric 2D structure and provided comparisons with overlap calculations. The offset he obtained for both the TE and TM modes is:

$$\delta = \frac{1}{k_0^2 (n_{\text{eff},0} - n_{\text{eff},1})^2} \left(\frac{1}{R}\right). \tag{2.38}$$

---

[52] This is due to differing degrees of mode field peak shift and deformation.

[53] As the field maxima in the curved section is located closer to the outer waveguide edge it makes sense to laterally offset the straight input waveguide in order to get a better match between the field profiles.

[54] Figure 2.33 shows that the mode waist is directly proportional to the waveguide width.

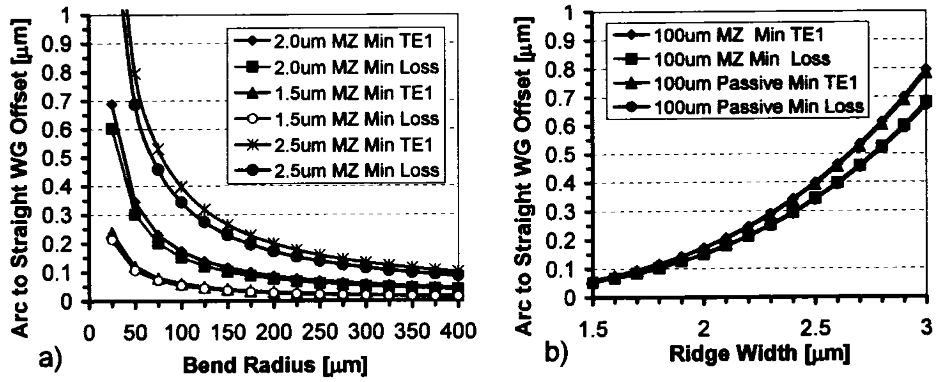

Figure 2.70: ***Calculated Offsets Required to Minimize the Transition Loss and the First Order Mode Excitation at a Straight-to-Curved Waveguide Junction: a) Offsets versus Bend Radius for 1.5µm, 2.0µm, and 2.5µm Ridge Widths in the Modulator Structure at 1546nm; b) Offsets versus Ridge Width for a 100µm Bend Radius in the Modulator and Passive Waveguide Structures at 1546nm.***

Figure 2.70a presents, for the modulator and passive waveguide structures, the calculated[55] offsets required to minimize the transition loss and the first order mode excitation at the straight-to-curved waveguide junction, as a function of the curved waveguide bend radius and the waveguide width. Almost identical offset requirements are obtained for the modulator and passive waveguide structures, along with the expected strong dependence on the ridge width. Note that these calculations show offsets that can be on the same order as the lithographical tolerance of i-line stepper lithography.

2.3.3 Curve Options for S-Bend Transitions

There are three simple waveguide configurations for a s-bend with a lateral offset h and a length l:

1. An s-curve made of two circular arcs with a constant radius of curvature: $R = \pm\frac{L^2}{4h}\left(1+\frac{h^2}{L^2}\right)$.

2. A cosine-based s-curve described by $x(z) = \frac{h}{2}\left[1-\cos\left(\frac{\pi}{L}z\right)\right]$. Marcuse [137] introduced the use of the raised cosine as a transition function in 1978 and Ramaswamy [138] experimentally demonstrated low-loss for the first time with this function in 1981.

3. A sin-based s-curve where the centre of the waveguide is defined by $x(z) = \frac{h}{L}z - \frac{h}{2\pi}\sin\left(\frac{2\pi}{L}z\right)$. For a given (x,z) point on the curve centre line the upper waveguide boundary is given by $(x+dx, z-dz)$ and the lower waveguide boundary is given by

---

[55] Calculations are made using the Effective Index Method.

$(x-dx, z+dz)$ where,

$$dx = \frac{W}{2}\cos(\theta) \tag{2.39}$$

$$dz = \frac{W}{2}\sin(\theta) \tag{2.40}$$

$$\theta = \tan^{-1}\left(\frac{h}{L} - \frac{h}{L}\cos\left(\frac{2\pi}{L}z\right)\right). \tag{2.41}$$

This form for the waveguide boundaries ensures the waveguide width will remain constant at all transverse planes within the s-bend.

Minford [139] introduced this transition curve, having no discontinuities in the first and second spatial derivatives, to minimize losses due to curvature reversals and straight-to-curved waveguide transitions. Rolland et al. [158] experimentally demonstrated negligible loss for a sin-based s-curve in a strongly-guided GaAs/AlGaAs rib waveguide having a 10μm lateral offset h and a s-bend length of 100μm. They also obtained good correspondence between the experimental loss measurements and theoretical loss calculations for s-bend lengths between 25μm and 200μm.

Under the assumption of $\frac{h}{L} \ll 1$ the curvature variations along the three different S-curves are respectively,

$$K_1 = \frac{1}{R_1} = \pm\left[\frac{L^2}{4h}\left(1+\frac{h^2}{L^2}\right)\right]^{-1} \tag{2.42}$$

$$K_2(z) = \frac{1}{R_2(z)} = \frac{2\pi h}{L^2}\sin\left(\frac{2\pi z}{L}\right) \tag{2.43}$$

$$K_3(z) = \frac{1}{R_3(z)} = \frac{\pi^2 h}{2L^2}\cos\left(\frac{\pi z}{L}\right). \tag{2.44}$$

(2.45)

Note the maximum curvature of the sin-based transition is $\frac{4}{\pi}$ greater than maximum curvature of the cosine-based transition.

The total insertion loss for a s-bend is comprised of both the curvature loss and the transition loss at the straight-to-curved or curvature reversal transition. Figure 2.71a shows the three different s-bend curves for a h=10μm offset, $l = 100\mu$m s-bend length, and a waveguide width of 2.0μm. In Figure 2.71b, the variation in curvature $\frac{1}{R}$ along the length of the three s-bend transitions is given. In Figure 2.71c, the instantaneous maximum bend radii for the cosine-based and sin-based s-bends are shown as a function of bend length l for the fixed offset h=10μm.

In Figure 2.71b, the cosine-based s-bend has discontinuous curvature at the entrance and exit ends of the bend, with the curvature varying monotonically towards the midpoint. Finite transition loss is, therefore, expected at the entrance and exit of the cosine-based s-bend. Although not explicitly discussed in the literature, these transition losses could

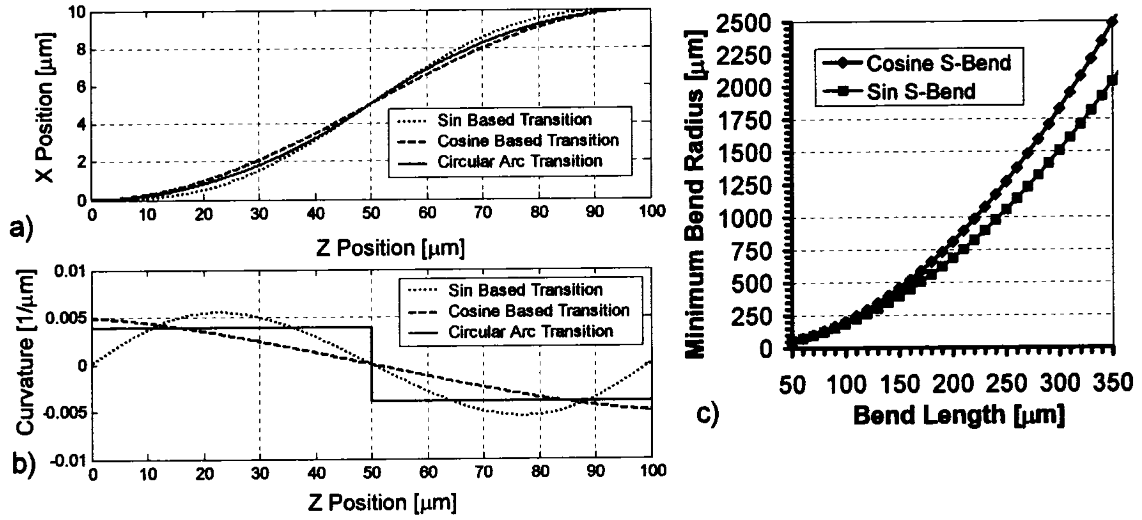

Figure 2.71: *a) Comparison of Circular Arc, Sin, and Cosine Based S-Bend Transitions for a 10µm Offset in a 100µm Length, b) Variation in Curvature $\frac{1}{R}$ along the Length of the Circular Arc, Sin, and Cosine Based S-Bend Transitions, c) Instantaneous Minimum Bend Radius for the Sin and Cosine Based S-Bend Transitions, as a function of Bend Length l, with Fixed Offset h=10µm.*

be minimized using a lateral offset at the straight-to-curved waveguide junction. A.M. Shajakhan and Sheel Anditya have proposed [141] the use of lateral offsets to minimize the straight-to-curve transition loss with slope-matched sin-based and cosine-based s-bends to inclined optical waveguides.

In Figure 2.71b, the sin-based s-bend, by comparison, has zero curvature at the entrance and exit ends, and at the midpoint, so lateral offsets are not required. However, the sin-based s-bend can potentially suffer from greater bending losses than the cosine-based s-bend due to its larger maximum instantaneous curvature for a given transition length[56]. Nadler et al. [168] have proposed the use of a sin-based s-bend as an adiabatic curvature transition connection between a straight waveguide and a circular arc. Kominato et al. [169] have demonstrated a clothoid curve connection for the desired adiabatic transition between a straight waveguide and a circular arc.

Of the three s-bend designs in Figure 2.71b, the s-bend with two circular arcs will have the highest transition loss at the midpoint due to an abrupt curvature reversal. Lateral offsets are definitely required at the midpoint for low-loss circular arc transitions.

From the above analysis, it is clear that for a strongly-guided waveguide, where the bending losses are negligible, a sin-based s-bend transition is the desirable choice since it minimizes both the transition losses and the excitation of the higher-order modes in the bend at the straight-to-curved transition. The greater maximum instantaneous curvature for the

---

[56] Curvature loss α has an inverse exponential dependence on the radius of curvature $\alpha(R) = C_1 \exp^{-C_2 R}$ where C_1 and C_2 depend on the waveguide characteristics only (independent of R).

sin-based s-bend, in comparison with the cosine-based s-bend transition, is of no practical relevance. In an extreme limit of the design space, where the difference in maximum bend radius is significant, it is possible to use lateral offsets at the straight-to-curved transition for a cosine-based s-bend. From Figure 2.71c and Figure 2.70, the appropriate offset can be determined[57]. It is also possible to use the concept of the matched bend with a cosine-based or sin-based s-bend, as shown in Section 2.3.7.

For a weakly-guided waveguide, the literature consensus is that the bending loss of the sin-based s-bend is more significant than the transition losses, so a cosine-based s-bend transition curve is recommended [159, 170].

2.3.4 General Approaches to Optical Path Design

There have been several attempts in the literature to reduce the optical loss in waveguide s-bends by allowing arbitrary curved functional forms for the waveguide geometry. Baets and Lagasse [172] derived a suboptimal S shape for a lateral offset bend by minimizing the pure bending loss. This approach, however, ignored the impact of the transition loss. Lerner [173] revisited the work of Baets and Lagasse by including independent minimization of the transition loss, through offsets between sections of waveguide with different curvatures. Mustieles et al. [174] furthered the analysis of pure bending loss, by considering the more general Marcuse expression for attenuation[58] as a function of radius, when deriving their analytic expression for the optimal profile to minimize the pure bending loss. Finally, in 1995 Ladouceur and Labeye [171] introduced a general approach to optical waveguide design. In [171] a general polynomial family of curves (p-curves) is proposed to link two arbitrary points on the optical circuit. The slope and curvature at both arbitrary points are fixed to minimize the transition loss, while a free variable remains to minimize the bending loss. Kumar and Aditya [170] have theoretically compared the optimal p-curve bend designs, with the well know sin-based and cosine-based bend designs, for a typical weakly-guided silica-based waveguide. They conclude that a p-curve bend design with a variable width waveguide is a marginal improvement over a cosine-based bend design.

All these general approaches to optical path design add little value[59] in strongly-guided waveguide structures, relative to a sin-based s-bend, since the contribution of pure bending loss is generally negligible, as discussed in Section 2.3.1.

---

[57] Figure 2.71c can be used since the smallest bend radius occurs at the straight-to-curved waveguide transition.

[58] The Marcuse expression used by Mustieles et al. is given in Equation 2.30

[59] They do, however, add great complexity.

2.3.5 Matched Bend Theory

Melloni et al. [135] have recently presented an effective method for determining bend mode characteristics, based on the expansion of the bend modes into modes of the straight waveguide. They show [133, 134] that when the bend length of a circular arc is an integer multiple of the beat length for the first two bend modes, the transition loss will vanish, and the output field will propagate unaffected in the output straight waveguide. They have termed a bend designed according to this criterion a matched bend. They claim that the matched bend offers superior performance relative to the more traditional approach of laterally offsetting the straight-to-bend waveguide transition as detailed in Section 2.3.2.

2.3.6 Measured Losses in Strongly-Guided Bends

The literature covering optical bend losses is almost exclusively limited to weakly-guided waveguide structures. A significant reference from 1995, by Spiekman et al. [151], aims to answer the question of whether ultra-small strongly-guided waveguide bends could match the size of a corner mirror but improve upon their insertion loss. The waveguide structure used in the study was an InGaAsP/InP strongly-guided waveguide, containing a 0.6μm thick core having a composition of Q=1.3μm. The ridge width was chosen as 1.4μm to cut-off the first order lateral mode. No lateral offsets were introduced at straight to circular arc waveguide transitions. An excess loss of $\approx$0.3dB per 90° bend was obtained for a 50μm bend radius. For a 100μm bend radius the excess loss was not resolvable within their 0.2dB measurement error.

Figure 2.72 provides my measured insertion loss at 1550nm in 90° circular arc bends, as a function of radius (r) and offset (d), in the 2.0μm wide passive waveguide structure given in Figure 2.6b. These measurements were performed using the same Fabry-Perot loss measurement method discussed in Section 2.1.6. The waveguides were defined using 5X i-line stepper based photolithography and they were etched using the CO_2:CH_4:H_2 RIE etch shown in Figure 2.11. In Figure 2.72a, the excess loss for a 90° bend with a 50μm bend radius, is shown to be as low as 0.3dB, for a 0.2μm lateral waveguide offset at the straight to circular arc waveguide transitions. In Figure 2.72b, the excess loss for a 90° bend with a 100μm bend radius, is shown to be as low as 0.05dB, for a 0.1μm lateral waveguide offset. These excess loss results are as good as those obtained in [151], however, very narrow waveguide widths were not required. The total insertion loss of these bends will be significantly less than those in [151] since the straight waveguide loss is 1.7dB/cm rather than 6.6dB/cm.

An offset of 0.3μm for the 50μm radius bends, and an offset of 0.15μm for the 100μm bend radius, are predicted by Figure 2.70a. Figure 2.70a uses the effective index method for the calculation of the required modal properties. The properties from the two-dimensional finite-difference mode calculations in Table 2.2, averaged for operation at 1550nm, give a N_{eff} of 3.201845 and a mode field σ_x of 0.727μm. Using these parameters in Equation 2.37

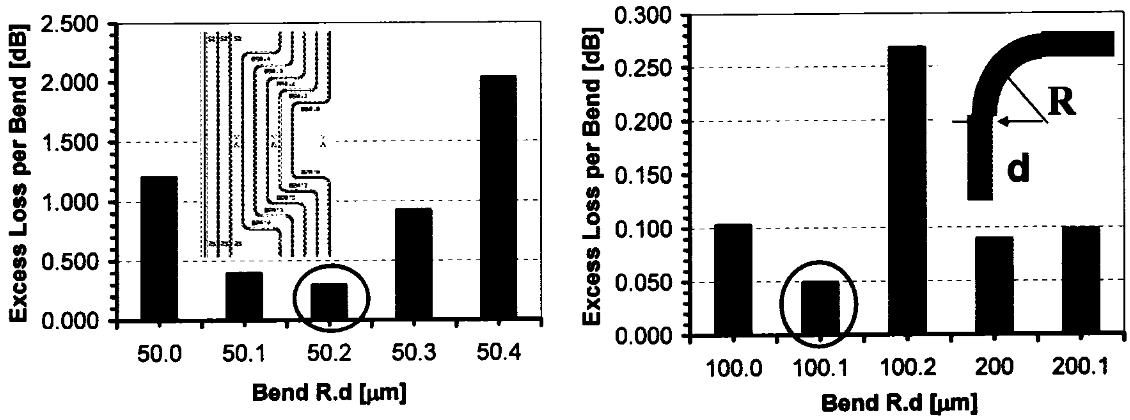

Figure 2.72: *Loss Measured by the Fabry-Perot Method in 90° Circular Arc Bends as a Function of Radius (R) and Offset (d) in the 2.0µm Wide Passive Waveguide Structure. The Lowest Loss Offsets are Circled and the Waveguide Layout Tested is given in the Insert.*

predicts an offset of 0.23µm for the 50µm radius bends, and an offset of 0.12µm for the 100µm bend radius. These calculations are more consistent with the experimental data in Figure 2.72. The use of the effective index modal parameters overestimates the required offset.

Figure 2.73 shows the poor bend loss results originally obtained using contact photolithography. The semiconductor etch process used for the results in Figure 2.73 is identical with the etch process used for the results in Figure 2.72. Figure 2.73c indicates that the losses actually increase with increasing radius, and that the different bend offset designs are poorly resolved within the data set. Figure 2.73b shows that the contact lithography process produces poor bend edge acuity relative to the 5X i-line stepper based lithography process given in Figure 2.73a. The proposed explanation for the results in Figure 2.73c is simply that additional scattering losses in the longer bends, due to poor edge acuity, accumulate, and result in greater excess losses.

C. van Dam et al. [154] have demonstrated, and Wayne W. Lui et al. [155] have theoretically verified, that polarization converters can be based on ultra short bends using very narrow (1.4µm) deeply-etched waveguides. It has, however, been experimentally verified that no polarization rotation occurs in the 50µm 90° bend test structure given in Figure 2.72. In Figure 2.74 the polarization extinction was also studied as a function of wavelength, for a s-bend waveguide representative of the requirement in the modulator application, and no polarization rotation was observed.

2.3.7 Waveguide Bends in the Mach-Zehnder Modulator

It is necessary to introduce s-bends, following the MMI splitter, and therefore also prior to the MMI combiner, in order to increase the separation between the modulator waveguide

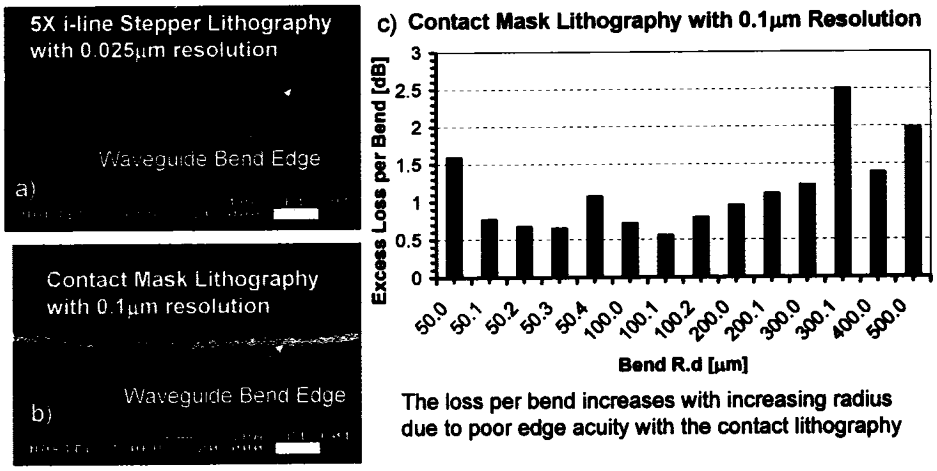

The loss per bend increases with increasing radius due to poor edge acuity with the contact lithography

Figure 2.73: *Edge Acuity on a 90° Circular Arc Waveguide Bend: Stepper Lithography shown in (a) versus Contact Lithography shown in (b). In c) the Loss Measured by the Fabry-Perot Method in 90° Circular Arc Bends defined by Contact Lithography is given as a Function of Bend Radius.*

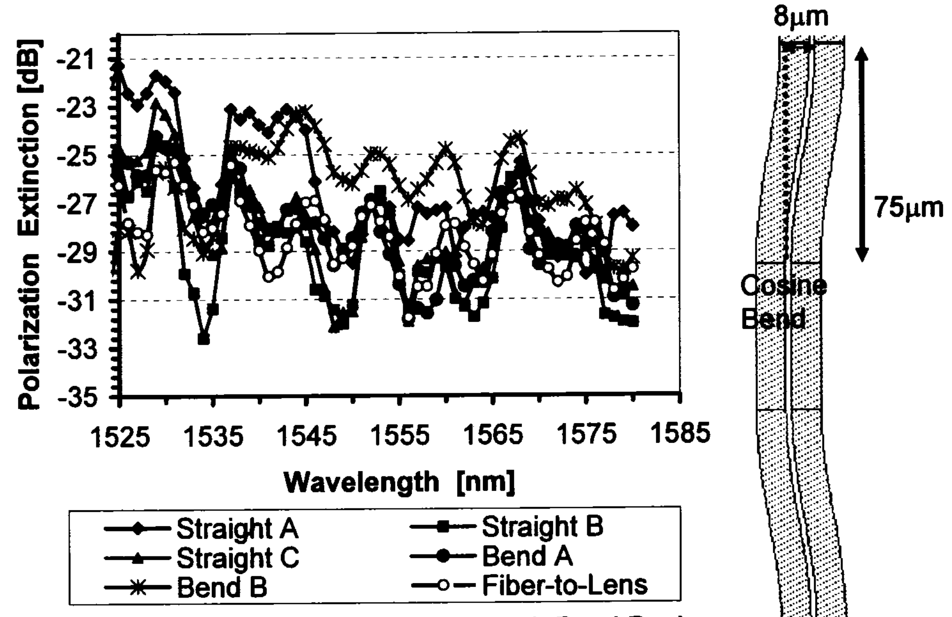

Cosine Bend is repeated 18 times in each Bend Device

Figure 2.74: *Measured Polarization Rotation through Eighteen 75μm Long Cosine-Based S-Bends with 8μm Offsets in the 2.0μm Wide Modulator Structure [No Optical Mode Spot-Size Mode Converters at the Input and Output Facets.] Each S-Bend is Separated by 50μm of Straight Waveguide. Straight Waveguide and Fiber-to-Lens References for Polarization Rotation are also Provided.*

arms. This is required to reduce the radio frequency (RF) coupling between the high speed modulation electrodes present on each modulator arm waveguide. The selected separation for the Mach-Zehnder modulator arms is 20μm between waveguide centres.

Only passing reference to the impact of the s-bends leading into and out of a MMI is given in the MMI literature. Mention is often given of low radiation losses, however, the possibility of higher order waveguide modes being excited in the bends is not addressed. Several authors [131,152] have reduced the access waveguides below the cut-off for the TE_1 mode, which is typically less than 1.5μm wide, prior to the s-bends leading to the MMI. These narrow access waveguides address the issue of higher order mode excitation in the bends, however, they also required very narrow MMI devices in order to have reasonable operating and fabrication tolerances. This design direction tends to lead to "hero-like" MMI dimensions[60]. The problem is that expensive E-beam lithography is required to fabricate the devices and the losses to date are not acceptable for a practical device.

Masanovic et al. [132] have proposed a cascaded 1X2 MMI design to increase the separation between the output waveguides of a splitter without introducing s-bends. This approach, although useful for weakly-guided waveguides, is longer than a MMI and s-bend together in a strongly-guided waveguide. It also requires the insertion loss of three MMI elements.

A TE semi-vectorial, three-dimensional, finite-difference beam propagation method, using PML boundary conditions, has been used to study the impact of s-bends following the MMI splitter, on the TE_0 spectral purity in the modulator arms. The preferred 10.3μm wide paired 2X2 MMI design without width tapered access waveguides, detailed in Section 2.2.3, is used for the MMI splitter. The BPM setup conditions and the simulation space used for all these calculations are identical to those used for the paired interference 2X2 MMI in Section 2.2.3.

In Figure 2.75a the impact of the s-bend length and functional form, on the total TE_0 and waveguide power insertion losses, are studied at 1545nm. As expected the total waveguide power loss is low for both functional forms of bend at all bending lengths; the pure bending loss is almost negligible in strongly-guided waveguide structures. The superior performance for the sin-based s-bend is evident in the TE_0 insertion loss parameter as a function of bend length. For bend lengths in excess of 100μm the TE_0 insertion loss is identical to the total waveguide power insertion loss. The curvature mismatch at the straight-to-bend transitions in the cosine-based bend, strongly excites the first order bend mode, and therefore invokes a matched bend phenomena at various bend lengths, similar to that discussed in Section 2.3.5. The TE_0 insertion loss variation with bend length continues to oscillate for all bend length in these simulations. TE_0 matched cosine-based s-bends are available for bend lengths of 65μm, 90μm and 110μm. It would not be straightforward to derive the TE_0 matched bend length for either the cosine-based or sin-based s-bends as has been done by Melloni [134] for circular arcs, since the bend radius varies continu-

---

[60] The adiabatic taper lengths required to reduce the access waveguides widths to these narrow dimensions is often not taken in account when listing the required dimensions to implement these structures.

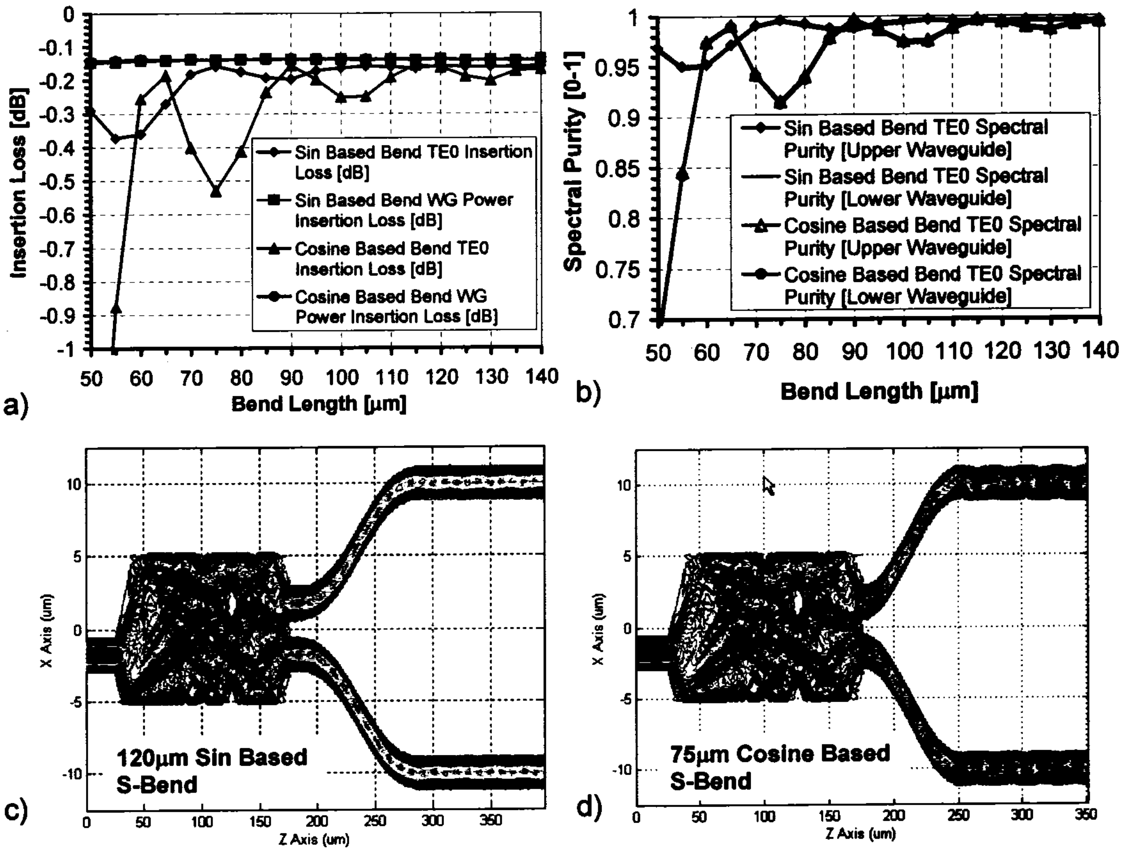

Figure 2.75: ***S-Bends Following the MMI Splitter: The Impact of the S-Bend Length And Functional Form, on the Total TE_0 and Waveguide Power Insertion Losses at 1545nm.***

ously along the length of the bend. In Figure 2.75b these TE_0 losses are expressed in terms of the TE_0 spectral purity in the modulator arm waveguides following the s-bends. Figure 2.75c shows the X–Z power contour map through the waveguide core (y=0) with a 120μm long sin-based s-bend following the MMI. No excitation of the TE_1 mode is evident. Figure 2.75d provides the same output as Figure 2.75c for a 75μm long cosine-based s-bend following the MMI. This cosine-based s-bend length corresponds to a local maxima for the excitation of the TE_1 mode.

Figure 2.76 demonstrates, for a 65μm long cosine-based s-bend, that the TE_0 bend match condition is maintained for all wavelengths within the bandwidth of the MMI. Figure 2.77 shows, for a 75μm long cosine-based s-bend, good TE_0 spectral purity in the modulator arms can be obtained by offsetting the straight-to-bend transitions[61], as discussed in Section 2.3.2. Optimal TE_0 spectral purity is obtained using an offset between 0.1μm and 0.15μm. This increases the width in the gap between the MMI output access waveguides by at least 0.2μm. The 75μm cosine-based s-bend with a 8.25μm lateral offset, used in

---

[61] The MMI exit to bend entrance is also a straight-to-bend transition.

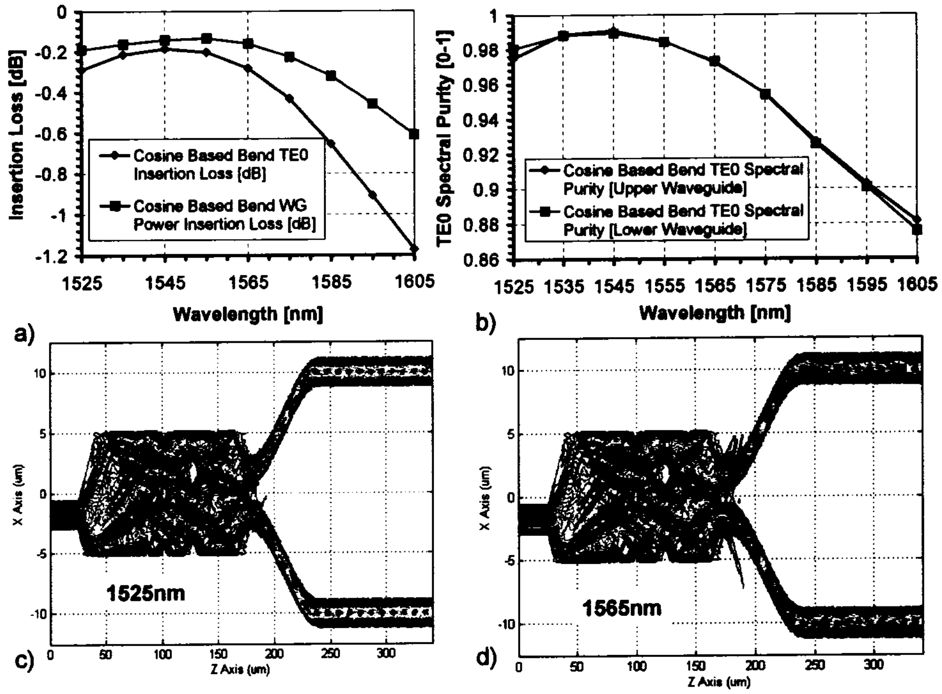

Figure 2.76: ***Over Wavelength Performance of a Matched 65μm Long Cosine-Based S-Bend Following the MMI Splitter.***

Figure 2.77, has a calculated minimum bend radius of 139μm. As shown in Figure 2.71a this minimum bend radius occurs at the straight-to-bend transitions. Figure 2.70a predicts an offset of ≈ 0.13μm to minimize the TE_1 excitation through a circular arc with a 139μm bend radius, consistent with these BPM simulations through the cosine-based s-bend.

A sin-based s-bend that is at least 100μm long is the preferred choice for the bends required to increase the separation between the Mach-Zehnder modulator arms. A TE_0 matched cosine-based s-bend, or a TE_0 matched sin-based s-bend would be a valid choice if the bend length needs to be shortened. Another alterative is to use a laterally offset cosine-based bend. With this bend design the gap between the MMI access waveguides can be increased by at least 0.2μm. Melloni et al. [134] have, however, theoretically shown that the lateral offset bend design has inferior wavelength performance relative to a matched bend condition.

A second waveguide bend is required to create an output dump port in the Mach-Zehnder modulator, since only one output of the 2X2 MMI combiner is required, as shown in Figures 1.15 and 1.20. The dump port output from the MMI combiner must be angled away from the output facet to prevent it coupling with the output optics. Figure 2.78 shows the matched bend condition for a 2.0μm wide 12° circular arc on this dump port waveguide. In Figure 2.78a, the transmission from the arc into the TE_0 and TE_1 modes of the 2.0μm wide dump port waveguide, is shown, as a function of the bend radius. A bend radius of 106μm minimizes the TE_1 conversion following the circular arc. Figure 2.78b shows the

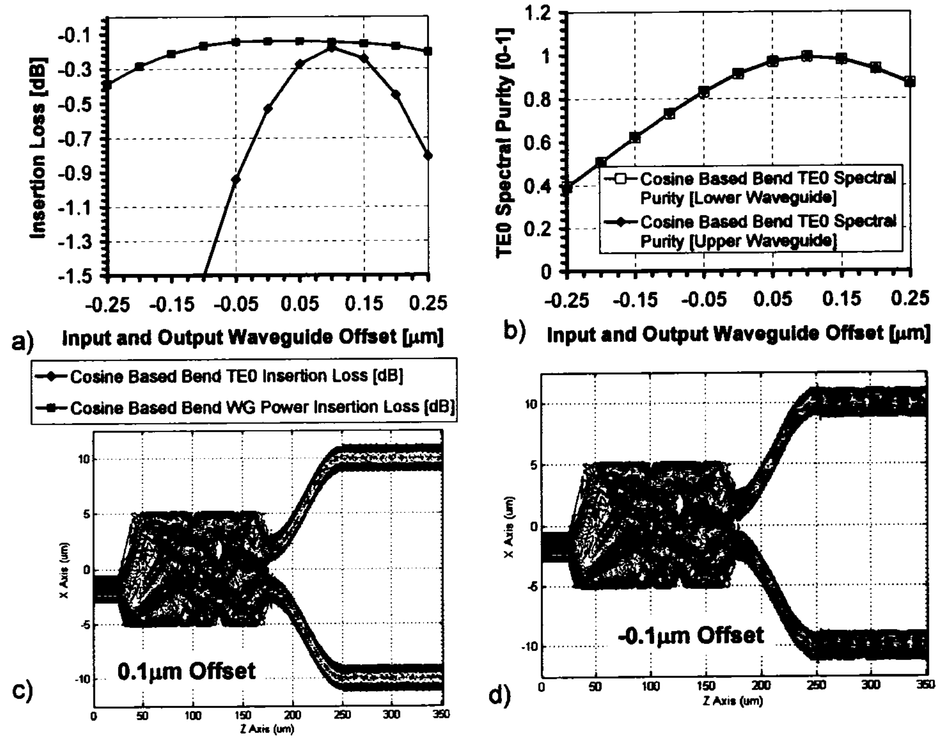

Figure 2.77: ***Performance of a 75μm Long Cosine-Based Bend Following the MMI Splitter as a Function of Offset Between the Straight-to-Bend Transitions at 1545nm.***

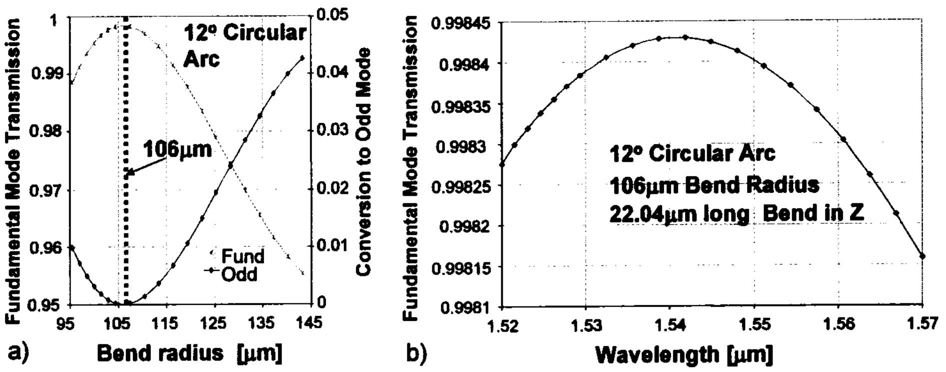

Figure 2.78: ***Matched Bend Condition for the 2.0μm Wide 12° Circular Arc on the Dump Port from the MMI Combiner in the Mach-Zehnder Modulator: a) Transmission from the Arc into the TE_0 and TE_1 Modes of the 2.0μm Wide Dump Port Waveguide as a Function of Bend Radius, b) Transmission from the Arc into the TE_0 Mode of the 2.0μm Wide Dump Port Waveguide as a Function of Wavelength at the 106μm Matched Bend Radius.***

transmission from the arc, into the TE_0 mode of the 2.0μm wide dump port waveguide, as a function of wavelength, at the 106μm matched bend radius. It is apparent the matching condition is wavelength independent over the full C-band wavelength range shown. This 12° circular arc with a 106μm bend radius is only 22.04μm long in the z direction.

2.4 Waveguide Layout for the Mach-Zehnder Modulator

In this Section the preferred Mach-Zehnder waveguide geometry[62], as developed in this Chapter and summarized in Figure 2.79, is modelled using a TE semi-vectorial, three-dimensional, finite-difference beam propagation method, using PML boundary conditions. The cross-sectional (x,y) simulation space uses a uniform grid of 401X251 points, running from $x=-12.5\mu m$ to $x=12.5\mu m$, and $y=-5\mu m$ to $y=3\mu m$, with $y=0$ the centre of the modulator core. The refractive index of a grid point (x,y) is given the area weighted average value of the materials contained between $(x\text{-}dx/2,x\text{+}dx/2)$ and $(y\text{-}dy/2,y\text{+}dy/2)$. The reference index for the simulations is N_0=3.18[63]. The propagation step size is dz=0.1μm. All simulations are performed at 1546nm unless stated otherwise, with no doping or bandedge losses included in the refractive indices for the materials used in the simulations. The modulator MQW core is taken to have a peak photoluminescence wavelength at Q=1411nm in these simulations. The spot-size converter design used is summarized in Section 3.7.

All simulations in this Section are excited by launching a Gaussian field into the input facet of the input optical mode spot-size converter. This Gaussian field has a near field waist σ=1.76μm, and it is representative of a tapered fiber with a lens radius of 10μm;

---

[62] This includes the optical mode spot-size converters developed in Chapter 3 and Chapter 4.

[63] This reference index is based on a calibration of the BPM model against the experimental insertion loss for the concatenated 1X1 MMI structure given in Figure 2.58.

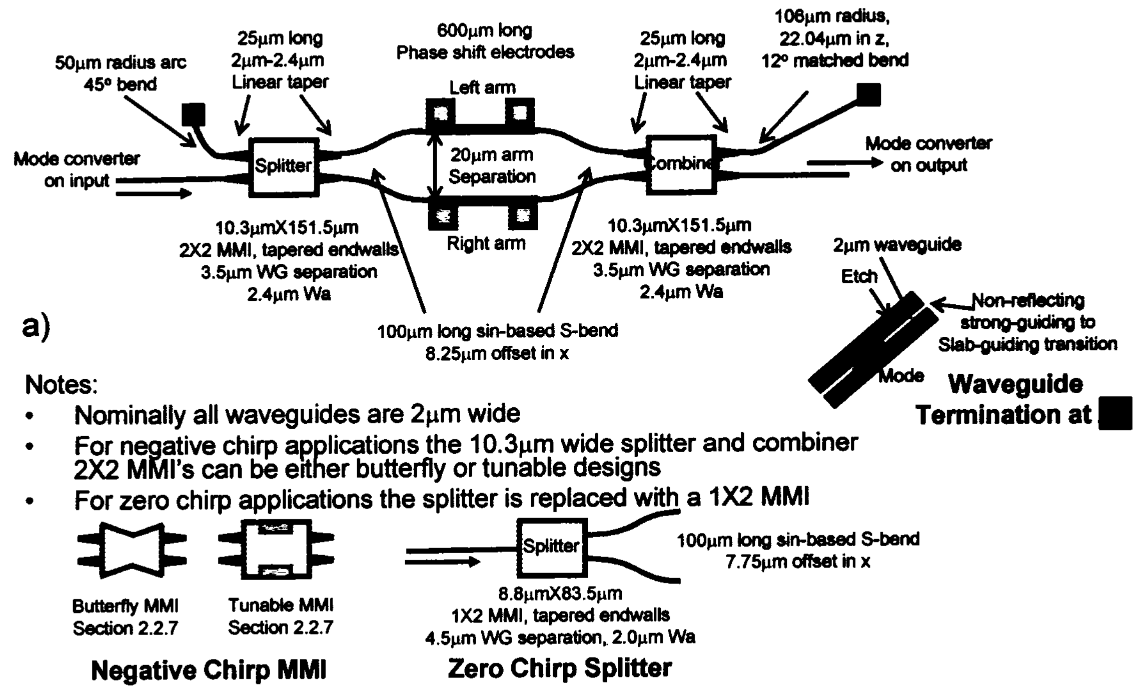

Notes:

- Nominally all waveguides are 2μm wide
- For negative chirp applications the 10.3μm wide splitter and combiner 2X2 MMI's can be either butterfly or tunable designs
- For zero chirp applications the splitter is replaced with a 1X2 MMI

Figure 2.79: *Preferred Mach-Zehnder Waveguide Layout.*

tapered fiber coupling optics are detailed in Section 3.2.3. The output field from the device simulations are overlapped to this same tapered fiber Gaussian near field, giving insertion losses and extinction ratios representative of coupling to the Mach-Zehnder modulator device output with a tapered fiber.

The majority of the simulations given in this Section are for the waveguide layout in Figure 2.79a. The negative chirp Mach-Zehnder implementation can be obtained from the waveguide layout in Figure 2.79a by either, linearly down-tapering the 2X2 MMI width to a minimum at its mid-point[64], or by including forward bias phase-shift electrodes at the midpoint edges of the 2X2 MMI. Both of these techniques are detailed in Section 2.2.7, and summarized in the notes on Figure 2.79; no change to the s-bends is required for either of these MMI modifications since the placement of the access waveguides is unchanged. The zero chirp Mach-Zehnder implementation can be obtained from the waveguide layout in Figure 2.79a by replacing the 2X2 MMI spitter with the preferred 1X2 MMI design detailed in Section 2.2.4. This 1X2 MMI design and the corresponding s-bends are summarized in notes on Figure 2.79.

---

[64] It is also necessary to adjust the length accordingly.

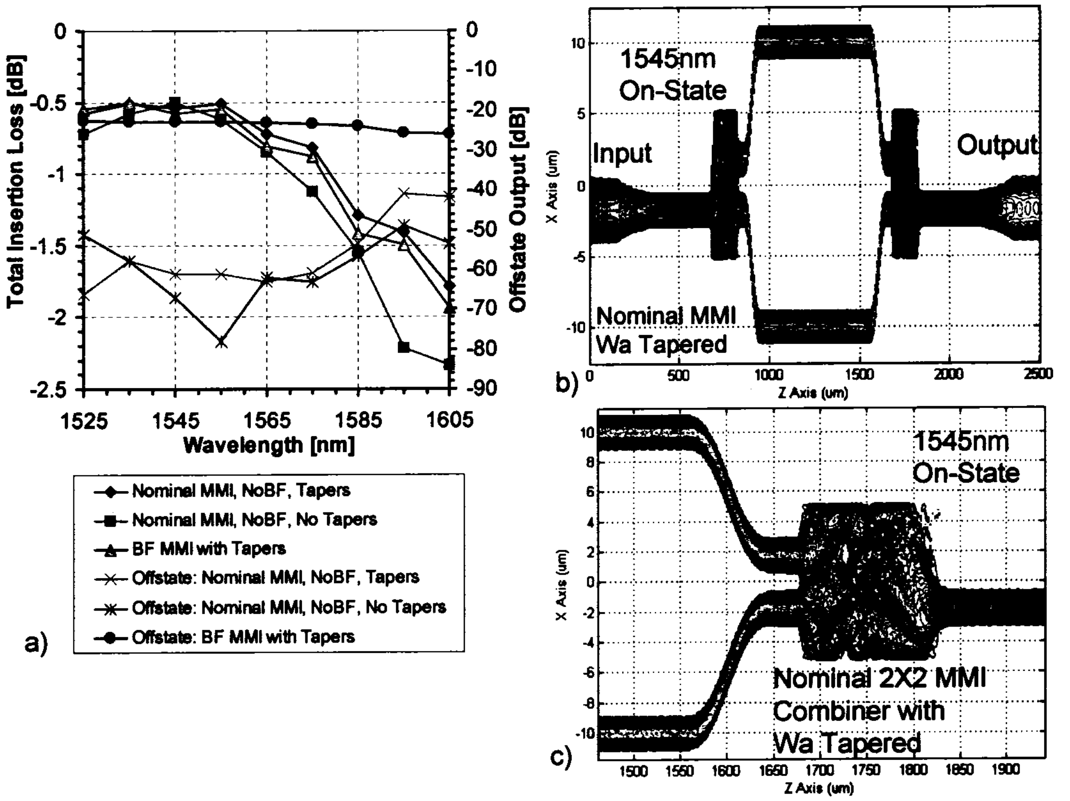

Figure 2.80: *a) 3D TE Semi-Vectorial BPM Simulations of the Mach-Zehnder Modulator Insertion Loss and Off-State Output Power as a Function of Wavelength for Several Waveguide Layouts, b) X–Z Power Contour Map through the Waveguide Core (Y=0) in the On-State of the Preferred Modulator Layout in Figure 2.79a at 1545nm, c) Expanded View of the MMI Combiner in (b).*

2.4.1 Wavelength Dependence

In Figure 2.80a the total TE_0 insertion loss in the on-state of the modulator is given, along with the off-state output power, for several modulator layouts based on the preferred waveguide layout in Figure 2.79a. Curves are provided for modulator layouts with and without MMI access waveguides having linear 2.0μm-2.4μm ridge width tapers. These tapers are removed from the simulations by setting the ridge width over the length of the taper to a constant 2.0μm, therefore, the length of the taper remains in the simulation. The insertion loss variation across C-Band[65] is reduced for the modulator designs with the 2.4μm wide MMI access waveguides, as expected from the MMI simulations in Section 2.2.3. In both cases, the insertion loss of the modulator increases monotonically (in dB) as the wavelength increases beyond the bandwidth tolerance of the MMI design, however, the modulator extinction ratio[66] remains greater than 40dB at all wavelengths.

---

[65] Recall C-Band is ≈1528nm-1565nm.

[66] The modulator extinction ratio is defined as the difference between the modulator off-state and on-state output power in dB.

Figure 2.80a also shows simulation results for a negative chirp modulator implementation using 2X2 butterfly MMI designs with a waist constriction of 0.5μm and a corresponding MMI length reduction to 144.5μm. The impact of this design on the modulator insertion loss is negligible, however, the off-state output power is increased significantly. This occurs because the power in the two arms can no longer cancel in the off-state; the left arm has increased contribution to the output due to the non-unity optical power split and combine ratios.

In Figure 2.80b the X–Z power contour map through the waveguide cores (y=0) is given for the on-state of the preferred waveguide layout in Figure 2.79a at 1545nm. In Figure 2.80c the X–Z power contour map through the waveguide cores (y=0) is shown for a close-up of only the MMI combiner in the on-state at 1545nm.

In Figure 2.81 the total power remaining in 3D TE semi-vectorial BPM simulations of the preferred waveguide layout in Figure 2.79a is given as a function of both the propagation in z and the wavelength. The power loss triggered by the output of the 2X2 MMI splitter can be seen to increase monotonically as the operating wavelength deviates from the optimal operating wavelength for the MMI, however, the power loss triggered by the output of the 2X2 MMI combiner is not monotonic far from the optimal operating wavelength–the loss triggered by the MMI at 1595nm appears to exceed the loss triggered by the MMI at 1605nm. It is also clear from Figure 2.81 that the power loss experienced in the output SSC appear to oscillate with wavelength. The minimum losses occur in the SSC at 1575nm and 1595nm, and the maximum losses occur in the SSC at 1565nm, 1585nm and 1605nm. These observations can be explained by examining the X–Z power contour maps of the splitter and combiner functions in Figure 2.82 at 1595nm and 1605nm. Less radiation scattering loss occurs at the output of the 2X2 MMI combiner at 1605nm in Figure 2.82b, relative to 1595nm in Figure 2.82d, however, the TE_0 spectral purity in the output waveguide prior to the SSC is also decreased. The wavelength variation in SSC power losses can be explained by increased losses for the TE_1 mode in the SSC.

2.4.2 MMI Ridge Width Error/MMI Length Error

In Figure 2.83a the total TE_0 insertion loss in the on-state of the modulator is given, along with the off-state output power, for the preferred waveguide layout in Figure 2.79a, as a function of MMI length and MMI width errors. Simulation results are provided for MMI length deviations of $\pm 3\mu$m from the optimal 151.5μm length for 1546nm operation, and for MMI width variations of $\pm 0.1\mu$m from the optimal 10.3μm width for 1546nm operation. These values for the deviations were chosen since they should have equivalent impact on the MMI performance according to Equation 2.23. From Figure 2.83a it is clear that the performance of a modulator with +0.1μm MMI width error is identical to a modulator with a -3μm MMI length error, and that the optimal operating wavelength for these modulators has increased to 1570nm. For a modulator with a -0.1μm MMI width error or a +3μm MMI length error the optimal operating wavelength has decreased to less than 1525nm. For these modulators, operating significantly outside the MMI wavelength bandwidth, a

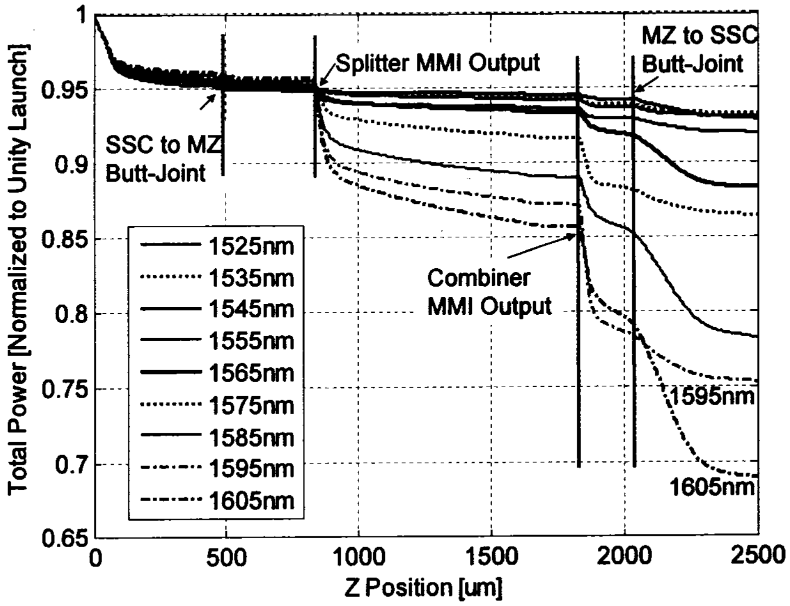

Figure 2.81: *The Total Power Remaining in 3D TE Semi-Vectorial BPM Simulations of the Preferred Modulator Waveguide Layout in Figure 2.79a as a Function of Both the Propagation In Z and the Wavelength.*

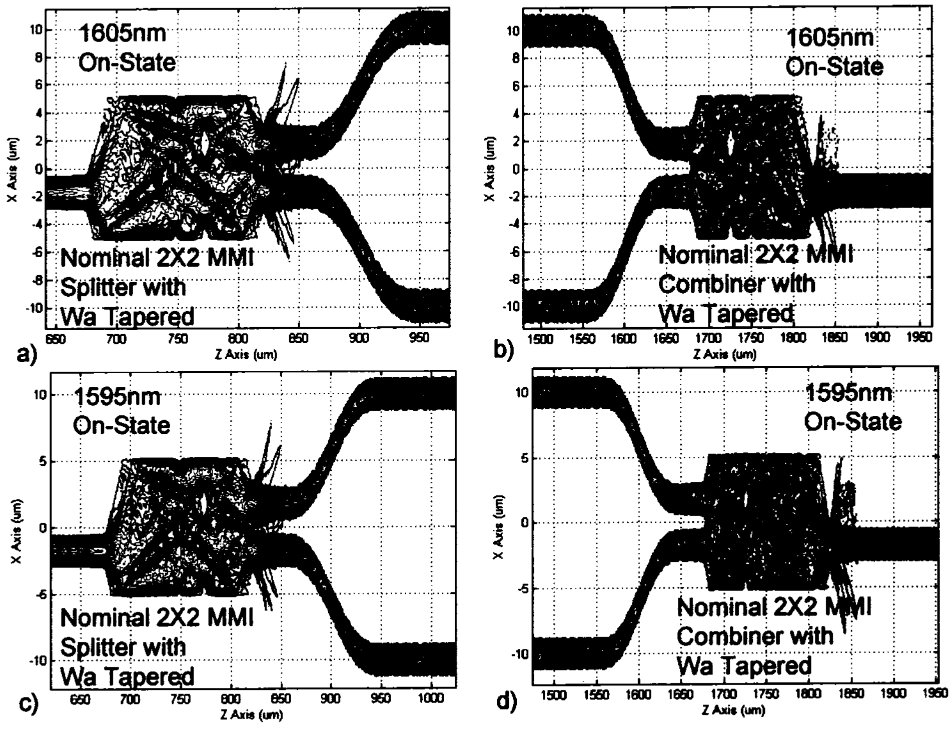

Figure 2.82: *X–Z Power Contour Maps through the Waveguide Core (Y=0) in the On-State of the Preferred Modulator Layout in Figure 2.79a at 1605nm and 1595nm.*

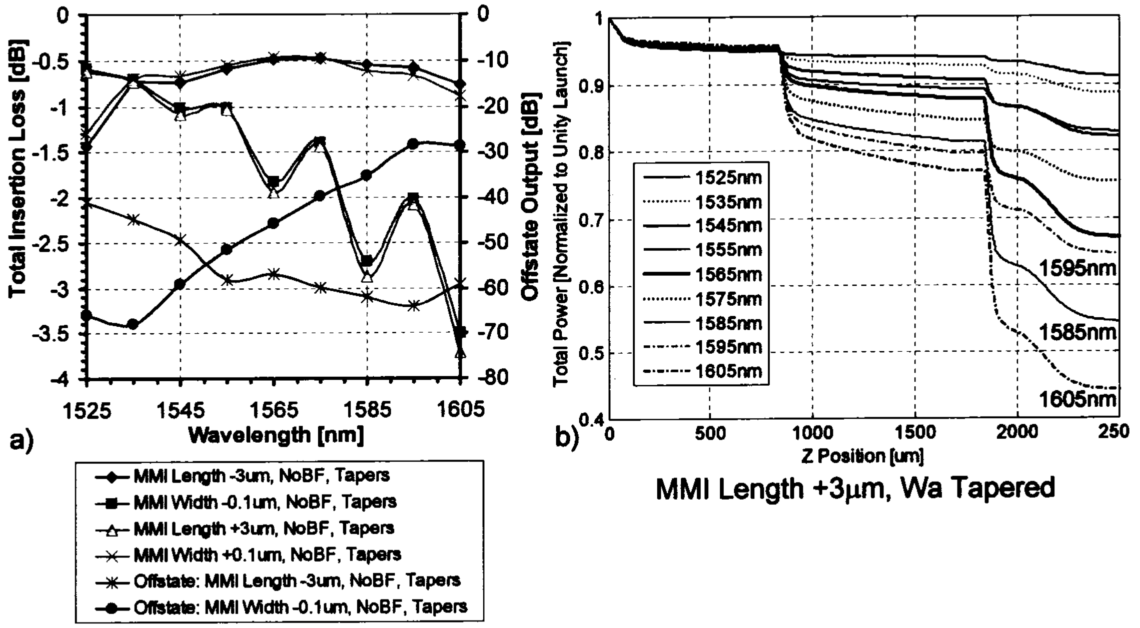

Figure 2.83: *3D TE Semi-Vectorial BPM Simulations of the Mach-Zehnder Modulator Insertion Loss and Off-State Output Power as a Function of Wavelength for the Preferred Modulator Layout in Figure 2.79a with MMI Length and Width Errors.*

wavelength periodicity in the insertion loss and a reduction in the modulator extinction ratio is seen. Figure 2.83b shows the total power remaining in the simulation for the modulator with +3μm MMI length error, as a function of both the propagation in z and the wavelength. The wavelength periodicity in insertion loss can be seen to originate at the output of the MMI combiner. This is confirmed in Figure 2.84 by the X–Z power contour maps of the combiner MMI at 1585nm and 1595nm. Less radiation scattering loss occurs at the output of the 2X2 MMI combiner at a wavelength of 1595nm relative to a wavelength of 1585nm.

Figure 2.83a makes it clear that, as expected, the primary process tolerance parameter is the width of the MMI. Deviations of $\pm 0.1\mu$m will be evident in the behaviour of the modulator insertion loss and extinction ratio versus wavelength.

2.4.3 Misalignment of Input Fiber Coupling Launch

Figure 2.85 shows that the only impact on the modulator performance for a -1μm misalignment of the Gaussian launch is the obvious increase in the device insertion loss. There is no impact on the modulator extinction ratio. In Figure 2.85c and 2.85d the TE_1 mode excited by the misaligned Gaussian launch can be seen to propagate through the modulator as expected[67].

---

[67] The 2X2 MMI does not mode filter its images.

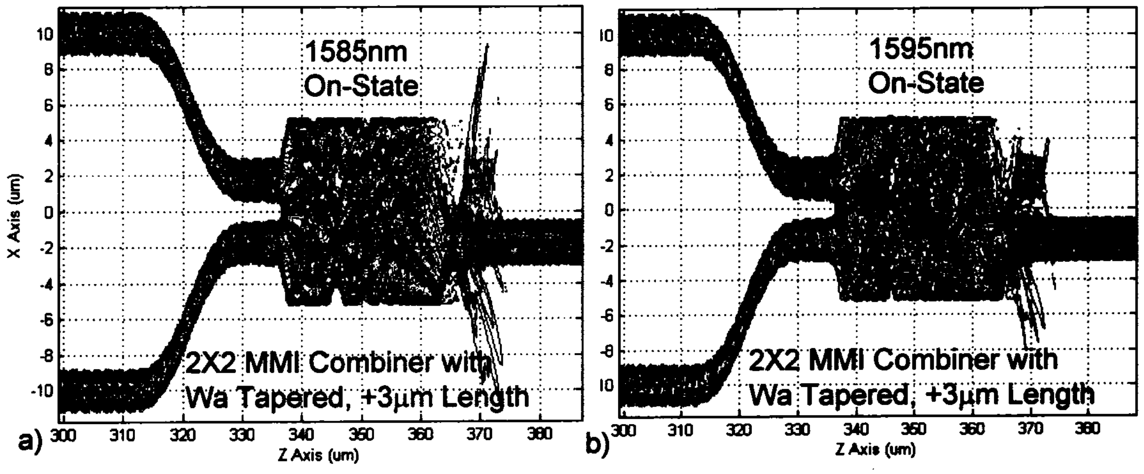

Figure 2.84: *X–Z Power Contour Maps through the Waveguide Core (Y=0) for the On-State of the Preferred Modulator Layout in Figure 2.79a with a +3μm MMI Length Error at 1585nm and 1595nm.*

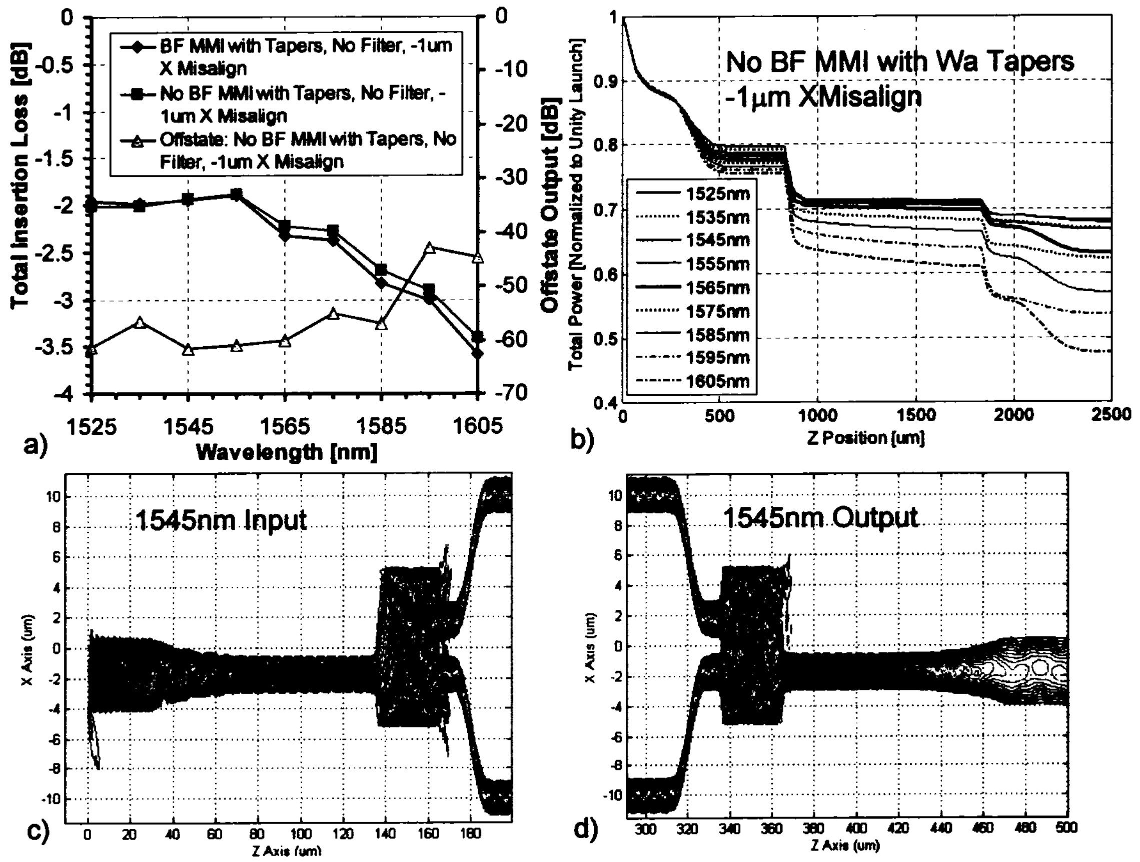

Figure 2.85: *3D TE Semi-Vectorial BPM Simulations of the Mach-Zehnder Modulator Insertion Loss and Off-State Output Power as a Function of Wavelength for Several Waveguide Layouts with a -1μm Misalignment of the Gaussian launch.*

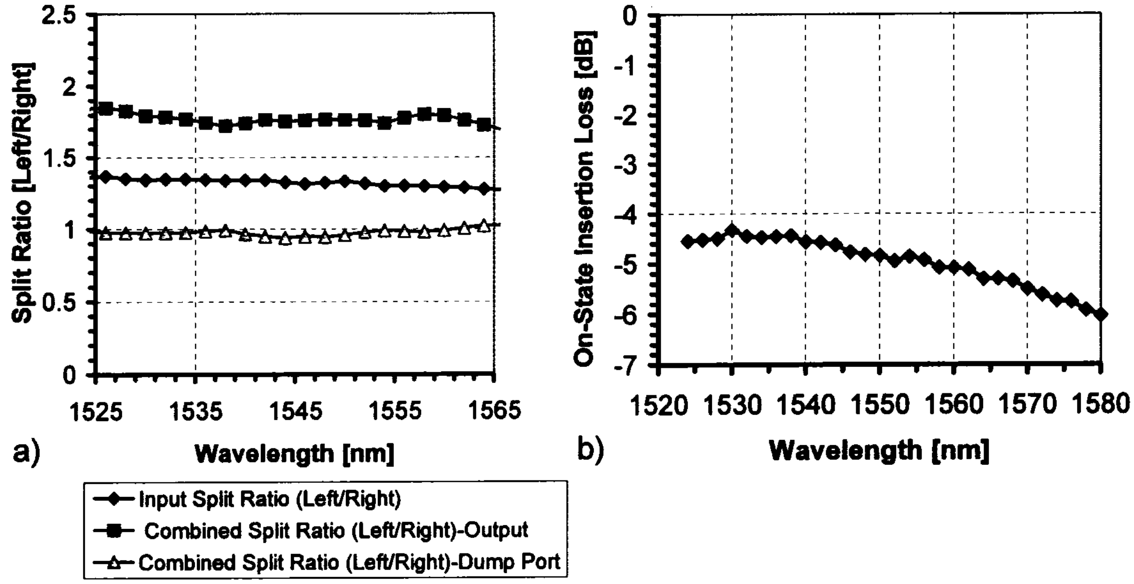

Figure 2.86: *Measured Performance of a Mach-Zehnder Modulator with Non-Uniform Optical Split and Combine Ratios as a Function of Wavelength.*

2.4.4 Experimental Measurements

Figure 2.86 shows the measured performance as a function of wavelength for the waveguide layout of a negative chirp modulator implemented using 2X2 butterfly MMI designs having a waist constriction of 0.8μm and a corresponding MMI length reduction to 139.5μm. The device was fabricated using an i-line stepper lithography process and both facets of the device were anti-reflection coated as detailed in Section 4.6. The coupling optics to the waveguide are the 10μm radius lensed tapered fibers discussed in Section 3.2.3.

In Figure 2.86a the input MMI optical power split ratio (left arm over right arm) is shown as a function of wavelength along with the combined split ratios collected at the SSC output and in the output dump port. The combined split ratio in the output should be the square of the split ratio for a single MMI, however, the combined split ratio in the dump port should be unity since the non-uniform split ratios from the input and output MMI's cancel each other out. The modulator functions as desired with excellent uniformity as a function of wavelength in C-Band.

In Figure 2.86b the measured on-state insertion loss for the modulator is given as a function of wavelength relative to a fiber-to-fiber reference. No periodic variation in insertion loss is seen as a function of wavelength. This is the lowest insertion loss reported for a strongly-guided InP-based Mach-Zehnder modulator.

2.5 Appendix: InP Material System and Refractive Index

Indium phosphide (InP) is a semiconductor material with a bandgap energy of 1.423eV and a lattice constant of 5.8697Å. It is commercially available in wafer form, with various dopants, and in diameters ranging from two to four inches. In this thesis the refractive index (n) of undoped InP is calculated using the modified Sellmeier coefficients determined by Martin et al. [100],

$$n^2 = 7.283 + \frac{2.337\lambda^2}{\lambda^2 - 0.387} \tag{2.46}$$

where λ must be above the material wavelength bandgap and it is given in microns. The impact of doping on the complex refractive index of InP is detailed in Section 2.1.7.

Electro-optic components for telecommunications are typically made from thin films of quaternary semiconductor $In_{1-x}Ga_xAs_yP_{1-y}$ deposited on InP substrates using thin film epitaxy. The $In_{1-x}Ga_xAs_yP_{1-y}$ bandgap and lattice constant are a function of the group III and group V composition, denoted by x and y respectively. The choice of x and y is restricted in alloys that are lattice-matched to InP by [101],

$$y = \frac{2.2020x}{1 + 0.0659x}. \tag{2.47}$$

The bandgap energies (E_g) of these lattice-matched alloys range from 0.750eV to 1.423eV according to [101],

$$E_g = 1.35 - 0.778y + 1.49y^2. \tag{2.48}$$

Alternatively, the bandgap energy (E_g) can be expressed by the corresponding photon wavelength, Q, in microns,

$$E_g(eV) = 1.2398/Q. \tag{2.49}$$

It is the wavelength range well above the material wavelength bandgap, Q, that is of most interest in passive waveguide devices, such as Mach-Zehnder modulators. In this thesis, the refractive index of an $In_{1-x}Ga_xAs_yP_{1-y}$ thin film is, therefore, calculated using the modified Sellmeier formula coefficients determined by Fiedler et al. [102],

$$\begin{aligned} a &= 7.255 + 1.15y + 0.489y^2 \\ b &= 2.316 + 0.604y - 0.493y^2 \\ c &= 0.3922 + 0.396y + 0.158y^2 \\ n^2 &= a + \frac{b\lambda^2}{\lambda^2 - c} \end{aligned} \tag{2.50}$$

where λ is above the material wavelength bandgap, Q, and it is given in microns.

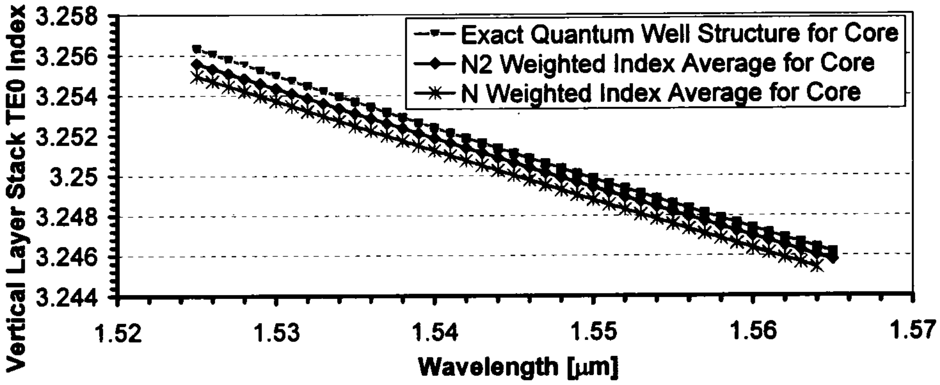

Figure 2.87: *Comparison of TE$_0$ Refractive Index for Various Representations of the Multi-Quantum Well Core.*

2.6 Appendix: Refractive Index of Multi-Quantum Well Materials

A multi-quantum well (MQW) structure must be replaced by a single homogeneous layer, with an equivalent refractive index and equivalent thickness, to enable efficient numerical calculations of waveguide properties. The simplest approximation sets the index of the equivalent replacement layer at the arithmetic average of the refractive index for the individual MQW layers [95]. The thickness remains unchanged. A further improvement to this mean-value approximation is obtained by considering a linear perturbation of the solutions for the wave equation [96,97]. This leads to a root-mean square approximation, with the refractive index of the replacement layer, n_{eq}, given by a weighted average of the dielectric constants of the individual MQW layers. Thus,

$$n_{eq}^2 = \frac{\sum\limits_j n_j^2 d_j}{\sum\limits_j d_j} \tag{2.51}$$

for TE modes, where n_j is the refractive index of the jth layer having width d_j. For TM modes, the equivalent refractive index is given by,

$$\frac{1}{n_{eq}^2} = \frac{\sum\limits_j \frac{1}{n_j^2} d_j}{\sum\limits_j d_j}. \tag{2.52}$$

Li et al. [94] have proposed an iterative equivalent replacement layer solution that offers the exact propagation constant of the MQW waveguide, at the cost of being numerically intensive. More recently, Saini et al. [98,99] have provided the exact analysis of a MQW waveguide, and introduced a semi-analytical approximation based on a variational analysis. They show the effective index and fractional power in their replacement layer solution compares extremely well with the exact solution. They also show that Li's replacement layer solution, though exact for the waveguide effective index, gives the maximum error in the prediction of the power fraction in the replacement layer.

Figure 2.87 compares the TE_0 refractive index for three representations of the modulator MQW structure: The exact solution, the mean-value approximation, and the root-mean square approximation. The root-mean square approximation has been used for all MQW calculations in this thesis due to its relative accuracy and simplicity. The additional computational complexity introduced by Saini's variational approximation was deemed to be counterproductive, given the accuracy of the available InGaAsP experimental refractive index data in the literature.

The incorporation of the well quantum size effect has a more significant contribution to the equivalent layer index than the method used for the calculation. All the above references for equivalent layer calculations assume the refractive index of the well and barrier layers are given by their bulk values. In this thesis it is assumed that the barrier layer index is given by its bulk value, and the well layer index is given by the value of a bulk layer with the same composition as the peak exciton absorption in the MQW.

Chapter 3

Design of an Optical Spot-Size Converter

3.1 Spot-Size Converter (SSC) Design Requirements

An optical mode spot-size converter (SSC) allows an adiabatic transition between an optical mode that is 'optimal' for an active semiconductor device function and an optical mode that is 'optimal' for interacting with the semiconductor device. In a strongly-guided InP-based semiconductor modulator the following characteristics are required from an integrated optical mode spot-size converter:

- Angular reduction and symmetrization of the modulator waveguide mode far field are necessary to enable efficient coupling to the device. Improvements in coupling alignment tolerances are secondary to the reduction in coupling insertion loss.
- Sub-millimeter length for the SSC is a practical requirement to maintain low chip costs since three inch wafers are typically used for device fabrication.
- Low polarization rotation in the SSC is required since the modulator function is not necessarily polarization independent. Any optical rotation in the SSC can impair the extinction ratio and chirp performance of the modulator device.
- Wavelength independent optical mode conversion is required since the Mach-Zehnder modulator is capable of being operated over a wavelength range on the order of 40nm.
- The SSC must be near single-mode. Light must be coupled from off-chip into the modulator so it is not practical to assume perfect modal launch conditions in the device. This places constraints on the modulator SSC design that are unnecessary on a SSC designed for an optical source[1].

---

[1] Misaligned excitation is not an issue in an optical source since only output coupling from the chip takes place.

- The modulator has an electrical p-i-n diode growth structure so the impact of the carrier doping profile must be accounted for in the SSC design and optimized to limit the doping contribution to the SSC optical loss.
- The inclusion of the SSC must not impair high optical extinction ratios in the modulator. Extinction ratios as high as 40dB do have practical applications.
- Low polarization dependent loss in the SSC is required for an electro-absorption modulator application presented in Section 4.7.6.
- The inclusion of the SSC must not hinder the thermal transport properties in the modulator cross-section. It is necessary for heat in the modulator core generated by optical absorption to be removed efficiently to prevent catastrophic damage to the device at high optical input powers [179].

Section 3.2 details practical off-chip options for the optical spot-size mode conversion of the LP_{01} mode in standard single-mode fiber. Section 3.3 follows with an overview of the on-chip optical spot-size mode converter design developed in this thesis.

3.2 On-Chip versus Off-Chip Mode Conversion

Angular reduction and symmetrization of the modulator waveguide mode far field are necessary to enable efficient coupling to the device. Since improvements in the coupling alignment tolerances are secondary to the reduction in coupling insertion loss, it is important to quantify to what degree the optical spot-size mode conversion can be practically obtained off-chip. In this Section calculations for determining far field angles from near field mode sizes are derived, the insertion loss tolerance to modal misalignment is discussed, and the spot-size reduction available using either tapered lensed fibers or fiber lens assemblies is experimentally evaluated.

3.2.1 Calculation of Far Field Angles from Near Field Mode Size

The determination of the far field for an optical waveguide mode is important because the mode coupling to a fiber or lens assembly will always take place in the far field. Zeng and Naqwi have presented the far-field solution for the Helmholtz equation using the boundary condition at the output plane of a hetero-structure laser [181], and Nermoto has experimentally verified the validity of their solution [183]. Here, the Zeng and Naqwi approach is followed, although the far field expression for a two dimensional Gaussian near field at the waveguide facet is solved instead. A two dimensional Gaussian near field solution is a better approximation to the fundamental mode in a modulator waveguide than the near field solution used by Zeng and Naqwi for a diode laser.

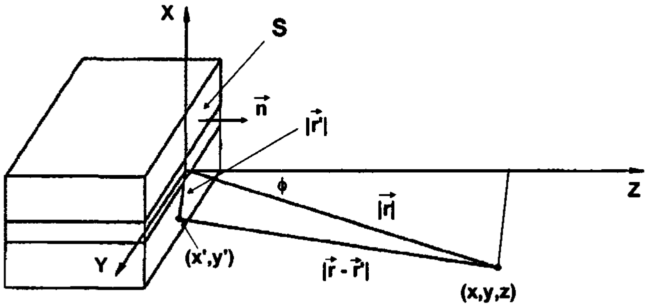

Figure 3.1: *The Coordinate System for the Solution of the Wave Equation. Source: Xiaodong Zeng, Amir Naqwi, "Far-field Distribution of Double Hetero-structure diode laser beams," Applied Optics, Vol. 32, No. 24, pp. 4491-4494, 20 August 1993.*

The far-field expression used by Zeng and Naqwi does not require paraxial approximations and can, therefore, be used for large beam-divergence angles. However, as pointed out by Li and Katz [182], the Zeng and Naqwi expression does not account for astigmatic aberration, thus perfectly spherical waves are predicted in the far field. Though this can be an issue for diode-laser beams, astigmatic aberration is negligible for eigenmode waveguide solutions in a passive dielectric structure.

The far field distribution of a waveguide mode can be determined by solving a diffraction problem. A three-dimensional monochromatic scalar wave expressed by $\Psi(\vec{r},t) = u(\vec{r})\exp(-i\omega t)$ is considered. In a vacuum the space dependent part satisfies the Helmholtz equation,

$$\nabla^2 u(\vec{r}) + k^2 u(\vec{r}) = 0 \tag{3.1}$$

where $k = \frac{2\pi}{\lambda}$. A solution to Equation 3.1 can be expressed in terms of its boundary value [184],

$$u(\vec{r}) = -\frac{1}{2\pi}\int_S u(\vec{r}')\frac{\partial G(\vec{r},\vec{r}')}{\partial \vec{n}}ds \tag{3.2}$$

where $G(\vec{r},\vec{r}') = \frac{\exp(ik|\vec{r}-\vec{r}'|)}{|\vec{r}-\vec{r}'|}$. Here S denotes the boundary surface (diffraction screen) and $\vec{n}$ is the local outward normal to this surface. Equation 3.2 is the first Rayleigh-Sommerfield integral formula for Dirichlet boundary conditions.[2] As shown in Figure 3.1, the boundary surface at the waveguide facet is defined by the x-y plane, therefore

$$\frac{\partial G(\vec{r},\vec{r}')}{\partial \vec{n}} = \frac{\partial G(\vec{r},\vec{r}')}{\partial z}. \tag{3.3}$$

Substituting Equation 3.3 and the definition of the boundary surface into Equation 3.2 gives [181],

$$u(\vec{r}) = -\frac{1}{2\pi}\int_{-\infty}^{\infty}\int_{-\infty}^{\infty} u(\vec{r}')\frac{z}{|\vec{r}-\vec{r}'|^3}(ik|\vec{r}-\vec{r}'|-1)\exp(ik|\vec{r}-\vec{r}'|)dx'dy', \tag{3.4}$$

---

[2] $G(\vec{r},\vec{r}') = 0$ on surface S

where $\vec{r} = x\vec{i} + y\vec{j} + z\vec{k}$ and $\vec{r}' = x'\vec{i} + y'\vec{j}$. For the far field condition it is assuming the distance from the source to the observation point is larger than both the wavelength and the size of the source,

$$|\vec{r} - \vec{r}'| \gg \frac{\lambda}{2\pi} \gg \frac{1}{k} \tag{3.5}$$

$$\frac{1}{|\vec{r} - \vec{r}'|} \approx \frac{1}{\vec{r}} \tag{3.6}$$

and a Taylor series expansion of the phase in the integrand allows the introduction of the following simplication [181],

$$|\vec{r} - \vec{r}'| \approx |\vec{r}| + (\nabla|\vec{r}|) \cdot r' = |\vec{r}| + \frac{1}{|\vec{r}|}\vec{r} \cdot \vec{r}'. \tag{3.7}$$

Substituting Equation 3.5 and Equation 3.7 into Equation 3.4 yields the far field solution,

$$\boxed{u(x,y,z) = -\tfrac{iz}{\lambda r}\tfrac{\exp(ikr)}{r} \int_{-\infty}^{\infty} \int_{-\infty}^{\infty} u(x',y') \times \exp\left[-\tfrac{ik}{r}(xx' + yy')\right] dx'dy'} \tag{3.8}$$

where $r = (x^2 + y^2 + z^2)^{\frac{1}{2}}$. Note Equation 3.8 could be used to determine the far field of a waveguide by numerically integrating an exact near field mode solution.

For the fundamental waveguide modes of interest[3], a separable two dimensional Gaussian is a reasonable approximation to the cross-sectional near field, thus

$$u(x',y') = \exp\left(\frac{x'^2}{\sigma_x^2} + \frac{y'^2}{\sigma_y^2}\right), \tag{3.9}$$

with σ_x and σ_y the near field Gaussian waist parameters in x and y.

Substituting Equation 3.9 into Equation 3.8 enables a closed form solution for the intensity profile,

$$I(x,y,z) = |u(x,y,z)|^2 = \frac{z^2\pi^2}{\lambda^4 r^4}\sigma_x^2\sigma_y^2 \exp\left(\frac{-k^2}{2r^2}\left(x^2\sigma_x^2 + y^2\sigma_y^2\right)\right). \tag{3.10}$$

The specification for an optical component far field is usually defined by the intensity angular full width at half maximum (FWHM) in both x and y. In the x-z plane the intensity distribution in Equation 3.10 reduces to,

$$I(x,0,z) = \frac{z^2\pi^2\sigma_x^2\sigma_y^2}{\lambda^4(x^2 + z^2)^2} \exp\left(\frac{-k^2x^2\sigma_x^2}{2(x^2 + z^2)}\right). \tag{3.11}$$

---

[3] Note the derivation now diverges from the Zeng and Naqwi derivation.

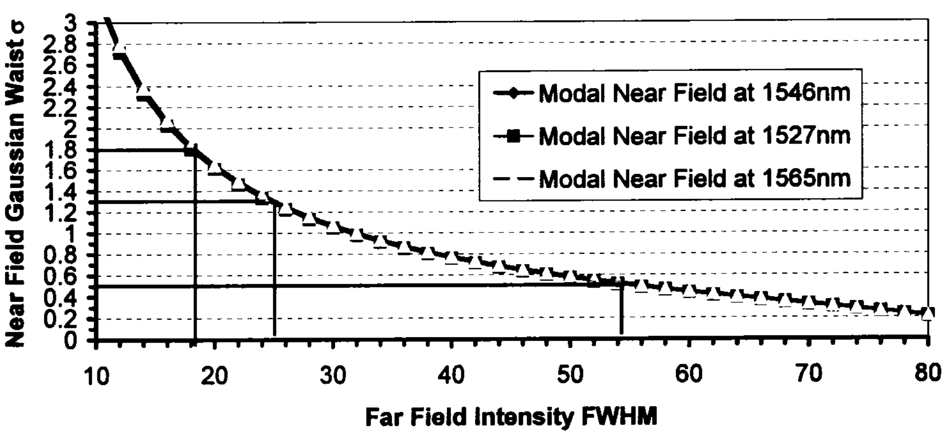

Figure 3.2: ***Relationship Between the Far Field Intensity FWHM and the Near Field Gaussian Waist Parameter σ over Wavelength in the Telecom C-Band using Equation 3.12.***

In spherical co-ordinates $z=r\cos\phi$ and $x=r\sin\phi\cos\theta$ with $\theta=0^{0}$ on the x-z plane. Solving $\frac{I(0,0,z=r)}{2}=I(x=r\sin\phi,0,r\cos\phi)$ gives the far-field angular half-width-at-half-maximum (ϕ_{HWHM}) in the x direction as a function of the near field Gaussian waist parameter σ_x:

$$\boxed{\sigma_x = \left(\frac{2\ln(2\cos^2\phi_{HWHM})}{k^2\sin^2\phi_{HWHM}}\right)^{\frac{1}{2}}} \tag{3.12}$$

A similar relation can be found between the near field Gaussian waist parameter σ_y and ϕ_{HWHM} in y. In Figure 3.2 the relationship between the near field Gaussian waist parameter σ_x or σ_y, and the far field intensity FWHM angle is plotted as a function of wavelength in the telecom C-Band window.[4]

3.2.2 Insertion Loss Tolerance to Modal Misalignments

Figures 3.3 and 3.4 show the impact of the misalignment of the near field image from the coupling optics, relative to the output mode of the SSC, assuming both modes have matched Gaussian profiles. It is evident that the tolerance to misalignment increases with increasing mode size. Strategies for active alignment allow placement accuracy of ~0.1μm in a manufacturing environment. A discontinuity in assembly costs is achievable if the alignment tolerances can be relaxed to ~1.0μm since this enables passive alignment technologies such as Si benches. [180]. The design intent for the modulator SSC is the reduction of the coupling losses in a manufacturing environment where active alignment is available.

---

[4] The following relationships are useful for converting mode dimensions in the near field: Mode Field$_{FWHM}=2\sqrt{\ln 2}\cdot\sigma_x$; Mode Intensity$_{FWHM}=\sqrt{\ln 2}\cdot\sigma_x$.

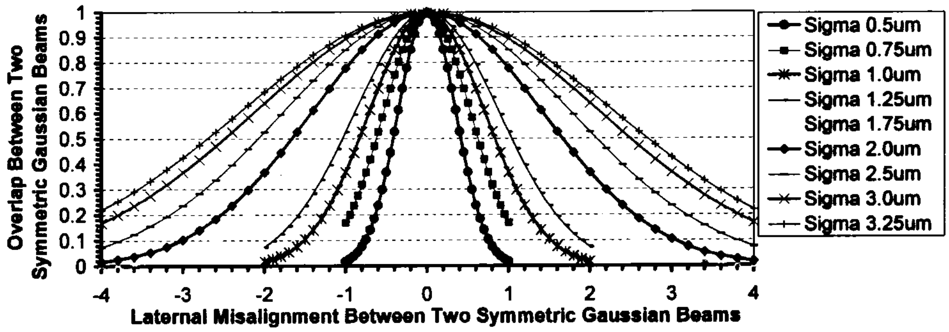

Figure 3.3: *Impact of Misalignment on the Coupling Loss between Two Symmetric Gaussian Beams I.*

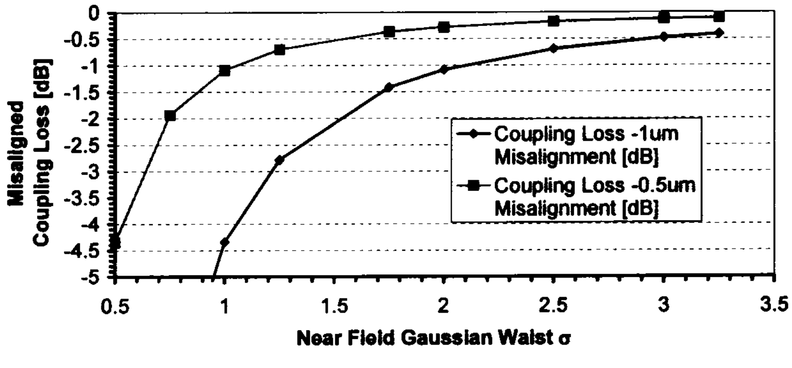

Figure 3.4: *Impact of Misalignment on the Coupling Loss between Two Symmetric Gaussian Beams II.*

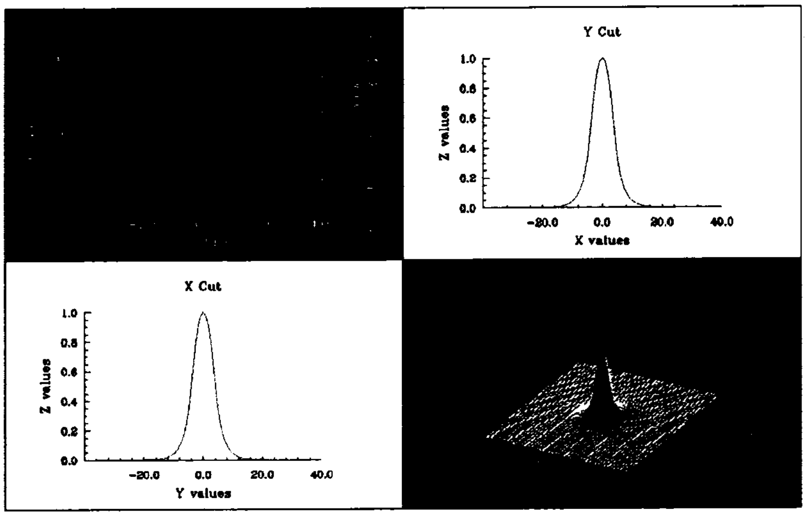

Figure 3.5: *The LP_{01} Mode of SMF-28e Single Mode Fiber. Calculated using LP Fiber Mode Solver in OptiWave BPMCAD™.*

3.2.3 Practical Off-Chip Optical Mode Conversion

Corning's SMF-28[5] is the most widely deployed single-mode optical fiber (SMF) in high-speed communication networks. The fundamental LP_{01} mode of SMF-28e fiber is shown at 1550nm in Figure 3.5. The mode field diameter ω_0 of this LP_{01} mode[6] is 10.4μm±0.5μm at 1550nm. The overlap loss of this SMF LP_{01} mode, with the TE_0 mode of the modulator given in Figure 2.7 and Table 2.1, is 10.4dB.

Obviously, the need for mode conversion to couple the modulator output to the SMF is acute. It is valuable to explore the options available for decreasing the mode size of the SMF LP_{01} mode before designing a mode conversion structure that can be integrated with the modulator. Two methods for focusing the SMF LP_{01} mode will be explored.

The first mode conversion method tapers the SMF and lenses its output as shown in the insert on Figure 3.6a. The radius of the lens defines the minimum size of the near field focused spot. A set of lensed tapered fibers were obtained commercially and the far fields were measured using a Photon Inc. LD8900 Goniometric Radiometer. The lensed facet of a fiber under test was placed normally incident at the centre of the scanner aperture. The far fields were sampled in both horizontal (x) and vertical (y) directions at a wavelength of 1557nm. The near field Gaussian waist parameters (σ_x and σ_y) for the fiber were determined by fitting to the experimentally measured horizontal and vertical far fields, re-

---

[5] The most recent specification is SMF-28e.

[6] The width of the field distribution in a single-mode fiber is given by a radial Gaussian waist fit parameter to the LP_{01} mode, known as the mode field diameter ω_0.

spectively. For the x-z plane, substituting $(x,y,z)=(r\sin\phi,0,r\cos\phi)$ into Equation 3.11 gives,

$$I(x,0,z) = \frac{\pi^2\cos^2(\phi+C)\sigma_x^2\sigma_y^2}{\lambda^4 r^2}\exp\left(\frac{-k^2\sigma_x^2}{2}\sin^2(\phi+C)\right) \tag{3.13}$$

with C a parameter added to allow for angular misalignment between the fiber and the far field scanner. Equation 3.13 was used to fit the experimental intensity versus ϕ far field data with fit parameters σ_x^2, $\frac{\sigma_y^2}{r^2}$, and C. This fit directly provided the near field Gaussian waist parameter σ_x. A similar procedure allowed the σ_y waist parameter to be obtained from the vertical far field scan. Figure 3.6c plots the extracted near field Gaussian waist parameters, σ_x and σ_y, versus the fiber lens radius for 29 different fibers. Independent measurements for the fiber-to-fiber insertion loss, give losses as low as 1.0dB for two 10.0μm radius lensed fibers, however, the insertion loss climbs to 3.1dB for two 7.0μm radius lensed fibers. The increased loss is likely due to optical abberations. Note the increased spread in σ for fibers with a lens radius less than 9.0μm. A lens radius of 10μm, having a far field *FWHM* of 18.6^o and a near field Gaussian waist of σ=1.76μm, is a practical limit for this approach to reducing the spot-size of a single-mode fiber.

Alternatively, the far field was sampled at various θ angles to assemble a two dimensional map of the far field intensity as shown in Figure 3.6a. This two dimensional contour map can be fit using the spherical co-ordinate form of Equation 3.10,

$$I(r,\theta,\phi) = \frac{\pi^2\sigma_x^2\sigma_y^2}{\lambda^4 r^2}\cos^2(\phi+C)\exp\left(\frac{-k^2}{2}\sin^2(\phi+C)\left(\sigma_x^2\cos^2(\theta+D)+\sigma_y^2\sin^2(\theta+D)\right)\right) \tag{3.14}$$

where C and D are parameters that allow for angular misalignment between the fiber and the scanner. This two dimensional fit function allowed both near field waist parameters, σ_x and σ_y, to be obtained directly. Note that the value of r is unknown and it is treated as a fit parameter in Equation 3.14. Figure 3.6b shows an example of the (θ,ϕ) contour plot of the far field intensity along with the corresponding fit using Equation 3.14.

A second off-chip optical mode conversion technique uses a lens to magnify the near field of the device facet onto the fiber mode. Figure 3.7a shows a magnifying lens assembly designed by a colleague Keith Anderson. In this figure a SELFOC GRIN lens is used to collimate the SMF output. This SELFOC is followed by an aspheric lens[7] with ≈4.5X demagnification to focus the collimated spot onto the device facet. The far field measured using the Photon Inc. LD8900 Goniometric Radiometer, from one of these lens assemblies, is shown in Figure 3.7b. In Figure 3.7c the measured horizontal and vertical far field scans are shown along with fits from Equation 3.13. The average extracted near field Gaussian waist parameters from four difference lens assemblies are σ_x=1.251μm and σ_y=1.257μm. The measured insertion loss between two lens assemblies is typically <1.8dB.

It is clear from the above two examples that off-chip mode conversion of the SMF LP_{01} mode can reduce the spot-size of the coupling mode into the range of σ=1.3μm-1.8μm. A

---

[7] Aspheric lenses are commercially available with numerical aperture up to 0.6.

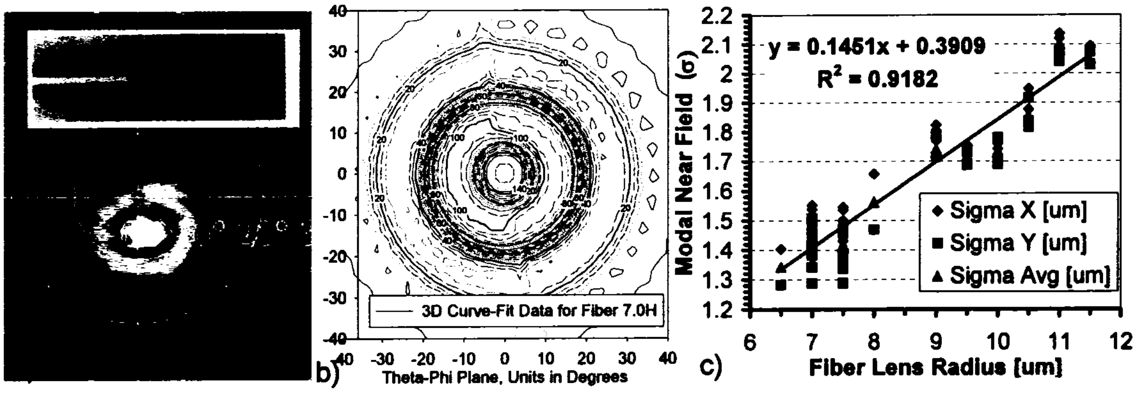

Figure 3.6: *Far Field Measurements on Tapered and Lensed Single Mode Fibers: a) Measured Far Field Intensity with Insert Picture of the Fiber, b) (θ,φ) Contour Plot of Far Field Intensity and Fit from Equation 3.14, c) Extracted Near Field Mode Gaussian Waist Parameter σ versus the Fiber Lens Radius for 29 Fibers.*

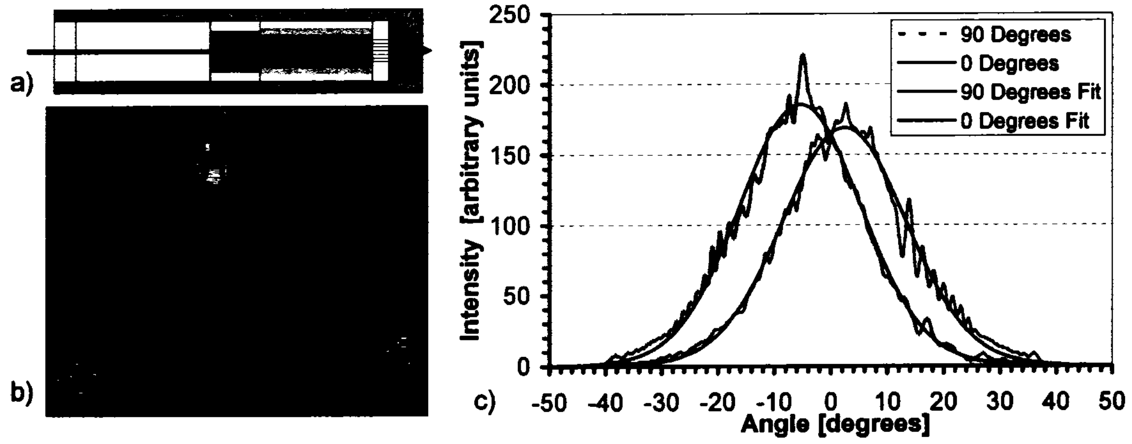

Figure 3.7: *Lens Assembly for High NA Coupling: a) Optics Design by Keith Anderson, b) Measured Two Dimensional Far Field, c) Measured Horizontal and Vertical Far Field Scans with Fits from Equation 3.13.*

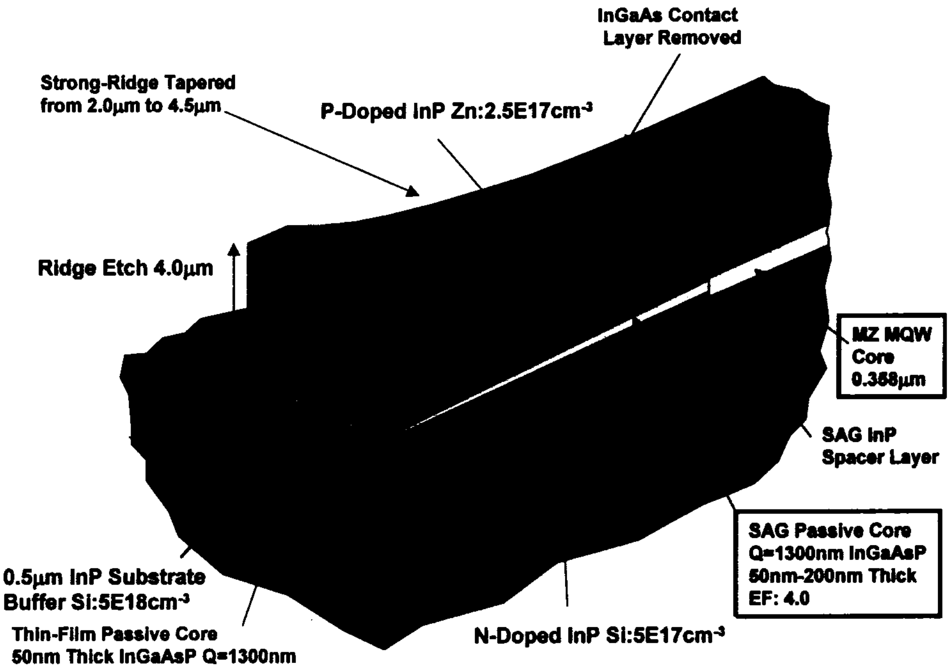

Figure 3.8: *Overview of the Spot-Size Converter Design.*

coupling spot-size at the upper end of this range, is shown in Figure 3.4, to give 0.5μm of misalignment tolerance for 0.5dB of additional insertion loss. This level of alignment tolerance can be comfortably achieved in a manufacturing environment using active feedback alignment processes.

3.3 Overview of the Spot-Size Converter Design

An illustration of the SSC design developed to couple with a tapered fiber or lens assembly is given in Figure 3.8. Each SSC has a vertically tapered passive waveguide core within a laterally flared strongly-guided ridge. The SSC core is butt-joined to the modulator section by a precision dry etch and MOCVD selective area growth (SAG) process. This SAG process enables the thickness of the passive core to adiabatically taper over 350μm, from 0.2μm at the butt-joint down to 0.05μm at the facet. Simultaneously, the lateral ridge width flares exponentially over 300μm, from 2.0μm at the butt-joint to 4.5μm at the facet. The SSC transitions the modulator mode at the butt-joint to a facet mode that has been designed for low-loss coupling to micro-lenses or tapered fiber.

The fabrication of the SSC is detailed in Chapter 4. Here the output facet waveguide design, the active modulator-to-SSC core butt-joint, the lateral and vertical taper designs, and BPM models of the full SSC structure are studied. The Chapter concludes with a summary of the growth structures required to integrate the Mach-Zehnder modulator developed in

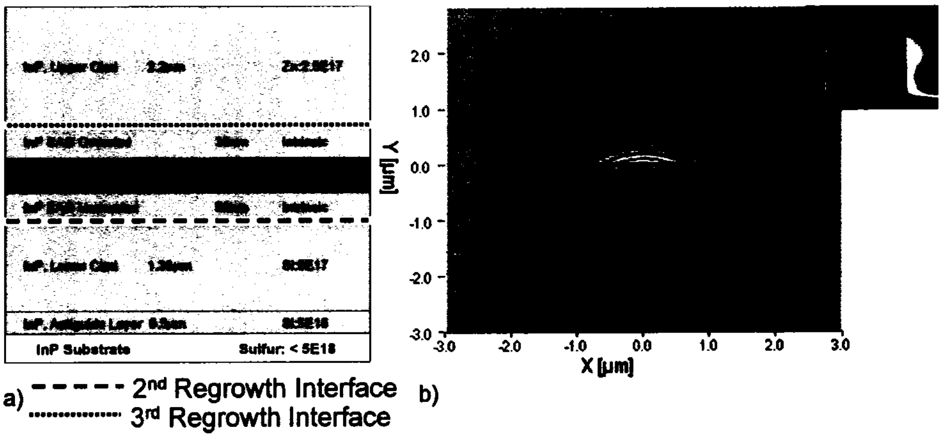

Figure 3.9: *a) Spot-Size Converter Facet Growth Structure, b) TE$_0$ Field Intensity at 1546nm with an Insert of a Facet SEM Cross-Section.*

Chapter 2 with the SSC design.

3.4 Output Facet Waveguide Design

In this Section, the selected facet waveguide design is summarized, and a discussion of the facet waveguide mode reflectivity is given. The details behind the selection of the core design and the ridge width are provided. The Section ends with a thorough investigation into higher order modes in the selected, and several alternative, SSC waveguide facet structures.

3.4.1 Summary of the Selected Facet Waveguide Design

Figure 3.9 presents the cross-sectional growth structure at the waveguide facet for the selected SSC design, along with the corresponding optical TE$_0$ coupling mode at 1546nm. The refractive indices used for the materials are defined in Appendix 1 and 2 of Chapter 2. The facet optical mode is calculated with a 128X128 point non-uniform grid finite-difference mode solver using perfectly matched layer boundary conditions in a 10μmX10μm space. The etch depth is 4.0μm, common to both the modulator and the SSC, with a waveguide ridge width of 4.5μm at the facet. The growth layers below the second regrowth interface, denoted in Figure 3.9a by the thick dashed line, and above the third regrowth interface, denoted in Figure 3.9a by the dotted line, are common to the modulator and SSC cross-sectional structures. The thickness of the underclad InP layer at the SSC facet is a function of the process used to etch away the modulator core, as discussed in Section 4.3.1.

Parameter	1527nm TE_0	1527nm TM_0	1565nm TE_0	1565nm TM_0
Overlap Si 5E17cm^{-3} N Doping	0.4168	0.4217	0.4138	0.4193
Overlap Si 5E18cm^{-3} N Doping	0.0124	0.0144	0.0133	0.0153
Overlap N Substrate	4.33E-3	5.30E-3	4.90E-3	5.90E-3
Overlap Zn P Doping	0.5246	0.5286	0.5278	0.53041
Mode Field σ_x	1.60259	1.65004	1.60352	1.65197
Mode Field σ_y	1.35219	1.38739	1.38078	1.40989
N_{eff}	3.17269	3.1717	3.16768	3.16679

Table 3.1: ***Waveguide Properties for the Spot-Size Converter Facet Structure.***

The optimal near field Gaussian waist parameters of the TE_0 mode have σ_x=1.603μm and σ_y=1.3665μm at 1546nm. The intensity angular FWHM far field for this TE_0 mode is 20.3°X23.7° using Equation 3.12. The experimental measurement of the far field is discussed in Section 4.7.3 and presented in Figure 4.34. In both lateral and vertical directions the experimental measurements have larger far fields, however the agreement within 1.5° laterally and 0.7° vertically, is excellent.

In Table 3.1 the TE_0 and TM_0 waveguide properties of the spot-size converter facet structure are summarized at the short and long ends of the C-Band telecom wavelength window. The mode effective indices (N_{eff}), the near field Gaussian waist parameters (σ_x,σ_y), and the optical overlaps to the Zn InP p-doping in the overclad and the Si n-doping in the InP underclad are provided.

The significant overlap between the dopants in the growth structure and the optical field intensity introduces optical free carrier absorption loss mechanisms into the SSC design, as discussed in Section 2.1.7. The impact of the optical mode dopant overlap is quantified in Figure 3.30 and Table 3.3. The inclusion of the dopants in the SSC design is a trade-off made for fabrication simplicity when monolithically integrating the SSC with the modulator structure.

3.4.2 Facet Waveguide Mode Reflectivity

An antireflection coating will be applied to the SSC waveguide facet as discussed in Section 4.6. The manufacturable target for the coated facet backreflectivity is 0.1%. There are, however, applications [47, 52] where it is desirable to have a backreflectivity below this coated facet limit. As shown in Figure 3.10, the backreflectivity of the SSC waveguide facet can be improved by angling the waveguide approach to the facet. The waveguide mode $E(x)$ has been overlapped with a 100% reflected image $E'(x)$ given by,

$$E'(x) = E(x) \cdot \exp\left[i\beta \cdot 2(x - x_0)\tan\alpha\right] \qquad (3.15)$$

where $\beta = n_{eff} \cdot k_o$ is the TE_0 mode propagation constant, and Figure 3.10b defines the geometric variables. Note the exit angle is approximately n_{eff} times the input facet angle

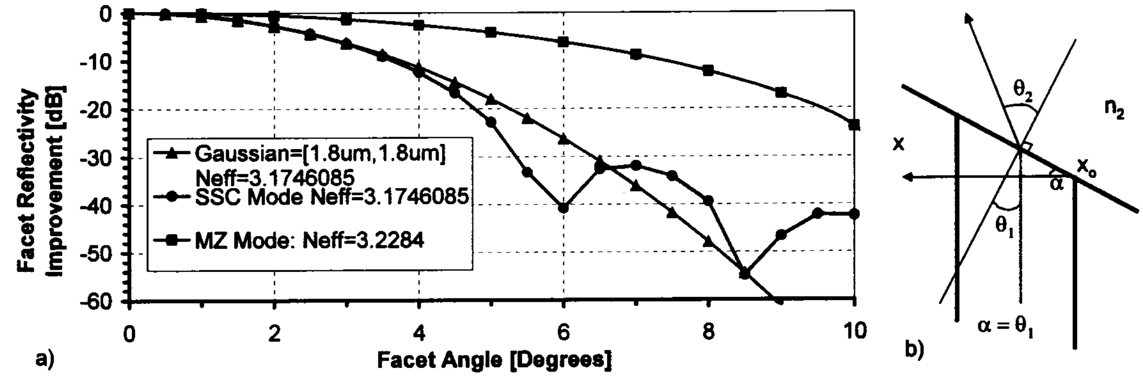

Figure 3.10: *Impact of Facet Angle on* TE_0 *Optical Backreflectivity*

from Snell's Law.[8]

For an input waveguide angle of 6°, corresponding to an output beam angle of 19°, Figure 3.10 shows it is possible to have <−60dB backreflection from the SSC output facet. Larger input waveguide angles are not desirable since the corresponding large output beam angles will significantly complicate the device package assembly. It is also clear from Figure 3.10 that the modulator waveguide without a SSC cannot benefit significantly from being angled at the output facet due to its limited lateral field extent in x.

The input waveguide angle of 6° can be implemented in the strongly-guided modulator structure prior to the spot-size converter butt-joint using a matched bend circular arc, 49.65μm long in z, with a radius of 474μm. The theory of matched bends is discussed in Section 2.3.5. The experimental improvement in SSC facet backreflection measured for a 5° input waveguide angle is discussed in Section 4.7.5.

3.4.3 Selection of the Core Design

The vertical extent of the TE_0 facet mode is determined by the thickness and composition of a single quaternary layer. Figure 3.11a gives the vertical near field Gaussian waist parameter σ of this TE_0 mode as a function of the thin quaternary layer thickness and composition. Figure 3.11a assumes the upper and lower InP clad layer thicknesses are of infinite extent. The selection of a thickness and composition for the thin quaternary layer at the facet requires a trade-off between the properties of the SSC waveguide mode at the facet and the butt-joint to the modulator.

The single quaternary layer is common throughout the SSC, however, the layer will vary in thickness and composition due to the use of the selective area growth technique discussed in Section 3.6.3. It is assumed here that a selective area growth thickness enhancement factor of four times the nominal facet growth thickness is technically feasible. In Section 3.2.3

---

[8] $\theta_2 = \sin^{-1}\left(\frac{n_1}{n_2}\cdot\sin\theta_1\right) \simeq \frac{n_1}{n_2}\theta_1$ where $n_1=n_{eff}$, $n_2=1$ and θ_1 is a small angle.

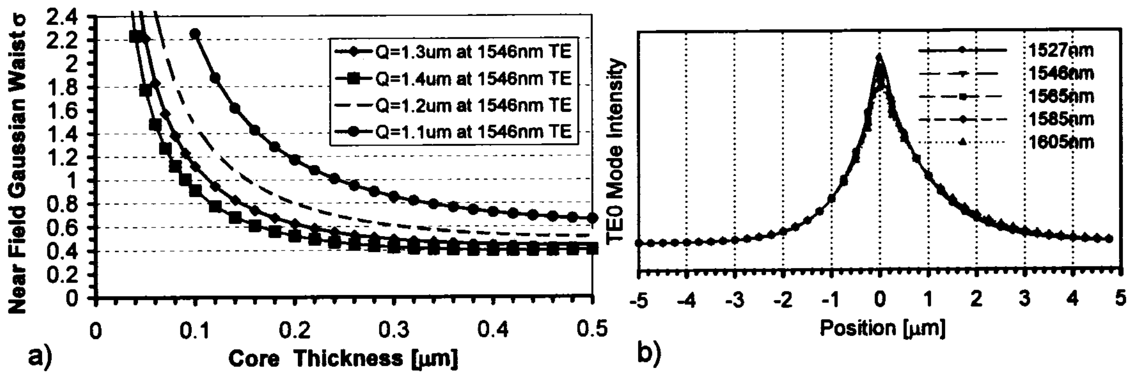

Figure 3.11: *One Dimensional Optical Mode Models for the Spot-Size Converter Facet Waveguide: a) Near Field Gaussian Waist σ as a Function of Thickness and Composition, b) TE_0 Mode Intensity Profiles across C and L Bands.*

it was determined that practical off-chip optical mode conversion can provide a coupling near field Gaussian waist σ between 1.3μm and 1.8μm. Also, Table 2.1 indicates the modulator TE_0 mode has a vertical Gaussian waist parameter σ_y of 0.50μm at 1546nm. Based on these three pieces of information, a facet quaternary design with a thickness of 0.05μm and a composition of 1.3μm was selected, from Figure 3.11a, as the best compromise between good coupling to the modulator TE_0 mode for the enhanced growth structure at the butt-joint, and good coupling to an optical lens assembly for the unenhanced growth structure at the waveguide facet. Figure 3.11b shows the facet TE_0 vertical mode profile of this layer design over the telecom wavelength window of interest from 1527nm to 1605nm. Near wavelength independent coupling to this facet mode is expected.

Figure 3.12a quantifies the impact of finite upper and lower InP clad layer thickness on the vertical extent of the TE_0 optical mode in the SSC facet structure. The near field Gaussian waist parameter σ increases by a maximum of ~10% when the underclad InP layer thickness increases (diamonds and squares) and the upper-clad InP layer thickness is fixed.[9] However, σ increases rapidly when the upper-clad InP layer thickness increases (triangle and circle) and the underclad InP layer thickness is fixed. It is apparent that the thickness of the overclad InP layer is more significant than the thickness of the underclad InP layer in determining the vertical extent of the optical TE_0 mode. The overclad InP layer thickness is practically limited by the available waveguide etch technology, and the underclad InP layer thickness is limited by the time and cost of growth in a MOCVD reactor. An overclad InP layer thickness of 2.23μm and an underclad InP layer thickness of 1.5μm have been selected for the SSC facet waveguide structure.

Figure 3.12b studies the impact of the doping concentration in the various layers under the core[10] on the vertical extent of the TE_0 optical mode in the SSC facet structure. The overclad InP layer thickness is fixed at 2.23μm and the underclad InP layer thickness is fixed at

---

[9] The fit parameter σ also saturates beyond an underclad InP thickness of ~4.0μm.

[10] Variation of the p-doping concentration in the layers above the core does not significantly change the refractive index of the material as discussed in Section 2.1.7.

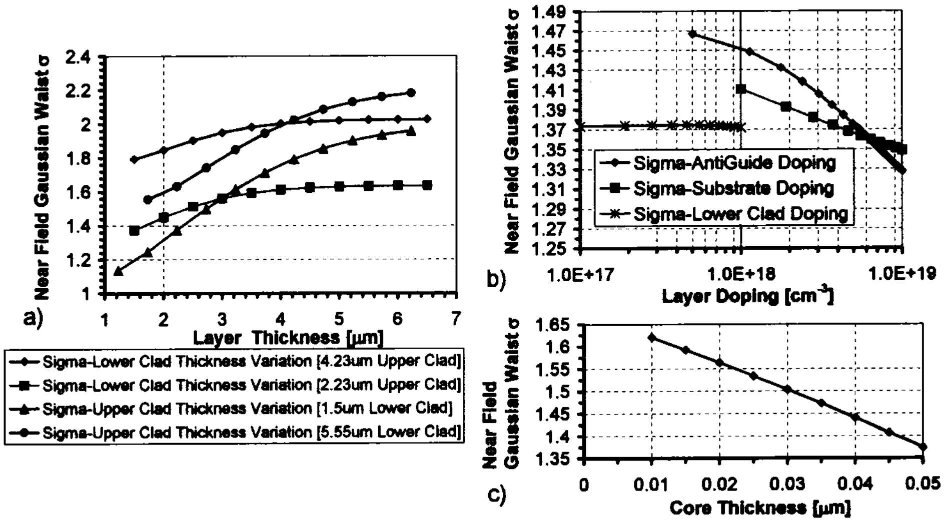

Figure 3.12: ***Vertical Optical Mode Size of the Spot-Size Converter Facet Waveguide: a) Impact of InP Upper and Underclad Thickness on the Near Field Gaussian Waist σ, b) Impact of the Doping in the InP Layers under the Core on the Near Field Gaussian Waist σ, c) Impact of the Core Thickness on the Near Field Intensity Gaussian Waist σ.***

1.5μm. Only one layer doping is modified at a time; the other layers have the nominal doping values shown in Figure 3.9a. Changes in the underclad InP layer doping or the substrate doping[11] have little to no impact on the near field Gaussian waist parameter σ. The antiguiding layer doping at 5E18cm^{-3}, however, does reduce σ by approximately 6% relative to a dopant concentration of 5E17cm^{-3}.[12] This reduction must be tolerated since the antiguiding layer is required to control higher order vertical modes as discussed in Section 3.4.5 and Section 2.1.12.

Figure 3.12c provides the near field Gaussian waist parameter σ as a function of the core thickness; all other layers have the nominal thickness and doping values shown in Figure 3.9a. At a core thickness of 0.05μm the near field Gaussian waist parameter σ is greater than the 1.3μm minimum desired for good coupling to a lens assembly. Obviously a thinner core could increase the facet mode σ by up to 18%, however, the reduction in lens assembly coupling losses would be swamped by a significant increase in the butt-joint coupling loss to the modulator waveguide TE$_0$ mode. The butt-joint coupling loss is discussed in Section 3.5.

3.4.4 Selection of the Ridge Width

Figure 3.13 presents intensity contour plots for the waveguide TE facet modes in the spot-size converter for ridge widths between 2.0μm and 6.0μm. The facet optical modes are

---

[11] The typical Sulfur doping range for a N$^+$ substrate is between 2-8E18cm^{-3}.

[12] 5E17cm^{-3} is the same dopant concentration as the underclad InP layer.

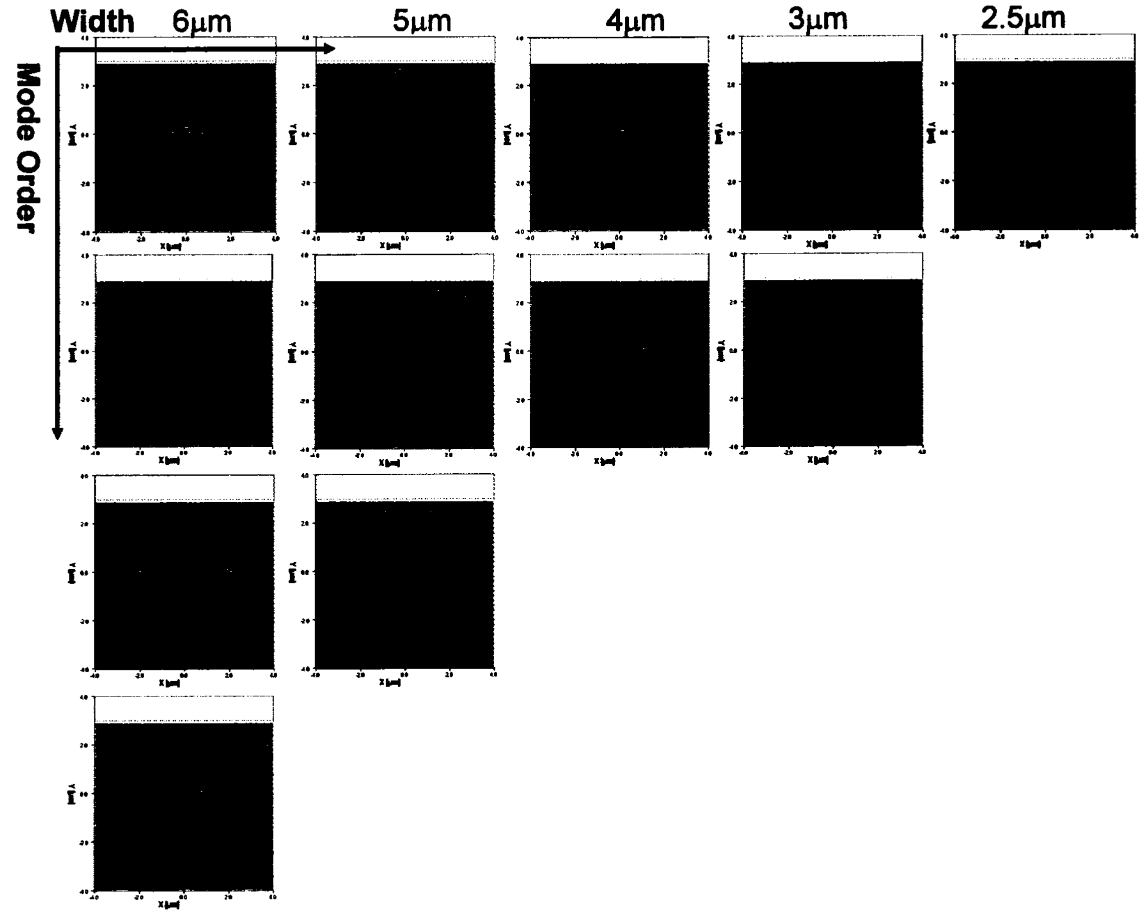

Figure 3.13: ***Intensity Contour Plots for the Waveguide TE Facet Modes in the Spot-Size Converter as a Function of Ridge Width.***

calculated at 1546nm with a 256X256 point non-uniform grid finite-difference mode solver using perfectly matched layer boundary conditions in a 10μmX10μm space. The etch depth is 4.0μm. Note that no higher-order vertical modes are found in the facet structure at any waveguide width. The lateral TE_2 mode is cut-off for a ridge width between 4.0μm and 5.0μm.

In Figure 3.14a the TE_0 mode near field Gaussian waist parameters σ_x and σ_y are given, along with the corresponding lateral far field intensity FWHM using Equation 3.12. It is clear from Figure 3.14a that a ridge width of 4.0μm best matches the vertical and lateral TE_0 mode extents. The selected width used in this thesis as the nominal design is actually 4.5μm. The insertion loss improvement available between a 4.5μm ridge width and the optimal 4.0μm width is <0.1dB. In Figure 3.14b the TE_0 mode N_{eff} values are tabulated as a function of the ridge width.

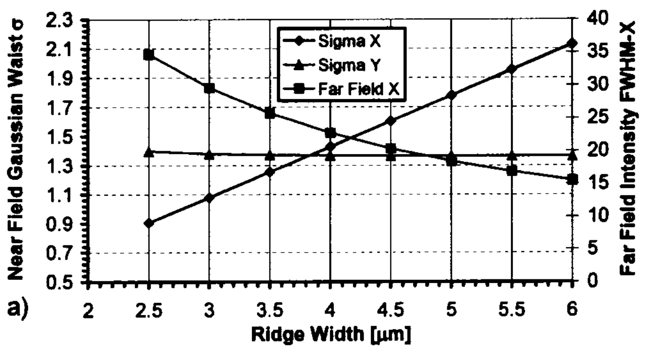

b)

Ridge Width	TE0 Neff
6	3.172118
5.5	3.171631
5	3.170992
4.5	3.170130
4	3.168928
3.5	3.167182
3	3.164505
2.5	3.160100
2	3.151885

Figure 3.14: *a) TE_0 Mode Near Field Gaussian Waist and Lateral FWHM Far Field at the SSC Facet as a Function of Ridge Width, b) TE_0 Effective Index at the SSC Facet as a Function of Ridge Width.*

3.4.5 Investigation of Higher Order Modes in the SSC Facet Structure

Figure 3.15 presents intensity contour plots for the waveguide TE facet modes in the spot-size converter, at 1546nm, as a function of the InP overclad and underclad layer thicknesses. All other waveguide parameters are as defined in Figure 3.9a. The facet optical modes are calculated with a 256X256 point non-uniform grid finite-difference mode solver using perfectly matched layer boundary conditions in a 10μmX10μm space. The etch depth is 4.0μm and the ridge width is 4.5μm.

In Figure 3.15a the TE_0, TE_1 and TE_2 facet modes are shown for the nominal thickness of the InP overclad and underclad layers as defined in Figure 3.9a. There are no higher order vertical modes in the structure. The lateral TE_2 mode leaks to the substrate with a loss of 37.5dB/cm.

In Figure 3.15b the underclad InP layer thickness has been increased by +0.6μm and the TE_0, TE_1 and TE_2 facet modes are again shown, along with a new leaky TE_{01} higher order vertical mode. The substrate leakage of the lateral TE_2 mode has increased to 100dB/cm due to the increased thickness of the underclad InP layer below the ridge etch. The vertical extent of the TE_0 mode has also increased slightly from σ=1.367μm to σ=1.464μm. Unfortunately the increased thickness of the underclad InP layer below the ridge etch introduced the TE_{01} mode with a leakage of 62dB/cm. Any further increase in the underclad InP layer thickness reduces the leakage of this TE_{01} mode.

Figure 3.15c uses the same structure as Figure 3.15b with an additional 0.2μm added to the overclad InP layer and an increase in the etch depth to 4.2μm. Note, a slight increase in the TE_0 vertical mode extent is obtained, from σ=1.464μm to σ=1.514μm. Unfortunately, the substrate leakage of the higher order TE_{01} mode is also reduced to 27dB/cm from 62dB/cm.

In summary, Figure 3.15 shows that it is possible to gain a slight reduction in the vertical far field of the TE_0 facet mode by increasing both the overclad and underclad InP layer thicknesses as expected. However, changes in the overclad and underclad layer thicknesses

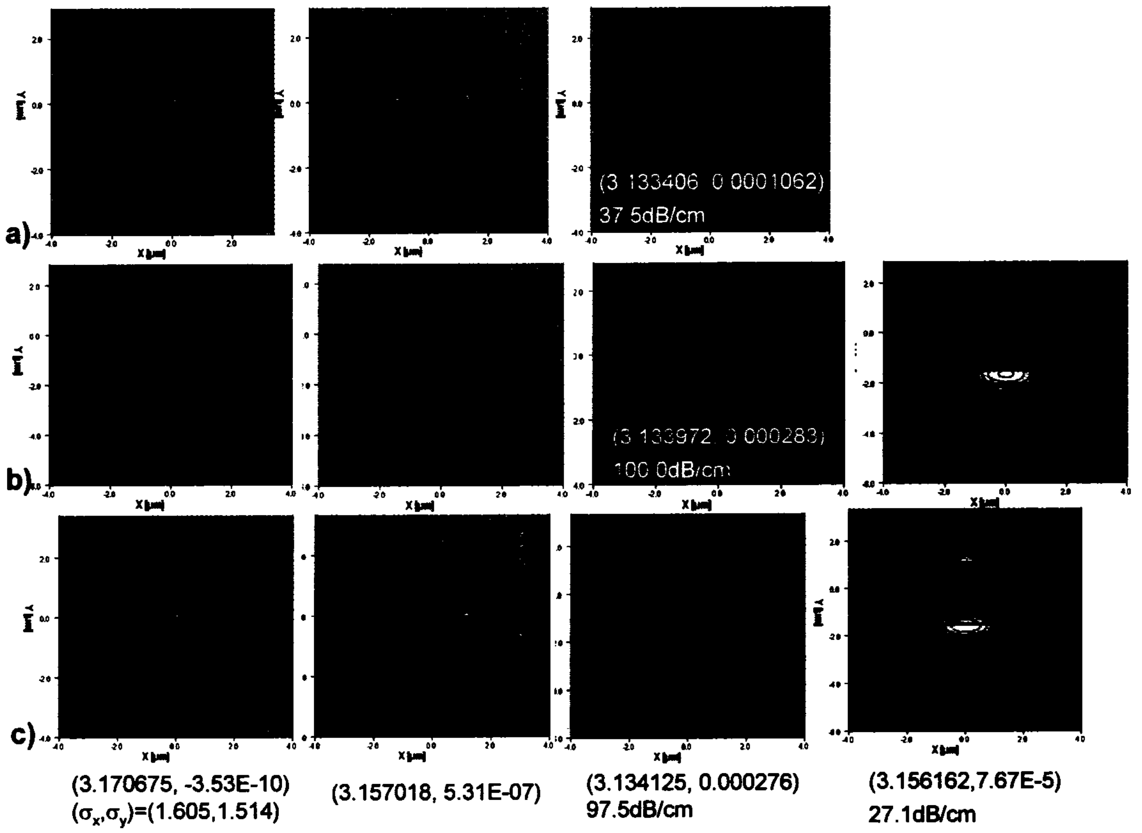

Figure 3.15: ***Intensity Contour Plots for the Waveguide TE Facet Modes in the Spot-Size Converter as a Function of the InP Cladding Design I-Antiguiding Layer: a) Nominal Design with 4µm Etch Depth, b) Additional 0.6µm of N=5E17cm^{-3} InP Underclad with a 4µm Etch Depth, c) Additional 0.6µm of N=5E17cm^{-3} InP Underclad and an Additional 0.2µm of P=2.5E17cm^{-3} InP Overclad with 4.2µm Etch Depth.***

make it difficult to avoid a higher order vertical TE$_{01}$ mode at the facet.

A modified waveguide facet structure, with no antiguiding layer[13], and a substantially thicker underclad InP layer was considered. The design goals for this modified waveguide were to improve the vertical extent of the TE$_0$ mode while simultaneously placing the higher order lateral waveguide modes beyond cut-off. The hypothesized cost for these improvements would be well defined guiding of the higher order vertical TE$_{01}$ mode.

Figure 3.16a presents intensity contour plots for the waveguide TE facet modes in a modified spot-size converter structure, at 1546nm, where the antiguiding layer Si doping is reduced to 5E17cm^{-3} and the substrate sulfur doping is increased to 5E18cm^{-3}. All other waveguide parameters are as defined in Figure 3.9a. The facet optical modes are calculated with a 256X256 point non-uniform grid finite-difference mode solver using perfectly

---

[13] Actually the low refractive index step associated with this layer is removed so that it is no longer an antiguiding layer. It is still physically present in the structure.

matched layer boundary conditions in a 10μmX10μm space. The etch depth is 4.0μm and the ridge width is 4.5μm.

Comparing the higher order modes in Figure 3.16a to the higher order modes in Figure 3.15a allows us to study the impact of removing the antiguiding layer refractive index step. From these figures it is clear that removing the antiguiding layer refractive index step increases the substrate leakage rate for the TE_2 mode, from 37dB/cm to 61dB/cm, but it has no impact on the TE_1 mode. This negligible improvement in the leakage rates of the higher order lateral modes is obtained at the cost of a guided higher order vertical TE_{01} mode. Figure 3.16b shows that increasing the etch depth from 4.0μm to 4.5μm has no impact on the leakage rate of this TE_{01} mode.

The structure and simulation conditions for the intensity contour plots in Figure 3.16c are identical with those in Figure 3.16a except the overclad InP layer thickness has been increased by 0.2μm and the underclad InP layer thickness has been increased to 2.2μm. These InP layer thickness increases have expanded the vertical extent of the TE_0 mode to σ=1.663μm, and also increased the leakage of the higher order lateral modes in the structure. The TE_1 mode now leaks with 16dB/cm to the substrate and the TE_2 mode leakage has increased substantially to 215dB/cm, however, the original design goal of placing both the TE_1 and TE_2 modes well beyond cut-off has not been achieved.

The modified waveguide facet structure, with no antiguiding layer, and a substantially thicker underclad InP layer was rejected since it introduced a higher order vertical TE_{01} mode in the structure without cutting off the higher order lateral TE_1 mode. It did, however, produce a TE_0 mode with a reduced vertical far field dimension.

An alternative waveguide facet structure was considered as shown in Figure 3.17a. In this structure two additional thin quaternary layers[14] were added to the n-doped InP underclad to move the centre of the TE_0 facet mode towards the substrate by 0.9μm, as shown in Figure 3.17b. The multi-core nature of this facet structure enables a larger symmetric TE_0 mode to be obtained without increasing the necessary etch depth. A convenient feature of this design is that it can be implemented with a simple modification to only the first growth of the structure. The underclad quaternary layers are far enough removed from the SAG core to have no impact on the modulator TE_0 mode. The total 0.1μm thickness for these two layers is small enough that the added thermal impedance in the path between the modulator core and the N^+ substrate is negligible.

This alternative waveguide facet design has not been pursued since, as shown in Figure 3.17c, it contains guided higher-order TE_1 and TE_{01} modes. A multimode coupling structure of this nature is most useful in optical sources, where the misalignment of the collection optics cannot excite the higher order modes in the waveguide structure, however, in device applications that can use a semi-insulating substrate[15], it is possible to re-

---

[14] To obtain the 0.93μm underclad between the SAG core and the first Q=1.3μm layer requires the grow of $\sim 1\mu m$ in the first growth due to the loss of material from the etch and regrowth for the SSC.

[15] A semi-insulating (SI) substrate is iron doped with a real refractive index nearly unchanged relative to undoped InP [92].

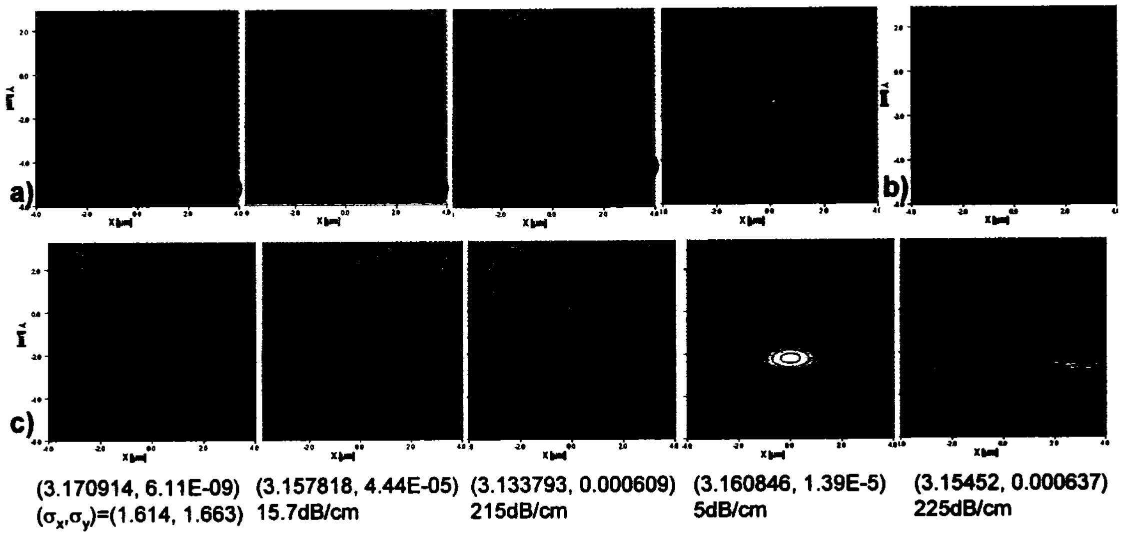

Figure 3.16: *Intensity Contour Plots for the Waveguide TE Facet Modes in the Spot-Size Converter as a Function of the InP Cladding Design II–No Antiguiding Doping: a) Nominal Design with an Antiguiding Layer Si Doping of 5E17cm^{-3} and a Substrate Sulfur Doping of 5E18cm^{-3}, b) Higher Order Vertical TE Mode for the Structure in (a) with an Additional 0.5μm Increase in Etch Depth, c) Structure in (a) with the Underclad 5E17cm^{-3} Si-Doped InP Layer Increased to 2.2μm and the Overclad Zn-Doped InP Layer increased by 0.2μm.*

move the higher-order vertical and lateral modes, as shown in Figure 3.18. In Figure 3.18 no higher-order modes are found in the facet or modulator waveguide structures when the thin underclad quaternary layers are present, since these higher-order modes are bled into the substrate by the substrate's higher refractive index than the adjacent n-doped InP layers.

The final facet structure design, shown in Figure 3.9, has been selected after accounting for the feasible off-chip SMF mode conversion, the material doping requirements in the Mach-Zehnder modulator, low-loss coupling at the SSC-to-modulator butt-joint, and control of the higher-order vertical modes in the structure.

3.5 Active Modulator and SSC Core Butt-Joint Design

The chosen optical mode spot-size converter design *does not* share a common active layer growth with the modulator. If a selective area growth process were employed generate a common core, it would be the more design sensitive modulator active region that would be grown with thickness enhancement. The thickness of the modulator active region would also have to be reduced in this scenario for two related reasons: the maximum available growth enhancement is technologically limited to approximately five times the nominal growth thickness; and, as shown in Figure 3.11a, a very thin core is required at the facet.

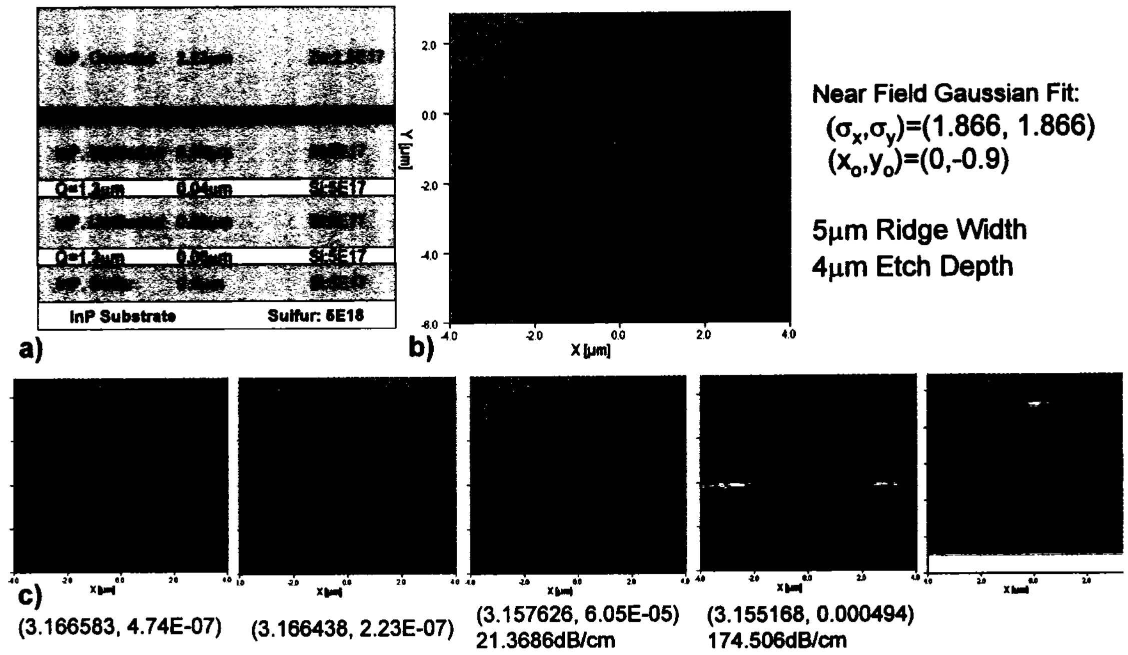

Figure 3.17: ***Waveguide TE Modes for an Alternative Spot-Size Converter Facet Structure on a N^+ Doped Substrate: a) Alternative Facet Growth Structure, b) Facet Mode TE_0 Field Intensity, c) Higher Order TE Facet Modes.***

Given the quantum well nature of the modulator core, under enhanced growth a significant absorption bandedge shift would also be expected, as shown in Figure 3.19. A common active layer growth process is, therefore, undesirable since it would compromise and strongly couple the spot-size converter and modulator core designs.

The chosen optical mode spot-size converter design deposits the SSC core growth butt-jointed to the modulator core growth by an etch-and-selective-area-regrowth technique. The selective-area-regrowth technique is discussed in Section 3.6.3. This approach allows the same SSC design to be adapted to a variety of active modulator core designs. For example, Section 4.7.6 details an electro-absorption modulator for 40Gb/s operation, fabricated using the same optical mode spot-size converter design as detailed here for the Mach-Zehnder modulator.

In this Section the optical loss and backreflectivity characteristics of the modulator-to-SSC butt-jointed waveguide discontinuity are explored. The implementation details for the etch and regrowth technique are discussed in detail in Section 4.3. The modulator core design was introduced in Figure 2.6a. For the waveguide butt-joint the points of practical consideration are:

- It is not technologically possible to achieve perfect vertical alignment between the modulator and mode converter cores. The impact of this on the loss and backreflectivity must be determined.

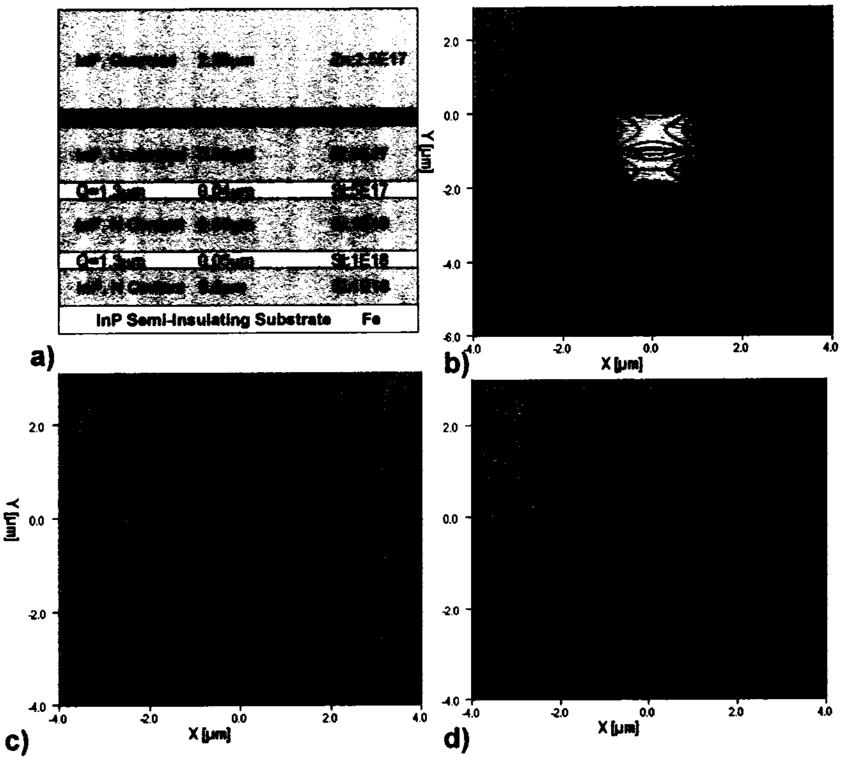

Near Field Gaussian Fit:
$(\sigma_x,\sigma_y)=(2.113, 2.242)$
$(x_0,y_0)=(0.0, -1.073)$
Far Field Intensity FWHM
(15.548°,14.671°)

5.5µm Ridge Width
4.0µm Etch Depth

Figure 3.18: *Waveguide TE Modes for an Alternative Spot-Size Converter Facet Structure on a Semi-Insulating Fe Doped Substrate: a) Alternative Facet Growth Structure, b) Facet Mode TE_0 Field Intensity, c) Modulator Mode TE_0 Field Intensity, d) Modulator Mode TE_1 Field Intensity.*

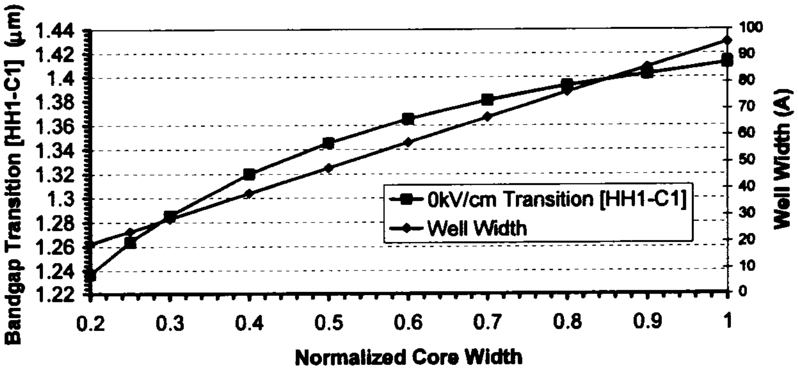

Figure 3.19: *Impact of Enhancement on a Mach-Zehnder Quantum Well for 0kV/cm Bandgap Transition [No Inter-Well Coupling.] Source: RecGen Material Model by Witold Bardyszewski*

- It is not always possible to achieve a perfect discontinuity in the z direction. A transition length is likely. If this transition remains on the order of less than a few wavelengths of light its impact on the loss and backreflectivity properties will be assumed to be negligible.
- Given the physics of the selective area MOCVD growth process, the exact composition of the mode converter core at the butt-joint is difficult to determine. The impact of the variations must be considered.
- The available enhancement by a selective area growth process is limited. A design trade-off has, therefore, been necessary between the size of the output mode and the overlap loss between the SSC and modulator modes at the butt-joint. To make this design trade-off the overlap loss must be understood as a function of the SSC core thickness.

3.5.1 Butt-Joint Losses

The vertical extent of the TE_0 mode at the modulator butt-joint in the SSC is determined by the thickness and composition of the single quaternary layer in the second growth under the maximum selective area growth enhancement. The reduced vertical extent of the TE_0 mode at the modulator butt-joint makes it less sensitive to the thickness and doping of the cladding InP layers. Figure 3.20a provides the vertical near field Gaussian waist parameter σ of this TE_0 mode as a function of the quaternary layer thickness and composition under maximum SAG enhancement at 1546nm.

Section 3.4.3 concluded that the nominal single layer quaternary design for the second growth should have a thickness of $0.05\mu m$ and a composition of $Q=1.3\mu m$. In Section 4.3.2 the thickness of the quaternary layer at the butt-joint in the optimized selective area growth process is shown to be $0.18\mu m$-$0.2\mu m$. The composition of the selective area grown quaternary layer is expected to increase in conjunction with the thickness enhancement as discussed in Section 3.9.2 and Section 4.3.2. Results from experimental measurements detailed in Section 4.4 and given in Figure 4.22 indicate this composition shift can be up to 100nm. Therefore, in Figure 3.20a the expected butt-joint SSC waveguide structure could have a composition up to $Q=1.4\mu m$ and a thickness of $0.18\mu m$-$0.2\mu m$. The vertical near field Gaussian waist parameter σ for these possible modes in Figure 3.20a are well matched with the modulator mode σ_y of $0.50\mu m$[16] in Table 2.1. In Figure 3.20b the mode field intensities are plotted for the $0.18\mu m$ thick butt-joint SSC mode with $Q=1.3\mu m$ and $Q=1.4\mu m$ along with the modulator waveguide mode, all at 1546nm. Excellent overlap losses are expected. In Figure 3.21 the calculated overlap losses are presented as a function of butt-joint vertical misalignment. As discussed in Section 4.3.2 the SSC butt-joint core and the modulator core can be aligned to within better than $0.05\mu m$, indicating a butt-joint loss of less than 0.2dB.

---

[16] Gaussian fit parameter σ_y at 1546nm.

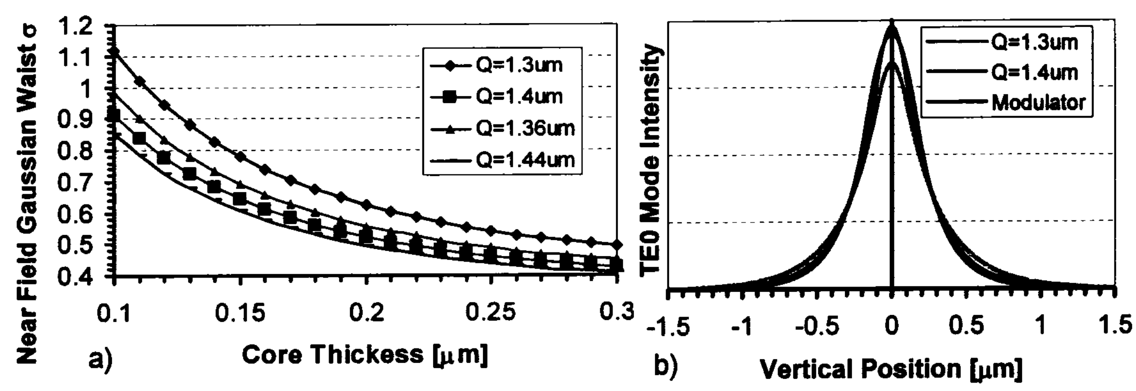

Figure 3.20: *a) Near Field Gaussian Waist as a Function of Thickness and Composition for the Spot-Size Converter Waveguide at the Butt-Joint, b) 1D Vertical Waveguide Modes on Either Side of the Butt-Joint.*

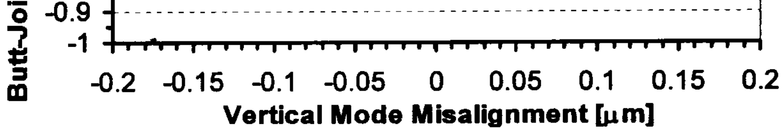

Figure 3.21: *Insertion Loss Impact of Vertical Misalignment between the Spot-Size Converter Core and the Modulator Core*

3.5.2 Backreflectivity Calculations for the Butt-Joint

In Figure 3.22a the butt-joint transition between the SSC waveguide structure and the modulator structure has been approximated as a zero length single interface transition having a variable offset between the centres of the waveguide cores. The associated refractive index values for the materials at 1546nm are given.

Deriving the reflection from a single interface using the scalar Helmholtz wave equation yields a square root operator within a reflection operator. Padé approximants have been employed to expand these square root operators [242], however, such methods suffer from accuracy limitations associated with the contributions of evanescent modes to the reflection operator. We have shown [239, 240] that the numerical instability associated with the use of real Padé primes can be removed by using branch-cut rotation [241] of the square-root operator.

In Figure 3.22b the TE_0 reflection from the modulator-to-SSC butt-joint is calculated according to the techniques detailed in [239] for a $\frac{\pi}{2}$ branch-cut rotation as a function of the Padé order. Beyond a Padé order of 9 the reflection stabilizes at -48.74dB[17].

In Figure 3.22c the TE_0 and total reflected power is mapped as a function of the core offsets for a $\frac{\pi}{2}$ branch-cut rotation and a Padé order of 10. Even with a core misalignment of 0.2μm the TE_0 reflected power remains below -35dB.

In Figure 3.22d the backreflectivity is explored for the possible variation in the SSC composition at the butt-joint and the two possible mode reflection directions, again using $\frac{\pi}{2}$ branch-cut rotation and Padé order 10 approximants in the reflection operator. In all cases the TE_0 backreflectivity remains below -42dB.

Backreflectivity of the TE_0 mode from the SSC-to-modulator butt-joint at the levels indicated in Figure 3.22 will have no impact on the performance of the device in all but the most demanding applications. The experimentally measured butt-joint backreflectivity is discussed in Section 4.7.4. In situations where the modulator and SSC are also monolithically integrated with a backreflection sensitive optical source, the transition can be angled as discussed below.

Backreflectivity Reduction with an Angled Butt-Joint

The backreflectivity of the SSC-to-modulator butt-joint can be improved by angling the transition. In Figure 3.23 the SSC waveguide mode at the butt-joint $E(x)$, has been overlapped with a 100% reflected image $E'(x)$, according to Equation 3.15 in Section 3.4.2. A butt-joint angle of 11^o is sufficient to obtain a 30dB reduction in the backreflectivity from

---

[17] The use of two decimal places is not indicative of the expected accuracy of this calculation against an experimental result.

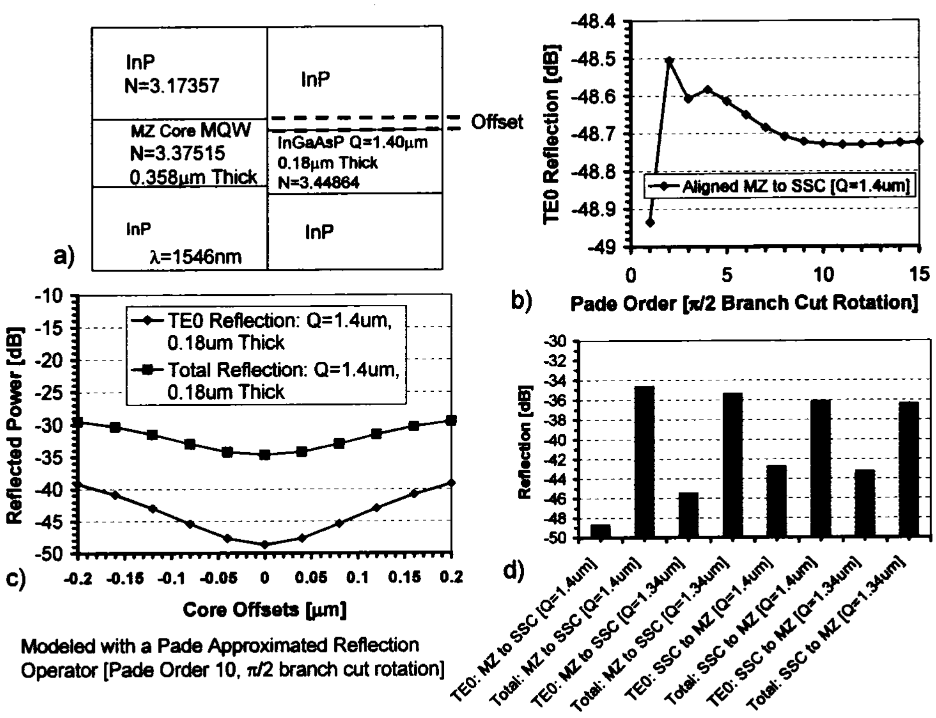

Modeled with a Pade Approximated Reflection Operator [Pade Order 10, π/2 branch cut rotation]

Figure 3.22: ***Reflection from a Spot-Size Converter to Mach-Zehnder Zero Length Single Interface Transition: a) Butt-Joint Model Parameters, b)*** TE_0 ***Reflection from the MZ-to-SSC Butt-Joint as a Function of the Padé Order, c)*** TE_0 ***and Total Reflection from the MZ-to-SSC Butt-Joint as a Function of the Core Misalignments, d)*** TE_0 ***and Total Reflection from the Butt-Joint as a Function of the Mode Propagation Direction and the SSC Core Composition under Enhancement.***

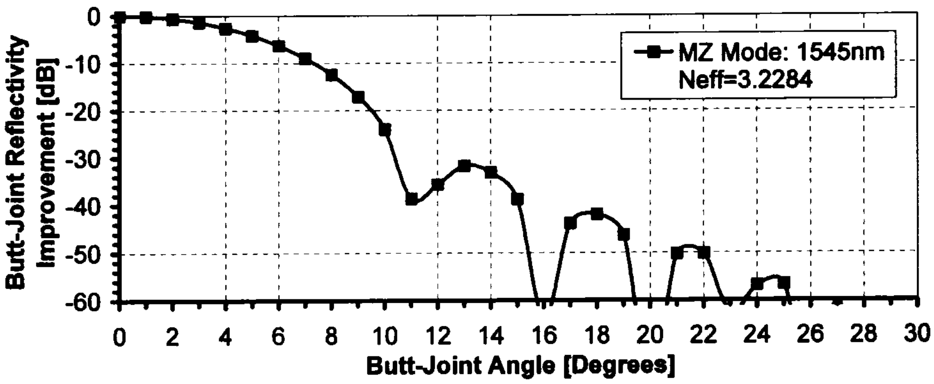

Figure 3.23: ***Impact of the MZ-to-SSC Butt-Joint Angle on the Backreflectivity of the Mach-Zehnder TE_0 Mode.***

the butt-joint transition. Angling the butt-joint is desirable in a device monolithically integrated with an optical source, as discussed in Section 4.7.5.

3.6 Lateral and Vertical Taper Designs

3.6.1 Love Theory of Modal Propagation in Adiabatic Waveguide Tapers

An adiabatic taper is defined by J.D. Love [186] to be one where, *"the taper angle is small enough everywhere to ensure that there is negligible loss of power from the fundamental mode as it propagates along the length of the taper. The fields and the propagation constant within an approximately adiabatic taper of a single-mode fiber can be described accurately by those of the local fundamental mode, which conserves power as it propagates and is the solution of the waveguide equation with the geometry of the local cross-section."*

The criterion for approximately adiabatic propagation, developed by J.D. Love [185, 186] and applied on a symmetric slab waveguide [189], is derived from the physical argument that the length scale of the taper must be significantly larger than the coupling length between the fundamental mode and the dominant coupling mode if radiation loss is to be minimized.

J.D. Love defines the local taper angle, between the tangent to the core-cladding interface and the waveguide centre axis, as $\Omega(z) = \tan^{-1}|\frac{d\rho}{dz}| \approx \frac{\rho}{z}$ where ρ is the local waveguide half width $w/2$, and z is the distance along the taper to the tangent intersection with the waveguide axis. The distance z is considered the length scale of the local taper angle.

The coupling length between the fundamental and the dominant coupling mode is taken to be the beat length z_b, where

$$z_b = \frac{2\pi}{(\beta_1 - \beta_2)} \tag{3.16}$$

with β_1 and β_2 the respective propagation constants.

The Love criterion for the local taper angle adiabatic limit occurs when the length scale of the taper z, equals the coupling length z_b, and is given by

$$\boxed{\Omega(z) = \frac{w(n_1 - n_2)}{2\lambda_0}} \tag{3.17}$$

where n_1 and n_2 are the effective indices of the fundamental and the dominant coupling modes, w is the waveguide width, and λ_0 is the operating wavelength. Assuming only symmetric tapers means the TE_1 mode in a strongly-guided waveguide structure will maintain odd symmetry with the TE_0 mode–the TE_1 mode, therefore, cannot be the dominant coupling mode. The dominant coupling effective index n_2 is, therefore, taken to be the InP substrate index.

Integrating Ω over all waveguide widths defines a critical taper length z_c. It is intuitive that for taper lengths $\gg z_c$, the coupling loss will be negligible and the fundamental mode will propagate approximately adiabatically, whereas for taper lengths $\ll z_c$ there will be significant loss into the substrate.

In a down taper the Love criterion allows the lateral width reduction to vary faster at the beginning of the tapered section relative to the end. Using a non-linear taper allows the Love criterion to be met while converting between different mode sizes in the shortest possible length. Besten et al. [190] have successfully used 50μm long linear tapers to reduce the width of a deeply etched waveguide from 3.5μm to 1.7μm. In a spot-size converter for a buried semiconductor optical amplifier, Sigogne et al. [191] have used the combination of two linear tapered sections with different slopes to approximate the optimal taper profile from the Love criterion. Finally, in a resonant coupling spot-size converter, Vusirikala et al. [187] have used a third order exponential taper shape from an initial width of 2.0μm to a final width of 1.4μm over a length of 100μm.

Suchoski and Ramaswamy [193] have show that the taper length for minimal loss is strongly dependent on the asymmetry in the waveguide structure, with higher asymmetries requiring smaller taper angles and, therefore, longer tapers. They also show that the minimum loss through a taper is determined strictly by the stair-casing introduced by the mask resolution. For Vawter et al. [192], a pixel size of 0.025μm was required to reduce radiation losses below 1dB in their down tapered rib waveguide spot-size converter.

Chang et al. [188] have proposed reducing the length for low-loss tapered waveguides with a Galilean telescope compensation structure. Though novel, the additional complexity adds little value in strongly-guided waveguide structures since the required taper length is already small by the Love criterion.

3.6.2 Design: Vertical Core Taper for the Spot-Size Converter

The N_{eff} of the TE_0 fundamental mode in the instantaneous material cross-section, normal to the propagation direction in the SSC, will be a function of the selective area growth (SAG) core thickness. In Figure 3.24a the TE_0 mode field solutions for the nominal SSC design are plotted as a function of the SAG core thickness. In Figure 3.24b the TE_0 mode field solutions for the alterative SSC design introduced in Figure 3.18 are also given. For simplicity, in Figure 3.24, the composition of the SAG core is assumed to scale linearly with thickness, from Q=1.3μm at a thickness of 0.05μm, to Q=1.4μm at a thickness of 0.2μm.

For an optimal SSC design, the evolution of the propagating field, from the TE_0 mode at the butt-joint, to the field output at the facet must occur adiabatically, i.e. the local power conserving TE_0 modes shown in Figure 3.24 must be representative of the actual propagating field in the SSC.

In Figure 3.25, the Love criteria from Equation 3.17 has been used to map the N_{eff} versus SAG core thickness relationship, obtained from the calculations for Figure 3.24, into the adiabatic transition limit for the SAG core thickness as a function of the length z. Thickness enhancement versus position z curves are given for a core with Q=1.3μm, Q=1.4μm, and for a core where the composition varies linearly with thickness, from Q=1.3μm at the facet to Q=1.4μm at the butt-joint. From Figure 3.25 an enhancement factor of four in the SAG core thickness can theoretically be obtained with an exponential taper only $\approx$150μm long.

The thickness enhancement versus z position curve, for the SAG core with the variable composition in Figure 3.25, has been fit using a 3rd order exponential fit function given by,

$$EF = 1 + \frac{(EF_{max} - 1)}{(e^{-s} - 1)} \left[\exp\left(\frac{-s(z - z_0)}{L} \right) - 1 \right] \tag{3.18}$$

where z_0 is the z position at the nominal thickness with EF=1, L is the length required to reach EF_{max}, and s is the exponential taper order. The fit quality with this exponential function indicates that the thickness of the SAG core can vary more rapidly near the butt-joint within an adiabatic transition limit, as expected from the discussion in Section 3.6. This is actually convenient for implementing the SSC design using a selective area growth process. The surface migration of precursors[18] during the MOCVD growth, from the dielectric protecting the first growth at the butt-joint, into the SAG growth region, tends to rapidly increase the core thickness in the vicinity of the butt-joint. If the adiabatic limit for the core thickness taper evolution is exceeded however, it be my possible to induce polarization rotation in the SSC since the core-to-cladding interfaces are intrinsically asymmetric; the core-to-overclad layer interface is tapered and the core-to-underclad layer interface is planar.

Finally, it can be observed from Figure 3.24 and Figure 3.25 that the same SAG core design can be used for both the nominal SSC and the alternate SSC design of Figure 3.18. The

---

[18] Precursors are the source compounds for the atomic In, Ga, As, and P deposited on the wafer in the MOCVD reactor.

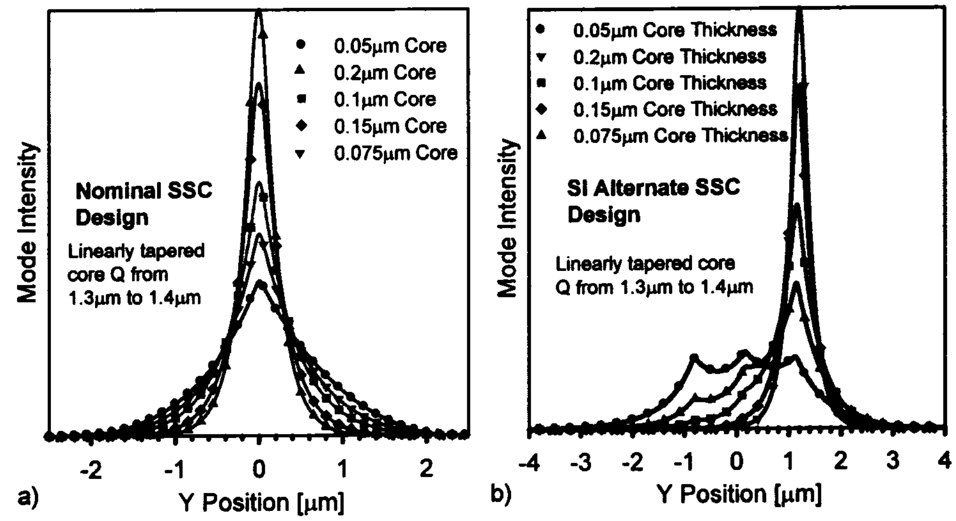

Figure 3.24: *Vertical TE_0 Mode of the SSC as a Function of the SAG Core Width: a) Nominal SSC Design, b) Semi-Insulating Substrate Alternate SSC Design. Note in both Cases the SAG Core Composition is Scaled Linearly by the Core Thickness from Q=1.3μm to Q=1.4μm.*

alternate SSC design can, therefore, be implemented if desired by a simple change in the first growth specification.

3.6.3 Implementation: Vertical Core Taper for the Spot-Size Converter

The vertical core taper in the SSC is implemented using a selective area growth (SAG) process. SAG is a MOCVD procedure for fabricating materials with different thicknesses and compositions laterally on the surface of a wafer; it is a key enabler for the monolithic integration of photonic devices. An overview of the technique is provided here to justify the vertical core taper varying in thickness by a factor of four in the SSC design.

In SAG growth a semiconductor film is deposited on a substrate[19] that is partially protected by a patterned inert mask such as SiO_2. During MOCVD growth the precursors[20] do not react on the oxide mask so they must diffuse to open areas of substrate where they produce a growth rate increase as shown in Figure 3.26. In addition to a growth rate increase, there will be a composition shift with ternary and quaternary alloys, due to the difference in diffusivity of the precursor molecules.

The two main physical processes involved in SAG film deposition are vapour phase diffusion and surface migration. Gibbon et al. [195] demonstrated that lateral movement of material on the 10-100μm length scale is caused by diffusion in the gas phase and not by

---

[19] This substrate could already contain epitaxial growth. It also does not necessarily have to be planar.

[20] Precursors are the source compounds for the atomic In, Ga, As, and P deposited on the wafer in the MOCVD reactor.

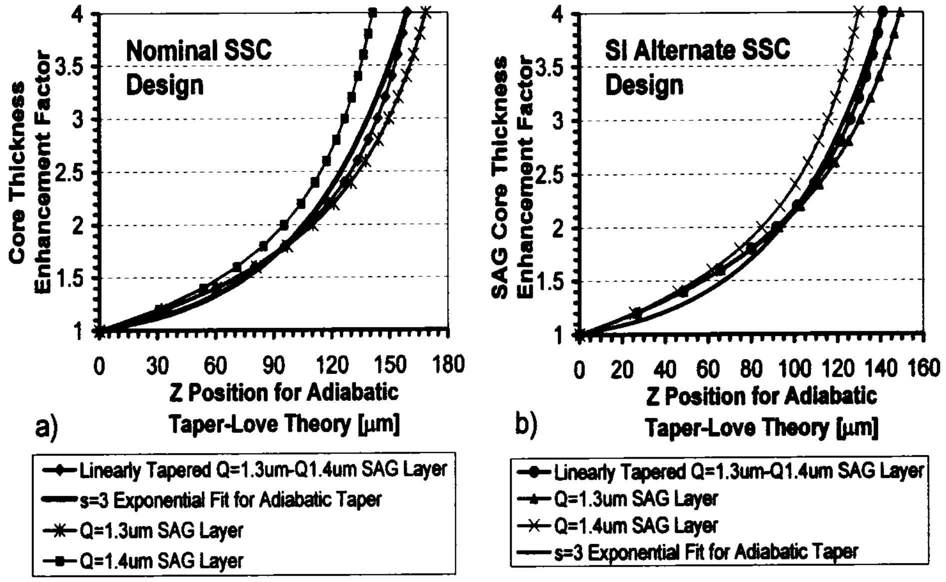

Figure 3.25: ***Love Theory for the SSC Adiabatic Vertical Core Thickness Taper: a) Nominal SSC Design as a Function of the Core Composition Function, b) Semi-Insulating Substrate Alternate SSC Design as a Function of the Core Composition Function.***

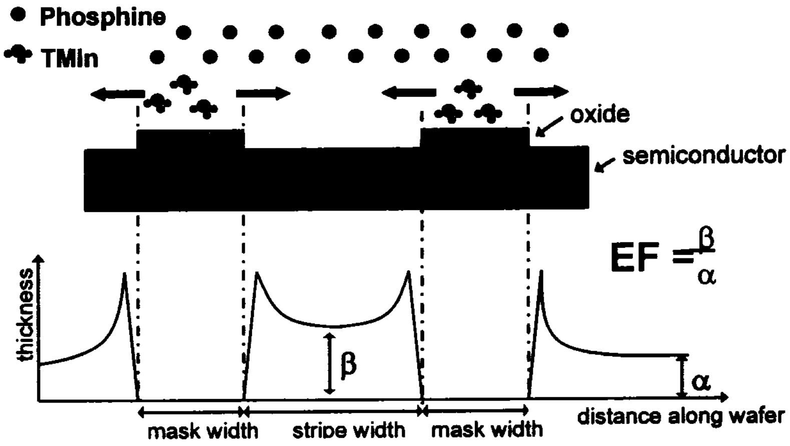

Figure 3.26: ***Principle of InP MOCVD Selective Area Growth.*** Source: *J.E. Greenspan, I. Betty, R. Glew, R. Foster and S. Campbell, "Design of Vertical Tapers Using Selective-Area Epitaxy with Quantitative Modeling," MOVPE 10th, 2001.*

surface migration. They presented a quantitative vapour phase diffusion model for SAG based on Laplace's equation in two dimensions. A single vapour phase diffusion parameter was used for each group III precursor with solutions presented for infinitely long dielectric masks of uniform width. The magnitude of the selective area enhancement was shown to be proportional to the width of the surrounding dielectric masks and inversely proportional to the open area between them. Alam et al. [194] extended this model to three dimensions to model SAG in the presence of non-uniform SiO_2 mask dimensions. Both Gibbon and Alam demonstrated excellent SAG model agreement to experimental results for semiconductor regions a few microns from the edge of the dielectric masks. Greenspan et al. [197,198] included the surface migration growth enhancement component to correctly predict the super growth enhanced regions adjacent to the oxide masks.

Here the Alam model is outlined. The model assumes laminar flow of the precursor gases and the existence of a stagnant layer[21] a few hundred microns thick above the wafer surface. The boundary condition for the group III precursor concentrations $n_i(x,y,z)$, at the top of the stagnant layer ($z=\delta$), is $n_i(x,y,\delta)=c_0$, where c_0 is a constant representing the steady supply of precursors from the MOCVD reactor inlet. Each precursor will diffuse through the stagnant layer, according to $D_i\nabla^2 n_i=0$, to react on the wafer surface. At the wafer surface (z=0), the normal component of the diffusion flux must balance the reaction flux,

$$D_i\frac{\partial n_i(x,y,0)}{\partial z}=k_i(x,y)n_i(x,y,0) \tag{3.19}$$

where k_i is the group III precursor incorporation rate of the semiconductor surface and D_i is the vapour phase diffusion constant for the group III precursor. At the wafer surface k_i is zero on the oxide mask. It is assumed that As and P are uniformly distributed over the surface of the substrate without regard to the presence of the dielectric mask.

The boundary conditions for the "sides" of the simulation space are chosen by selecting x_{min}, x_{max}, y_{min}, and y_{max} to be larger than the lateral diffusion length so that,

$$\frac{\partial n_i}{\partial x}\Big|_{x=x_{min}}=\frac{\partial n_i}{\partial x}\Big|_{x=x_{max}}=\frac{\partial n_i}{\partial y}\Big|_{y=y_{min}}=\frac{\partial n_i}{\partial y}\Big|_{y=y_{max}}=0 \tag{3.20}$$

In this physical model the solutions for the group III precursor concentrations $n_i(x,y,z)$ are determined by a single effective "diffusion" length parameter for each species: D_i/k_i. This parameter describes the decay of the growth enhancement as a function of the distance from the oxide mask. The growth rate enhancement for the indium component is given by, $R_{In}(x,y)=n_{In}(x,y,z=0)/n'_{In}(x,y,z=0)$, where n'_{In} is the solution with no dielectric mask present. The growth rate enhancement for the gallium component can be similarly found. The growth rate enhancement for a quaternary alloy will be the linear combination of the growth rates for the two components.

---

[21] Everstyn et al. revealed that the net velocity of gas molecules at the wafer surface during growth is zero [206]. Surface friction was believed to be the cause.

Alloy	$D/k\|_{In}$ [μm]	$D/k\|_{Ga}$ [μm]
InP	40	N/A
Q=1.10μm	40	150
Q=1.25μm	40	120
Q=1.62μm	36	96
InGaAs	36	96

Table 3.2: *Effective Diffusion Length Coefficients for InGaAsP Alloys. Source: Jonathan E. Greenspan, "Alloy composition dependence in selective area epitaxy on InP substrates," Journal of Crystal Growth, 236, pp. 273280, 2002. Used with permission.*

Greenspan [196] has found that the "diffusion" length parameters vary with alloy composition due to changes in incorporation rates. As shown in Table 3.2, gallium incorporation is reduced in low wavelength alloys whereas, indium incorporation is affected only slightly. The group V alloy composition is not significantly affected since the group V precursors are available in excess.

For the Q=1.3μm alloy required in the SSC SAG design, $\frac{D}{k}|_{In} = 40\mu$m and $\frac{D}{k}|_{Ga} = 110\mu$m were chosen as the vapour phase diffusion model input parameters. The dielectric mask designed by Jonathan Greenspan to implement the required 4X growth rate enhancement factor in the Q=1.3μm SAG core is shown in Figure 4.2. Experimentation with the SSC core selective area growth temperature and pressure conditions are discussed in Section 4.3.3. Finally, Section 4.4 provides a comprehensive analysis of the SSC core grown with the selective area growth process.

Based on our studies of high growth enhancement selective area growth we have proposed a method for integrating optical devices in a single growth step by utilizing a combination of SAG and etch (SAGE) [203].

3.6.4 Ridge Waveguide Lateral Taper Design

The lateral ridge width must be up-tapered between the 2.0μm width used in the modulator, and the 4.0μm-4.5μm width desired at the SSC output facet as determined in Section 3.4.4. This ridge width up-taper will be lithographically defined, hence it is important that a sufficiently small pixel size is used in the manufacture of the masking reticle to limit any sidewall scattering losses as discussed in Section 2.1.6 and Section 2.3.6.

In Figure 3.27 the Love criteria of Equation 3.17 has been used to determine the adiabatic taper limit for a 2.0μm to 4.0μm ridge width up-taper in the modulator structure. A quality fit to this adiabatic taper limit can be obtained using a 1st order exponential fit function given by,

$$x = x_0 + \frac{\Delta w}{2(e^s - 1)}\left[\exp\left(\frac{s(z - z_0)}{L}\right) - 1\right] \tag{3.21}$$

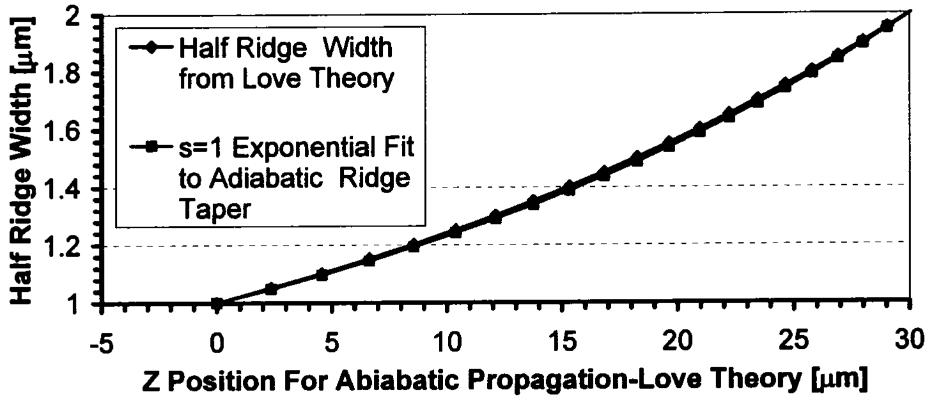

Figure 3.27: *Love Theory for an Adiabatic Lateral Ridge Taper in the Modulator Structure from 2.0µm to 4.0µm Wide.*

where x_0 is the nominal half ridge width at z_0, L is the length of the taper, Δw is the change in the full ridge width over the length of the taper, and s is the exponential taper order. Note in the modulator structure this ridge width change can be achieved over a length of $\approx 30\mu$m.

It is more difficult to calculate the adiabatic limit for the ridge width taper in the SSC because the variation in the N_{eff} of the TE_0 mode, as function of the position z, depends on both the SAG core thickness and the ridge width. The determination of an appropriate ridge width taper order and length will be left to three-dimensional BPM simulations in Section 3.7.

3.7 Beam Propagation Method Optical Models for the SSC Design

A TE semi-vectorial, three-dimensional, finite-difference beam propagation method, using PML boundary conditions, has been used to refined the SSC design developed in this Chapter. The cross-sectional (x,y) simulation space uses a uniform grid of 267X401 points, running from $x = -4\mu$m to $x = 4\mu$m, and $y = -5\mu$m to $y = 3\mu$m, with (0,0) the centre of the modulator core. The refractive index of a grid point (x,y) is given the area weighted average value of the materials contained between $(x\text{-}dx/2, x\text{+}dx/2)$ and $(y\text{-}dy/2, y\text{+}dy/2)$. The reference index for the simulations is N_0=3.1996[22], The propagation step size is dz=0.1μm. All simulations are performed at 1546nm unless stated otherwise, with no doping or band-edge losses included in the refractive indices for the materials used in the simulations.

All simulations launch a Gaussian field centred at (0,0) into the SSC facet. This Gaussian field has a waist with σ=1.76μm, and it is representative of a tapered fiber with a lens radius of 10μm.

---

[22] This reference index corresponds to the average of the modulator TE_0 and the SSC facet TE_0 mode at 1546nm.

The nominal design for the SSC has the following characteristics:

- The SAG core is 0.05μm thick at the facet with a composition of Q=1.3μm. The core thickness increases from the minimum of 0.05μm to a maximum of 0.19μm at the butt-joint, over a length of 350μm, according to a 3rd order exponential taper function[23]. Note this length scale is more than twice the adiabatic transition length calculated in Section 3.6.2.
- The composition of the SAG core is based on the 0 to 350μm quadratic fit to the experimental photoluminescence (PL) measurement given in Figure 4.22. A offset of 20.605nm has been added to the measured composition to obtain a Q=1.3μm PL 350μm from the butt-joint, and a Q=1.402μm PL at the butt-joint to the modulator core.
- The SAG core is centred vertically relative to the modulator core.
- The ridge width is 2.0μm in the modulator section of the device. The waveguide ridge width varies in the SSC, according to a 1st order exponential taper function[24], from 2.0μm at the modulator butt-joint, to 4.5μm over a length of 300μm.
- The cover index over the semiconductor is taken to be 1.44, representative of SiO_2. The substrate is taken to have a N^+ doping of 3.2E18cm^{-3}.
- The assumed modulator cross-section is as shown in Figure 4.3a. The etch depth is 4.0μm, ending 0.508μm above the antiguiding layer. The modulator core has a Q=1406nm PL for operation in C-Band as discussed in Section 3.9.1.
- In the SSC the etch depth must also be 4.0μm since both sections of the device are etched simultaneously. The etch ends 0.29μm above the antiguiding layer at the butt-joint and it penetrates 0.09μm into the antiguiding layer at the facet.
- The facet is placed 425μm from the butt-joint. This is 75μm beyond the end of ridge width and waveguide composition changes.

In Figure 3.28 the TE semi-vectorial three-dimensional BPM simulation results are presented for the nominal SSC design at 1545nm. In Figure 3.28a the X–Z power contour map through the waveguide cores (y=0) is given, where z=0μm is the modulator structure butt-joint and z=-425μm is the SSC waveguide facet. In Figure 3.28b the Y–Z power contour map through the growth cross-section (x=0) is shown. In Figure 3.28c the X–Y power contour map of the input Gaussian field launch is presented, overlapped with the refractive index of the SSC facet. Finally, Figure 3.28d provides the X–Y power contour map of the simulation output field at z=75μm in the modulator waveguide structure, overlapped with the refractive index distribution. From these plots it is clear the SSC design provides an excellent adiabatic transition, from a realistic coupling mode, into the fundamental mode

---

[23] The exponential functional form is discussed in Section 3.6.2

[24] The exponential functional form is discussed in Section 3.6.4

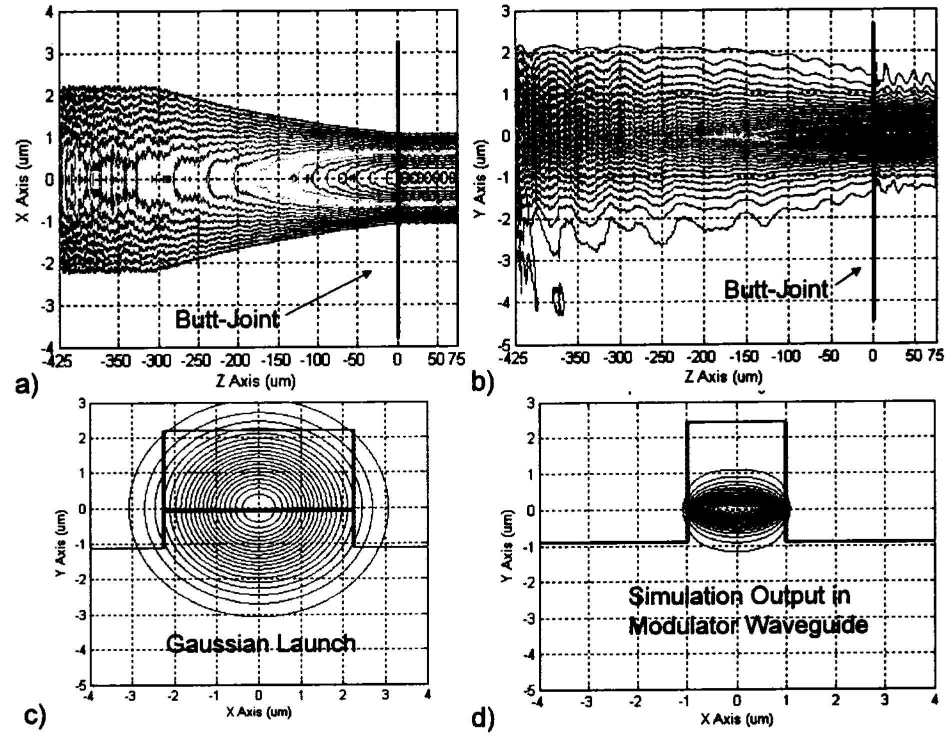

Figure 3.28: ***3D TE Semi-Vectorial BPM Simulation for the Nominal SSC Design with No Doping or Bandedge Losses at 1545nm: a) X–Z Power Contour Map through the Waveguide Core (Y=0) where Z=0μm is the Modulator Structure Butt-Joint and Z=-425μm is the Waveguide Facet. b) Y–Z Power Contour Map through the Growth Cross-Section (X=0) where Z=0μm is the Modulator Structure Butt-Joint and Z=-425μm is the Waveguide Facet. c) X–Y Power Contour Map of the Symmetric Input Gaussian Field Representative of a 10μm Tapered Fiber overlaid on the SSC Facet Structure. d) X–Y Power Contour Map of the Output Field at Z=75μm in the Modulator Waveguide Structure.***

of the modulator structure. Figure 3.29 provides the extracted insertion loss for the Gaussian launched mode, into the TE_0 mode of the modulator as a function of wavelength. This insertion loss varies from 0.23dB at 1510nm to 0.19dB at 1610nm.

The insertion loss extracted in Figure 3.29 does not include any doping or bandedge losses. In Figure 3.30 the optical mode overlap to the grown dopant cross-section is plotted as a function of z position in the SSC. Integrating these positional dependent layer confinements, over the full length of the SSC, allows the effective length[25] for each dopant layer to be determined. The effective length of each dopant layer is provided on the table in Figure 3.30. The relationships between doping and optical loss, quantified in Section 2.1.7, predict 0.5dB of doping induced optical loss in each SSC. This is the penalty that must be paid to have a common overgrowth structure in the modulator and SSC sections of the device.

---

[25] The effective length of a dopant layer in the SSC is an equivalent length that assumes 100% optical confinement to the layer.

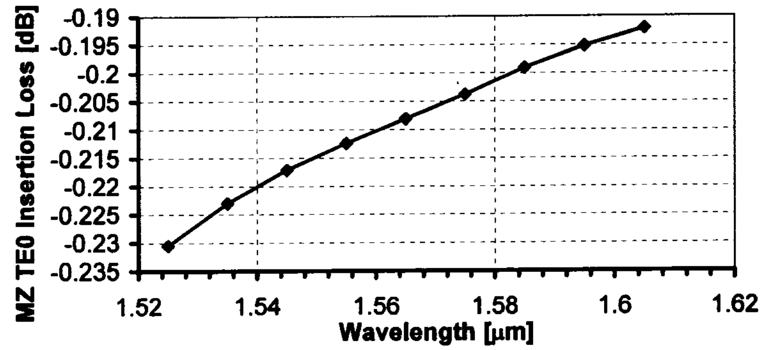

Figure 3.29: *3D TE Semi-Vectorial BPM Simulation for the MZ TE$_0$ Insertion Loss of the Nominal SSC Design versus Wavelength [No Doping or Bandedge Losses.] The Input Field to the SSC is a Symmetric Gaussian Representative of a 10μm Tapered Fiber.*

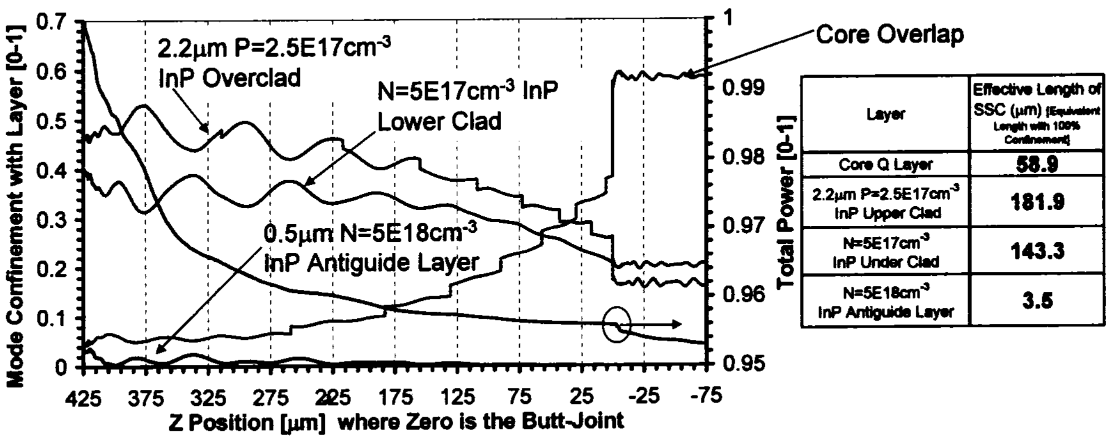

Layer	Effective Length of SSC (μm) [Equivalent Length with 100% Confinement]
Core Q Layer	58.9
2.2μm P=2.5E17cm^{-3} InP Upper Clad	181.9
N=5E17cm^{-3} InP Under Clad	143.3
N=5E18cm^{-3} InP Antiguide Layer	3.5

Figure 3.30: *3D TE Semi-Vectorial BPM Simulation for the Mode Overlap to the Growth Doping Structure as a Function of Z Position along the Length of the Spot-Size Converter. Z=0μm is the Modulator Structure Butt-Joint and Z=425μm is the Waveguide Facet. The Input Field to the SSC is a Symmetric Gaussian Representative of a 10μm Tapered Fiber.*

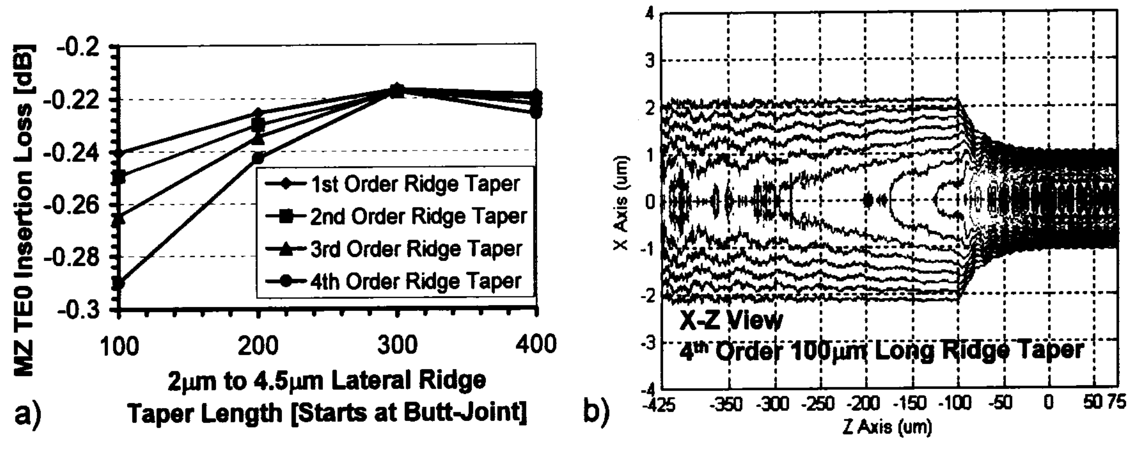

Figure 3.31: ***a) 3D TE Semi-Vectorial BPM Simulation for the SSC Insertion Loss at 1545nm, into the MZ*** TE_0 ***mode, as a Function of the Lateral Taper Profile and Length [No Doping or Bandedge Losses.] The Input Field to the SSC is a Symmetric Gaussian Representative of a 10µm Tapered Fiber. b) X–Z Power Contour Map through the Waveguide Core (Y=0) for a 4th Order 100µm Long Lateral Taper. Z=0µm is the Modulator Structure Butt-Joint and Z=-425µm is the Waveguide Facet.***

Figure 3.31 explores the SSC insertion loss at 1545nm, into the modulator TE_0 mode, as a function of the lateral ridge width taper profile and length. The ridge width taper length was varied from 100µm to 400µm, and the exponential profile, given by Equation 3.21, was varied from the 1st to 4th order. All other parameters were the same as the nominal design. A small penalty, which is a function of the exponential taper order, is paid if the taper length is shortened from the nominal 300µm.

Figure 3.32 explores the SSC insertion loss at 1545nm, into the modulator TE_0 mode, as a function of the vertical taper composition and thickness profile. The core thickness exponential taper order was varied from one to four, and the composition shift along the taper varied from none to 100nm using the same 3rd order exponential taper function as the nominal SAG core thickness taper. There is practically no dependence on the taper order in Figure 3.32, since the 350µm transition length for the vertical taper is more than twice that required for an adiabatic transition. The insertion loss improves continuously as a function of the total composition shift in these simulations. It is difficult to measure the composition shift experimentally, however from Figure 3.32a, it is clear that the SSC insertion loss will not vary significantly if the composition shift changes over time in a manufacturing environment where it is not monitored.

Figure 3.32 and Figure 3.31 together show that the 425µm long SSC design is robust against variation in the vertical and lateral mode expansion. The cost for this robustness is additional optical loss from the increased mode overlap with the doping in the upper and lower InP cladding layers as quantified in Figure 3.30. Assuming the enhancement facet is maintained, variation[26] in the SSC insertion loss will be dominated by the alignment error

---

[26] Variations can be wafer-to-wafer as well as across a wafer.

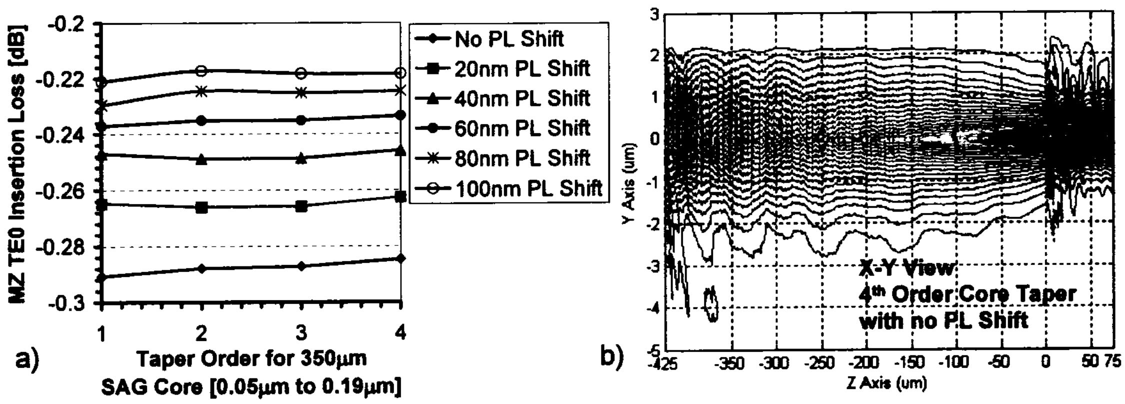

Figure 3.32: *a) 3D TE Semi-Vectorial BPM Simulation for the SSC Insertion Loss at 1545nm, into the MZ TE_0 mode, as a Function of the Vertical Taper Composition and Profile [No Doping or Bandedge Losses.] The Input Field to the SSC is a Symmetric Gaussian Representative of a 10μm Tapered Fiber. b) Y–Z Power Contour Map through the Growth Cross-Section (X=0) for a 4th Order 350μm Long Vertical Taper with No PL Composition Shift. Z=0μm is the Modulator Structure Butt-Joint and Z=-425μm is the Waveguide Facet.*

between the SSC and modulator cores, as presented in Figure 3.21.

3.7.1 Impact of Launch Misalignment into the Nominal SSC Design

It is prudent to explore the insertion loss impact of a misalignment in the coupling optics. In a manufacturing environment it is imperative that only one global minimum exists for the insertion loss. Figure 3.33 provides the SSC insertion loss at 1545nm, into the modulator TE_0 mode, as a function of x and y misalignment of the input coupling field. A two-dimensional space for misalignment is explored with 0.5μm steps for x=-1μm to x=1μm, and y=-1μm to y=1μm. It is evident in Figure 3.33a that only one global minimum exists for the insertion loss. It occurs with no misalignment in either the x or y launch position.

Figure 3.33c shows the Y–Z power contour map through the growth cross-section (x=0) for a [-0.5μm, -0.5μm] misaligned input coupling field. It is evident that the y misaligned launch does not excite any higher order vertical modes, as expected from the modal calculations in Section 3.4.5. Figure 3.33b provides the X–Z power contour map through the waveguide core (y=0) for this same [-0.5μm, -0.5μm] misaligned input coupling field. Obviously the launch misalignment in x does excite the higher order TE_1 mode in the SSC and modulator waveguides. The impact of this TE_1 higher order mode on the modulator performance has been studied in Section 2.4.3.

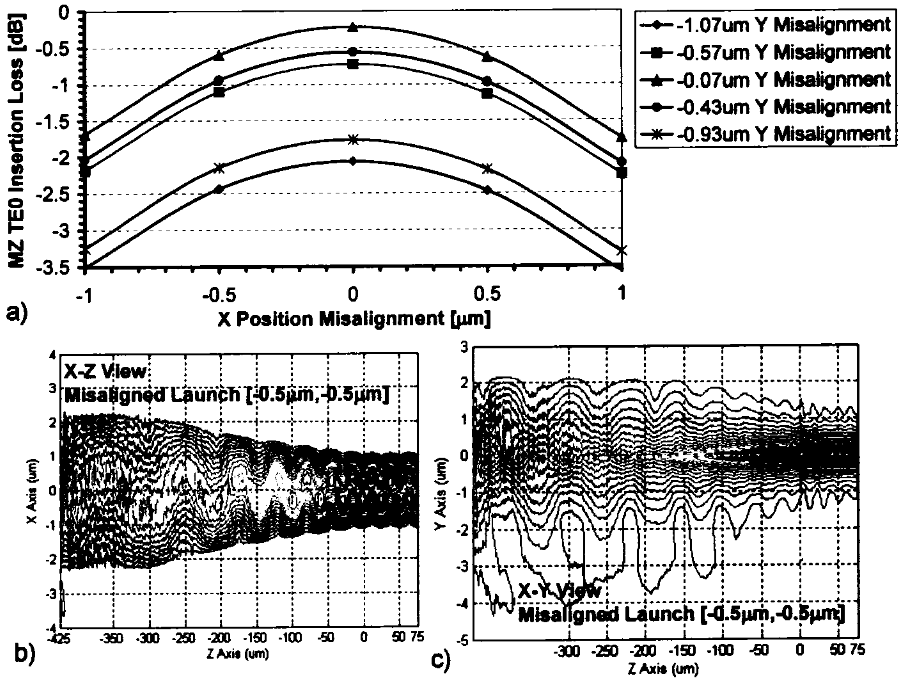

Figure 3.33: ***a) 3D TE Semi-Vectorial BPM Simulation for the SSC Insertion Loss at 1545nm, into the MZ TE$_0$ mode, as a Function of the X and Y Misalignment of the Input Coupling Field [No Doping or Bandedge Losses.] The Input Field to the SSC is a Symmetric Gaussian Representative of a 10μm Tapered Fiber. b) X–Z Power Contour Map through the Waveguide Core (Y=0) for a [-0.5μm, -0.5μm] Misaligned Input Coupling Field. c) Y–Z Power Contour Map through the Growth Cross-Section (X=0) for a [-0.5μm, -0.5μm] Misaligned Input Coupling Field. In (b) and (c) Z=0μm is the Modulator Structure Butt-Joint and Z=-425μm is the Waveguide Facet.***

3.7.2 SSC Design for Minimized Wafer Footprint

The nominal 425μm long SSC structure is significantly longer than the required adiabatic limit for length. Figure 3.34 gives the SSC insertion loss at 1545nm, into the modulator TE_0 mode, as a function of the vertical and lateral taper lengths, and the SAG core vertical taper order. The ridge width taper order was fixed at one, and the ridge width taper length was set to 50μm less than the SAG core vertical taper length in each simulation. The SAG core composition was fixed at Q=1.3μm at the end of the taper and Q=1.4μm at the butt-joint to the modulator. The composition of the SAG core varied according to the same 3rd order exponential function used for the SAG core thickness.

In Section 3.6.2 it was shown that the adiabatic length limit for the vertical taper was approximately 150μm. In Figure 3.34a the insertion loss starts to increases rapidly for a SAG core thickness taper length less than this 150μm long adiabatic length. By extrapolation it also appears that higher order tapers will be lossier for taper lengths below the adiabatic limit. The TE semi-vectorial BPM simulations in Figure 3.34 cannot capture the effects of polarization rotation, therefore, calculations with SSC lengths significantly less than the adiabatic limit may be of questionable accuracy. The design length of the SSC structure however, could safely be reduced by more than 50%, to 200μm, if minimizing the wafer footprint was required. The ability of a SAG growth process to achieve the required 4X growth enhancement factor, over this 200μm length, would have to be verified.

3.8 Summary of SSC Optical Losses

Table 3.3 summarizes the contributing factors to the insertion loss in each SSC. The predicted insertion loss excluding coupling optics given in Table 3.3, compares well with the experimental value of 0.79dB, extracted from Figure 2.18 in Section 2.1.9. The most significant contributor to the SSC loss is the optical overlap with the InP dopants. This dopant contribution was determined in Figure 3.30 to be 0.51dB, however, it could be reduced in practice if significant H passivation of Zn dopant occurs in the fabrication process.

The calculated insertion loss from the BPM simulations is 0.22dB at 1546nm. This loss includes the overlap loss between the facet mode and a 10μm radius lensed tapered fiber, the loss of the SSC butt-joint with the modulator when the cores are perfectly aligned, and radiative loss from lateral and vertical tapers. Figure 3.21 gives 0.05dB as the contribution from only the butt-joint loss when the waveguide cores are perfectly aligned. Based on Figure 3.21, an additional 0.05dB has been budgeted for the butt-joint loss, to allow for 0.1μm of misalignment between the modulator and SSC waveguide cores.

Figure 2.21 quantifies the scattering losses measured in a passive, strongly-guided waveguide[27], as a function of the ridge width. Based on Figure 2.9, the ridge sidewall scattering

---

[27] These devices also had a bulk core.

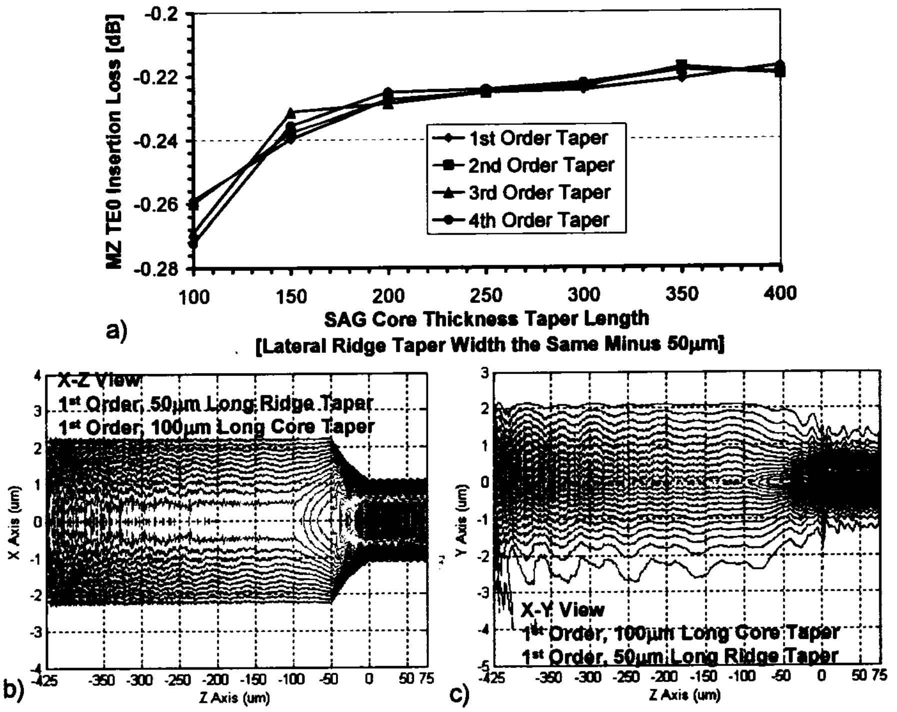

Figure 3.34: ***a) 3D TE Semi-Vectorial BPM Simulation for the SSC Insertion Loss at 1545nm, into the MZ TE$_0$ mode, as a Function of the SSC Taper Function Lengths [No Doping or Bandedge Losses.] The Input Field to the SSC is a Symmetric Gaussian Representative of a 10µm Tapered Fiber. b) X–Z Power Contour Map through the Waveguide Core (Y=0) for a 1st Order 100µm Long SAG Core Vertical Taper with a 1st Order 50µm Long Lateral Ridge Taper. c) Y–Z Power Contour Map through the Growth Cross-Section (X=0) for a 1st Order 100µm Long SAG Core Vertical Taper with a 1st Order 50µm Long Lateral Ridge Taper. In (b) and (c) Z=0µm is the Modulator Structure Butt-Joint and Z=-425µm is the Waveguide Facet.***

Loss Mechanism	Contribution [dB]
P and N Doping Absorption	0.51dB
3D-BPM Simulation Loss: -Taper Radiation -Nominal Butt-Joint -Facet-Coupling Mode Mismatch	0.22dB
Additional Butt-Joint Loss for Core Misalignment of ±0.1μm	0.05dB
Strongly Guided Ridge Scattering Loss [25nm Lithography]	0.05dB
Diffraction/Aberration Tapered Fiber Loss	0.5dB
Total Losses per Facet (Including Coupling Optics)	1.33dB
Total Losses per Facet (Excluding Coupling Optics)	0.83dB

Table 3.3: ***Contributions to the SSC Insertion Loss.***

losses in the SSC exponential ridge width taper can be assumed to vary between 0.03dB/cm and 1.7dB/cm depending on the cross-sectional ridge width. For the insertion loss budget a pessimistic contribution of 0.05dB has been assumed for the 425μm long SSC.

3.9 Growth Structures

This section presents the three MOCVD growths required to combine the optimized strongly-guided modulator structure, given in Figure 2.6a, with the SSC design developed in this Chapter.

3.9.1 First Growth

The structure for the first MOCVD growth is shown in Figure 3.35. It is grown on a highly conductive three inch N-type sulphur doped InP substrate. As detailed in Section 2.1.12 and Section 3.4.5, novel use is made of the n-type doping profile in the waveguide undercladding to leak higher-order guided vertical optical modes into the substrate. This requires the substrate N-type carrier concentration to be less than 5E18cm^{-3}.

The first layer deposited onto the substrate is a 0.5μm thick 5E18cm^{-3} Si-doped InP film. This anti-waveguiding layer is followed by 1.5μm thick layer of 5E17cm^{-3} Si-doped InP to form the waveguide underclad. Next the waveguide core is deposited as a multi-quantum well stack with twenty 95Å thick Q=1.47μm unstrained InGaAsP wells and twenty-one 80Å thick Q=1.1μm unstrained InGaAsP barriers [16–18]. The waveguide core is not intentionally doped. The exciton photoluminescence peak resonance at zero volt bias is 140nm detuned from the centre 1546nm operating wavelength. A thin 0.05μm thick undoped InP spacer layer follows the waveguide core as discussed in Section 2.1.8. The final deposition

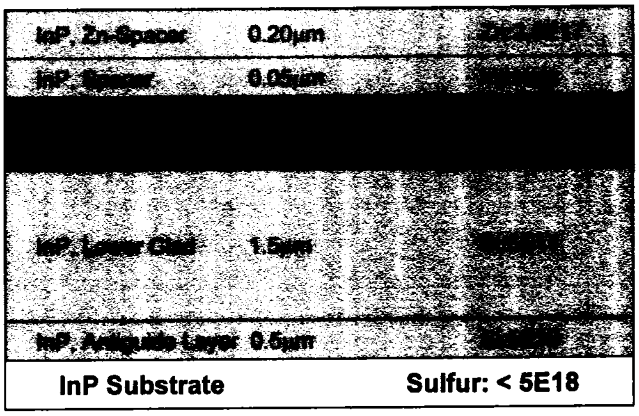

Figure 3.35: *First Growth Structure [Modulator Core Growth]*

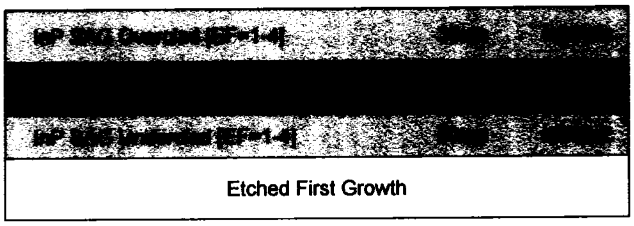

Figure 3.36: *Second Growth Structure [SAG SSC Growth]*

in the first growth that forms part of the device is a 0.2μm thick 2.5E17cm^{-3} p-type Zn-doped InP layer. This layer separates the regrowth interface from the intrinsic core in the final p-i-n diode electrical structure.

3.9.2 Second Growth

The structure for the second MOCVD growth is shown in Figure 3.36. This is a SiO_2-masked selective-area-growth which deposits the non-planar spot-size converter waveguide core butt-joined to the active modulator core. This second growth takes place on a first growth wafer that has been processed as detailed in Sections 4.2 and 4.3.

The Triethyl Gallium (TEG) is used as the group III precursor for gallium since its lateral diffusion length is closest to that of the Trimethyl Indium (TMI) group III precursor used for indium. The -0.2% strain value was determined by a MOCVD colleague, Jonathan Greenspan, to partially compensate for the expected non-uniform red-shift on the group III sub-lattice under SAG enhancement due to the different lateral diffusion lengths for the group III precursors at a pressure of 100mBar [199,200]. The group V sub-lattice composition is not significantly affected under SAG enhancement because the group V precursors are available in excess under standard growth conditions [201].

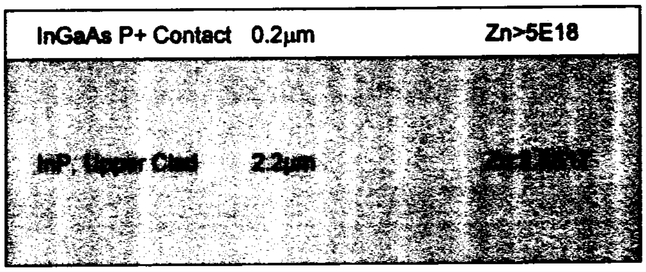

Figure 3.37: *Third Growth Structure [Common Overclad Layer Growth]*

3.9.3 Third Growth

The structure for the third MOCVD growth is shown in Figure 3.37. This growth provides the common blanket p-doped overclad layers for both the modulator and the spot-size converter.

Chapter 4

Spot-Size Converter Implementation

4.1 Introduction

This chapter details the fabrication process developed for the spot-size converter (SSC) design presented in Chapter 3. A high level overview of the final optimized process is described. This is followed by a description of the novel fabrication technique for the active-to-passive waveguide core butt-joint, and the characteristics of the selective area MOCVD grown vertically tapered passive waveguide core. The impact of contamination at regrowth interfaces on the modulator device performance is detailed and a solution to the problem is provided. The chapter ends with a study on the optical characteristics of the spot-size converter integrated with the Mach-Zehnder modulator. The flexibility of the SSC design is demonstrated by including performance details for a 40Gb/s electro-absorption modulator enabled by the SSC design.

4.2 Overview of the Spot-Size Converter Fabrication Process

Section 3.9 outlines the structure for each of the three growth steps required to integrate the spot-size converter design developed in Chapter 3 with the Mach-Zehnder modulator design developed in Chapter 2. The fabrication process that connects these three growth steps is pictorially presented in Figure 4.1.

The first growth detailed in Section 3.9.1 constitutes the Mach-Zehnder modulator structure up to and including an InP buffer layer above the active waveguide core. The modulator and spot-size converter will share a common set of underclad waveguide layers defined by this first growth. Following this growth a 3000Å layer of SiO_2 is deposited by plasma enhanced chemical vapour deposition [221] and patterned using i-line photolithography [207] to produce the pattern shown in Figure 4.2. This dielectric pattern is

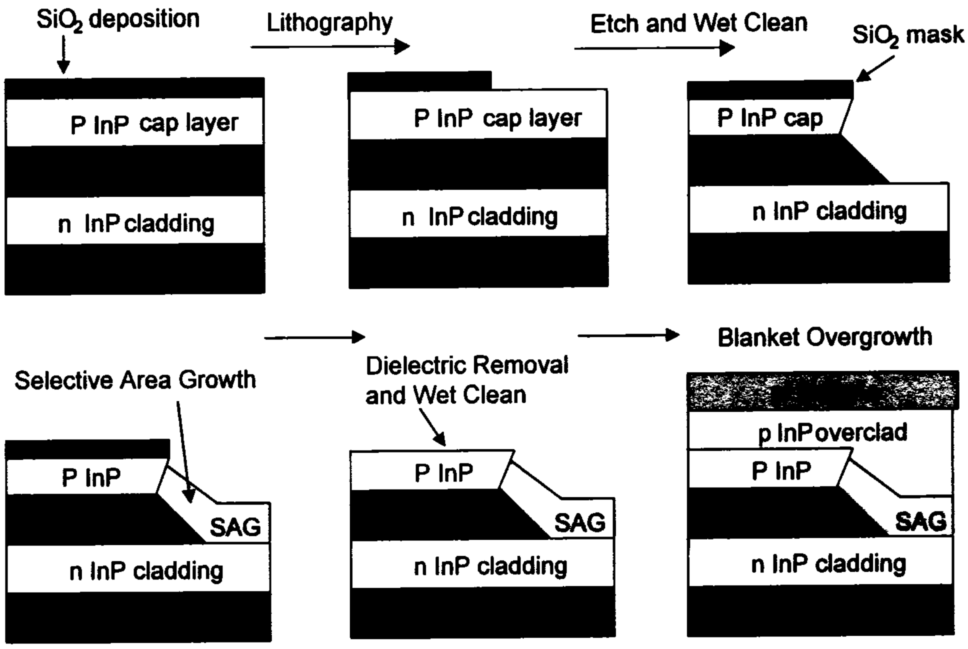

Figure 4.1: ***Outline of the Process Flow for Integrating the Spot-Size Converter with the Mach-Zehnder Waveguide Structure.***

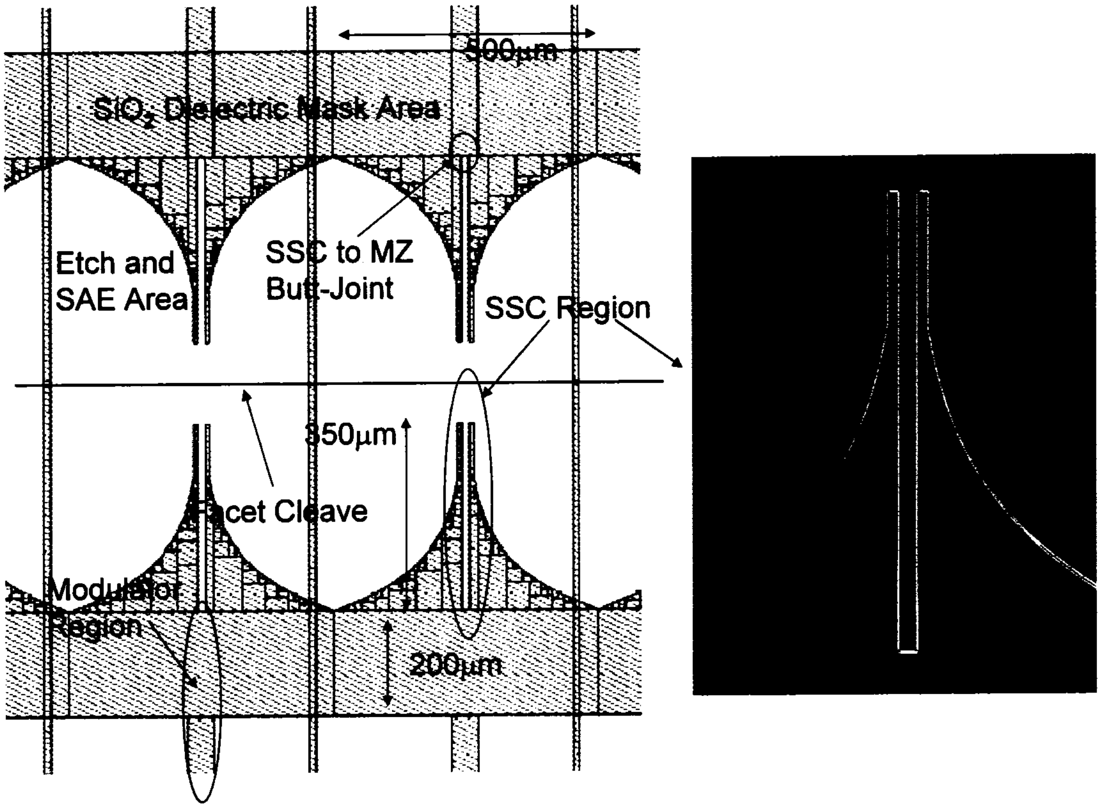

Figure 4.2: *SAG Dielectric Mask Structure.*

then used as the hard mask for a Cl_2O_2 inductive coupled plasma (ICP) semiconductor etch [210, 211]. This etch is monitored *in-situ* to accurately target its depth to the bottom of the modulator waveguide core [0.55μm deep.] The wafer is then cleaned in a series of chemical solutions to repair the damage to the semiconductor surface sustained during the etch. The SiO_2 dielectric geometry as shown in Figure 4.2 serves two purposes. It acts to protect from the semiconductor etch, those areas on the wafer that will contain the active modulator core, and it also serves as the mask for the selective-area second growth.

The purpose of the selective-area second growth presented in Section 3.9.2 is to grow the passive waveguide core of the spot-size converter butt-joined to the etched active modulator core. The selective-area epitaxial process is used to vary the thickness, strain and composition of the passive waveguide core along the length of the spot-size converter[1] as discussed in Section 3.6.3. Following selective area epitaxy, the wafer is removed from the MOCVD reactor and the patterned SiO_2 mask is removed from the wafer with ultrasonic agitation in hydrofluoric acid (HF). The wafer surface is exposed to ozone to oxidize Si contamination and any oxidized contaminates are stripped from the wafer using a sec-

---

[1] Film growth rate enhancement, composition shift and strain will be greatest in proximity to the largest surface area of dielectric.

ond treatment of HF. The wafer is now ready to receive the third and final conventional MOCVD growth. The third growth structure is presented in Section 3.9.3. This blanket growth deposits an overclad p-doped InP layer and a p+ InGaAs contact layer. The blanket nature of this growth makes these p-doped layers common to both the modulator and the spot-size converter waveguide structures.

At this point, all epitaxial growth steps are completed and the wafer topology is nominally flat.[2] The vertical taper of the SSC waveguide core is contained within the growth structure and the SSC lateral waveguide taper will be defined by the SSC ridge waveguide semiconductor etch.

The SSC ridge waveguide and the modulator ridge waveguide structures are etched simultaneously to a depth of 4.0μm using an ICP HBr semiconductor etch with better than 2% wafer uniformity [210] or an CO_2:CH_4:H_2 RIE etch. A 5500Å layer of SiO_2 is used as the dielectric hard mask for this etch. A depth of 4.0μm (accounting for a 10% depth tolerance) etches 0.55μm below the active core in the modulator ridge waveguide, and up to 1.0μm[3] below the passive core in the SSC ridge waveguide. As discussed in Chapter 2.2, the geometrical accuracy requirements imposed on this etch by the multi-mode interference coupler design are challenging.

Figure 4.3 gives the fully grown wafer cross-sections for both modulator and SSC sections of a device. The locations of the regrowth interfaces are indicated.

4.3 Novel Fabrication Technique for an Active/Passive Waveguide Core Butt-Joint

A robust method to laterally connect any two waveguide cores is a key building block for monolithic integrated circuits. Here the innovative etch and regrowth processes developed to enable high-enhancement passive-to-active waveguide core butt-joints are reviewed. Two other groups have reported in the literature on waveguide butt-joint formation in MOCVD growth, both using low-enhancement SAG in buried waveguide devices [204, 205].

4.3.1 Removal of the Active Waveguide Core

The first step in the process, as outlined in Figure 4.1, requires the removal of the active material core. Two approaches for removing this material have been pursued. The first and simplest approach uses an SiO_2 mask for a wet chemical etch of the core that will

---

[2] The wafer has 0.582μm of surface topology by design.

[3] The maximum ridge etch depth below the passive core occurs at the facet of the device where the growth enhancement is a minimum.

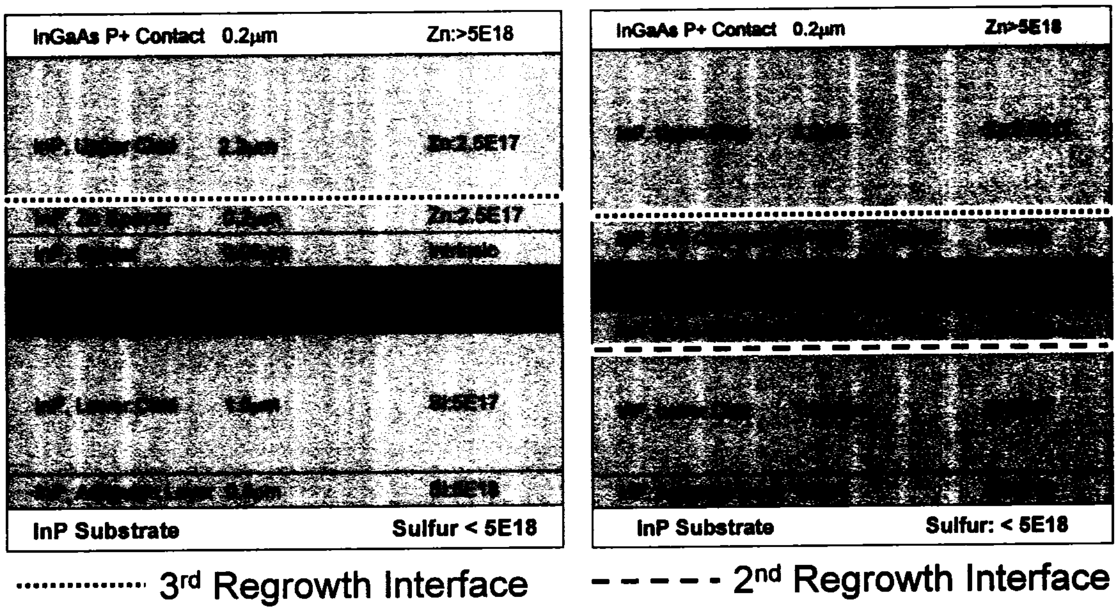

Figure 4.3: *Final Wafer Growth Cross-Sections: a) Modulator Section, b) SSC Section.*

terminate on the InP underclad layers beneath the core. This approach provides accurate etch depth control, however, it is limited by available selective etches to applications where the material to be removed is a combination of bulk InP and bulk InGaAsP quaternary with a bandgap >1.2μm. The wet chemical etch rate non-uniformity across a 3" wafer, also means the degree of dielectric undercut will vary from the centre-to-edge of the wafer with the undercut typically greatest at the centre. These wet etches leave the semiconductor surface free of defects so no chemical cleans are required prior to the selective area passive core growth.

The wet etch approach is not compatible with the MQW Mach-Zehnder modulator core; however, it was used to form the butt-joint on the 40Gb/s electro-absorption modulator (EAM) discussed in Section 4.7.6. The InP cap layer in this EAM application was removed using a 45 second etch in 2:3 solution of $HCl:H_3PO_4$. HCl is well known for selectively etching InP over InGaAsP and InGaAs [218, 219]. The 0.35μm bulk EAM core with a bandgap of $Q=1.47\mu m$ was removed using a three minute 1:5:50 Q-etch solution of $H_2SO_4:H_2O_2:H_2O$ [220]. In Figures 4.4a and 4.4c early trials show the dielectric undercut and the crystallographic <111> plane exposed by the Q-etch for EAM waveguide butt-joints parallel and perpendicular to the major wafer flat. The waveguide butt-joint of interest in the EAM is parallel to the major flat. Note these structures had no Zn-doped InP spacer layer above the active core.

The second approach uses a dry III-V etch followed by a series of wet chemical cleans to repair the damage to the semiconductor lattice at the surface sustained during the dry etch [222–224]. This approach was developed to enable the accurate removal of the Mach-

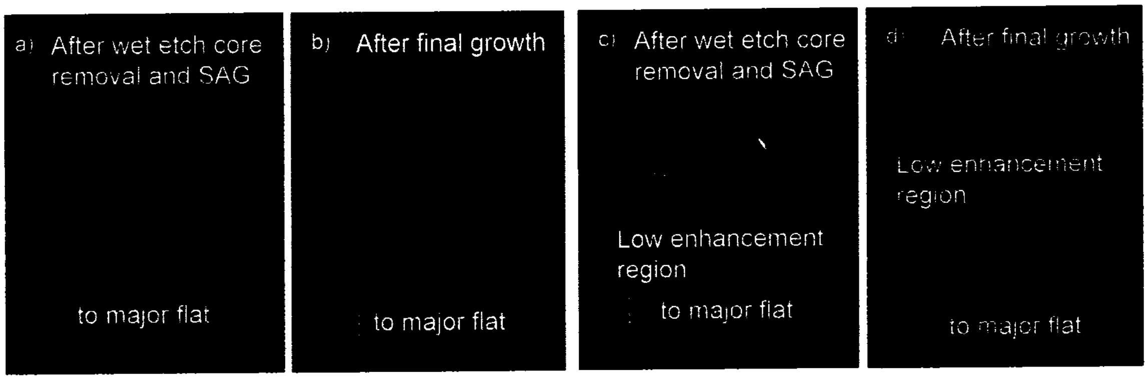

Figure 4.4: *Wet Etch Active Core Removal.*

Zehnder active material. It is a more robust method since it is nearly independent of the material composition to be removed.

In Figure 4.5 SEM views are shown of a wafer following an optimized III-V dry etch using Cl_2-Ar plus Cl_2O_2 chemistries in a Trikon Omega 201 ICP etcher [208,210,211]. This etch technology combines a high density ICP source with a heated electrostatic chuck equipped with helium-backside cooling. High density plasma etchers are capable of anisotropic etching due to their low pressure operation (less than 10mT); plasma sources with this design maintain high etch rate and good reproducibility due to the high ion densities (more than 10^{11} cm^{-3}), and the independent control of ion energy and density allows anisotropic profiles to be etched through multi-layer structures [208]. Etch depth uniformity within 2% has been demonstrated over a 3" InP wafer with 2% wafer-to-wafer repeatability using a laser interferometry end-point detection system on the etcher. From Figure 4.5, it is clear this etch produces a smooth etched floor and a non-reentrant[4] sidewall profile, at what will be the butt-joint interface (Figure 4.5b). The hard mask for this etch process is a 3000Å thick SiO_2 dielectric deposited by plasma-enhanced chemical vapour deposition (PECVD) and etched with a C_4F_8 plasma in a MORI tool [209]. Approximately 1100Å of this hard mask is removed during the 0.55μm deep III-V etch.

The impact of the series of wet chemical cleans used to remove the III-V dry etch induced damage to the semiconductor lattice [225,226] is seen in Figure 4.6. In Figure 4.6a the wafer cross-section following the ICP dry etch is shown again for reference. Approximately 1900Å of SiO_2 dielectric hard mask remains. The chemical clean consists of a 1% HF preclean dip for 30 seconds, followed by a Bromine (HBr) diluted in methanol etch for 90 seconds, and a final 60 second sulfuric acid (H_2SO_4) rinse. The HF preclean removes oxidants to enable the Br clean to etch the semiconductor [213]. The etch rate of the Bromine diluted in methanol is controlled by the dilution and a smooth semiconductor surface can be obtained with relatively slow etch rates [227,228]. The sulfuric acid rinse quenches hydrocarbon contamination introduced by the methanol [229] and leaves a sulfided surface passivation. For both wafer orientations of the butt-joint, shown in Figures 4.6b and

---

[4] The sidewall profile angles inward from the bottom of the etch, not from the top of the etch.

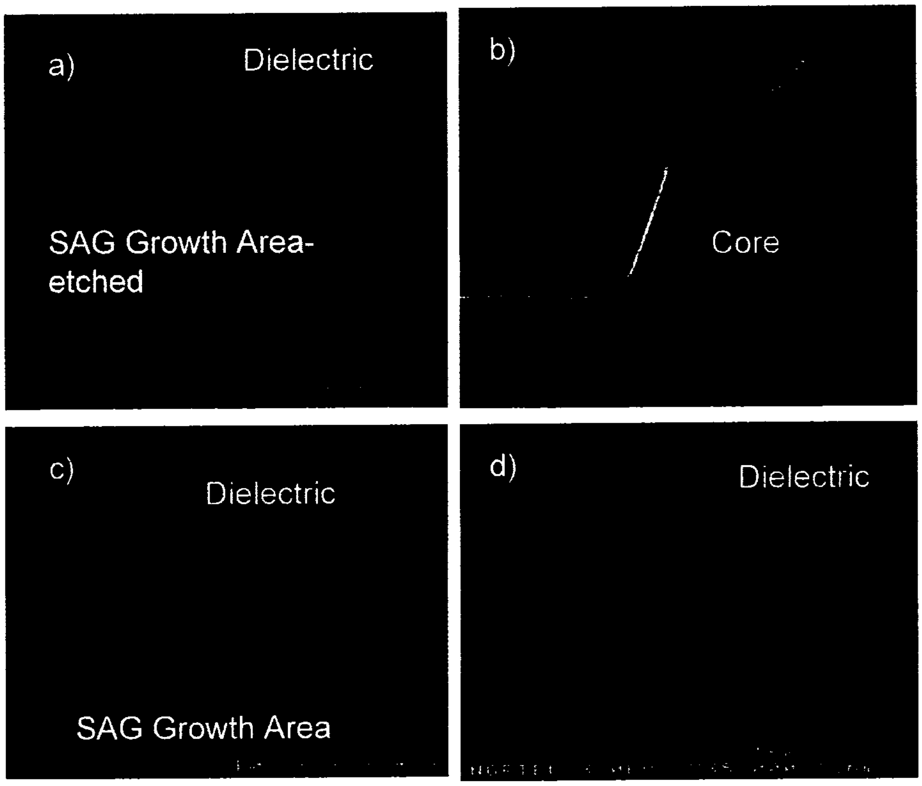

Figure 4.5: *ICP Etch for Active Material Removal.*

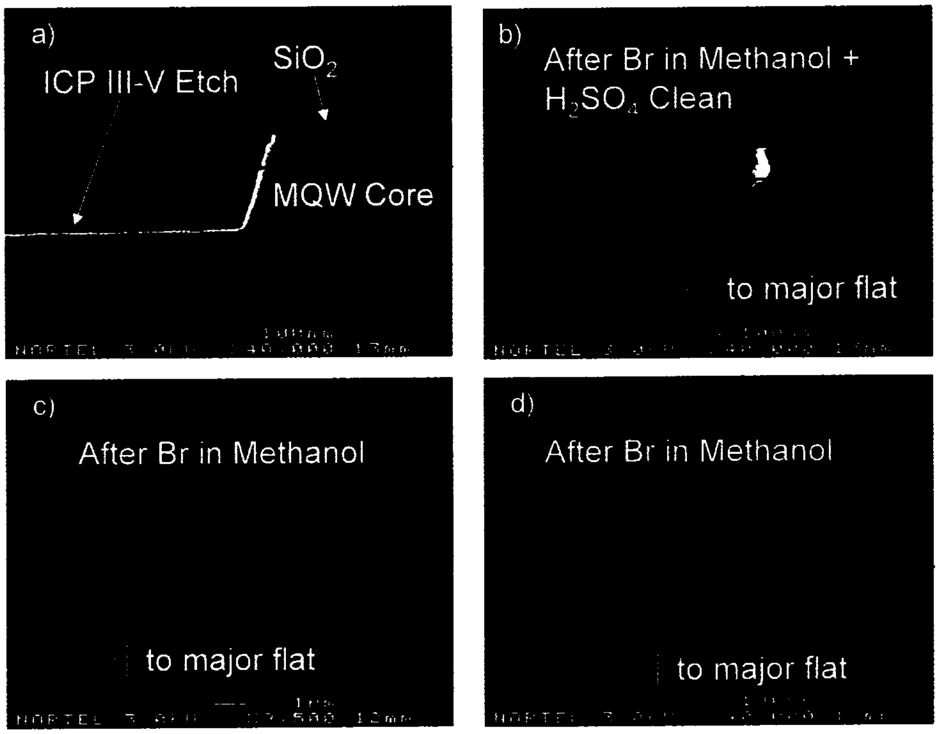

Figure 4.6: *Impact of Wet Chemical Clean Prior to SAG.*

4.6d, the clean introduces a slight undercut of the dielectric. Note also the difference in the post-clean profile angles introduced by the wafer orientations. This is due to the crystallographic dependence of the Bromine in methanol etch, not due to the exclusion of the sulfuric acid rinse in Figure 4.6d. Sulfuric acid is known to etch InP at a rate on the order of tens of angstroms per minute. An increase in this etch rate was observed due to dielectric loading effects when approaching the butt-joint along the length of the gap in the dielectric shown in Figure 4.2.

4.3.2 Optimized Selective Area Growth Butt-Joint for the Mach-Zehnder Modulator

Once the active core material has been removed and the semiconductor surface prepared for expitaxy by either of the methods discussed in Section 4.3.1, the tapered passive spot-size converter core can be deposited by selective area MOCVD growth. The nominal second growth structure has been outlined previously in Section 3.9.2. No modifications in the growth condition are required relative to the planar growth calibration runs, even though the second growth occurs on a dielectric-patterned, and non-planar surface. The first deposited layer is an undoped 50nm thick InP film. The purpose of this layer is to centre the waveguide core of the SSC with the waveguide core of the active modulator. The impact of waveguide core misalignments on the butt-joint optical loss has been previously quantified in Section 3.5.1. Figure 4.7a shows the first attempt made at aligning the cores by

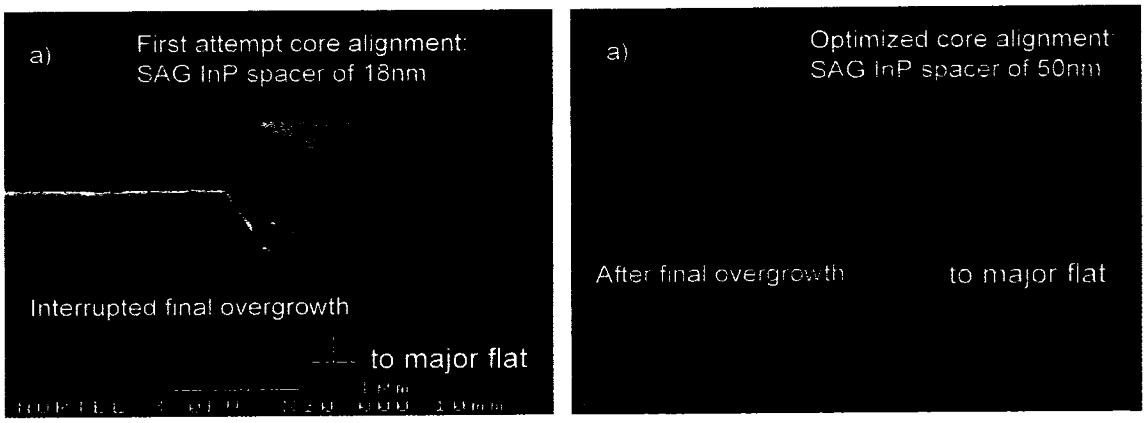

Figure 4.7: ***Waveguide Core Alignments with the Waveguide Butt-Joint Perpendicular to the Major Wafer Flat.***

using an 18nm thick InP spacer layer. This 18nm thick spacer would have been optimal if there was no over-etch introduced by the chemical clean and the expected InP SAG enhancement factor of 4.0 was achieved. Figure 4.7b shows that the optimal core alignment is actually achieved with a 50nm thick InP spacer layer. A spacer thickness of 50nm is optimal by design if 1200Å of over-etch is introduced by the chemical clean along with the expected InP SAG enhancement factor of 4.0.

The second layer deposited is an undoped 46nm thick film of strained $Q=1.3\mu m$ InGaAsP. The -0.2% strain value was determined to partially compensate for the expected non-uniform red-shift on the group III sub-lattice under SAG enhancement due to the different lateral diffusion lengths for the group III precursors at a pressure of 100mBar [196,199,200]. A selective area growth thickness enhancement of 3.8 for the Q layer has been predicted by Jonathan Greenspan at the centre of the 15μm gap in the dielectric at the butt-joint.

The selective area second growth finishes with a final 30nm of undoped InP. This layer serves to protect the SSC tapered core and provide a uniform InP surface for the third blanket overgrowth.

Figure 4.8 shows SEM pictures of the optimized Mach-Zehnder to spot-size converter butt-joint structure where the waveguide butt-joint is perpendicular to the major wafer flat. In Figure 4.8a the structure is shown following the ICP dry etch and wet chemical clean for reference. In Figure 4.8b the structure is shown following the selective area second growth. Note the "hockey stick" formation of the spot-size converter core. It has shown that precursors transported via surface migration from the exposed dielectric sidewall facets account for the parasitic growth enhancement of a semiconductor film within a few microns of the mask during planar growth, and that this parasitic growth is not a function of the dielectric loading growth enhancement factor [197,198]. I hypothesize that a similar mechanism, due to the depth of the etch, is responsible for the "hockey stick" formation seen in Figures 4.8b, 4.8c and 4.8d.

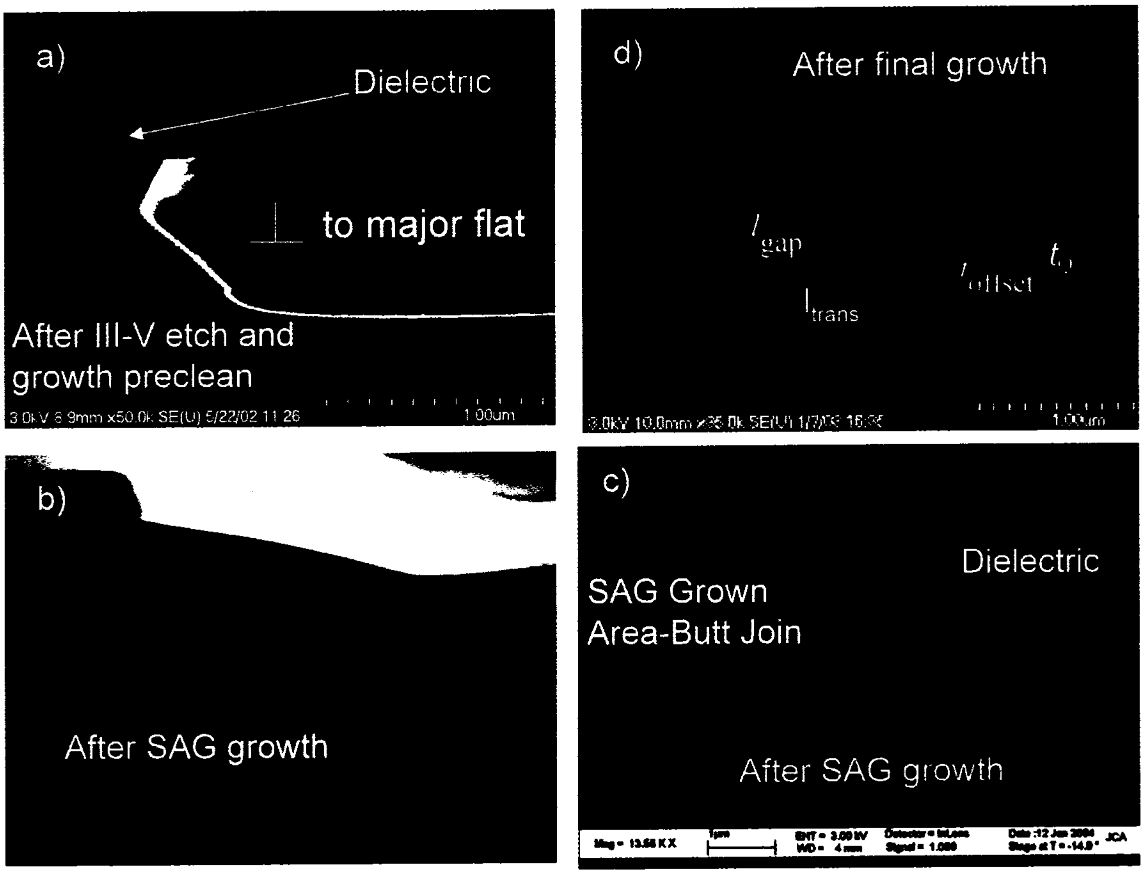

Figure 4.8: ***Optimized Butt-Joint Process for the Mach-Zehnder Modulator with the Waveguide Butt-Joint Perpendicular to the Major Wafer Flat.***

Figure 4.8d defines four quantitative parameters for the butt-joint that have proven to be quite reproducible wafer-to-wafer. Nominal values for these parameters are: l_{gap}=0.3-0.4μm, l_{trans}=0.8-1.0μm, t_{offset}=70-90nm, and t_Q=0.18-0.2μm.

4.3.3 Experiments with Selective Area Growth Temperature and Pressure

Figure 4.9 shows examples of a butt-joint region for a 2X2 experimental matrix of growth temperature and pressure. Note the first growth wafers for these experiments use the 40Gb/s electro-absorption modulator layer structure without a p-doped InP cap layer over the Q=1.47μm core. Jonathan Greenspan has explored the dependence of the SAG growth process on temperature and pressure using controlled experiments on patterned planar wafers [202]. Increasing the pressure should reduce the lateral diffusion length for the group III precursors, which will increase the observed growth enhancement, however, the pressure change should also increase the probability of polycrystalline formations on the surface of the SiO_2 dielectric. The impact of the temperature increase from 650°C to 675°C was not clear *a priori* but it was included to test the sensitivity of the growth pressure variable space. Figures 4.9d and 4.9f show the butt-joint under nominal growth conditions. In Figure 4.9b a 25°C temperature increase at the nominal 100mBar pressure shows no significant change in the growth enhancement, surface morphology or polycrystalline growth. In Figures 4.9c and 4.9e the butt-joint region is shown for a growth pressure of 200mBar at the nominal 650°C growth temperature. The growth enhancement factor has been increased from 3.8 to 7.0 with only a slight degradation in the surface morphology. However an additional 25°C temperature increase, as shown in Figure 4.9a, produced extremely poor growth morphology in the butt-joint region and significant patches of polycrystalline growth on the dielectric. It is clear that pressure can be used to increase the growth enhancement factor, however, doubling the pressure would likely lead to an unstable operating regime for a manufacturable process.

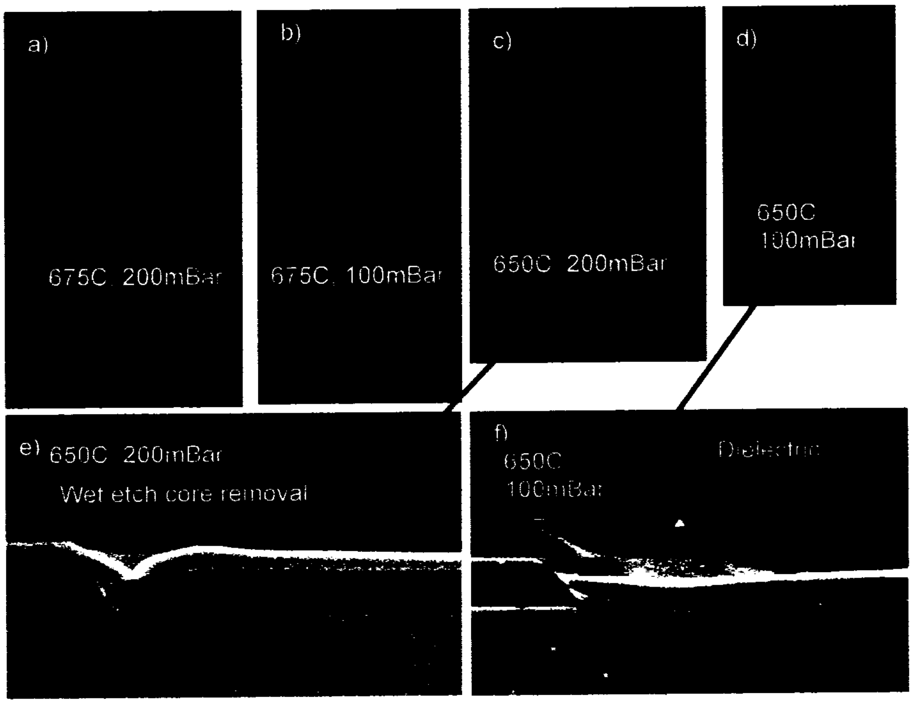

Figure 4.9: *SAG Design of Experiments I: Temperature and Pressure with the Waveguide Butt-Joint Parallel to the Major Wafer Flat.*

In Figure 4.10 two follow-up experiments are presented using the standard Mach-Zehnder modulator first growth with a dry etched core and the standard wet chemical clean discussed in Section 4.3.1. In Figure 4.10a no significant change in the parasitic growth from the <111> interface is seen when the III-V pressure ratio is changed during the 50nm InP spacer layer growth. This was done by reducing the PH_3 flow from 400sccm[5] to 200sccm. In Figure 4.10b the SAG growth pressure was increased to 150mBar. An additional 1.4X

---

[5] sccm is a flow rate in standard cubic centimeters per minute.

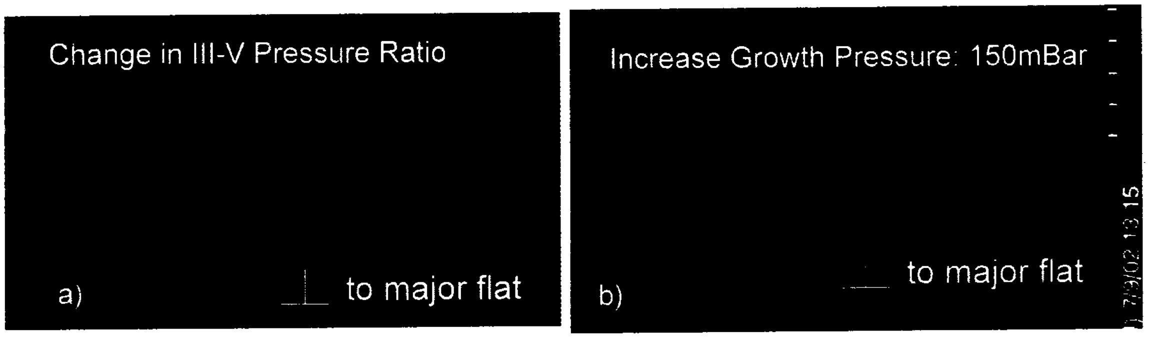

Figure 4.10: *SAG Design of Experiments II: Pressure with the Waveguide Butt-Joint Parallel to the Major Wafer Flat.*

enhancement of the passive core is observed relative to the standard 100mBar growth pressure. The observed core misalignment is due to the additional enhancement of the 50nm InP spacer layer. No degradation in the surface morphology or increase in polycrystalline deposit on the dielectric was observed. These experiments show the "hockey stick" butt-joint profile is robust and growth enhancement factors up to 5.2 could be used in a manufacturable selective area growth process if required. This robust enhancement factor is among the highest reported.

4.3.4 Optimized Selective Area Growth Butt-Joint for the 40Gb/s Electro-absorption Modulator

Figure 4.11 presents cross-sectional SEM pictures of the optimal passive-to-active butt-joint on the 40Gb/s electro-absorption modulator at both 100mBar and 150mBar growth pressures. The waveguide butt-joints are parallel to the major wafer flat. The active cores were removed using the semiconductor wet etch process described in Section 4.3.1 and shown in Figure 4.4. The semiconductor etch times were optimized to minimize the dielectric undercut. Similarly to Figure 4.4, no p-doped InP spacer was present above the modulator active core in the first growth structure. The butt-joints shown in Figure 4.11 have some of the highest enhancement factors found in the literature, in conjunction with being qualitatively the most aesthetically pleasing.

It is reasonable to ask why the optimized butt-joint for the Mach-Zehnder modulator shown in Figure 4.8 has a "hockey stick" shape, while the optimized EAM butt-joint shown in Figure 4.11 does not. After reviewing material available from both developments, the wafer orientation and composition can be eliminated as the cause. This leaves either the semiconductor etch used[6], or the depth of the hole into which the SAG growth is taking place as options. Even in Figure 4.9e no parasitic growth is seen on the sidewall for SAG enhancement factors as high as 7.0. No opportunity was available to definitely answer this

---

[6] The relevant feature of the etch is likely the crystallographic plane it exposes to the SAG growth.

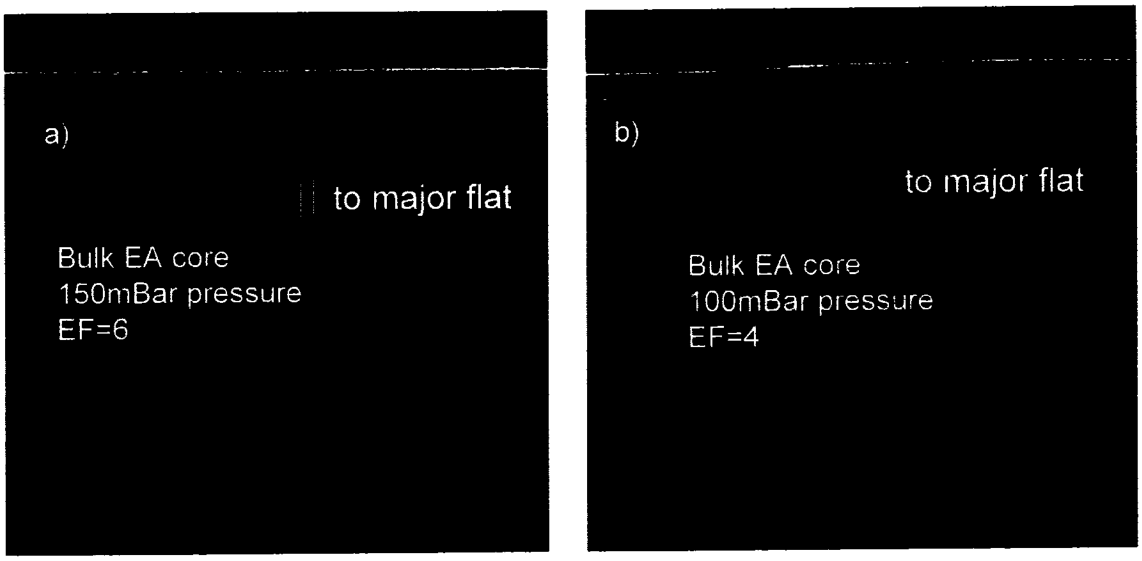

Figure 4.11: ***Optimized Butt-Joint for a 40Gb/s Electro-absorption Modulator-Wet Etch Removal of the Active Material.***

question. As discussed in Section 4.3.2, the most likely explanation is the depth of the hole into which the SAG growth is taking place.

4.3.5 Waveguide Properties of a Non-Enhanced Butt-Joint

Two waveguides exist at the output of the Mach-Zehnder modulator. The primary output obviously passes through the output spot-size converter to enable low-loss coupling to the output optics. The secondary output is an optical dump port complementary to the primary output with a throughput loss that is immaterial. The optical backreflectivity of this dump port, however, must be constrained to better than -50dB.

As shown in Figure 4.12 this dump port waveguide will cross the SAG dielectric boundary at an angle of 59°. The waveguide will abruptly transition from having the active modulator core to having the SAG core without enhancement, as shown in 4.12b.

In Figure 4.13 the spatially resolved optical backreflectivity of the angled low enhancement waveguide core transition, given in Figure 4.12b, was found to be <-65dB using optical low-coherence reflectometry (OLCR). The two distinct peaks for the each reflection point seen in Figure 4.36 are due to the polarization mode dispersion in the semiconductor material.

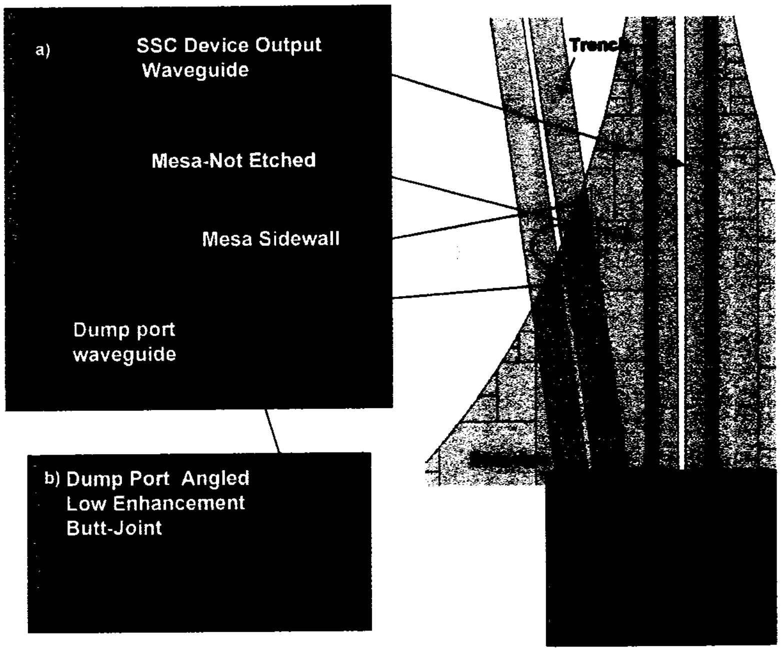

Figure 4.12: *Angled Butt-Joint without Enhancement.*

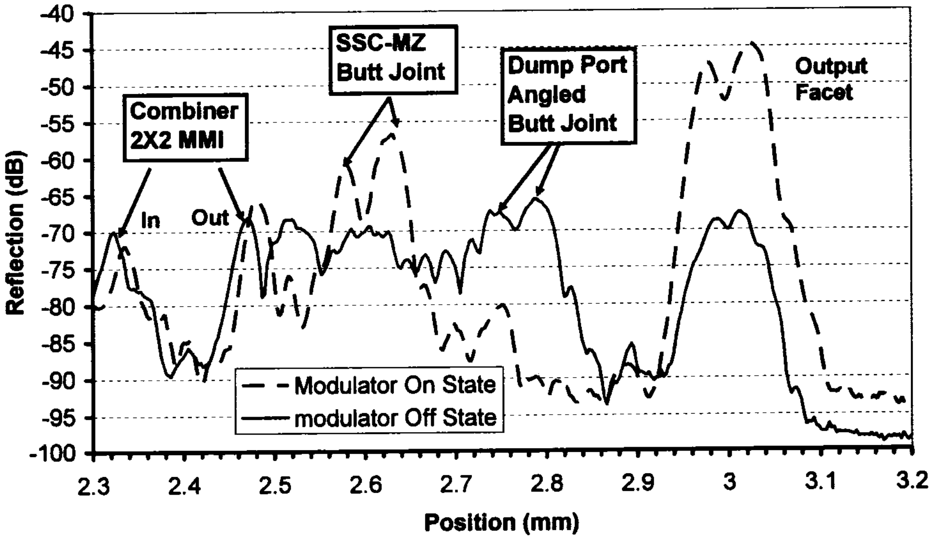

Figure 4.13: *Optical Backreflections from the Angled Butt-Joint without Enhancement.*

4.3.6 The Dielectric Mask

Ideally, no growth will occur on the patterned SiO_2 dielectric mask. However, it has been shown that improper growth conditions can lead to polycrystalline formations on the oxide [230]. High growth temperatures and low growth rates are factors that promote good semiconductor selectivity during growth [231]. Polycrystalline formations are to be avoided since they will change the profile of the enhancement factor in the regions between the oxide, and the defects they induce during the third growth can greatly complicate post growth wafer processing.

The quality of the dielectric mask can impact the selectivity of the growth to the semiconductor [232]. Polycrystalline growth on the dielectric can occur once the partial pressure (or reactant concentration) of the reagents above the mask surface reaches the value required to form stable nuclei. Defect sites or contamination on the dielectric surface can act as nucleation sites for this polycrystalline growth. Obviously, the local partial pressure of the reagents near the mask surface will depend on the growth pressure and the ratio of oxide to exposed semiconductor. Qualitatively, SiO_2 appears to be a better dielectric mask for SAG growth than SiN_x, and the thickness of the dielectric, in the range of 1000Å to 3000Å, has no impact on the surface morphology or the amount of growth that occurs on the dielectric surface.

Figure 4.14 shows the stepper lithography alignment mark structure located at several sites near the edge of the wafer. This structure is etched in the first growth and protected by a $1mm^2$ dielectric box during the selective growth. In Figures 4.14a and 4.14b facetted polycrystalline deposits can be clearly seen on the dielectric. FE-AES analysis[7] verified that the material on the mask is InP. The SAG dielectric is stripped prior to the third growth by immersion in a HF bath. However, this alone did not remove the polycrystalline deposits. In fact, the deposits remained at exactly the same coordinates: They were now, however, on the semiconductor, instead of on the dielectric surface. It was found that the majority of the deposits could be removed by including ultrasonic agitation along with immersion in the HF bath, as shown by the clean mark in Figure 4.14c. Qualitatively, the use of thicker dielectrics aided the removal of the deposits and an InGaAs surface was found to have a greater affinity for the deposits. Figure 4.14d shows the clean alignment mark structure following the third and final growth.

4.4 Analysis of Passive Core Vertical Taper Grown by Selective Area Growth

Figure 4.15 shows high resolution optical microscope views of a wafer following the selective area growth. It is clear the wafer surface has excellent morphology and is free of polycrystalline deposits.

---

[7] Field Emission Auger Spectroscopy

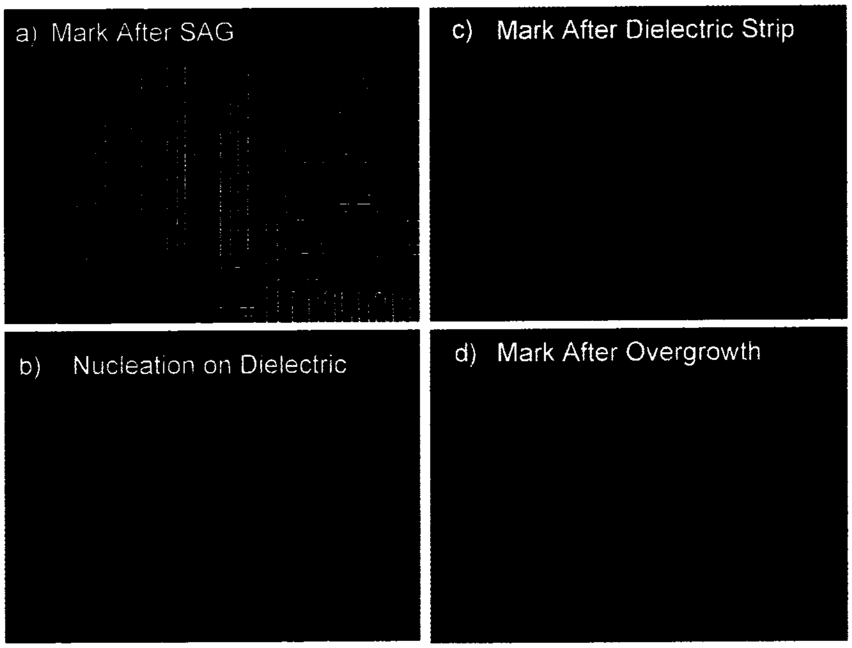

Figure 4.14: *Polycrstalline Deposits on the SAG Dielectrics.*

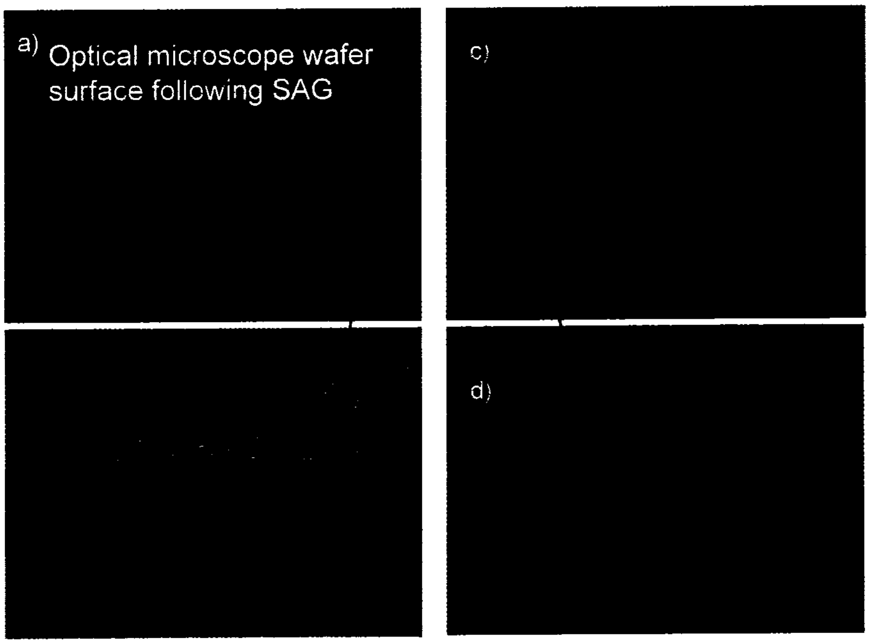

Figure 4.15: *High Resolution Optical Microscope View after SAG Growth.*

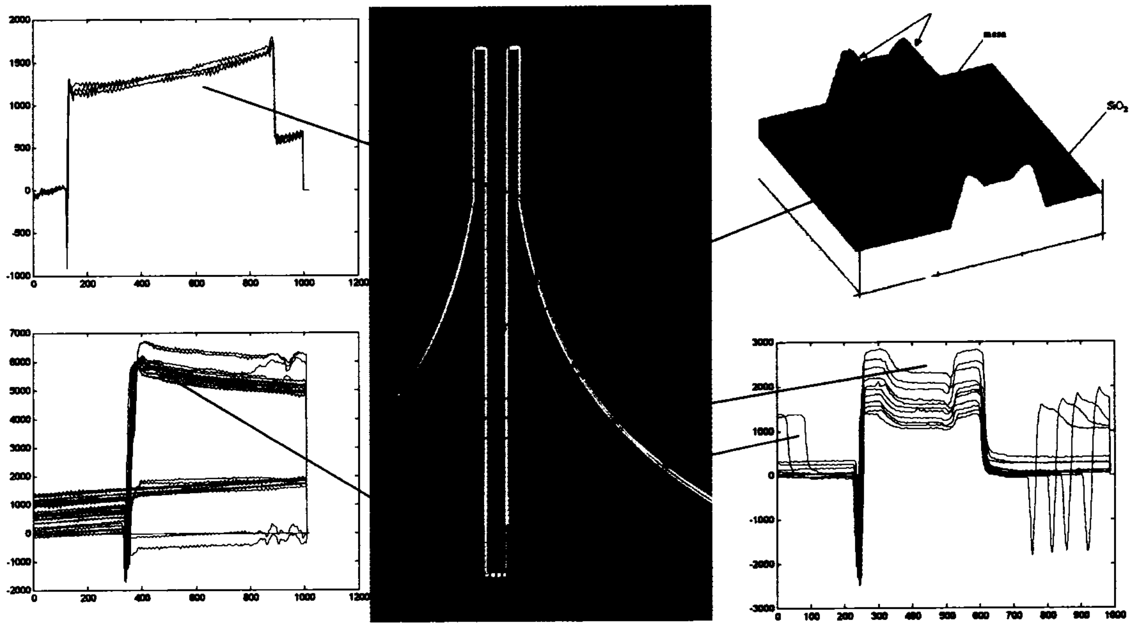

Figure 4.16: *DEKTAK Surface Profile Measurement.*

To study the enhancement factor under SAG growth along the length of the gap in the dielectric mask a DEKTAK surface profiler[8] was used to measure patterned planar InP test wafers that had not received a semiconductor etch. The measurements were made following the removal of the SiO_2 SAG mask at a scan rate of 5μm/s and a sampling rate of 100Hz. Figure 4.16 indicates where the line profiles were taken with the DEKTAK instrument in x and y. Examples of the raw data files collected are also shown. From this collected data, algorithms were used to correct linear slope offsets and to extract the height of the growth at the centre of the gap relative to the height of the wafer under the dielectric mask that had no growth deposition. An inset is also shown of an AFM[9] measurement from a section of the growth in the gap. Near the oxide mask the semiconductor surface was occasionally rough and irregular, however, it was always uniform and smooth in the centre of the gap. A gap width of 15μm was chosen to be certain the 2.0μm to 4.5μm wide ridge waveguide will be located in a growth region with good morphology.

In Figure 4.17 the results of the DEKTAK analysis discussed above are shown for four different dielectric mask designs explored during the development of the 40Gb/s electro-absorption modulator. The selected shapes for all four of these dielectric structures were based on SAG vapor phase diffusion models[10] provided by Jonathan Greenspan. Design A shows the least growth enhancement, and very little difference is seen in the enhancement

---

[8] This device has a needle in contact with the sample that is connected to a transformer coil mounted on a moveable support by a spring. The second transformer coil is fixed. Moving the sample under the needle converts the vertical displacement into a change in effective transform turn ratio.

[9] Atomic Force Microscopy

[10] The models do not contain the surface migration component of SAG growth.

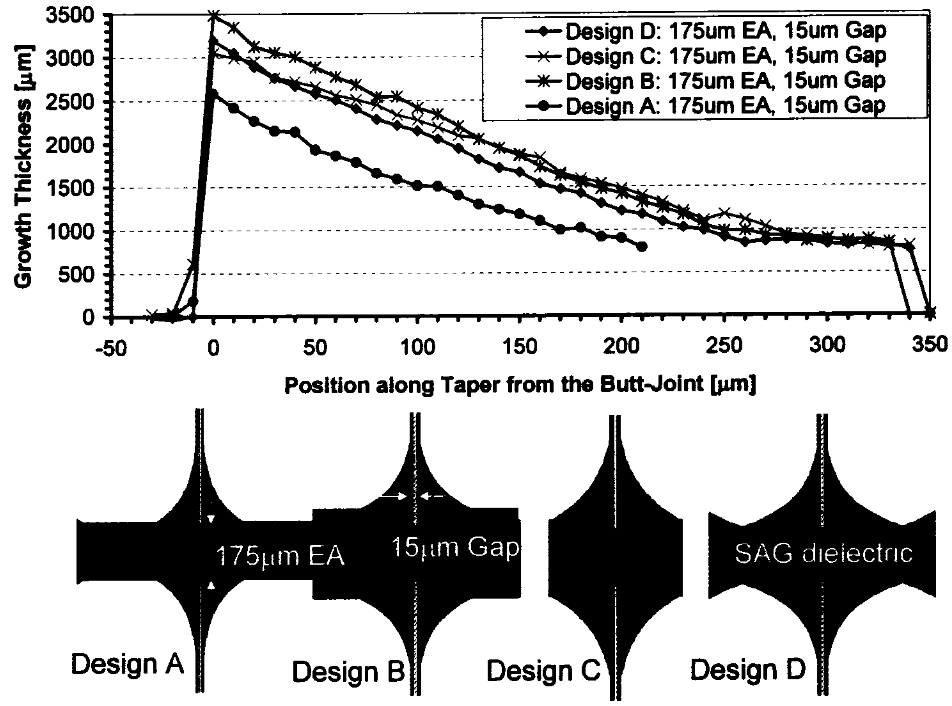

Figure 4.17: *DEKTAK Growth Enhancement Measurement as a Function of Dielectric Design for a 175µm Long Electro-Absorption Modulator.*

factor for designs B, C and D. In Figure 4.18 two variants of dielectric design D are shown. There is obviously a significant increase in the enhancement observed for a 10μm gap compared to a 15μm gap. There is also a notable decrease seen in the enhancement factor when the dielectric block between the butt-joints is 100μm long in y instead of 175μm. This last observation is consistent with the predictions of the growth model which indicates the enhancement should increase with the block length but saturate for lengths greater than 200μm.

Figure 4.19 presents the DEKTAK analysis on a dielectric structure that stabilizes the growth enhancement at 3.9 following the taper. Note that Figure 4.19 shows good device-to-device reproducibility for the enhancement profile. This structure can be used to provide a p-i-n doped waveguide cross-section following the taper that has a core composition lying between the spot-size converter facet waveguide core composition and the active modulator waveguide core composition. This approach has been successfully used by us to integrate monolithically a carrier-injection based Mach-Zehnder attenuator with the active 10Gb/s Mach-Zehnder modulator. If this integration approach is used with the 40Gb/s electro-absorption modulator first growth, it allows the monolithic integration of a tandem EAM modulator[11], or a tandem phase modulator[12].

---

[11] Bandedge of the tandem EAM will be detuned by ~70nm.

[12] This requires the SAG growth core to be reduced from the nominal Q=1295nm.

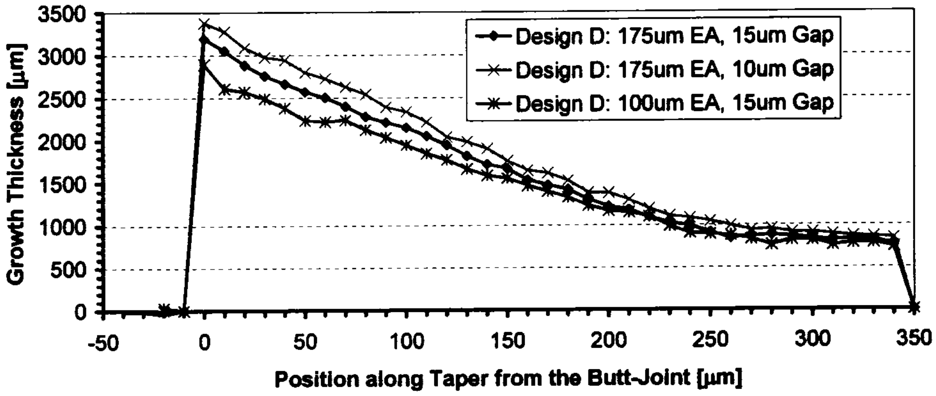

Figure 4.18: *DEKTAK Growth Enhancement Measurement as a Function of the Gap Size in the Dielectric, and the Dielectric Block Dimension Following the Butt-Joint, in an Electro-Absorption Modulator.*

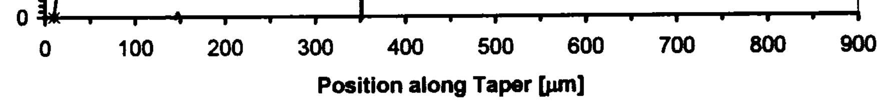

Figure 4.19: *DEKTAK Growth Enhancement Measurement on a Dielectric Structure that Stabilizes the Enhancement Following the Spot-Size Converter Taper.*

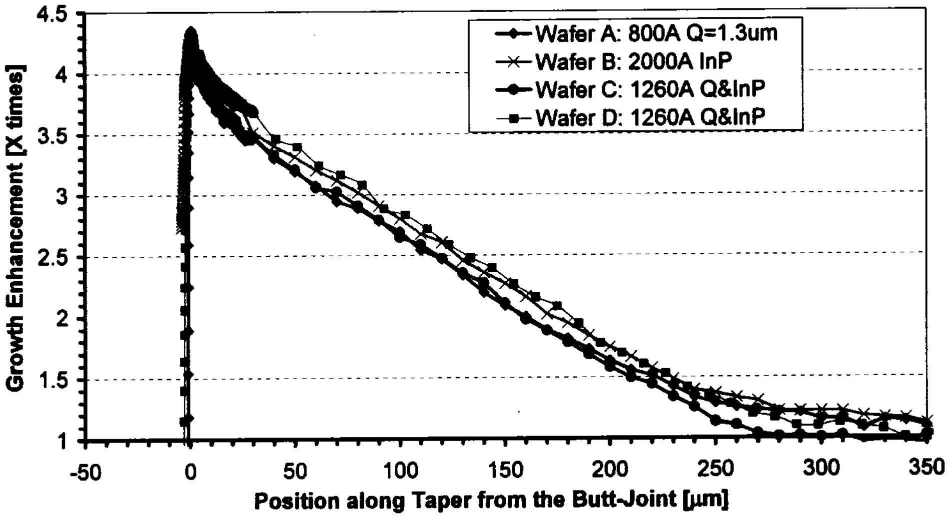

Figure 4.20: ***DEKTAK Growth Enhancement Measurements on the Dielectric Structure used to Define the Spot-Size Converter integrated with the Mach-Zehnder Modulator.***

Figure 4.20 gives the DEKTAK analysis on the dielectric structure used to define the spot-size converter integrated with the Mach-Zehnder modulator. Here the enhancement of the InP and the Q=1.295μm InGaAsP layer have been determined separately. The enhancement of the InGaAsP layer is slightly lower than the enhancement of the InP layer. Enhancement measurements from two additional wafers using the nominal second growth discussed in Section 4.3.2 are also provided in Figure 4.20. It should be noted that the noise on this enhancement data as a function of position is a result of the measurement technique. The selective area growth process is dominated by gas phase diffusion, so minimal local variations in the thickness are expected. Qualitatively, based on Figure 4.20, the wafer-to-wafer variation appears to fall within the accuracy of the experimental measurement technique. In Figure 4.21 an experimental fit to the Q=1.3μm InGaAsP enhancement versus position data has been plotted against the desired profile developed in Section 3.6.2, and the modelled SAG profile provided by Jonathan Greenspan. Obviously, the model, which does not include surface migration effects, underestimates the enhancement within 100μm of the butt-joint, however, it is clear that a dielectric design and set of growth conditions providing a desirable growth thickness taper profile has been achieved[13].

As discussed in Section 4.3.2, the composition of the quaternary core layer in the SAG growth is expected to vary along with the layer thickness. Figure 4.22 presents a spatially resolved photoluminescence measurement along the length of the gap in the SiO_2 dielectric. This measurement was done by a colleague using a modified Waterloo Scientific SPM-200 Scanning Photoluminescence (PL) Mapper. The SPM-200 mapper is equipped with a X–Y translation stage having a 0.25μm step size. A sapphire lens was used as an objective

---

[13] The experimental data fits well to a 2nd order exponential thickness taper function. The nominal thickness taper function for the SSC simulations in Section 3.7 uses a 3rd order exponential taper, however, Figure 3.32 demonstrates that no impact on SSC insertion loss will result from this change.

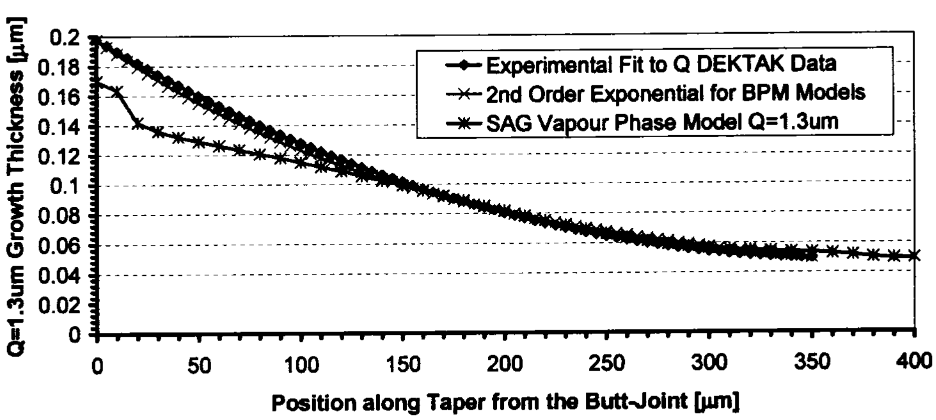

Figure 4.21: *Comparison of the Measured Growth Enhancement against the Desired Profile and a SAG Model.*

to focus the HeNe excitation source to a ~ 20μm spot-size on the sample. A telescope was installed in the measurement path so only the central portion of the PL signal would enter the scanning monochromator and be sampled by the InGaAs detector. The expected spot-size of the kit was ~ 1μm. In Figure 4.22 several different averages of the measured PL wavelength are provided along with a polynomial fit that has been used for the taper design in Section 3.6. The total shift in the material composition along the taper is ~100nm. This compositional shift has been used in the taper design to minimize the transmission losses at the passive-to-active waveguide butt-joint, as discussed in Section 3.5.

4.5 Third Growth and the Impact of Re-Growth Interface Contamination

The third growth, as previously defined in Section 3.9.3, provides the p-doped InP overclad and p+ doped InGaAs contact layers common to both the spot-size converter and the Mach-Zehnder modulator. Therefore, prior to this growth the selective area SiO_2 mask must be stripped from the wafer surface by the HF etch process discussed in Section 4.3.6. This dielectric strip does not damage the semiconductor lattice, as does a dry etch plasma, so no further preparation of the surface is required prior to the third growth. The initial samples of electro-absorption modulators prepared in this manner, however, suffered from sulfur (S), oxygen (O), and silicon (Si) contamination at the interface between the second and third growths[14] This was determined from the Secondary Ion Mass Spectroscopy (SIMS) profiles as a function of depth provided in Figure 4.23, where the gallium concentration is plotted along with the Si and Zn dopants to identify the relative position of the waveguide core. The depth profiles for sulfur and oxygen are not available, but their integrated concentration profiles (dose) at the second-to-third growth interface are quantified in Figure 4.23 along with interface Si dose. The SIMS measurement has a spatial resolution

---

[14] These airborne contaminates are known to adsorb to InP [214,215].

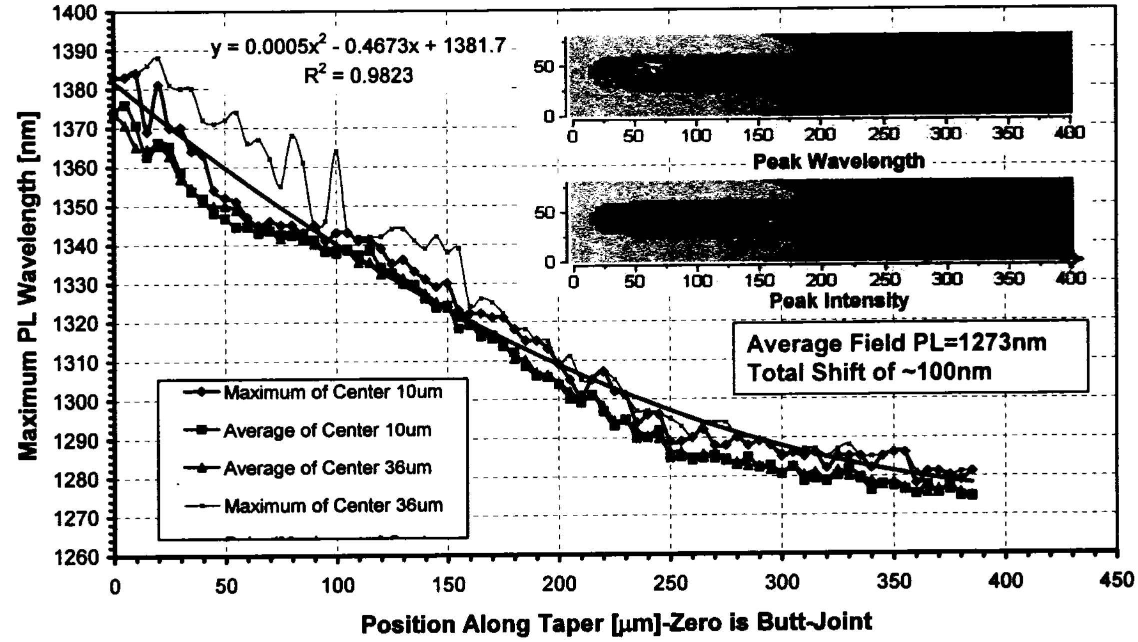

Figure 4.22: *High Resolution Photoluminescence along the SSC Taper.*

of 33nm, so it was not possible to determine with SIMS the thickness of the contamination layer.

Semiconductor p-i-n junction modulators rely on changes in the optical properties of a waveguide core in the presence of large electric fields (kV/cm). The existence of a N^+ Si contamination layer in the p-doped region of the device will reduce the external voltage efficiency of the modulator by introducing an electric field drop, outside of the waveguide core, to deplete the contamination layer[15]. Comparing curves A and B in Figure 4.24 clearly shows the impact of the Si contamination layer at the 3rd MOCVD regrowth interface. Both these curves are DC light transmission versus voltage in a 40Gb/s electro-absorption modulator. Curve A is for a device on the wafer with the SIMS profile given in Figure 4.23. Curve B is from an identical structure on a wafer where the interface clean defined below has been implemented prior to the third growth. It is clear that the device in Curve B has superior external voltage efficiency.

E.H. Sargent et al. encountered a large turn-on voltage in multi-growth lateral current injection lasers and attributed the problem to interface contamination [216]. No solution, however, was proposed. A series of experiments aimed at reducing interface contamination was undertaken by the Nortel Networks MOCVD growth team. To avoid Si contamination originating from the walls of the MOCVD chamber, no Si doping sources were used in the reactor once it had been cleaned prior to the third growth. The MOCVD team suc-

---

[15] From Gauss's law $\frac{dE}{dx} = \frac{\rho}{\epsilon}$, the total field drop across the contamination layer will be proportional to the total net charge given by the difference in the Si and Zn concentration profiles in the layer ($N_{Si} - N_{Zn}$.)

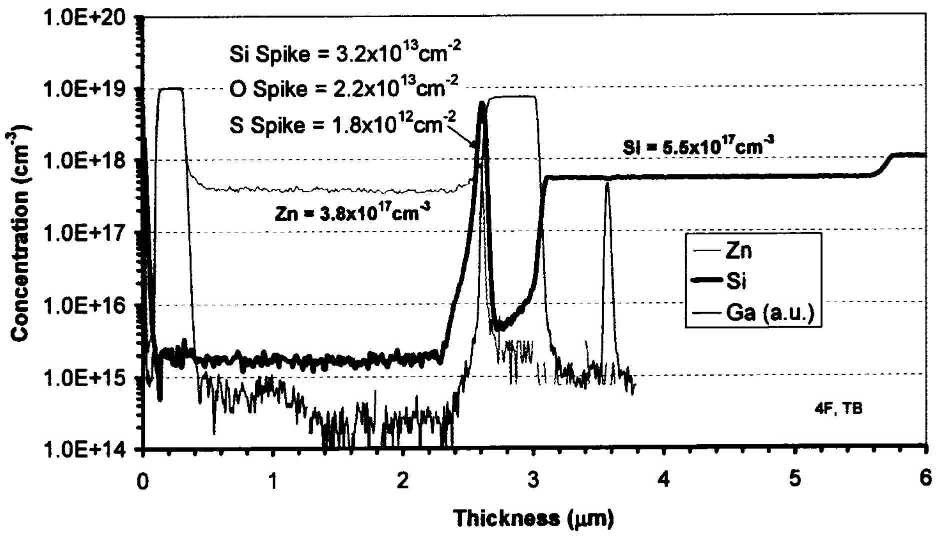

Figure 4.23: *SIMS Measurement of an Electro-absorption Modulator with Si Contamination at the 3rd MOCVD Re-Growth Interface.*

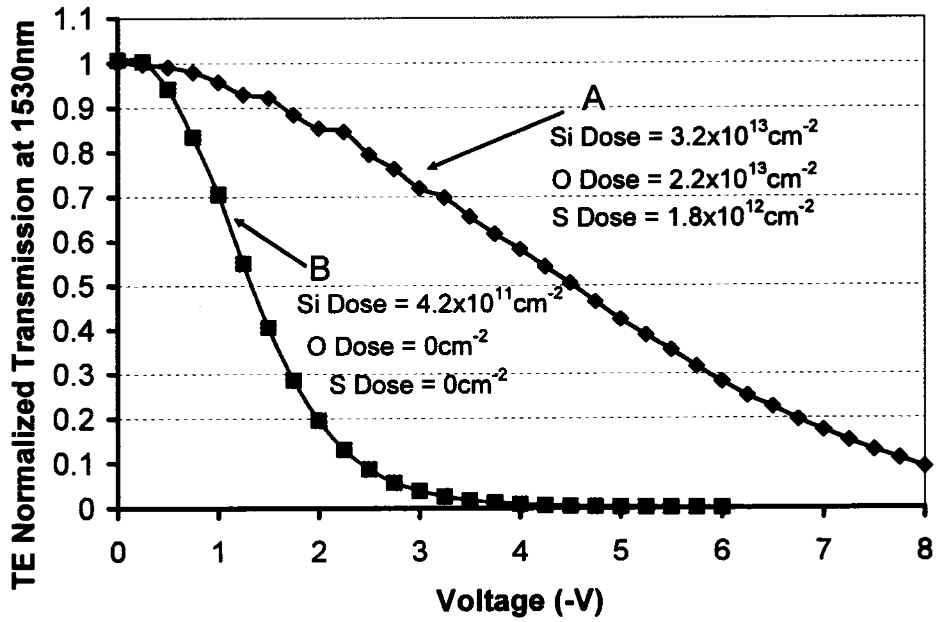

Figure 4.24: *Impact of Si Contamination at the 3rd MOCVD Regrowth Interface on a Electro-absorption Modulator LV Transfer Curve: Curve A-Prior to Introducing 3rd Growth Preclean, Curve B-With the 3rd Growth Preclean*

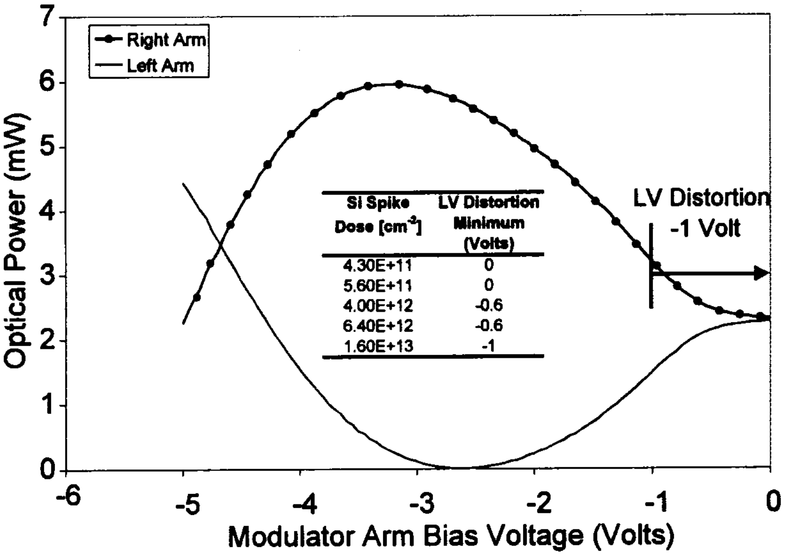

Si Spike Dose [cm^{-2}]	LV Distortion Minimum (Volts)
4.30E+11	0
5.60E+11	0
4.00E+12	-0.6
6.40E+12	-0.6
1.60E+13	-1

Figure 4.25: ***Impact of Si Contamination at the 3rd MOCVD Regrowth Interface on a Mach-Zehnder Modulator LV Transfer Curves.***

ceeded in minimizing the interface contamination by treating the wafers with a series of UV exposures followed by 1% HF immersions. The UV exposure formed ozone that oxidized the Si (and InP) on the wafer surface. The immersion in a 1% HF solution dissolved the oxidized material. This process has been previously demonstrated by Ingrey [217]. The process was repeated multiple times instead of extending the duration of UV exposure since the oxidation rate of InP is known to be logarithmic with time. It can be seen from the SIMS data provided in Figure 4.24 that implementing this procedure reduced S and O below the sensitivity limit of SIMS and it reduced the Si dose from 3.2E13cm^{-2} to 4.2E11cm^{-2}.

Figure 4.25 provides an example of the impact a Si contamination layer has on the light versus voltage (LV) transfer curves in a Mach-Zehnder modulator. A distortion in the LV transfer curves at greater than -1V is observed along with a significant drop in voltage efficiency[16]. This device was measured by SIMS to have a Si contamination layer with a dose of 1.6E13cm^{-2}. The Figure enumerates the low voltage LV distortion limit as a function of the measured Si contamination dose.

4.6 SSC Facet Coating

It is necessary to coat the cleaved spot-size converter semiconductor facets in order to reduce the TE optical backreflectivity from the semiconductor-to-air interface to below 0.1%.

---

[16] The right arm maximum is usually reached by -2.5V.

Numerous numerical procedures have been applied to calculate optical reflections within integrated optical components [237, 240, 243]. The Free Space Radiation Mode (FSRM) method [237, 238] is a numerically efficient procedure developed specifically to determine waveguide facet reflectivity in the presence of multi-layer thin-film dielectrics. The method as developed by Kendall et al. is based on the following three assumptions:

- The waveguide is approximated by a one dimensional three layer waveguide of infinite extent perpendicular to the propagation direction. Real waveguide geometries can be approximated using the effective index method [103] where appropriate.
- The input waveguide supports only one guided mode.
- The input waveguide is transversely symmetric, such that all radiation modes will radiate symmetrically in the transverse direction perpendicular to the direction of propagation. No radiation modes should exist that radiate in only one transverse direction.

The calculation efficiency of this method enables the full design space to be searched numerically for the optimal coating designs to minimize the optical backreflectivity from the SSC waveguide facet as a function of wavelength.

The coating design space is experimentally restricted since an ion beam deposition (IBD) system [236] is used to deposit a stack of thin-film dielectrics, where each layer is either Ta_2O_5 or SiO_2, onto the facet of a freshly cleaved[17] waveguide. With this IBD system it is possible to accurately control both the thickness and refractive index of the as-deposited dielectric films. The deposition rate for Ta_2O_5 is controlled to 1.25± 0.05Å/sec with the material refractive index specified to 2.200± 0.005. The deposition rate for SiO_2 is controlled to 0.95± 0.05Å/sec with the material refractive index specified to 1.49± 0.005.

To minimize the facet reflectivity of the SSC waveguide, a two layer coating composed of an inner layer of Ta_2O_5 and an outer layer of SiO_2 is used. With the limitation of a two layer coating, and given the dispersive nature of the semiconductor waveguide materials, it is not possible to find a single two layer coating design that is optimal for the full wavelength range of interest (1528nm-1609nm).

To determine the optimal coating designs for minimum facet reflectivity the SSC vertical (y) refractive index distribution is used to define the one dimensional waveguide for the FSRM method calculations. Specifically, the waveguide core is a 50nm thick $Q=1.3\mu m$ InGaAsP layer clad on either side by InP layers of infinite extent. In Figure 4.26 the calculated optimal two layer coating designs for the SSC waveguide are presented as a function of the device operating wavelength. For these calculations the refractive indices of the InP and $Q=1.3\mu m$ InGaAsP waveguide materials have been recalculated at each wavelength, according to the formula presented in Appendix 2.5, however, the refractive indices of

---

[17] Cleaving immediately prior to coating minimizes the thickness of oxidized contaminants present on the cleaved surface.

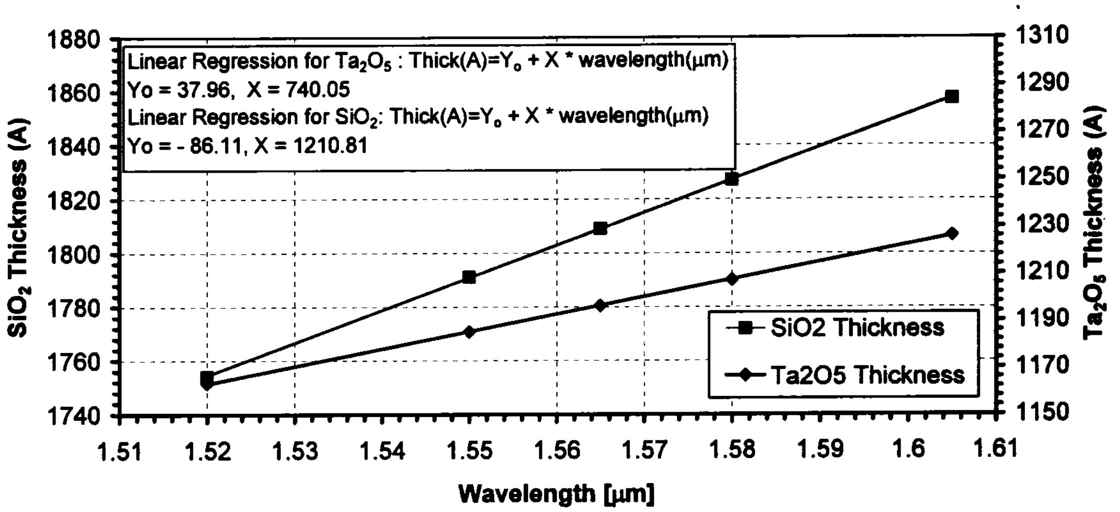

Figure 4.26: *Optimal Two Layer Coating Design for the Spot-size Converter versus Wavelength.*

Band	C-Blue	C-Red	L-Blue	L-Red
Centre Wavelength (nm)	1536	1554.5	1575.5	1598.25
Min Wavelength (nm)	1527	1545	1564	1587
Max Wavelength (nm)	1545	1564	1587	1609.5
Ta_2O_5 Thickness (Å)	1175	1188	1204	1221
SiO_2 Thickness (Å)	1774	1796	1822	1849

Table 4.1: *2 Layer Facet Coating Designs for the Spot-Size Converter as a Function of Wavelength.*

the dielectric coating materials have been taken as constant over the wavelength range of interest.

To minimize the number of required coating designs, the operating wavelength range is divided into four bands with a single coating design selected for use in each band. The TE_0 facet reflectivity is guaranteed by design to be less than 0.1% within each band for the given tolerances on coating index and thickness. This has been experimentally verified [236]. The bands are defined in Table 4.1. It is also possible to use a four layer coating to enable a single coating design for the full wavelength range in either C-Band or L-Band.

4.7 Optical Characterization of the Spot-Size Converter

In this Section experimental measurements verifying the SSC design are outlined. Insertion loss measurements are described on a uniform ridge waveguide structure identical to the SSC facet structure, and on a 2.0μm wide modulator waveguide with the SSC coupling structure on both facets of the device. Measurements of the optical far field from the

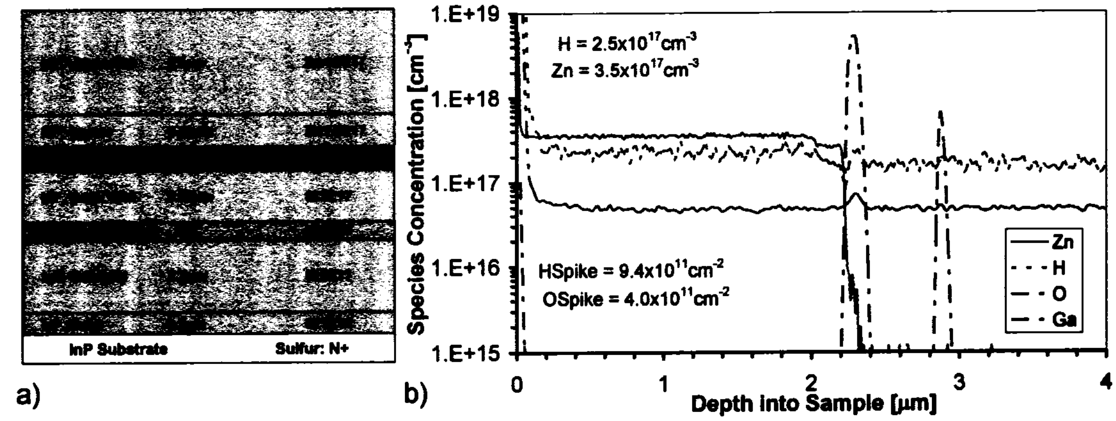

Figure 4.27: ***a) Single Growth Structure Representative of the Initial SSC Facet Design, b) SIMS Measurement on the Processed Growth Structure.***

modulator waveguide, and measurements of its SSC-to-modulator butt-joint reflectivity by OLCR are described. OLCR measurements are also given for the facet backreflectivity improvement available by angling the SSC facet. The section ends with a discussion of a best-in-class 40Gb/s electro-absorption modulator enabled by the SSC design.

4.7.1 Measurements on a Uniform Ridge Waveguide Structure Identical to the SSC Facet Structure

When a SSC structure based on a single thin quaternary layer in a strongly-guided waveguide was proposed, it was deemed prudent to study initially the facet mode of this structure in isolation. Figure 4.27a shows a single growth structure that is representative of the initial SSC facet design. This facet design does not include the controlled n-side doping discussed in Section 3.4.5. The closest comparable simulation is given in Figure 3.16c. This SSC design was used on the 40Gb/s Electro-absorption modulator to be presented in Section 4.7.6.

Straight waveguides were defined in the growth structure of Figure 4.27a, to a depth of 3.0μm, using contact lithography and the CO_2:CH_4:H_2 reactive ion etch (RIE) process show in Figure 2.11. Waveguides were available with ridge widths of 2.0μm, 4.0μm, 4.5μm, 5.0μm, 5.5μm, and 6.0μm. A back-to-back tapered ridge width structure was also included, from 4.5μm at the facet, down to 2.0μm in the middle of the device. Due to the impact of the contact lithography on the side wall roughness, as discussed in Section 2.1.6, the optical losses of this tapered ridge width structure was always higher than expected. The profile of the ridge etch can be seen in Figure 4.28b.

Figure 4.27b gives the SIMS profile through the growth structure after process. The as-grown Zn doping concentration is 3.5E17cm^{-3} relative to a request of 4E17cm^{-3}. A concentration of 2.5E17cm^{-3} for hydrogen indicates that significant hydrogen passivation of

Zn has occurred in the overclad layers.

Figure 4.28a provides the measured fiber-to-fiber insertion loss, and polarization dependent loss (PDL), for 1mm long straight waveguide devices, with all the available ridge widths. 10μm radius lensed tapered fibers were used for the input and output coupling optics. Both facets of the 1mm devices were anti-reflection coated as detailed in Section 4.6. The quoted device insertion loss is relative to a fiber patch-cord in the place of the two tapered fibers, so it includes the coupling and conversion losses in the tapered fibers themselves. The solid red line marks the 1.01dB insertion loss, obtained at best coupling, between the two matched 10μm radius tapered fibers. With the exception of the 2.0μm wide waveguides and the 2.0μm-4.5μm tapered ridge waveguides, all ridge widths have approximately 0.5dB of excess loss relative to the fiber-to-fiber measurement. This 0.5dB excess loss must include both the on-chip losses, and the coupling loss between the tapered fiber mode near field and the waveguide mode.

The loss of the 2.0μm wide waveguides appears better than would be expected. Following calculations for the guided modes in this structure, it was hypothesized that the loss measurement was actually performed with the coupling fibers alignment to the underclad slab mode[18], since this would produce the lowest coupling loss. This was confirmed by measuring the lateral far field from this waveguide by the same technique discussed in Section 4.7.3. The measured lateral FWHM far field was 8.2°. This is consistent with the measured insertion loss, and input coupling to the underclad slab mode.

The measured polarization dependent loss (PDL) for the straight waveguide devices in Figure 4.28a is <0.2dB. Measuring PDL at these very low levels is difficult. The measurement was made by launching light through a fiber-based polarizer. The polarization was swept over the Poincaré sphere until a maximum and minimum transmission at each wavelength was found. All splitters and combiners were removed from the test-bed to obtain a fiber-to-fiber reference PDL of 0.09dB.

In Figure 4.29 the measured on-chip losses are given, obtained using the cut-back Fabry-Perot method [175–178] discussed in Section 2.1.6. The measurement samples are 4mm long uncoated straight waveguides with a calculated[19] and assumed TE facet reflectivity of 27.6%. All the measurements use a TE polarized launch from the input tapered fiber, and samples from 4 different wafers are included in the data set. Similar results were obtained on all wafers. The insert provides the averaged on-chip loss in dB/cm across the four wafers as a function of ridge width. A value of 5dB/cm is representative.

Figure 2.21 shows that the ridge sidewall scattering loss drops rapidly with increasing ridge width. If we assume approximately 0.4dB/cm of sidewall scattering loss from Figure 2.21, then approximately 4.6dB/cm of loss remains to be attributed to the growth layer dopants. With 52% confinement to the Zn-doped layers, based on Table 3.1, this requires

---

[18] This slab mode is similar to the fourth plot on the right in Figure 3.16c, except the ridge width is only 2.0μm.

[19] The cleaved facet reflectivity was calculated using the techniques described in Section 4.6.

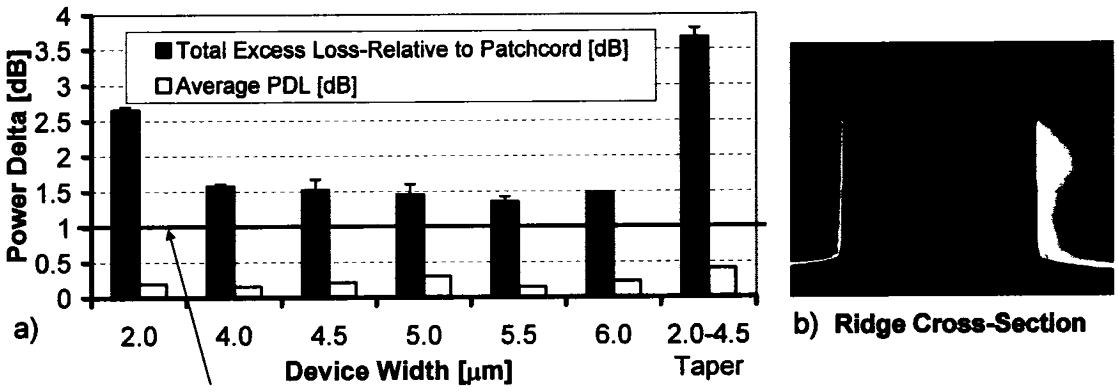

Fiber-to-Fiber Loss of 1.01dB over a patch cord, 0.09dB PDL

Figure 4.28: *a) Total Insertion Loss and PDL of 1mm Long Uniform Ridge Waveguide Devices having the Initial SSC Facet Design Growth Structure as a Function of Ridge Width, b) Cross-Section SEM View of the Ridge Waveguide.*

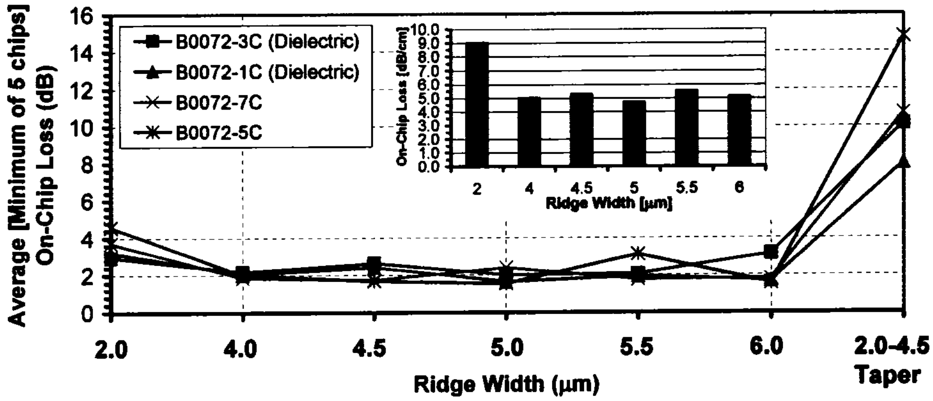

Figure 4.29: *a) On-Chip Insertion Loss Measured by a Fabry-Perot Technique for 4mm Long Uniform Ridge Waveguide Devices having the Initial SSC Facet Design Growth Structure as a Function of Ridge Width.*

an effective Zn doping of 1.02E17cm^{-3}. This is consistent with nearly 100% compensation of Zn by the background hydrogen in Figure 4.27b.

Together Figure 4.29 and Figure 4.28 indicate that any excess coupling loss from mode matching the SSC facet mode with the tapered fiber near field mode must be negligible, relative to the match in the fiber-to-fiber mode near fields already included in the fiber-to-fiber loss reference.

In Figure 4.30 the change in fiber-to-fiber insertion loss and PDL is given, as a function of wavelength, for an antireflection coated, 1mm long, and 4.5μm wide uniform ridge waveguide device. The insertion loss is measured relative to the value at 1546nm. There is obviously negligible variation as a function of wavelength.

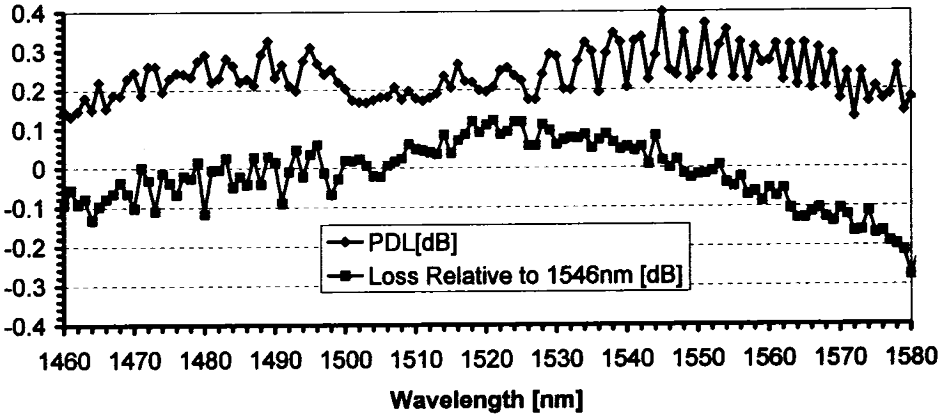

Figure 4.30: ***a) Change in Fiber-to-Fiber Insertion Loss and the Polarization Dependent Loss [PDL] as a Function of Wavelength for a 1mm Long 4.5μm Wide Uniform Ridge Waveguide Device having the Initial SSC Facet Design Growth Structure. The Insertion Loss is Measured Relative to the Value at 1546nm.***

Figure 4.31 shows the change in insertion loss as a function of misalignment between the antireflection coated, 1mm long, uniform ridge waveguide devices and the output tapered fiber. These results are consistent with the expectations from the calculation of two misaligned Gaussian beams in Figure 3.4.

The results presented in this Section indicate that the SSC facet structure in Figure 4.27a, based on a single thin quaternary layer in a strongly-guided ridge, can provide excellent coupling to a 10μm radius tapered fiber mode as a function of wavelength, polarization, and small positional misalignments.

4.7.2 Insertion Loss Measurements of Straight Waveguide in Mach-Zehnder Growth Structure

Figure 4.32 presents the measured TE insertion loss as a function of wavelength for nine 2150μm long and 2.0μm wide straight waveguides in the modulator structure with input and output spot-size converters. The coupling optics to the waveguide are the 10μm radius lensed tapered fibers discussed in Section 3.2.3. The device-to-device and wafer-to-wafer reproducibility are good, with a 3dB mean excess loss for the devices, relative to a fiber-to-fiber measurement, at the nominal 1550nm operating wavelength. A breakdown of the losses in these straight waveguide devices has been given previously in Section 2.1.9. If the input coupling optics are misaligned towards the substrate in the $-y$ direction, as shown for device 3 on wafer A, the only impact is an increase in the insertion loss. There is no evidence of a higher order vertical mode being excited. If the input coupling optics are misaligned in the x direction, however, an ≈15nm periodic variation in the insertion loss as a function of wavelength is observed. This is consistent with the excitation of both the TE_0 and TE_1 modes in the modulator structure, and spatial filtering of the waveguide

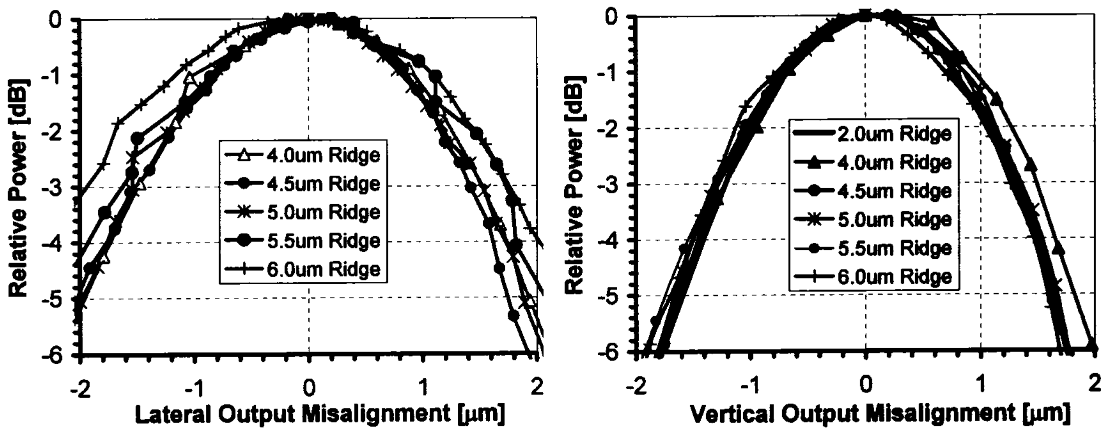

Figure 4.31: *Insertion Loss Tolerances to Lateral and Vertical Tapered Fiber Output Coupling Misalignment in 1mm Long Uniform Ridge Waveguide Devices having the Initial SSC Facet Design Growth Structure as a Function of Ridge Width.*

output field by the symmetric Gaussian near field of the collection optics. The wavelength spacing of the expected periodic variation in insertion loss is 16.5nm given by,

$$\Delta\lambda = \frac{\lambda^2}{L(\Delta N_{eff})} \tag{4.1}$$

where L is the 2150μm length of modulator waveguide, λ=1.55μm, and ΔN_{eff} is the difference in the two dimensional TE$_0$ and TE$_1$ N$_{eff}$ values given in Figure 2.22.

Figure 4.33 shows the measured extinction ratio as a function of voltage and wavelength for a 1200μm long phase modulator on the waveguide in Figure 4.32. The TE$_0$ modal purity in the modulator structure is demonstrated by a maximum extinction ratio in excess of 40dB, and the observed monotonic decrease in extinction with increasing wavelength[20]. No periodic variations in the extinction ratio[21] are seen as a function of wavelength even with heavy extinction of the fundamental mode.

4.7.3 The SSC Coupling Mode

The SSC far field characteristics were assessed using the Photon Inc. LD8900 Goniometric Radiometer introduced in Section 3.2.3. A 10μm tapered fiber was used as the input coupling optics. The measured FWHM far field of this tapered fiber was 17.2°X17.2°.

Figure 4.34 provides a typical measurement for the horizontal and vertical far field from the SSC on the Mach-Zehnder modulator. The average measured FWHM far field from 12 different chips on three different wafers was 21.8°X24.4° with a standard deviation of

---

[20] Increasing wavelength corresponds to an increasing offset from the material absorption bandedge.

[21] Periodic variations would be indicative of a mode beating phenomena.

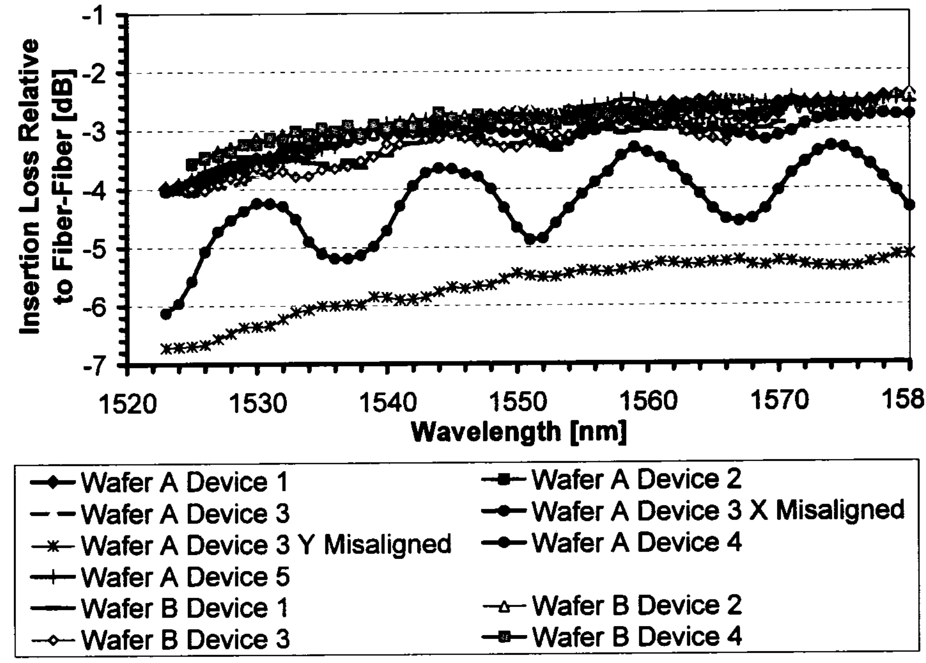

Figure 4.32: *Measured TE Insertion Loss for 2150μm long 2.0μm Wide Straight Waveguides in the Modulator Structure with Input and Output Spot-Size Converters as a Function of Wavelength.*

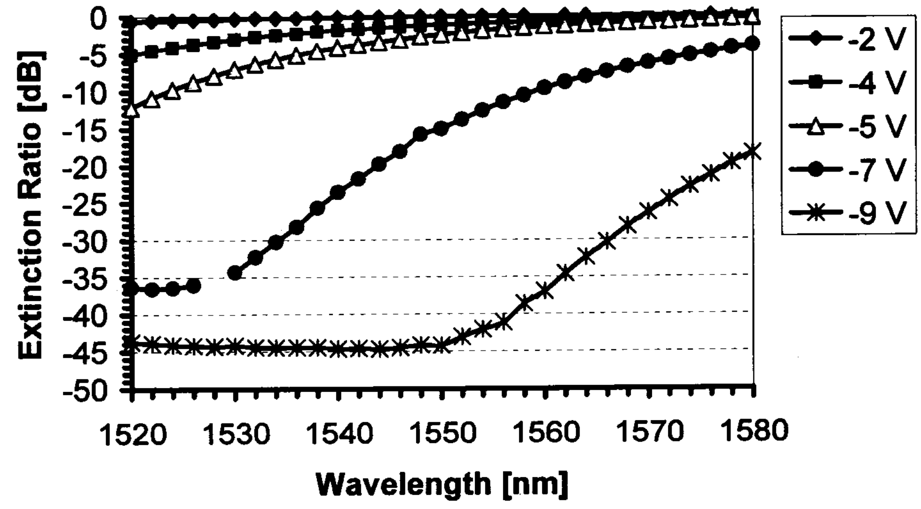

Figure 4.33: *Measured Extinction for a 1200μm Long Phase Modulator on the 2150μm long and 2.0μm Wide Straight Waveguide in the Modulator Structure having Input and Output Spot-Size Converters as a Function of Wavelength.*

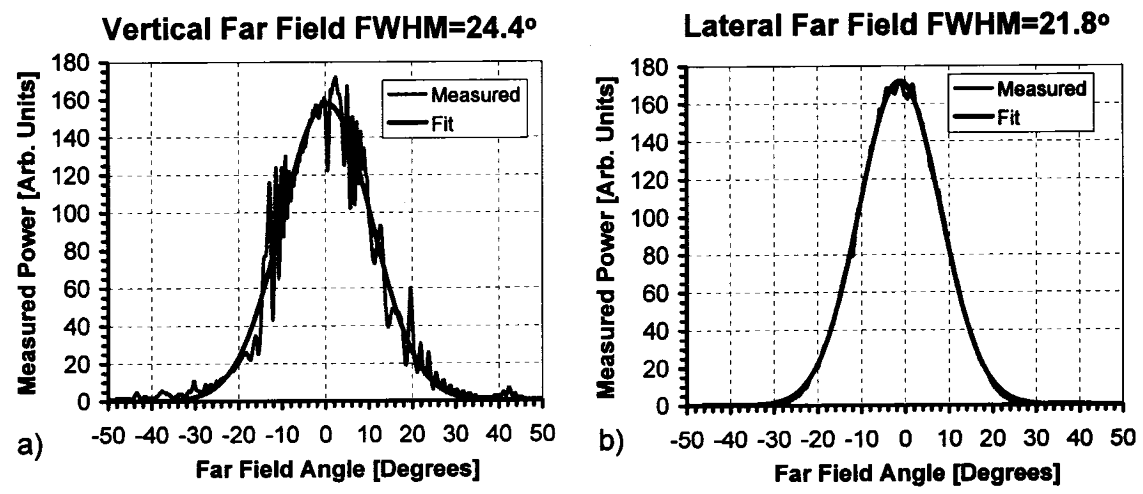

Figure 4.34: *Far Field Measurement on the Mach-Zehnder Modulator.*

0.4°X0.6°. This compares well with the expected FWHM dimensions of 20.4°X23.7° given in Section 3.4.

Figure 4.35 provides a typical measurement for the horizontal and vertical far field from the SSC on the 40Gb/s electro-absorption modulator presented in Section 4.7.6. The facet structure of this SSC is the same as the structure shown in Figure 4.27. The measured FWHM far field is 18.3°X17.7°. This compares reasonably well with the expected FWHM dimensions of 20.2°X19.7° calculated using Equation 3.12, from the fit dimensions to the TE_0 mode in Figure 3.16c.

4.7.4 Backreflectivity of the SSC-to-Modulator Butt-Joint

In Section 3.5.2 the backreflectivity of the SSC-to-modulator butt-joint has been calculated. The experimentally measured reflectivity of the butt-joint can be observed in Figure 4.13 and Figure 2.62. The input SSC-to-modulator butt-joint in Figure 2.62 has the least accumulated losses and polarization dispersion in the semiconductor material. The measured backreflectivity is between -50dB and -55dB. The output on-state modulator-to-SSC butt-joint backreflectivity in both Figure 4.13 and Figure 2.62 is between -55dB and -60dB. The calculated zero transition length backreflectivity for the SSC-to-modulator butt-joint is -43dB and for the modulator-to-SSC butt-joint it is -49dB in Figure 3.22. The 10dB offset in the experimental data is not unexpected since the experimental butt-joints, shown in Figure 4.8, are not the zero length transitions assumed in the theoretical calculations shown in Figure 3.22.

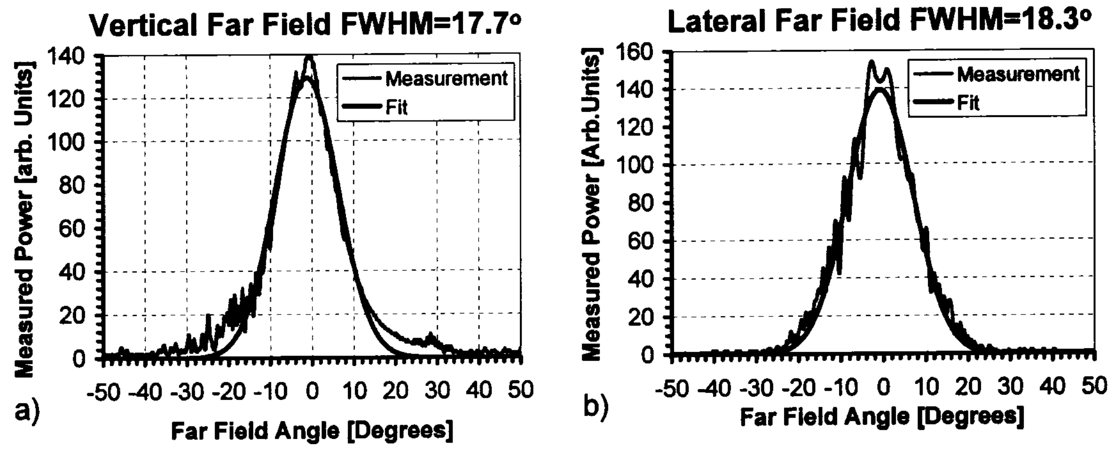

Figure 4.35: *Far Field Measurement on the 40Gb/s Electro-absorption Modulator: SAG Dielectric Design B, 175μm long EAM, 15μm Gap.*

4.7.5 Angled Facet SSC Backreflectivity

Section 4.6 concluded it is possible to manufacture a coated facet on the SSC design with better than 0.1% optical backreflectivity. The resonant Fabry-Perot cavity formed by device facets at this level of reflectivity will have no impact on the modulator performance. For applications where a semiconductor laser source is directly butt-coupled to the InP Mach-Zehnder modulator [47,52], without the use of an intervening optical isolator, much lower modulator output facet reflectivity is required. Any optical feedback from the SSC output facet that returns to the laser source will vary in both magnitude and phase due to the presence of the modulation. This optical feedback acts to increase the source linewidth [234] and/or introduce frequency pulling [235] on the source wavelength. Both of these effects negatively impact the transmission characteristics of the modulated signal over optical fiber. Therefore, it is desirable to minimize, as much as possible, any post-modulation backreflections in the modulator device for this integrated[22] laser-modulator application. As discussed in Section 3.4, a significant benefit available with the introduction of the SSC onto the Mach-Zehnder modulator is the ability to reduce the output facet reflectivity by simply introducing an angled output.

Figure 4.36 compares the output facet backreflectivity of a coated SSC waveguide at normal incidence to the facet, with a coated SSC waveguide having an incident angle of 5 degrees using OLCR[23]. The 24dB improvement in facet reflectivity observed in Figure 4.36 is in excellent agreement with the theoretical prediction given in Figure 3.10. The two distinct peaks for the output facet seen in Figure 4.36 are due to the polarization mode dispersion in the semiconductor material. With an absolute output facet backreflectivity now better than -65dB in Figure 4.36 there is no practical value in further reductions to the SSC front facet reflectivity for the Mach-Zehnder modulator application. If the SSC output facet is

---

[22] The integration could be either hybrid or monolithic.

[23] Optical Low Coherence Reflectometry

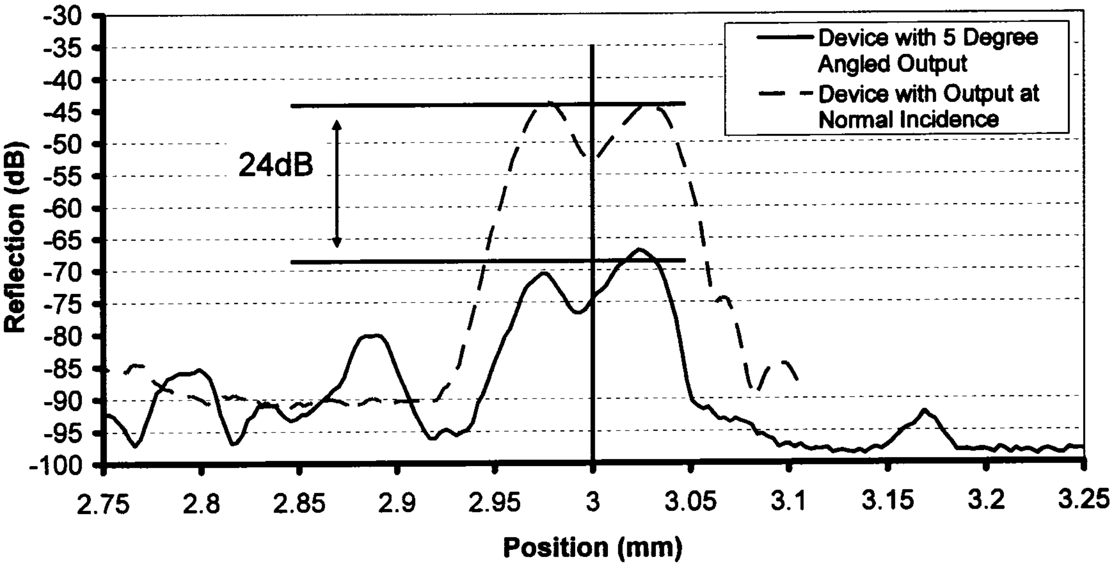

Figure 4.36: *Output Facet Backreflectivity in the InP Mach-Zehnder Device as measured by Optical Low Coherence Reflectometry.*

angled then the next most significant backreflections in the modulator device are the SSC-to-modulator butt-joints. These butt-joint interfaces should, therefore, also be angled, as discussed in Section 3.5.2.

4.7.6 Best-In-Class 40Gb/s Electro-Absorption Modulator Enabled By The SSC Design

The flexibility of the SSC design is demonstrated by the best-in-class performance it enables in a 40Gb/s electro-absorption modulator. At the Optical Fiber Communications Conference in 2003 a 40GHz electro-absorption modulator (EAM) module was presented with record unamplified loss (3.6dB fiber-to-fiber), extremely low PDL (0.3dB over 15dB extinction), and low absolute chirp ($|\alpha_H| < 0.6$ over the full dynamic range), using a highly manufacturable design [244]. A very low RC time constant was achieved by a short 100μm active modulator length, practically enabled using the integrated spot-size mode converters developed in this Chapter, to increase the total device length to 1mm. The EAM core design for this modulator, and the presented measurements in Figure 4.38, are the work of Kelvin Prosyk and Ron Moore. I designed the photonic integrated circuit (PIC) and produced the chips in partnership with the NORTEL growth and fabrication engineering groups.

The photonic integrated circuit (PIC) containing the EAM is shown in Figure 4.37. The core of the deeply-etched active region is a 0.29μm thick layer of bulk quaternary with a photoluminescence (PL) peak centered at 1460nm at room temperature. The fraction of the optical mode overlapping with the core is calculated to be 0.67 and 0.62 for TE and TM po-

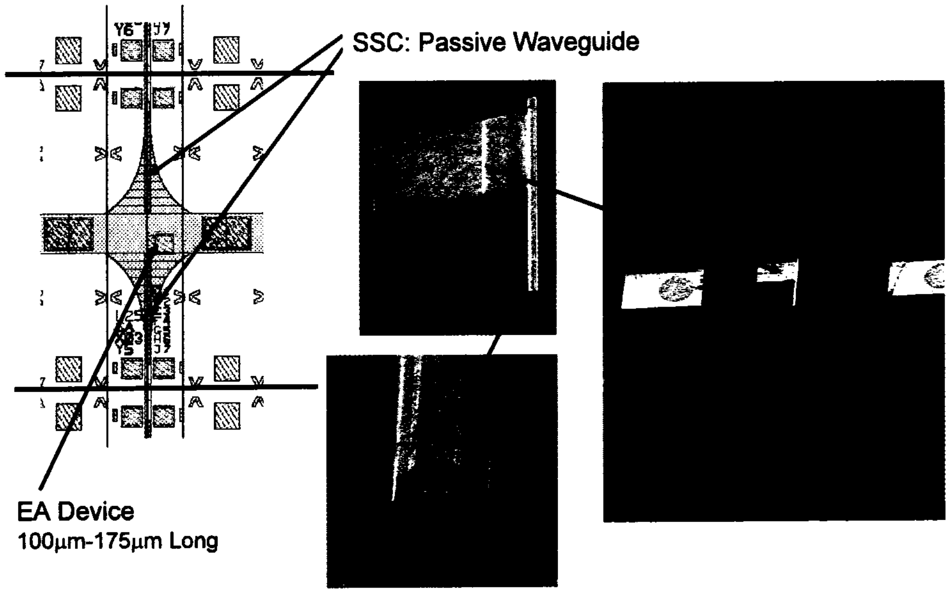

Figure 4.37: ***Photonic Integrated Circuit Containing a 40Gb/s Electro-absorption Modulator.***

larized light, respectively. The bulk layer was grown with a small amount of compressive micro-strain (lattice mismatch of 0.08%) to counter the slightly higher absorption of TM light expected in a bulk material in an electric field [247, 248]. Although a similar result could be achieved by using a thinner core with a greater difference between the TE and TM confinement factors, higher capacitance and an undesirable polarization dependence of the butt-joint loss between the SSC and EAM core would result.

The switching curves of the modulator were measured by launching light through a fiber polarizer. The polarization was swept over the Poincaré sphere until a maximum and minimum transmission at each wavelength was found. The resulting pairs of curves are shown in Figure 4.38a, with the difference between the curves defined as the polarization dependent loss (PDL), shown in Figure 4.38b. At 1540nm, the fiber-to-fiber insertion loss is 4dB while maintaining an extinction ratio of >10dB at 2.5V. At 1550nm, the insertion loss is 3.6dB, which is the lowest reported for an EAM [249]. By applying a pre-bias of 0.75V at 1540nm, a further 3dB of extinction ratio can be achieved with an on-state insertion loss of 5.5dB. With or without pre-bias, the PDL is less than 0.3dB over the entire dynamic range at 1540nm, and less than 0.6dB from 1530 to 1550nm, which is the lowest PDL ever reported for an EAM over a wide wavelength range [245, 246].

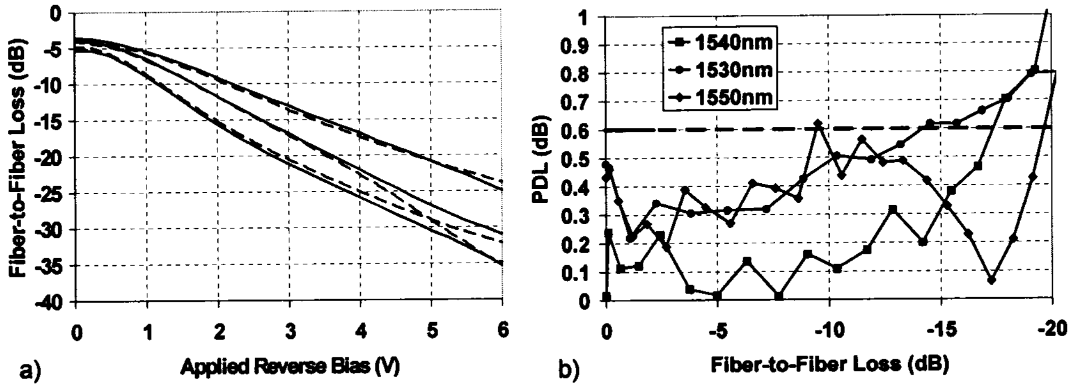

Figure 4.38: *DC Performance of the 40Gb/s Electro-absorption Modulator. Source: K. Prosyk, R. Moore, I. Betty, R. Foster, J. Greenspan, P. Singh, S. O'Keefe, J. Oosterom, P. Langlois, "Low-Loss, Low Chirp, Low Voltage, Polarization Independent 40Gb/s Bulk Electro-Absorption Modulator Module," Optical Fiber Communications Conference, TuP3, 2003.*

Chapter 5

Conclusions and Suggestions for Future Research

5.1 Conclusions

The original contributions contained in this thesis are summarized in three categories: Mach-Zehnder modulator design, strongly-guided waveguide design, and optical mode spot-size converter design.

5.1.1 Modulator Design

Strongly-guided InP/$In_{1-x}Ga_xAs_yP_{1-y}$ based Mach-Zehnder optical modulators for digital 10Gb/s optical communication systems have been developed. The modulators have insertion losses, including coupling losses, as low as 4.5dB due to the incorporation of monolithically integrated optical mode spot-size converters. These insertion losses are the lowest reported to date for an InP-based Mach-Zehnder modulator. They were presented at the 2005 Optical Fiber Communications Conference [56].

Phase shifts in the Mach-Zehnder modulator arms are obtained using a combination of LEO and electro-absorption effects in a MQW core design that has been previously reported by C. Rolland and W. Bardyszewski [16–18]. The published performance data for this MQW core design has been primarily theoretical, and no information has been provided on the wavelength dependence of the MQW material properties as a function of voltage bias. An empirical model that fully quantifies the phase and absorption properties of the MQW, as a function of voltage bias and the wavelength detuning from the bandedge, is provided in this thesis. This empirical model has been extracted from a large sample of 1900 devices taken from 10 different wafers. It is shown that excellent uniformity in the MQW performance can be obtained across a 3″ wafer.

A device model for the InP-based Mach-Zehnder modulator is provided which incorporates the derived empirical model for the phase and absorption properties of the MQW core. This device model has been used to define a modulator design and operating condition that enables controlled frequency chirping to occur during bit transitions in the modulator output power from a "1" to "0" or "0" to "1". The amount of negative frequency chirp generated by the modulator is tailored by varying the optical imbalance between the modulation arms, as originally proposed by Cartledge and Rolland et al. [12]. It is determined that the system performance of this chirped Mach-Zehnder modulator design is dominated by the selected optical split ratio, and that full C-Band operation for the modulator is feasible. The easily measured DC extinction ratio of the modulator is shown to be capable of predicting the optical system performance. It is also shown that this chirped InP Mach-Zehnder modulator design gives improved dispersion-limited reach for 10Gb/s ON/OFF-keying modulation, relative to a negatively chirped $LiNbO_3$ modulator.

A Mach-Zehnder modulator design and operating condition that invokes nearly no transient frequency shifts under intensity modulation is also presented, for the first time, using phase-shifter implementations based on electro-absorption effects.

Variants of these InP-based Mach-Zehnder modulators have been made commercially available co-packaged with semiconductor laser sources.

5.1.2 Strongly-Guided Waveguide Design

A design for a strongly-guided passive waveguide has been provided. The design is a compromise attempting to achieve reasonable birefringence in a low-loss, 2.0μm wide, single-mode waveguide, capable of achieving low-loss bend radii <200μm without offsets. This waveguide structure has been used to optimize ridge etch processes for defining strongly-guided waveguides. It is shown that i-line stepper-based photolithography is critical for obtaining the lowest possible scattering losses at the semiconductor-to-air interfaces. A ridge width of 2.0μm provides a good compromise between low propagation losses (1.7dB/cm) and single mode operation. The measured straight waveguide losses, as a function of ridge width, are comparable to the best in the literature.

A thorough review of the literature on optical bends has been provided in the context of strongly-guided waveguide design. Circular arc bends have been fabricated in the strongly-guided 2.0μm wide passive waveguide structure. These circular arc bends have the lowest reported insertion losses for a 90° waveguide bend with a 50μm bend radius. The optimal lateral offsets required at straight-to-curved waveguide transitions were found to agree with the theory provided by Neumann [143] when two-dimensional mode solutions were used, however, mode calculations based on the effective index method were found to overestimate the required offset. It is shown that i-line stepper-based photolithography is required to obtain low-losses in bent waveguides. No polarization rotation was observed on any of the waveguide bends in the 2.0μm wide strongly-guided passive waveguide structure.

The optimized strongly-guided waveguide structure for the InP-based Mach-Zehnder modulator has been provided. This modulator structure introduces a new and novel method to control higher-order vertical modes on a N^+ InP substrate. This method uses the n-dopant induced refractive index change in InP to create an antiguiding layer in the underclad that can leak the "composite waveguide cavity" modes into the N^+ substrate. The new method was devised because the existing approach in the literature, which uses a thin underclad InGaAs layer to absorb the "composite waveguide cavity" modes, was not compatible with the incorporation of an optical mode spot-size converter.

The provided modulator structure forms a p-i-n electrical diode. To enable significant electrical isolation between the multiple electrical contacts on the modulator structure, a deep helium implantation process has been developed [82, 83]. This implantation process enables five orders of magnitude increase in the resistance between on-chip electrodes simultaneously with a 1dB/cm reduction in optical losses.

The operating principles for strongly-guided multi-mode interference (MMI) couplers have been reviewed and optimal restricted interference 1X2 and 2X2 MMI designs have been given. The criteria for MMI optimization included: low insertion loss for wavelength operation across C-Band, an optical split ratio invariant to both the input coupling misalignments and the expected fabrication tolerances, optical backreflections directed towards the laser source to be less than -65dB for all operating states of the Mach-Zehnder, and optical backreflections directed towards the output fiber to be less than -27dB for all operating states of the Mach-Zehnder. The desired optical backreflectivities have been confirmed experimentally using OLCR.

Two implementations for obtaining freely selectable optical power split ratios in 2X2 MMI's have been demonstrated. The observed optical power split ratio in fabricated devices, based on the butterfly MMI design concept proposed by Besse et al. [106], were found to be in agreement with analytic theory and BPM modeling. A 2X2 MMI design having an optical power split ratio that is actively tuned by forward bias carrier injection into the MQW core has also been demonstrated. This device uses the developed helium implantation process to localize the carrier injection. A tunable optical power split ratio between 1 and 2.5 was obtained with <10mA of current injection and <0.3dB of induced optical loss. This tuning performance is a significant improvement on the existing literature results published by Leuthold and Joyner [108].

Higher order lateral modes have been found to be unavoidable in the low-loss strongly-guided waveguides used for optical modulators. The cut-off width for the TE_1 mode is $\approx 1.7\mu m$ in the provided modulator design, however, even for a ridge width of $1.4\mu m$, the unguided TE_1 mode has a low attenuation coefficient that causes it to persist for propagation lengths up to 1mm. A TE_1 mode filter based on a 1X1 MMI has been studied as a means to deal with this unavoidable higher-order lateral mode. Using OLCR it has been experimentally shown that the implemented 1X1 MMI mode filter does strip the TE_1 mode from the waveguide, and that the backreflectivity from its tapered end-walls is <-55dB, even with the maximum feasible input mode coupling misalignment. The insertion loss, however, was not negligible, so this 1X1 MMI design has not been included in the optical path of the final modulator designs. Alternative designs for a 1X1 MMI mode filter optimized for inclusion with the optimal 1X2 and 2X2 MMI splitter designs has been provided. It is expected that these new mode filter designs will have lower insertion losses, however, no opportunity to fabricate them was available.

Lateral offset waveguide s-bends are required to separate the modulation arms in a Mach-Zehnder modulator to limit the RF crosstalk between the phase-shift electrodes. Sin-based s-bends in strongly-guided waveguides are shown theoretically to be superior to the cosine-based s-bends typically used with weakly-guided optical waveguides. The lower minimum bend radius in a sin-based s-bend is insignificant because radiation losses are nearly negligible in strongly-guided waveguides, however, the lack of curvature mismatch at straight-to-curved waveguide transitions in the sin-based s-bend is significant because the excitation of the TE_1 mode at curvature mismatched transitions can cause significant impairments in modulator performance as a function of wavelength.

A strong matched bend phenomena was observed theoretically for cosine-based s-bends. The optimal waveguide offset required to minimize the TE_1 excitation at the straight-to-curved waveguide transitions for a cosine-based s-bend was found, using BPM modeling, to agree with the analytic theory provided by Neumann [143], when the local bend radius at the straight-to-curved waveguide transition is assumed for the waveguide bend radius. It has been shown theoretically that the gap between the MMI access waveguides could be increased by 0.2μm using lateral waveguide offsets on a TE_1 matched cosine-based s-bend. The s-bend selected for implementation on the Mach-Zehnder modulator designs was a more conservative 120μm long sin-based s-bend with an offset of 8.25μm.

BPM models are provided for the full Mach-Zehnder waveguide layout as a function of wavelength, MMI width and length errors, and input coupling misalignment. It is shown that an operating wavelength outside the wavelength bandwidth of the MMI components (due to length error, width error, or wavelength directly) can cause wavelength oscillations in the device insertion loss and a reduction in the maximum extinction ratio. Input coupling misalignments are shown to have no impact on device performance other than the obvious increase in insertion loss. Modulator insertion loss and optical split and combine ratios are provided for a device measured as a function of wavelength in C-Band. Excellent uniformity in the device parameters is obtained across C-Band. This is the lowest reported insertion loss for an InP-based Mach-Zehnder modulator.

5.1.3 Optical Mode Spot-Size Converter Design

The degree to which the optical mode spot-size conversion between the modulator and a single mode fiber (SMF) can be practically obtained off-chip has been explored. The far fields and coupling losses for lensed tapered fibers and aspheric lens assemblies have been measured and the relationship between the far field and near field mode sizes has been derived for Gaussian beams. An $\approx 20^{o}X20^{o}$ *FWHM* far field is proposed as the optimal modulator chip far field in a manufacturing environment where active optical alignment is available.

An optical spot-size mode converter (SSC) design requiring no compromises from the strongly-guided modulator has been theoretically and experimentally detailed. The design uses a vertically tapered passive waveguide core within a laterally flared strongly-guided ridge. The SSC passive core is butt-joined to the modulator section by a precision dry-etch and MOCVD selective-area-growth (SAG) process. This SSC design is the first application for this mode-conversion approach in a strongly-guided modulator, and it has enabled the lowest insertion losses in the literature for strongly-guided modulator devices.

An overview of the developed spot-size converter fabrication process has been provided. It details how the monolithic integration between the SSC and modulator is achieved in three growth steps. The various etching techniques used to enable the modulator-to-SSC waveguide core butt-joint are fully detailed. Selective area growth enhancement factors as high as 7X have been demonstrated at the butt-joint while maintaining good surface morphology and minimum nucleation on the SAG dielectrics. This SAG result has one of the highest controlled growth enhancement factors reported in the literature for $In_{1-x}Ga_xAs_yP_{1-y}$ materials. Ideal butt-joints between a bulk Q=1.47μm layer and the SSC passive core have been demonstrated, while the butt-joints between the modulator MQW and the SSC passive core were found to have a characteristic "hockey stick" shape that did not contribute significantly to optical loss or backreflectivity.

The backreflectivity of a zero length transition butt-joint has been studied theoretically using a reflection calculation technique we developed [239], and it has been measured experimentally using OLCR. The measured backreflectivity was found to vary between -50dB and -60dB and it was ≈10dB lower than the calculated values. This is not unexpected given the experimental butt-joints in the Mach-Zehnder modulator do not have the zero length transition assumed in the theoretical calculations. A 59° angled butt-joint with the worst possible mode mismatch (unenhanced SAG growth at the butt-joint) was experimental shown to have an optical backreflectivity of ≈-65dB. It was also theoretically shown, but not demonstrated, that an 11° angle for the modulator-to-SSC butt-joint could reduce the expected backreflectivity of the butt-joint by 30dB.

The Love theory for modal propagation in adiabatic waveguide tapers has been reviewed and applied to determine the appropriate vertical and lateral SSC taper profiles in the SSC design. The thickness and composition profile for the SSC passive core, obtained using a selective area growth process, have been studied as a function of the loading dielectric shape and the width of the growth region gap. It is shown that a growth region gap of 15μm enables a profile for the SSC passive core vertical taper that matches a desired profile obtained with BPM modeling. High resolution PL measurements indicate a 100nm Q red-shift in the SSC passive core composition between the unenhanced growth at the SSC facet and the enhanced growth at the modulator butt-joint. The SSC design in this thesis is one of the first to explicitly use the significant composition shift caused by differences in growth precursor lateral diffusion lengths, to reduce mode-mismatch losses at a waveguide butt-joint.

A thorough study of higher-order modes in the facet structure of the SSC waveguide has been undertaken. It is shown that the controlled n-doping introduced in the common underclad layers below the modulator and SSC cores, does effectively control higher-order vertical modes in the SSC waveguide structure, however, it does also limit the vertical extent of the coupling mode at the SSC facet. An alternative SSC facet structure, with an improved vertical extent, is proposed for applications where the possibility of misaligned coupling to the SSC is limited, or where a semi-insulating substrate can be used.

Silicon contamination at the regrowth interface above the modulator core, between the first and third growth, was found to have a significant impact on modulator voltage efficiency. This contamination and its impact have been minimized by introducing a rigorous sample preparation procedure prior to the third growth. This procedure was proposed by the crystal growers and it reduced the silicon interface contamination to below 5E11cm^{-3}.

BPM models have been used to study the tolerances of the SSC design to variations in the taper properties, and to quantify the optical losses expected from the overclad p-doping layers that are common between the modulator and SSC waveguide structures. The SSC design is longer than required to be adiabatic, so it is very tolerant to variations in the taper properties. The doping losses are the single largest contributor to the insertion loss of the SSC. This was know *a priori*, however, it was a compromise required to enable fabrication simplicity.

A phase modulator incorporating input and output SSC structures is demonstrated, with excellent single mode operation, to have the lowest insertion loss reported for a strongly-guided modulator. The sum of the calculated losses in the SSC is found to agree with the extracted value of SSC loss obtained from this phase modulator device. The measured far-fields from the SSC were found to agree with the calculated values to within 1.5^o laterally and 0.7^o vertically. Coating recipes are given that enable the backreflectivity from a normally incident SSC facet to be <1%. It is also demonstrated that the backreflectivity from the SSC device facet can be reduced by an additional 24dB, by angling the SSC to intercept the facet 5^o off normal, in line with provided theoretical calculations.

Finally, the flexibility of the SSC design is demonstrated by the best-in-class performance it also enables in a 40Gb/s electro-absorption modulator. At the Optical Fiber Communications Conference in 2003 a 40GHz electro-absorption modulator (EAM) module was presented with record unamplified loss (3.6dB fiber-to-fiber), extremely low PDL (0.3dB over 15dB extinction), and low absolute chirp ($|\alpha_H| < 0.6$ over the full dynamic range) [244].

5.2 Suggestions for Future Work

Applications for the InP-based Mach-Zehnder modulator at the system level could evolve in two different directions: The available modulation schemes could be expanded, or the modulator with its current functionality could be monolithically integrated with a tunable semiconductor laser.

Monolithic integration with a tunable semiconductor laser could enable high-performance, long-reach, digital communications at 10Gb/s in an XFP transceiver. Significant groundwork for monolithic integration has been completed in this thesis with the minimization of all the possible sources of optical backreflection from within the modulator device.

There are several options available for expanding upon the available modulation schemes:

- The system performance of the zero chirp modulator design could be experimentally verified as a function of wavelength across the C-Band. A C-Band zero chirp transmitter solution could then be made by co-packaging the zero chirp modulator with a tunable semiconductor laser, in similar fashion to what has been done with the negative chirp modulator [57].
- The modulator design could be adapted for use with more advanced modulation formats than simple ON/OFF keying. We have published preliminary studies on the use of the modulator for duobinary modulation [46,58].
- The modulator bandwidth could be increased beyond the current value of 14GHz. The next highest bit rate of commercial interest is 40Gb/s. A move to 40GHz bandwidth would involve a change to traveling-wave electrode designs for the phase-shift electrodes on the modulation arms of the Mach-Zehnder.

A number of activities could advance the understanding of the strongly-guided waveguide design used in the InP-Based Mach-Zehnder modulator:

- The benefits of E-Beam lithography for the definition the ridge etch mask could be explored. Are any further improvements in ridge sidewall roughness available relative to i-line stepper based lithography?
- The sin-based s-bends between the MMI's and the modulation arms could be merged with the 2.0μm to 2.4μm linearly tapered MMI access waveguides. Currently these waveguide structures occur one after the other.
- The use of 1.5μm wide waveguides in the modulation arms could be tried for the reasons discussed in Section 2.1.10.
- A controlled study on hydrogen passivation of Zn doping could be undertaken. This study would also be valuable for understanding loss trade-offs in the SSC designs.
- An explicit experiment could be done to determine the optical loss contribution from the MQW interfaces.

- Additional experiments could be run to determine if a 1X1 MMI mode filter can be added to the modulator without significantly increasing the insertion loss of the device. The designs in Figure 2.55c and Figure 2.57 could be implemented to further study the induced optical loss of a 1X1 MMI.
- Additional theoretical analysis of the matched bend phenomena in cosine-based and sin-based s-bends could be undertaken.
- A matched cosine-based s-bend with 0.1μm offsets could be used to increase the separation between the access waveguides at the MMI. The impact of ridge etch processing non-uniformities in the narrow gap between the access waveguides could be explored further.

There are also a number of activities that could improve the functionality and/or flexibility of the optical mode spot-size converter:

- It could be experimentally verified that an angled modulator-to-SSC butt-joint will reduce the optical backreflections from the butt-joint interface as discussed in Section 3.5.2.
- A 4-layer facet coating design for the SSC could be pursued to enable extremely low facet reflectivity across the complete C-Band.
- Further experiments could be designed to definitively determine the origin of the "hockey stick" profile that occurs in the SSC core at the modulator-to-SSC butt-joint.
- Additional applications for the stabilized enhanced SAG growth structure, shown in Figure 4.19, could be studied.
- The length of the SSC could be reduced by a factor of two, as detailed in Section 3.7.2, without sacrificing the adiabatic nature of the design. To enable this reduction in the SSC length, additional SAG growth experiments would be required to identify new SAG growth conditions, and a new design for the dielectric layout. Analysis of the vertical taper profiles generated in these growth experiments could be improved upon by using a white light interferometry measurement technique to replace the DEKTAK surface profiler measurement technique used in Section 4.4.
- As discussed in Section 3.6.3, Greenspan [196] has found that the "diffusion" length parameters for SAG growth vary with alloy composition due to changes in incorporation rates. Different quaternary compositions for the SAG grown vertical taper in the SSC could be explored to determine the impact of alloy composition on the growth rate enhancement and PL shifts with enhanced growth.
- The multi-mode SSC coupling structures presented in Figures 3.17, 3.18, and 3.25, could be studied in optical propagation models to quantify the impact of the higher-order vertical modes. These multi-mode SSC coupling structures could also be easily fabricated for experimental study, using the processes developed in this thesis, since only a change in the first growth structure is required.

- The SSC design could be modified for use in applications requiring optical coupling to a cleaved fiber mode, or for applications where passive optical alignment is desired. The length of the SSC would increase significantly to allow for adiabatic coupling to a much larger facet mode.

Bibliography

[1] J. K. White, G. Knight, S. Das, R. J. Finlay, T. Jones, C. Blaauw, A. Fekecs, H. Walters, T. Grevatt, N. Brooks, P. Firth, L. Nelson, A. Grabham, I. Woods, K, Hinzer, D. Goodchild, A. J. SpringThorpe, R. Glew, and G. J. Letal, " High performance directly modulated lasers: device physics," Proc. of SPIE, 4986, pp. 222-236, 2003.

[2] G.L. Li, and P.K.L. Yu, "Optical Intensity Modulators for Digital and Analog Applications," Journal of Lightwave Technology, Vol. 21, No. 9, pp. 2010-2030, September 2003.

[3] K. Prosyk, R.S. Moore, P.J. Williams, D.J. Robbins, J.E. Haysom, M.Q. Kearley, P. Britton, P. Firth, A. Ait-Ouali, "Common shallow ridge waveguide laser-electroabsorption modulator using lateral ion implantation," Optical Fiber Communication Conference, 2005. Technical Digest. OFC/NFOEC Volume 2, pp. 256-258, March 6-11, 2005.

[4] F.J. Leonberger, Opt. Lett., Vol. 5, pp. 312, 1980.

[5] J.P. Donnelly, N. L. DoMeo, G.A. Ferrante, K.B. Nichols, and F.J. O'Donnel, Appl. Phys. Lett., Vol. 45, pp. 360-362, 1984.

[6] D.A.B Miller, D.S. Chemla, T.C. Damen, A.C. Gossard, W.Wiegmann, T.H. Wood, and C.A.Burrus, Phys. Rev. Lett., Vol. 53, pp. 2174, 1984.

[7] D.A.B Miller, D.S. Chemla, T.C. Damen, A.C. Gossard, W.Wiegmann, T.H. Wood, and C.A.Burrus, Phys. Rev., Vol. B53, pp. 1043, 1985.

[8] A Yariv, "Quantum Electronics," 2nd Edition, pp. 347-351, John Wiley & Sons, 1975.

[9] C. Rolland, R. S. Moore, F. Shepherd, G. Hillier, "10 Gbit/s, 1.56μm multiquantum well InP/InGaAsP Mach-Zender optical modulator," Electronics Letters, Vol. 29, No. 5, pp. 471-472, 1993.

[10] C. Rolland, D.M. Adams, D. Yevick, B. Hermansoon,"Optimization of Strongly Guiding Semiconductor Rib Waveguide Y-Junctions," Photonic Technology Letters, Vol. 2, No. 6, pp. 404-406, 1990.

[11] Jun Yu, Claude Rolland, David Yevick, Azmina Somani, Scott Bradshaw, "Phase-Engineered III-V MQW Mach-Zehnder Modulators," IEEE Photonics Technology Letters, Vol. 8, No. 8, pp.1018-1020, August 1996.

[12] J.C. Cartledge, C. Rolland, S. Lemerie, and A. Solheim, "Theoretical Performance of 10Gb/s Lightwave Systems Using a III-V Semiconductor Mach-Zehnder Modulator," IEEE Photonics Technology Letters, Vol. 6, No. 2, pp. 282-284, 1994.

[13] Claude Rolland, M.S. O'Sullivan, H.B. Kim, R.S. Moore, and G. Hillier,"10Gbit/s 120km normal fiber transmission experiment using a 1.56μm mulitiple quantum well InP/InGaAsP Mach-Zehnder modulator," Optical Fiber Communications, PD27, San Diego, 1993.

[14] D. M. Adams, C. Rolland, N. Puetz, R. S. Moore, F. R. Shepherd, H. B. Kim, S. Bradshaw,"Mach-Zehnder modulator integrated with a gain-coupled DFB laser for 10Gbit/s, 100km NDSF transmission at 1.55μm," Electronics Letters, Vol. 32, No. 5, pp. 485, 1996.

[15] D.M. Adams, C. Rolland, A. Fekecs, D. McGhan, A. Somani, S. Bradshaw, M. Poirier, E. Dupont, E. Cremer, K. Anderson, "1.55μm transmission at 2.5Gbit/s over 1102 km of NDSF using discrete and monolithically integrated InGaAsP/InP Mach-Zehnder modulator and DFB laser," Electronics Letters, Vol. 34, No. 8, pp. 771-772, 1998.

[16] W. Bardyszewski, D. Yevick, Y. Liu, C. Rolland, S. Bradshaw, "Theoretical and experimental analysis of Mach-Zehnder quantum-well modulators," Journal Of Applied Physics, Vol. 80, No. 2, pp. 1136-1141, 1996.

[17] W. Bardyszewski, D. Yevick, C. Rolland, "Numerical studies of excitonic effects in the optical spectra of quantum well modulators," Invited Paper [2146-29], Proceedings-SPIE The International Society For Optical Engineering Physics And Simulation Of Optoelectronic Devices II, Issue 2146, pp. 249-255, 1994.

[18] Witold Bardyszewski, Claude Rolland, Scott Bradshaw, David Yevick, "Resonant-level effects in absorption spectra of shallow quantum wells," CThX6, CLEO 1998.

[19] Ph. Delansay, D. Penninckx, S.Artigaud, J.G. Provost, J.P. Hebert, E.Bouchherez, J.Y. Emery, C. Fortin, and O. Le Gouuezigou, "10Gbit/s transmission over 90-127km in the wavelength range 1530-1560nm using InP-based Mach-Zehnder modulator," Electronics Letters, Vol. 32, No. 19, pp. 1820-1821, 12th September 1996.

[20] D. Penninckx, Ph. Delansay, , E.Bouchherez, C. Fortin, and O. Le Gouuezigou, "InP/GaInAsP π-phase-shifted Mach-Zehnder modulator for wavelength independent (1530-1560nm) propagation performance at 10Gbit/s over standard dispersive fiber," Electronics Letters, Vol. 33, No. 8, pp. 697-698, 10th April 1997.

[21] A. Shen, J. Damon-Lacoste, M. Le Pallec, C. Duchet, J.L. Gentner, F. Devaux, and M. Renaud, "Low Insertion Loss and Polarization Insensitive InP-based Mach-Zehnder modulator for 40Gbit/s optical regeneration," Optical Fiber Communications, WV3, 2002.

[22] H.Sano et al., "A multi-quantum well modulator for high bit rate transmission systems," 4th OEC, 17C3-2 (invited), 1992.

[23] H.Sano et al., "A High Speed InGaAs/InAlAs MQW Mach-Zehnder Type Optical Modulator," Conference on Optical Fiber Communications 1993.

[24] Shigeru Nakagawa, Haruhisa Soda, Chandra Khandavalli, Toshio Nakamura, Yasuhito Suzuki, Nobuaki Oguro, "Compact 10Gbps InP Directional-Coupler Modulators with Full C-Band Coverage," European Conference on Optical Communications, Postdeadline paper Th4.3.5, pp. 36-37, Sept. 2004.

[25] Suguru Akiyama, Hiroaki Itoh, Tatsuya Takeuchi, Akito Kuramata, and Tsuyoshi Yamamoto, "Wide-Wavelength-Band (30 nm) 10Gb/s Operation of InP-Based MachZehnder Modulator With Constant Driving Voltage of 2 Vpp," Photonic Technology Letters, Vol. 17 No. 7 pp. 1408-1410, July 2005.

[26] S. Akiyama, H. Itoh, T. Takeuchi, A. Kuramata and T. Yamamoto, Low-chirp 10 Gbit/s InP-based Mach-Zehnder modulator driven by 1.2V single electrical signal," Electronics Letters Vol. 41, No. 1, Jan 6th 2005.

[27] Akiyama, S., Hirose, S., Itoh, H., Takeuchi, T., Watanabe, T., Sekiguchi, A., Kuramata, A., and Yamamoto, T, "40 Gb/s InP-based Mach-Zehnder modulator with a driving voltage of $3V_{p-p}$,". 16th Int. Conf. on Indium Phosphide Related Materials, Paper ThA1-4, pp. 581584, Kagoshima, Japan, MayJune 2004.

[28] K. Tsuzuki, T. Ishibashi, T. Ito, S. Oku, Y. Shibata, R. Iga, Y. Kondo, and Y. Tohmori, "40 Gb/s n-i-n InP MachZehnder modulator with a π voltage of 2.2V," Electron. Lett., vol. 39, no. 20, pp. 14641466, 2003.

[29] Akiyama, S., Hirose, S., Watanabe, T., Ueda, M., Sekiguchi, S., Morii, N., Yamamoto, T., Kuramata, A., and Soda, H., "Novel InP based Mach-Zehnder modulator for 40 Gbit/s integrated lightwave source," ISLC02, Paper TuC1, pp. 5758, Garmisch-Partenkirchen, Germany, 2002.

[30] R.G. Walker, "High-Speed III-V Semiconductor Intensity Modulators," IEEE J. Quantum Electronics, Vol. 27, No. 3, pp. 654-667, Mar. 1991.

[31] Hoffmann, D., Staroske, S., and Velthaus, K.O., "45 GHz bandwidth traveling wave electrode Mach-Zehnder modulator with integrated spot size converter," 16th Int. Conf. on Indium Phosphide Related Materials, Paper ThA1-5, pp. 585588, Kagoshima, Japan, MayJune 2004.

[32] L. Morl, C.M. Weinert, F. Reier, L. Stoll, H.P. Nolting, "Uncladded InGaAsP/InP rib waveguides with integrated thickness tapers for efficient fiber-chip butt coupling," Electronics Letters, Vol. 32, No. 1, pp. 36-37, 1996.

[33] N. Yoshimoto, Y. Shibata, S. Oku, S. Kondo, Y. Noguchi, K. Wakita, and M. Naganuma, "Fully polarization independent Mach-Zehnder optical switch using a

lattice-matched InGaAlAs/InAlAs MQW and high-mesa waveguide structure," Electronics Letters, Vol. 32, No. 15, pp. 1368-1369, 18th July 1996.

[34] Tsuzuki, K., Ishibashi, T. Yasaka, Ito T., Oku S., Shibata Y., Iga R., Kondo Y., and Tohmori Y, "40Gbit/s n-i-n InP Mach-Zehnder Modulator with a π Voltage of 2.2V," Electronics Letters, Vol. 39, No. 20, 2nd October 2003.

[35] Ken Tsuzuki, Tadao Ishibashi, Tsuyoshi Ito, Satoshi Oku, Yasuo Shibata, Toshio Ito, Ryuzo Iga, Yasuhiro Kondo, and Yuichi Tohmori, "A 40-Gb/s InGaAlAsInAlAs MQW n-i-n MachZehnder Modulator With a Drive Voltage of 2.3 V," Photonic Technology Letters, Vol. 17, No. 1, pp. 46-48, 1st January 2005.

[36] Tsuzuki K., Yasaka H., Ishibashi T., Ito T., Oku S., Iga R., Kondo Y., and Tohmori Y, "10Gbit/s, 100-km SMF transmission using an InP based n-i-n Mach-Zehnder modulator with a driving voltage of 1.0 Vpp," Optical Fiber Communications, Paper PDP14, Los Angeles, CA, USA, February 2004.

[37] L. Zhang, J. Sinsky, D. Van Thourhout, N. Sauer, L. Stulz, A. Adamiecki, S. Chandrasekhar, "Low-Voltage High-Speed Travelling Wave InGaAsP-InP Phase Modulator," Photonic Technology Letters, Vol. 16, No. 8, pp. 1831-1833, August 2004.

[38] W. Pascher, J.H. Den Besten, D. Caprioli, X. Leijtens, M. Smit, R. Van Dijk, "Modelling and Design of a Travelling Wave Electro-Optic Modulator on InP," Optical and Quantum Electronics, Vol. 35, pp. 453-464, 2003.

[39] J.H. Besten, D. Caprioli, R. van Dijk, F.E. van Vliet, W. Pascher, J.J.M. Binsma, B. Smalbrugge, T. de Vries, X.J.M Leijtens, M.K. Smit, "A Velocity-Matched Traveling-Wave Mach-Zehnder Modulator on InP," Proceeding Symposium IEEE/LEOS Benelux Chapter, Enschede, 2003.

[40] Fumio Koyama, and Kenichi Iga, "Frequency Chirping in External Modulators," Journal of Lightwave Technology, Vol. 6, No. 1, pp. 87-93, 1988.

[41] Agrawal, Govind P., "Fiber-Optic Communication Systems, Second Ed. Wiley Series in Microwave and Optical Engineering, 1997.

[42] P. Bravetti, G. Ghislotti, and S. Balsamo, "Chirp-Inducing Mechanisms in Mach-Zehnder Modulators and Their Effect on 10Gb/s NRZ Transmission Studied Using Tunable-Chirp Single Drive Devices," Journal of Lightwave Technology, Vol. 22, No. 2, February 2004.

[43] S. Balsamo, P. Bravetti, R. Brouard, V. Rouffiange, "Effects of Chirp Mechanism on Spectrum Broadening of External Modulators," OME43, Optical Fiber Communications Conference (OFC) 2005.

[44] Agilent White Paper, "Improving Optical Transceiver Extinction Ratio Measurement Accuracy By using Reference Receiver Correction Factors."

[45] Per O. Andersson and Kurt Akermark, "Accurate Optical Extinction Ratio Measurements," IEEE Photonics Technology Letters, Vol. 6 No. 11, pp. 1356-1358, November 1994.

[46] R. A. Griffin, A. Tipper, and I. Betty, "Performance of MQW InP Mach-Zehnder Modulators for Advanced Modulation Formats," Optical Fiber Communications Conference (OFC) 2005.

[47] D.M. Adams, C. Rolland, N. Puetz, R.S. Moore, F.R. Shepherd, H.B. Kim, S. Bradshaw, "Mach-Zehnder modulator integrated with a gain-coupled DFB laser for 10Gbit/s, 100 km NDSF transmission at 1.55μm," Electronics Letters, Vol. 32, No. 5, pp. 485-486, 1996.

[48] Rick Clayton, Andy Carter, Ian Betty, Timothy Simmons, "Cost-effective monolithic and hybrid integration for metro and long-haul applications," SPIE, Semiconductor Optoelectronic Devices for Lightwave Communication, Vol. 5248, No. 1, pp.67-79, 2003.

[49] K. Anderson and I. Betty, Laser Focus World 39 (3): 101-104 March 2003.

[50] K. Anderson, "Design and Manufacturability Issues of a Copackaged DFB/MZ Module," Electronics Components and Technology Conference, pp. 197-200, 1999.

[51] Ian Betty, CITO/OCRI Tech Talk-Optical Networks: Disruptive Components and Materials. Talk on "Integrated Optoelectronics: What Matters," February 20th 2001.

[52] Jonathon S. Barton, Erik J. Skogen, Milan L. Masanovic,Steven P. Denbaars, and Larry A. Coldren, "A Widely Tunable High-Speed Transmitter Using an Integrated SGDBR Laser-Semiconductor Optical Amplifier and MachZehnder Modulator," IEEE Journal of Selected Topics in Quantum Electronics, Vol. 9, No. 5, pp. 1113-1117, September/October 2003.

[53] Barton JS., Skogen, E.J. , Masanovic M., S. Denbaars, L. A. Coldren, Integration of a Mach-Zehnder Modulator with Sampled Grating Distributed Bragg Reflector Laser, Proc. Integrated Photonics Research Conference, paper no. 1FC3-1, Vancouver, Canada, July 17-19 2002.

[54] Barton JS, Skogen EJ, Masanovic ML, DenBaars SP, Coldren LA., "Tailorable chirp using integrated Mach-Zehnder modulators with tunable sampled grating distributed Bragg reflector lasers, 2002 IEEE 18th International Semiconductor Laser Conference, Conference Digest (Cat. No.02CH37390), TuB3, Garmisch, Germany (Sept. 29-Oct. 3) IEEE. 2002, pp.49-50.

[55] Jonathan S. Barton, Milan L. Masonovic, Anna Tauke-Pedretti, Erik J. Skogen, Larry A. Coldren, "Monolithically-integrated 40Gbit/s widely-tunable transmitter using series push-pull Mach-Zehnder modulator SOA and Sampled-Grating DBR laser," Optical Fiber Communications, OTuM3, 2005.

[56] I. Betty, M. G. Boudreau, R. A. Griffin, A. Fekces, "An Empirical Model for High Yield Manufacturing of 10Gb/s Negative Chirp InP Mach-Zehnder Modulators," Optical Fibre Communications Conference 2005.

[57] R. A. Griffin, B. Pugh, J. Fraser, I. B. Betty, K. Anderson, G. Busico, C. Edge, T. Simmons, "Compact, High Power, MQW InP Mach-Zehnder Transmitters with Full-band Tunability for 10 Gb/s DWDM," European Conference on Communications (ECOC) 2005.

[58] Betty, "Duobinary Modulation Scheme for a Mach-Zehnder Optical Modulator," granted US patent 6795594, September 21st 2004.

[59] Kelvin Prosyk, Ian Betty, "Electro-optic Modulator with Continuously Adjustable Chirp", granted US patent 6,650,458, November 18th, 2003.

[60] Hatem El-Rafaei, "An InGaAsP/InP On-Chip Polarization Bit Interleaver for 40Gb/s Optical Transmission Systems, Electrical and Computer Engineering Ph.D., Queen's University, 2002.

[61] U. Niggebrugge, M. Klug, and G. Garus, Inst. Phys. Conf. Ser. 79, pp. 367, 1985.

[62] A. Beaurain, S. Dupont, H.W. Li, J.P. Vilcot, C. Legrand, J. Harari, M. Constant, and D. Decoster, "Characterization and Fabrication of InGaAsP/InP Deep-Etched Micro-Waveguides," Microwave and Optical Technology Letters, Vol. 40, No. 3, pp. 216-218, February 5th 2004.

[63] P.P. Absil, J.V. Hryniewicz, B.E. Little, R.A. Wilson, L.G. Joneckis, and P.T. Ho, "Compact Microring Notch Filters," IEEE Photonics Technology Letters, Vol. 12, pp. 1008-1010, 1994.

[64] D.L. Melville, S.M. Ohja, R. Moore and F.R. Shepherd, "Application of CH_4/Ar and $CH_4/CO_2/H_2$ Plasma Chemistries in Hydrocarbon RIE of InP-based Optoelectronic Devices", 43rd AVS National symposium, November 1996.

[65] W.C. Dautremont-Smith, J. Lopata, S.J. Pearton, "Hydrogen Passivation Of Acceptors in P-InP," Journal Of Applied Physics, Vol. 66, No. 5, pp. 1993-1996, September 1st 1989.

[66] R. Rousina-Webb, I. Betty, D. Sieniawski, F.R. Shepherd and James B. Webb, "The Effect of Process-Induced Stress in InP/InGaAsP Weakly Confined Waveguides Switch," Optoelectronic Interconnects VII, Photonics Packaging and Integration II, SPIE Vol. 3952, No. 1, pp. 168-177, 2000.

[67] Y.C. Zhu, F.H. Groen, D.H.P. Maat, Y.S. Oei, J. Romijn, I. Moerman, "A compact PHASAR with low central channel loss", Proc. ECIO '99, pp. 219-222, 1999.

[68] Masaki Kohtoku, Hiroaki Sanjoh, Satoshi Oku, Yoshiaki Kadota, Yuzo Yoshikuni, "Polarization Independent Semiconductor Arrayed Waveguide Gratings Using a Deep-Ridge Waveguide Structure," IEICE Trans. Electon., Vol. E81-C, No. 8, pp. 1195-1204, August 1998.

[69] Ivey DG, Ingrey S, Noel JP, Lau WM, "Microstructural study of Ti/Pt/Au contacts to p-InGaAs," Materials Science And Engineering B-Solid State Materials for Advanced Technology Vol. 49 No. 1, pp. 66-73, September 5th 1997.

[70] Ian Betty, Roghieh Rousina-Webb, Chi Wu, "A Robust, Low-Crosstalk, InGaAsP/InP Total-Internal-Reflection Switch For Optical Cross-Connect Applications," Integrated Photonics Research Conference, JWA2, Santa Barbara 1999.

[71] Gregory A. Fish et al., IEEE Photonic Technology Letters, Vol. 10, No. 9, pp. 1256-58, 1998.

[72] T. Kirihara, et al., IEEE Photonic Technology Letters, Vol. 6, No. 2, pp. 218-21, 1994.

[73] Chi Wu, U.S. Patent No. 5581643, Dec. 3rd 1996.

[74] Kwang-Ryong Oh et al., IEEE Photonic Technology Letters Vol. 6, No. 1, pp. 65-67, 1994.

[75] Zhuang Wanru et al., Fiber and Integrated Optics, Vol. 15, pp. 27-36, 1996.

[76] W.G. Pfann, "Principles of zone melting," Trans. Am. Inst. Min. metall. Engrs, Vol. 194, pp. 747, 1952.

[77] R.W. Glew, K. Hinzer, J.K White, D. Goodchild, G. Knight, A.J. SpringThorpe, St. J. Dixon-Warren, "New DFB grating structure using dopant-induced refractive index step," Journal of Crystal Growth, Vol. 261, pp. 349-354, 2004.

[78] Claude Rolland, Gary Mak, Witold Bardyszewski, David Yevick, "Improved Extinction Ratio of Waveguide Electro-absorption Optical Modulators Induced by an InGaAs Absorbing Layer," Journal of Lightwave Technology, Vol. 10, No. 12, pp. 1907-1911, December 1992.

[79] Gary Mak, Claude Rolland, K.E. Fox, C. Blaauw, "High Speed Bulk InGaAsP-InP Electro-absorption Modulators with Bandwidth in Excess of 20GHz," IEEE Photonics Technology Letters, Vol. 2, No. 10, pp. 730-733, Oct. 1990.

[80] G.M. Berry, S.V. Burke, J.M. Heaton, and D.R. Wight, "Analysis of multilayer semiconductor rib waveguides with high refractive index substrates," Electronics Letters, Vol. 29, No. 22, pp. 1941-42, 1993.

[81] J.E. Haysom, R. Glew, C. Blaauw, R. Driad, D. MacQuistan, C.A. Hampel, J.E. Greenspan, and T.Bryskiewicz, Proc. 14th IPRM, 2002.

[82] J.E. Haysom, I. Betty, K. Wong, M. Poirier, R.S. Moore, A. Ait-Ouali, J. Lu , "Implant Isolation Applied to an InP Mach-Zehnder Modulator," Eleventh Canadian Semiconductor Technology Conference Ottawa, Canada - 18-22 August 2003.

[83] St. J. Dixon-Warren, J. E. Haysom, I. Betty, J. Lu, and K. Hewitt, "Implant isolation in an indium phosphide optoelectronic device: A scanning spreading resistance microscopy study", J. Vac. Sci. Technol. A, Vol. 22, No. 3, pp. 925-929, May/Jun 2004.

[84] D. Yevick, "A guide to electric field propagation techniques for guided-wave optics," Invited Paper, Optical and Quantum Electronics, Vol. 26, S185-S197, 1994.

[85] J.P. Bérenger, "A Perfectly Matched Layer for the Absorption of Electromagnetic Waves," Journal of Computational Physics, Vol. 114, pp. 185-200, 1994.

[86] D. Yevick, C. Rolland, and B. Hermansson, "Fresnel equation studies of longitudinally varying semiconductor rib waveguides: Reference wavevector dependence," Electronic Letters, Vol. 25, No. 18, pp. 1254-1256, 1989.

[87] J. Saijonmaa, D. Yevick, "Beam-Propagation Analysis of Loss in Bent Optical-Waveguides and Fibers," Journal Of The Optical Society Of America, Vol. 73, No. 12, pp. 1785-1791, 1983.

[88] B. Hermansson, D. Yevick, J. Saijonmaa, "Propagating-Beam-Method Analysis of Two-Dimensional Microlenses and 3-Dimensional Taper Structures," Journal of the Optical Society of America A-Optics Image Science and Vision, Vol. 1, No. 6, pp.663-671, 1984.

[89] B. Hermansson, D. Yevick, "A Propagating Beam Analysis of Optical-Waveguide Couplers," Optical And Quantum Electronics," Vol. 16, No. 2, pp. 131-139, 1984.

[90] B.R. Bennett, R.A. Soref, J. Del Alamo, IEEE J. Quantum Electronics, Vol. 26, pp. 113, 1990.

[91] M.S. Whalen, J. Stone, J. Appl. Phys., Vol. 53, pp. 4340, 1982.

[92] L. Chusseau, P. Martin, C. Brasseur, C. Albert, P. Herve, P. Arguel, F. Lopez-Dupuy, E.V.K. Rao, Appl. Phys. Lett. Vol. 69, pp. 3054, 1996.

[93] H.C. Casey, Jr. and P.L. Carter, "Variation of intervalence band absorption with hole concentration in p-type InP," Applied Physics Letters, Vol. 44, No. 1, pp. 82-83, 1994.

[94] Y.F.Li, K.Iizuka, and J.W.Y. Lit, "Equivalent-layer method for optical waveguides with a multipl-quantum-well structure," Optics Letters, Vol. 17, pp. 273-275, 1992.

[95] W. Streifer, D.S. Seifres, and R.D.Burnham, "Optical analysis of multiple quantum well lasers," Applied Optics, Vol. 18, pp. 3547-3548, 1979.

[96] G.M. Alman, Lynne A. Molter, H. Shen, M. Dutta, "Refractive Index Approximations from Linear Perturbation Theory for Planar MQW Waveguides," IEEE Journal of Quantum Electronics, Vol. 28, No. 3, pp. 650-657, March 1992.

[97] S. Ohke, T. Umeda, and Y. Cho, "Optical waveguides using GaAs-$Al_xGa_{1-x}As$ multiple quantum well," Optical Communications, Vol. 56, pp. 235-239, 1985.

[98] Mamta Saini and Enakshi K. Sharma, "Equivalent refractive index of multiple-quantum-well waveguides by variational analysis," Optics Letters, Vol. 20, No. 20, pp. 2081-2083, Oct 15th 1995.

[99] Mamta Saini and Enakshi K. Sharma, "Equivalent Refractive Index of MQW Waveguides," IEEE Journal of Quantum Electronics, Vol. 32, No. 8, pp. 1383-1390, August 1996.

[100] P. Martin, Appl. Phys. Lett. Vol. 67, No. 7, pp. 881-883, 1995.

[101] T.P. Pearsal (Editor), "GaInAsP Alloy Semiconductors," Wiley, New York, 1982.

[102] F. Fiedler and A. Schlachetzki, "Optical Parameters of InP-Based Waveguides," Solid-State Electronics, Vol. 30, No. 1, pp. 73-83, 1987.

[103] T Tamir (Editor), "Integrated Optics 2nd Edition," Springer-Verlag, 1985.

[104] R. Ulrich, "Image formation by phase coincidences in optical waveguides," Optics Communications, Vol. 13, No. 3, pp. 259-264, 1975.

[105] R. Ulrich, G. Ankele, "Self-imaging in homogeneous planar optical waveguides," Appl. Phys. Lett., Vol. 27, No. 6, pp. 337-339, 1975.

[106] P.A. Besse, E.Gini, M.Bachmann, H. Melchoir, "New 1X2 multimode interference couplers with free selection of power splitting ratios," Proc. 20th European Conf. Optic. Commun., ECOC'94, Florence, Sept. 25-29, 1994, pp. 669-672.

[107] P.A. Besse, E.Gini, M.Bachmann, H. Melchoir, "New 2X2 and 1X3 multimode interference couplers with free selection of power splitting ratios," Journal of Lightwave Technology, Vol. 14, No. 10, pp. 2286-2293, Oct. 1996.

[108] Juerg Leuthold, Charles H. Joyner, "Multimode Interference Couplers with Tunable Power Splitting Ratios," Journal of Lightwave Technology, Vol. 19, No. 5, pp. 700-707, May 2001.

[109] D.S. Levy, R. Scarmozzino, Y.M. Li, R.M. Osgood Jr, "A New Design for Ultracompact Multimode Interference-Based 2X2 Couplers," IEEE Photonics Technology Letters, Vol. 10, No. 1, pp. 96-98, Jan. 1998.

[110] D.S. Levy, R. Scarmozzino, R.M. Osgood Jr, "Reduction of Tapered NxN MMI Devices," IEEE Photonics Technology Letters, Vol. 10, No. 6, pp. 830-832, June 1998.

[111] M. Kohtoku, Y. Shibata, Y. Yoshikuni, "Evaluation of the Rejection Ratio of an MMI3-Based Higher Order Mode Filter Using Optical Low-Coherence Reflectometry," IEEE Photonics Technology Letters, Vol. 14, No. 7, pp. 968-970, July 2002.

[112] J. Leuthold, R. Hess, J. Eckner, P.A. Besse, H. Melchior, "Spatial Mode Filters realized with Multimode Interference Couplers," Optics Letters, Vol. 21, No. 11, pp. 836-838, June 1st 1996.

[113] D.Erasme, L.H.Spiekman, C.G.P. Herben, M.K. Smit, F.H. Groen, "Experimental Assessment of the Reflection of Passive Multimode Interference Couplers," IEEE Photonic Technology Letters, Vol. 9, No. 12, pp. 1604-1606, Dec. 1997.

[114] Y. Shibata, S. Oku, M. Yamamoto, M. Naganuma, "Quantitative Analysis of Optical Reflection in a Multimode Interference 3dB coupler using a Low Coherence Interferometric Reflectometer," Electronic Letters, Vol. 32, No. 24, pp. 2266-2268, 21st Nov. 1996.

[115] Y. Gottesman, E.V.K. Rao, B. Dagens, "A Novel Design Proposal to Minimize Reflections in Deep-Ridge Multimode Interference Couplers," IEEE Photonic Technology Letters, Vol. 12, No. 12, pp. 1662-1664, December 2000.

[116] Y.Gottesman, E.V.K. Rao, D. Piot, E. Vergnol, B. Dagens, "An in-depth analysis of reflections in MMI couplers using optical low-coherence reflectometry: design optimization and performance evaluation," Appl. Phys. B., Vol. 73, pp. 609-612, 2001.

[117] Ian Betty, "Experimental and Theoretical Determination of Backreflections in a III-V Semiconductor Device," M.Sc., Queen's University, Canada, 1998.

[118] E.C.M. Pennings, R. van Roijen, M.J.N. van Stralen, P.J. de Waard, R.G.M.P. Koumans, B.H. Verbeek, "Reflection Properties of Multimode Interference Devices," IEEE Photonic Technology Letters, Vol. 6, No. 6, pp. 715-718, June 1994.

[119] O. Bryngdahl, "Image Formation using Self-Imaging Techniques," J. Optic. Soc. Amer., Vol 63, pp. 416-419, Apr. 1973.

[120] R. Ulrich and T. Kamiya, "Resolution of self-images in planar optical waveguides," J. Opt. Soc. Amer., Vol. 68, No. 5, pp. 583-592, 1978.

[121] H. F. Talbot, "Facts relating to optical science," Philos. Mag., Vol. 9, No. IV, p. 401-407, 1836.

[122] L. B. Soldano and E. C. M. Pennings, "Optical multimode interference devices based on self-imaging: Principles and applications," J. Lightwave Technology, Vol. 13, pp. 615-27, Apr. 1995.

[123] N.S. Kapany and J.J. Burke, "Optical Waveguides," Academic, New York, 1972.

[124] J.Z. Huang, R. Scarmozzino, and R.M. Osgood, "A New Design Approach to Large Input/Output Number Multimode Interference Couplers and Its Application to Low-Crosstalk WDM Routers," IEEE Photonics Technology Letters, Vol. 10, No. 9, pp. 1292-1294, September 1998.

[125] J.Z. Huang, M.H. Hu, J. Fujita, R. Scarmozzino, and R.M. Osgood Jr., "High-Performance Metal-Clad Multimode Interference Devices for Low-Index-Contrast Material Systems," IEEE Photonics Technology Letters, Vol. 10, No. 4, pp. 561-563, April 1998.

[126] M. Bachmann, P.A. Besse, and H. Melchior, "General Self-Imaging Properties in NXN Multimode Interference Couplers Including Phase Relations," Applied Optics, Vol. 33, No. 18, pp. 3905-3911, 20th June 1994.

[127] P.A. Besse, M. Bachmann, H. Melchior, L.B. Soldano, and M.K. Smit, "Optical Bandwidth and Fabrication Tolerances of Multimode Interference Couplers," Journal of Lightwave Technology, Vol. 12, No. 6, pp. 1004-1009, June 1994.

[128] Atma Ram Gupta, "Optimization of Access Waveguide Width of Multimode Interference (MMI) Couplers," Optics Communications, No. 221, pp. 99-103, 2003.

[129] Martin T. Hill, X.J.M Leijtens, G.D. Khoe, M.K. Smit, "Optimizing Imbalance and Loss in 2X2 3dB Multimode Interference Couplers via Access Waveguide Width," Journal of Lightwave Technology, Vol. 21, No. 10, pp. 2305-2313, October 2003.

[130] Christos Themistos, Muttukrishnan Rajarajan, B.M. Azizur Rahman, Salah S.A. Obayya, and Kenneth T.V. Grattan, "Rigorous comparison of parabolically tapered and conventional multimode-interference-based 3dB power splitters in InGaAsP/InP waveguides," Applied Optics, Vol. 43, No. 27, pp. 5228-5235, Sept. 20th 2004.

[131] Yong Ma, Seoijin Park, Liwei Wang, and Seng Tiong Ho, "Ultracompact Multimode Interference 3-dB Coupler with Strong Lateral Confinement by Deep Dry Etching," Photonic Technology Letters, Vol. 12, No. 5, pp. 492-494, May 2000.

[132] Milan L. Masanovic, Erik J. Skogen, Jonathon S. Barton, Joseph M. Sullivan, Daniel J. Blumenthal, and Larry A. Coldren, "Multimode Interference-Based Two-Stage 1X2 Light Splitter for Compact Photonic Integrated Circuits," Photonic Technology Letters, Vol. 15, No. 5, pp. 706-708, May 2003.

[133] Andrea Melloni, Giuseppe Cusmai, Mario Martinelli, "Experimental Confirmation of Matched Bends," Optics Letters, Vol. 29, No. 5, pp. 465-467, March 1st 2004.

[134] Andrea Melloni, Paolo Monguzzi, Raffaella Costa, and Mario Martinelli, "Design of Curved Waveguides: The Matched Bend," J. Opt. Soc. Am. A, Vol. 20, no. 1, pp. 130-137, Jan. 2003.

[135] Andrea Melloni, Federico Carniel, Raffaella Costa, and Mario Martinelli, "Determination of Bend Mode Characteristics in Dielectric Waveguides," Journal of Lightwave Technology, Vol. 19, no. 4, pp. 571-577, April 2001.

[136] T. Hirono, M. Kohtoku, Y. Yoshikuni, W.W. Lui, K. Yokoyama, "Optimized Offset to Eliminate First-Order Mode Excitation at the Junction of Straight and Curved Multimode Waveguides," IEEE Photonics Technology Letters, Vol. 10, no. 7, pp. 982-984, July 1998.

[137] D. Marcuse, "Length Optimization of an S-shaped transition between offset optical waveguides," Applied Optics, Vol. 17, No. 5, pp. 763-768, 1978.

[138] V. Ramaswamy, "Loss-loss bends for integrated optics," in Proc. Conf. on Lasers and Electrooptics, Washington, DC, 1981, paper THP1.

[139] William J. Minford, Steven K. Korotky, Rod C. Alferness, "Low-Loss Ti:LiNbO$_3$ Waveguide Bends at λ=1.3μm," IEEE Journal of Quantum Electronics, Vol. QE-18, No. 10, pp. 18021806, 1982.

[140] Mordehai Heiblum, "Analysis of Curved Optical Waveguides by Conformal Transformation," IEEE Journal of Quantum Electronics, Vol. QE-11, No. 2, pp. 75-83, 1975.

[141] A.M. Shajakhan, Sheel Aditya, "Slope-Matched S-Bends for Inclined Integrated-Optic Waveguides," Microwave and Technology Letters, Vol. 24, No. 4, pp. 267-271, 2000.

[142] Tsutomu Kitoh, Norio Takato, Mitsuho Yasu, Masao Kawachi,"Bending Loss Reduction in Silica-Based Waveguides by Using Lateral Offsets," Journal of Lightwave Technology, Vol. 13, No. 4, pp. 555-562, 1995.

[143] Ernst-Georg Neumann, Rer. Nat., "Curved dielectric optical waveguides with reduced transition losses", IEE Proceedings, Vol. 129, Pt. H, NO. 5, October 1982.

[144] W.A. Gambling, H. Matsumura, C.M. Ragdle, "Field deformation in a curved sinigle-mode fiber", Electronics Letters, Vol. 14, No. 5, pp. 130-132, 2nd March 1978.

[145] D. Marcuse, "Bending Losses of the Asymmetric Slab Waveguide," Bell System Technical Journal, Vol. 50, No. 8, pp. 2551-2563, October 1971.

[146] D. Marcuse, "Theory of Dielectric Optical Waveguides," Academic, New York, 1974.

[147] E.A.J, Marcatili, "Bends in Optical Dielectric Guides," Bell System Technical Journal, pp. 2103-2132, September 1969.

[148] Chulhun Seo, Jihoon Kim, Dong Sung Kim,"Reduction of Transition Losses in Bent Rib Waveguides," Microwave and Optical Technology Letters, Vol. 15, No. 3, pp. 184-188, 1997.

[149] Meint, K. Smit, Cor van Dam, "Phasar-Based WDM-Devices: Principles, Design and Applications," IEEE Journal of Selected Topics in Quantum Electronics, Vol. 2, No. 2, pp. 236-250, June 1996.

[150] Matthias Heinbach, Meinrad Schienle, Anton Schmid, Bruno Acklin, Gustav Müller, "Low-Loss Bent Connections for Optical Switches," Journal of Lightwave Technology, Vol. 15, No. 5, pp. 833-837, 1997.

[151] L.H. Spiekman, Y.S. Oei, E.G. Metaal, F.H.Groen, P.Demeester, M.K. Smit, "Ultra-small Waveguide Bends: The Corner Mirrors of the Future?," IEE Proc.-Optoelectron., Vol. 142, No. 1, pp. 61-65, February 1995.

[152] Spiekman L.H., Oei Y.S., Metaal E.G., Green F.H., Moerman I., Smit M.K., "Extremely small multimode interference couplers and ultrashort bends on InP by deep etching", IEEE Photonics Technology Letters, Vol. 6, No. 8, pp. 1008-1010, Aug. 1994.

[153] B. H. Verbeek, E.C.M. Pennings, J.W.M. van Uffelen, P.J.A. Thijs, "Fabrication and analysis of low-loss InGaAsP/InP optical waveguides with extremely small bends," 15th European Conference on Optical Communication, September 10-14 1989, Gothenburg, Sweden, pp. 78-81.

[154] C. van Dam, L.H. Spiekman, F.P.G.M. van Ham, F.H. Groen, J.J.G.M. van der Tol, I. Moerman, W.W.Pascher, M.Hamacher, H.Heidrich, C.M. Weinert, M.K. Smit,"Novel Compact Polarization Converters Based on Ultra Short Bends," IEEE Photonics Technology Letters, Vol. 8, No. 10, pp. 1346-1348, October 1996.

[155] Wayne W. Lui, K. Margari, N. Yoshimoto, S. Oku, T. Hirono, K.Yokoyama, W.P. Huang, "Modeling and Design of Bending Waveguide Based Semiconductor Polarization Rotators," IEEE Photonics Technology Letters, Vol. 9, No. 10, pp. 1379-1381, Oct. 1997.

[156] T.C. Lee, G.D. Vernstrom, S.K. Mohapatra, D.K. Misemer, "Comparison of Propagation loss of sin-generated and constant radius S-bends in AlGaAs waveguides," J. Appl. Phys., 74 (1), pp. 730-731, 1st July 1993.

[157] Claude Rolland, D.M. Adams, David Yevick, Björn Hermansson,"Optimization of Strongly Guiding Semiconductor Rib Waveguide Y-Junctions," IEEE Photonics Technology Letters, Vol. 2, No. 6, pp. 404-406, June 1990.

[158] Claude Rolland, G. Mak, K.E. Fox, D.M. Adams, A.J. Springthorpe, "Analysis of Strongly Guiding Rib Waveguide S-Bends: Theory and Experiment," Electronic Letters, Vol. 25, No. 18, pp. 1256-1257, 31st August 1989.

[159] Kwang T. Toai, Pao-Lo Liu, "Modeling of Ti:LiNbO$_3$ Waveguide Devices: Part II-Shaped Channel Waveguide Bends," Journal of Lightwave Technology, Vol. 7, No. 7, pp. 1016-1022, July 1989.

[160] P. Ganguly, J.C. Biswas, S.K. Lahiri, "Modelling of Titanium indiffused lithium niobate channel waveguide bends: a matrix approach," Optics Communications, No. 155, pp. 125-134, October 1st 1998.

[161] Peter Bienstman, E. Six, M. Roelens, M. Vanwolleghem, Roel Baets,"Calculation of Bending Losses in Dielectric Waveguides Using Eigenmode Expansion and Perfectly Matched Layers," IEEE Photonics Technology Letters, Vol. 14, No. 2, pp. 164-168, February 2002.

[162] E.C.M. Pennings, "Bends in Optical Ridge Waveguides, Modeling and Experiments," Ph.D. Thesis, Delft University of Technology, Delft, The Netherlands, 1990. ISBN 90-9003413-7.

[163] E.C.M. Pennings, G.H. Manhoudt, M.K. Smit, "Low-Loss Bends in Planar Optical Ridge Waveguides," Electronics Letters, Vol. 24, No. 16, pp. 998-999, 4th August 1988.

[164] Vijaya Subramaniam, Gregory N. De. Brabander, David H. Naghski, Joseph T. Boyd, "Measurement of Mode Field Profile and Bending and Transition Losses in Curved Optical Channel Waveguides," Journal of Lightwave Technology, Vol. 15, No. 6, pp. 990-997, June 1997.

[165] Meint K. Smit, Erik C.M. Pennings, Hans Blok, "A Normalized Approach to the Design of Low-Loss Optical Waveguide Bends," Journal of Lightwave Technology, Vol. 11, No. 11, pp. 1737-1742, November 1993.

[166] C. van Dam, A.A.M. Staring, E.J. Jansen, J.J.M. Binsma, T. van Dongen, M.K. Smit, and B.H. Verbeek, "Elimination of ghost images in the response of PHASAR-demultiplexers," in 8th Eur. Conf. on Integrated Optics, Stockholm, Sweden, 1997, pp. 268-271, paper EThE4-1.

[167] C Dragone, "Optimum Planar Bends," Electronics Letters, Vol. 29 No. 12, pp. 1121-1122, 10th June 1993.

[168] C.K. Nadler et al., "Polarization Insensitive, Low-Loss, Low-Crosstalk Wavelength Multiplexer Modules," IEEE Journal Of Selected Topics In Quantum Electronics, Vol. 5, No. 5, pp. 1407-1412, September/October 1999.

[169] T.Kominato, et al, "Extremely Low-Loss (0.3dB/m) and Long Silica-Based Waveguides with Large Width and Clothoid Curve Connection," European Conference on Optical Communications, 2004.

[170] Apurva Kumar, Sheel Aditya, "Performance of S-Bends for Integrated-Optic Waveguides," Microwave and Optical Technology Letters, Vol. 19, No. 4, pp. 289-292, November 1998.

[171] Francois Ladouceur, Pierre Labeye, "A New General Approach to Optical Waveguide Path Design," Journal of Lightwave Technology, Vol. 13, No. 3, pp. 481-492, March 1995.

[172] R. Baets, P.E. Lagasse, "Loss Calculation and Design of Arbitrarily Curved Integrated-Optic Waveguides," J. Opt. Soc. Am., Vol. 73, No. 2, pp. 177-182, February 1983.

[173] L. Lerner, "Minimum Bending Loss interconnection for integrated optics waveguides," Electronics Letters, Vol. 29, No. 9, pp. 733-735, 29th April 1993.

[174] F.J. Mustieles, E. Ballesteros, P. Baquero, "Theoretical S-Bend Profile for Optimization of Optical Waveguide Radiation Losses," Photonics Technology Letters, Vol. 5, No. 5, pp. 551-553, May 1993.

[175] R.G. Walker,"Simple and accurate loss measurement technique for semiconductor optical waveguides," Electronics Letters, Vol. 21, No. 13, pp. 581-583, 20 June 1985.

[176] Haruna M., Segawa Y., Nishihara H.,"Nondestructive and simple method of optical-waveguide loss measurement with optimisation of end-fire coupling," Electronics Letters, Vol. 28, No. 17, pp. 1612-1613, 13 Aug. 1992.

[177] K. H. Park, M. W. Kim, Y. T. Byun, D. Woo, S. H. Kim, S. S. Choi, Y. Chung, W. R. Cho, S. H. Park, and U. Kim, "Nondestructive propagation loss and facet reflectance measurements of GaAs/AlGaAs strip-loaded waveguides," Journal of Applied Physics, Vol. 78, No. 10, pp. 6318-6320, November 15, 1995.

[178] L. S. Yu, Q. Z. Liu, S. A. Pappert, P. K. L. Yu, and S. S. Lau, "Laser spectral linewidth dependence on waveguide loss measurements using the Fabry-Perot method," Applied Physics Letters, Vol. 64, No. 5, pp. 536-538, January 31, 1994.

[179] M. Allard, R.A. Masut, M Boudreau, "Temperature Determination in Optoelectronic Waveguide Modulators," Journal of Lightwave Technology, Vol. 18, No. 6, pp. 813-818, 2000.

[180] Henry Blauvelt, Al Benzoni, Jerry Byrd, Mark Downie, Charles Grosjean, Stuart Hutchinson, Robert Lee, Frank Monzon, Michael Newkirk, Joel Paslaski, Peter Sercel, David Vernooy, Rolf Wyss, "High Performance Planar Lightwave Circuit Triplexer with Passive Optical Assembly," Optical Fiber Communications, 2005, Paper OThU7.

[181] Xiaodong Zeng, Amir Naqwi, "Far-field Distribution of Double-Heterostructure diode laser beams," Applied Optics, Vol. 32, No. 24, pp. 4491-4494, 20 August 1993.

[182] Yajun Li, Joseph Katz, "Nonparaxial analysis of the far-field radiation patterns of double-heterostructure lasers," Applied Optics, Vol. 35, No. 9, pp. 1442-1451, 20 March 1996.

[183] Shojiro Nemoto, "Experimental evaluation of a new expression for the far field of a diode laser beam," Applied Optics, Vol. 33, No. 27, pp. 6387-6392, 20 September 1994.

[184] M. Nieto-Vesperinas, "Scattering and Diffraction in Physical Optics, " Section 6.4, Wiley, New York, 1991.

[185] J.D. Love, "Application Of A Low-Loss Criterion To Optical Waveguides And Devices," IEE Proceedings–J Optoelectronics, Vol. 136, No. 4, pp. 225-228, Aug. 1989.

[186] J.D. Love, W.M. Henry, W.J. Stewart, R.J. Black, S. Lacroix, F. Gonthier, "Tapered Single-Mode Fibers And Devices–Adiabaticity Criteria," IEE Proceedings–J Optoelectronics, Vol. 138, No. 5, pp. 343-354, Oct. 1991.

[187] V. Vusirikala, S.S. Saini, R.E. Bartolo, M. Dagenais, D.R. Stone, "Compact mode expanders using resonant coupling between a tapered active region and an underlying coupling waveguide," IEE Photonics Technology Letters, Vol. 10, No. 2, pp. 203-205, Feb 1998.

[188] C.W. Chang, M.L. Wu, W.F. Hsieh, "Design of low-loss tapered waveguides using the telescope structure compensation," IEEE Photonics Technology Letters, Vol. 15, No. 10, pp. 1378-1380, Oct. 2003.

[189] I.F. Lealman, L.J. Rivers, M.J. Harlow, S.D. Perrin, M.J. Robertson, "1.56μm InGaAsP/InP tapered active layer multiquantum well laser with improved coupling to cleaved singlemode fiber," Electronics Letters, Vol. 30, No. 11, pp. 857-859, 26th May 1994.

[190] J.H. den Besten, M.P. Dessens, C.G.P. Herben, X.J.M. Leijtens, F.H. Groen, M.R. Leys, M.K. Smit, "Low-Loss, Compact, and Polarization Independent PHASAR Demultiplexer Fabricated by Using a Double-Etch Process," Photonics Technology Letters, Vol. 14, No. 1, pp. 62-64, Jan. 2002.

[191] D. Sigogne, A. Ougazzaden, D. Meichenin, B. Mersali, A. Carenco, J.C. Simon, I. Valiente, C. Vassallo, L. Billes, "1.55μm polarization insensitive InGaAsP strained MQW optical amplifier integrated with short spot-size converters," Electronics Letters, Vol. 32, No. 15, pp. 1403-1405, 18th July 1996.

[192] G.A. Vawter, C.T. Sullivan, Joel R. Wendt, Robert E. Smith, Hong Q. Hou, John F. Klem, "Tapered Rib Adiabatic Following Fiber Couplers in Etched GaAs Materials for Monolithic Spot-Size Transformation," IEEE Journal of Selected Topics in Quantum Electronics, Vol. 3, No. 6, pp. 1361-1371, December 1997.

[193] Paul G. Suchoski, Ramu V. Ramaswamy, "Design of Single-Mode Step-Tapered Waveguide Sections," IEEE Journal of Quantum Electronics, Vol. QE-23, No. 2, pp. 205-211, Feb. 1987.

[194] M.A. Alam, et al., "Simulation and Characterization of the Selective Area Growth Process," Applied Physics Letters, Vol. 74, No. 18, pp. 2617-2619, 1999.

[195] M. Gibbon et al., "Selective-area low-pressure MOCVD of GaInAsP and related materials on planar InP substrates," Semiconductor Science and Technology, Vol. 8, pg. 998 1993.

[196] Jonathan E. Greenspan, "Alloy composition dependence in selective area epitaxy on InP substrates," Journal of Crystal Growth, 236, pp. 273280, 2002.

[197] J.E. Greenspan, C. Blaauw, B. Emmerstorfer, R.W. Glew, I. Shih,"Analysis of a time-dependent supply mechanism in selective area growth by MOCVD," Journal of Crystal Growth, 248, pp. 405410, 2003.

[198] J. E. Greenspan, X. Zhang, N. Puetz, and B. Emmerstorfer, "Growth mechanisms and modeling for metalorganic chemical vapor deposition selective-area epitaxy on InP substrates," J. Vac. Sci. Technol. A, Vol. 18, No. 2, pp.648-651, Mar/Apr 2000.

[199] J.E. Greenspan, I. Betty, R. Glew, R. Foster and S. Campbell, "Design of Vertical Tapers Using Selective-Area Epitaxy with Quantitative Modeling," MOVPE 10th, 2001.

[200] O. Kayser, R. Westphalen, B. Opitz and P. Balk, J. Cryst. Growth, 112, pp. 111, 1991.

[201] J.S.C. Chang, K.W. Carey, J.E. Turner and L.A. Hodge, J. Elec. Mat., 19, pp. 345, 1990.

[202] Jonathan E. Greenspan,"Selective Area Epitaxy for Indium Phosphide Based Photonic Integrated Circuits," Department of Electrical and Computer Engineering Ph.D. Thesis, McGill University, Montreal, August 2002.

[203] Richard Glew, Ian Betty, Jonathan Greenspan, "Method for Integrating Optical Devices in a Single Epitaxial Growth Step," U.S. Patent Publication, Pub. No. US2004/0147053 A1, July 29th 2004.

[204] R. Strzoda, G. Ebbinghaus, T. Scherg, N. Emeis, "Studies on the butt-coupling of InGaAsP-waveguides realized with selective area metalorganic vapour phase epitaxy," Journal of Crystal Growth, Vol. 154, pp. 27-33, 1995.

[205] Su Hwan Oh, Chul-Wook Lee, Ji-Myon Lee, Ki Soo Kim, Hyunsung Ko, Sahnggi Park, and Moon-Ho Park, "The Design and the Fabrication of Monolithically Integrated GaInAsP MQW Laser with Butt-Coupled Waveguide," Photonic Technology Letter, Vol. 15, No. 10, pp. 1339-1341, October 2003.

[206] F.C. Everstyn, P.J.W. Severin, C.H.J. van der Brekel and H.L. Peel, J. Electrochem. Soc., Vol. 119, pp. 925, 1970.

[207] R.A. Colclaser, "Microelectronics: Processing and Device Design", Wiley, New York, New York, 1980.

[208] D J Thomas, K Powell, M B Bourke, Y P Song, C Fragos, F.R. Shepherd and D. Ducharme, GaAs MANTECH Proceedings, May 2001

[209] D J Thomas, K Powell, M B Bourke, Y P Song, C Fragos, F.R. Shepherd and D. Ducharme, GaAs MANTECH Proceedings, May 2001

[210] N. Kim, F.R. Shepherd, M. Boudreau, I. Betty, "ICP Etching of optical waveguides in InP-based materials using HBr and Cl2 Chemistry," Eleventh Canadian Semiconductor Technology Conference Ottawa, Canada – 18-22 August 2003.

[211] J. Lu, X. Meng, A. J. SpringThorpe, F. R. Shepherd, M. Poirier, "Inductively coupled plasma etching of GaAs low loss waveguides for a traveling waveguide polarization converter, using chlorine chemistry," J. Vac. Sci. Technol. A Vol. 22, No. 3, pp. 1058-1061, May/Jun 2004.

[212] S. Vicknesh and A. Ramam, "Etching Characteristics of HBr-Based Chemistry on InP Using the ICP Technique," Journal of The Electrochemical Society, Vol. 151 No. 12, pp. C772-C780, 2004.

[213] K. Akita, T. Kusunoki, S. Komiya and T. Kotani, J. Crys. Growth, 46, pp. 783, 1979.

[214] H. Ishikawa, S. Miwa, T. Maruyama and M. Kamada, J. App. Phys., Vol. 71, pp. 3898, 1992.

[215] D.G. Knight, G. Kelly, J. Hu, S.P. Watkins, M.L.W. Thewalt, J. Cryst. Growth, 182, pp. 23, 1997.

[216] E.H. Sargent, D.A. Suda, A. Margittai, F.R. Shepherd, M. Cleroux, G. Knight, N. Puetz, T. Makino, A.J. Springthorpe, G. Chik and J.M. Xu, IEEE Phot. Tech. Lett., Vol. 10, pp. 1536, 1998.

[217] S. Ingrey, W. M. Lau, and N. S. McIntyre, J. Vac. Sci. Technol. A, Vol. 4, pp. 983, 1986.

[218] L.A. Coldren, K. Furuya, and B.I. Miller, J. Electrochem. Soc., 130, pp. 1918, 1983.

[219] R.D. Dupuis, D.G. Deppe, C.J. Pinzone, N.D. Gerrard, S. Singh, G.J. Zydzik, J.P. van der Ziel, and C.A. Green, J. Cryst. Growth, 107, pp. 790, 1991.

[220] H. Nishi, M. Yano, Y. Nishitani, Y. Akita, and M. Takusagawa, Appl. Phys. Lett., Vol. 35, pp. 232, 1979.

[221] A.C. Adams, "Dielectric and Polysilicon Film Deposition" in VLSI Technology, ed. S.M. Sze, McGraw Hill

[222] T.R. Hayes, M.A. Dreisbach, P.M. Thomas, W.C. Dautremont-Smith and L.A. Heimbrook, J. Vac. Sci. Technol. B, Vol. 7, pp. 1130, 1989.

[223] S.J. Pearton, U.K. Chakrabarti and F.A. Baiocci, Appl. Phys. Lett., Vol. 55, pp. 1633, 1989.

[224] M. Heinbach, J. Kaindi, G. Franz, "Lattice Damage in III/V Compound Semiconductors caused by dry etching," Appl. Phys. Lett., Vol. 67, No. 14, pp. 2034-2036, October 1995.

[225] B. Garrett and E.J. Thrush, J. Cryst. Growth, 97, pp. 273, 1989.

[226] V.S. Ban, G.C. Erikson, S. Mason and G.H. Olsen, J. Electrochem. Soc., 137, pp. 2904, 1990.

[227] F. Capasso, R.A. Logan, P.W. Foy, S. Sumski, and D.D. Manchon, Electron. Lett., Vol. 16, pp. 241, 1980.

[228] T. Brenner and H. Melchior, J. Electrochem. Soc., Vol. 141, pp. 1954, 1994.

[229] J.F. Wagner and C.W. Wilmsen, Physics and Chemistry of III-V Compound Semiconductor Interfaces, Plenum Press, New York, New York, 1985.

[230] C. Tomiyama, A. Kuramata, S. Yamazaki and K. Nakajima, J. Crys. Growth, 84, pp. 115, 1987

[231] J. Finders and J. Geurts, J. Crys. Growth, 107, pp. 151, 1991.

[232] Y.D. Galeuchet, P. Roentgen and V. Graf, J. Appl.Phys., Vol. 68, pp. 560, 1990.

[233] H. Chou, and W.V. Sorin, "High Resolution and High Sensitivity Optical Reflection Measurements using White Light Interferometry," Hewlett-Packard Journal, Vol. 44, No. 1, pp. 39-48, 1993.

[234] S.F. Yu, N.Q. Ngo, "Simple Model for a Distributed Feedback Laser Integrated with a Mach-Zehnder Modulator," IEEE Journal of Quantum Electronics, Vol. 38, No. 8, pp. 1062-1074, August 2002.

[235] Xun Li, W.P. Huang, D.M. Adams, C. Rolland, and Toshihiko Makino, "Modeling and Design of a DFB Laser Integrated with a Mach-Zehnder Modulator," IEEE Journal of Quantum Electronics, Vol. 34, No. 10, pp. 1807-1815, October 1998.

[236] Adrian J. Devasahayam et al., "Material properties of ion beam deposited oxides for the optoelectronic industry," J. Vac. Sci. Technol. A, Vol. 20, No. 3, pp. 1135-1140, May/June 2002.

[237] Kendall P.C., Roberts D.A., Robson P.N., Adams M.J., Robertson M.J., "New formula for semiconductor laser facetreflectivity", IEEE Photonics Technology Letters, Vol. 5 No. 2, pp. 148-150, Feb. 1993.

[238] M. Reed, T.M.Benson, P.C. Kendall, and P. Sewell, "Antireflection-coated angled facet design," IEE Proceedings J-Optoelectronics, Vol. 143, No. 4, pp 214-220, Aug. 1996.

[239] H. El-Refaei, I. Betty, and D. Yevick, "The Application of Complex Pad Approximants to Reflection at Optical Waveguide Facets, IEEE Photon. Technol. Lett., Vol. 12, No. 2, pp. 158160, Feb. 2000.

[240] Hatem El-Refaei, David Yevick, Ian Betty, "Stable and noniterative bi-directional beam propagation method," IEEE Photonics Technology Letters, Vol. 12, No. 4, pp. 389-391, Apr. 2000.

[241] F. A. Milinazzo, C. A. Zala, and G. H. Brooke, "Rational square root approximations for parabolic equation algorithms, J. Acoust. Soc. Amer., Vol. 101, No. 2, pp. 760766, Feb. 1997.

[242] C. Yu and D. Yevick , "Application of the bidirectional parabolic equation method to optical waveguide facets, J. Opt. Soc. Amer. A, Vol. 14, No. 7, pp. 14481450, July 1997.

[243] J. Yamauchi, M. Mita, S. Aoki, and H. Nakano, "Analysis of Antireflection Coatings using the FD-TD Method with the PML Absorbing Boundary Condition," IEEE Photonics Technology Letters, Vol. 8, No. 2, pp. 239-41, 1996.

[244] K. Prosyk, R. Moore, I. Betty, R. Foster, J. Greenspan, P. Singh, S. O'Keefe, J. Oosterom, P. Langlois, "Low Loss, Low Chirp, Low Voltage, Polarization Independent 40Gb/s Bulk Electro-Absorption Modulator Module," Optical Fiber Communications Conference, TuP3, 2003.

[245] C. Duchet, et al., ECOC 97, p. 179, 1997.

[246] R. Weinmann, et. al., Photon. Tech. Lett., Vol. 8, No. 7, p. 891, 1996.

[247] L. Keldysh, et al., Sov. Phys. Semicond., Vol. 3, p. 876, 1970.

[248] C. Duchet, et al., Electron. Lett., Vol. 33, No. 3, p. 233, 1997.

[249] K. Wakita, et al., OFC97, WG3, p. 137, 1997.